Eddy Vertical Structure and Variability: vortex evolution and the geography of geostrophic turbulence

Jacob Steinberg

A dissertation

submitted in partial fulfillment of the

requirements for the degree of

Doctor of Philosophy

University of Washington

2020

Reading Committee:

Charles C. Eriksen, Chair

Parker MacCready

Craig Lee

Program Authorized to Offer Degree:

School of Oceanography

University of Washington

Abstract

Eddy Vertical Structure and Variability: vortex evolution and the geography of geostrophic turbulence

Jacob Steinberg

Chair of the Supervisory Committee:

Charles Eriksen

School of Oceanography

Glider observations of submesoscale and mesoscale eddy structure, behavior, and evolution are analyzed revealing both processes of eddy decay and statistical properties of geostrophic turbulence (i.e. mesoscale eddy-eddy interactions resulting in energy transfer across scales). These observations, made by Seaglider and Deepglider autonomous underwater vehicles, and their interpretation are split into three sections: 1) the observed evolution and decay of a single California Undercurrent eddy, 2) sampling platform biases and aliasing diagnosed via simulated glider sampling in high resolution ocean models, and 3) observations of geostrophic turbulence from eddy vertical structure in the North Atlantic (analysis of hundreds of full-depth profiles of isopycnal vertical displacement and geostrophic velocity).

Three Seagliders, deployed off of the Washington coast in 2013, located a subsurface intensified California Undercurrent eddy completing repeat eddy-bisecting transects over a three month period. These transects were used to create and compare 'snapshots' of eddy depth-radial structure at different times. The observed evolution of this eddy can be explained by both adjustment to new background conditions, weaker stratification at the eddy core depth and translation multiple degrees northward, and decay via lateral thermohaline intrusions. Eddy total mechanical energy, salt content, and the magnitude of the core potential vorticity anomaly all decreased while core spice and dissolved oxygen variance increased tenfold. While these coherent eddies are capable of translating hundreds of kilometers away from their formation sites, both adjustment and decay appear as relevant processes moderating their behavior.

The idealized simulation of full-depth glider sampling in two high resolution ocean models was then carried

out to quantify the accuracy of glider derived profiles of isopycnal vertical displacement and geostrophic velocity. These profiles are interpreted in the context of mesoscale eddy structure, interactions, and energetics. Glider vertical velocity, glide slope, and instrument noise were varied while simulating the sampling of hundreds of profiles in ROMS and HYCOM numerical simulations. The error in glider derived geostrophic velocity profiles, calculated as the difference from model velocity fields, is found to be on average less than 0.02 m s^{-1}. Projection of both model and glider derived profiles of displacement and velocity onto normal modes reveals the glider sampling framework to be capable of resolving model eddy vertical structure from the first through at least the tenth baroclinic mode, with increased resolution for steeper glide slopes.

This glider analysis framework was then employed to explore eddy vertical structure from hundreds of full-depth temperature and salinity profiles completed by Deepgliders in the North Atlantic between 2014 and 2019. Gliders were deployed and piloted to five sites, each associated with varied levels of mesoscale eddy energy. At each site, gliders completed multi-month missions, the longest nearly 9 months, to observe eddy vertical structure and variability. Full-depth profiles permit the projection of displacement and velocity profiles onto dynamical modes and calculation of vertical wavenumber spectra of eddy potential and kinetic energy. These spectra, with a dominant fraction of energy in the first baroclinic mode, follow a linear log-log slope not different than the k^{-3} slope predicted by Charney [1971] and reveal potential energy to dominate kinetic at modes three and higher. Displacements of order 100 m and velocities exceeding 0.05 m s^{-1} at depths greater than 2000 m were regularly observed suggesting bottom friction to be dynamically relevant in the dissipation of eddy kinetic energy. Subsurface intensified coherent vortices with core depths greater than 1000 m were also observed in multiple years with full-depth structure noticeable at the surface in concurrent altimetric observations and at the seafloor with order 100 m displacements. Away from sites of rough topography and boundary currents these full depth observations of eddy vertical structure, collected on a near-daily basis for months at a time, reveal geostrophic turbulence theory to well describe low mode mesoscale eddy energetics and evolution.

Contents

1 Chapter 1: Introduction

1.1 Overview

This thesis combines analyses from two observational efforts, the first carried out to observe and characterize the decay of a single California Undercurrent eddy in the eastern North Pacific, and the second to interpret full-depth eddy vertical structure through the lens of geostrophic turbulence in the North Atlantic. These observational efforts center around the use of buoyancy driven Seaglider and Deepglider autonomous underwater vehicles (gliders), originally developed at the University of Washington to persistently sample remote regions of the ocean with high spatial and temporal resolution for durations as long as one year. These vehicles principally measure temperature, salinity, and pressure along slant-profiles and are employed to explore eddy structure, evolution, and influence on oceanic energy and tracer transport across a range of spatial and temporal scales.

The following analyses of glider observations from deployments spanning the last six years have specifically focused on sampling across meso- and submesoscales. These terms are associated with dynamics that well describe the behavior of ocean flows on spatial scales ranging from a few to hundreds of kilometers evolving on times scales of a few days to months. Motions of these classes represent a dominant fraction of oceanic kinetic energy and are responsible for the redistribution of ocean heat content as well as the stirring and mixing of salt and tracers. Using glider observations from the last six years to test theoretical relationships as well as to quantify the role of specific processes responsible for the redistribution of heat and salt, we can develop more accurate predictive tools for a changing climate.

It is important early on to offer a definition of an eddy, and whether it is best considered a noun or a verb. In an oceanic context, two distinct definitions, each relevant in different settings, are: 1) an eddy is an isolated, coherent, near azimuthally symmetric rotating feature capable of material transport and 2) an eddy is a perturbation in both density and velocity fields from some predefined mean state. These definitions can be used to described sea level anomalies identified and tracked from satellite altimetry, but also as instabilities and the meandering of slowly evolving flows at the surface or at depth. In this thesis we refer to eddies in both the individual sense (identified as coherent vortices: the California Undercurrent eddy in chapter two and the two cold core subsurface intensified

lenses observed at station BATS in chapter four) and in the more general sense of the eddy field (identified as perturbation densities and velocities observed at stationary sampling sites evolving on weekly/monthly time scales).

The results of analyses completed for my master's degree are included here as the second chapter of this thesis and detail the deployment of three Seagliders off of the Washington coast in 2013 to find, profile, and observe the evolution of a single California Undercurrent eddy for as long as vehicle endurance allowed. Observations of eddy depth-radial structure throughout a three-month period reveal evolution and decay patterns moderated by changing background conditions in addition to lateral thermohaline intrusions. These results suggest that as eddies propagate away from sites of formation, they adjust in aspect ratio and experience decay via along-isopycnal mixing at time scales much longer than advective time scales. Documenting eddy behavior over the course of their lifetimes in this manner is important because it enables the estimation of tracer and heat transport from sites of eddy generation to destruction. These long-lived eddies are found throughout the world ocean while their contribution to the large scale redistribution of heat, salt, and tracers is still not fully resolved.

The third and fourth chapters of this thesis focus on the use of recently developed Deepgliders to observe full-depth eddy structure with high spatio-temporal resolution. Traditionally, observations of full-depth structure, inherently difficult to collect, offer either high spatial or temporal resolution but not both. Following the development of these vehicles, gliders were deployed at multiple locations throughout the North Atlantic where they each repeatedly profiled on a near-daily basis for multi-month missions. These profiles, collected at sites associated with varied background levels of mean eddy kinetic energy, first permit an analysis of the temporal evolution of full-depth eddy structure with high vertical resolution, and second, enable a comparison across sites to explore factors controlling the geographic variability of vertical structure. These analyses focus on near-daily high vertical resolution observations at depths greater than 2000 m, newly available as a result of the capabilities of Deepglider. Geographic and temporal variability of density and velocity anomalies from the surface to the seafloor then reveal how and where bottom friction becomes relevant in the ocean energy cycle.

Chapter three considers the effects of various glider sampling speeds and geometries on isopycnal vertical displacement and geostrophic velocity profile estimate accuracy. These effects are quantified though simulation

of glider sampling in two high resolution ocean models to diagnose biases and aliasing inherent in the framework employed to analyze vertical structure. Normal modes, a set of dynamically relevant orthogonal functions derived from quasi-geostrophic equations of motion, provide a basis from which to quantify both model and glider vertical structure resolution. Results from this chapter largely validate the framework employed to detail vertical structure and justify its use with observations. Observations from ten different Deepglider missions, completed at various locations in the North Atlantic over the past five years, are analyzed in the fourth and final chapter. This chapter employs the analysis framework tested in the third chapter to explore eddy vertical structure and variability in the North Atlantic. Eddy vertical structure is primarily considered from profiles of isopycnal vertical displacement and geostrophic velocity (calculated from along-track density gradient estimates). The observed vertical structures are interpreted using empirical orthogonal functions alongside vertical modes. Results reveal both spatial and temporal variability across sampling sites as well as full-depth structure of both surface and subsurface intensified eddies. Predictions from geostrophic turbulence theory regarding the partitioning of kinetic and available potential energy across vertical scales agree with observations of eddy vertical structure, but with important differences at each mission site. Spectral slopes predicted from traditional scaling arguments and associated with the isotropic cascade of enstrophy from large to small scales generally agree with observations.

The thesis is organized with each main chapter written as a stand-alone paper; the first published in the Journal of Physical Oceanography (`https://journals.ametsoc.org/doi/full/10.1175/JPO-D-18-0033.1`), the second recently accepted for publication in the Journal of Atmospheric and Oceanic Technology ("Glider Sampling Simulations in High Resolution Ocean Models", Steinberg and Eriksen, J-TECH, *in press*), and the third to be submitted shortly in an abbreviated form.

1.2 Acknowledgements

This work would not have been possible without the support of National Science Foundation grants 1153980 and 1736217. I'm extremely grateful to have had the opportunity to carry out this research at the University of Washington. I would first like to thank my advisor Charlie for all of his support, guidance, and advice throughout the last six years. As a result of such encouragement and patience, I have learned how to carry out meaningful

research and gained valuable experience deploying, piloting, and recovering gliders in a variety of settings. I'm also grateful for the independence I was given to do my work and explore new ideas while learning both the basics and details of observational physical oceanography. Having had the opportunity to work with an experienced, competent, and excited team (James Bennett, Fritz Stahr, and Kirk O'Donnell), I am sad to leave, but happy to have a standard with which to hold future research groups accountable. I am grateful for their patience and support in welcoming me into the world of gliders and am thankful for their encouragement and willingness to teach me proper piloting skills as well as trusting me to carry out successful deployments and missions. I would additionally like to thank those at the Seaglider Fabrication Center and those involved with small boat operations here in Seattle for their help readying, deploying, and testing gliders to ensure their field readiness. Thanks to the officers and crew of the *R/V Atlantic Explorer*, *CCGS John P. Tully*, *M/V Tommy Cod*, *F/V Valentine*, and Seakeepers (*M/Y Mystique*) for their professionalism and capability in carrying out numerous glider deployments and recoveries.

I'd also like to thank my advisory committee (Parker, Craig, Steve, and Jim) for their advice, interest in my research, and investment in my progress. They have always been willing to discuss thoughts and ideas while ensuring I made good progress. I would likewise have been unable to make such progress without the assistance and advice of many faculty and administrative staff here at the University of Washington. In particular, I'd like to thank Peter Rhines for his mentorship during my time at UW. I am extremely fortunate to have had the opportunity to take classes taught by Peter, but also work alongside him in the geophysical fluid dynamics lab. Both teaching and experimenting in the lab has proven invaluable in my development as a physical oceanographer. I'd also like to thank Miguel Jimenez-Urias for showing me the ropes in the lab while both having fun and offering needed interpretations of difficult concepts.

Throughout my time at the University of Washington the community of friends and colleagues that I have been fortunate enough to interact with have made coming to work everyday more than enjoyable. From the graduate students in my cohort (Elizabeth Brasseale, Hally Stone, Shirley Leung, Elisa Bonnin, and Marta Wolfshorndl...also those from the earlier days...Will, Ben, Tessa) to my friends and neighbors Sarah Ragen, Katy Christensen, Amy Wyeth, Erik Fredrikson and Earle Wilson, I am grateful to have all of you in my life. Special thanks to Elizabeth

for the near-daily camaraderie, without which my time at UW would have been much less enjoyable. And of course thanks to my good friend Justin Penn who has helped me recognize the importance of not taking ourselves too seriously. I'd also like to thank my good friends Micah, Adam, and Adam who have been excellent compatriots in the quest to get outside and play in the both the desert and the mountains. Of course all of this work would have been impossible without the help, encouragement, and support of my family (Susie, Al, and Katey). You all are the best.

2 Chapter 2: Observed Evolution of a California Undercurrent Eddy

2.1 Introduction

Eddies play important yet often undetected roles in the transport and distribution of oceanic heat, salt, and nutrients. They occupy a range of spatial scales, are found at various depths in all oceans, and are inherently transient. Submesoscale coherent vortices (SCVs) – gradient-wind balanced, preferentially anticyclonic, subsurface intensified, isolated lenses with horizontal length scales comparable to or smaller than the first baroclinic deformation radius and Rossby numbers $\mathcal{O}(1)$ [McWilliams, 1985, D'Asaro, 1988a] – are a distinctive class of long-lived eddies capable of trapping and transporting core waters for many months over hundreds of kilometers [McWilliams, 2016]. Their ubiquity, potential role in the transfer of energy from large to small scales, and ability to redistribute bulk quantities of heat, salt, and nutrients motivates the study of their behavior and evolution.

The prevalence of SCVs has been recognized through frequent observations that are often unintentional [*e.g.,* Huyer et al., 1998, Collins et al., 2013]. Due to a strong potential vorticity gradient bounding an isolated relatively homogeneous core [Elliot and Sanford, 1986], SCVs that avoid disintegration due to collisions with topography [*e.g.,* Torres and Gomez-Valdes, 2017], or merging and interaction with other eddies, exhibit a relatively slow decay driven by dissipative processes. Persistent, high-resolution observations of a Mediterranean water eddy ("Meddy", an archetypal SCV) over a multi-year period illustrated losses of heat and salt driven by lateral intrusions [Armi et al., 1989, Hebert et al., 1990], similar to those observed elsewhere along sharp thermohaline fronts [*e.g.,* Shcherbina et al., 2009, 2010]. Similar extended tracking and observation of individual features is informative of the processes moderating SCV translation, longevity, and decay, but is a challenge due to these eddies' small size and subsurface intensification and is as a consequence more rare. As a result, quantitative estimates of the contribution of coherent submesoscale eddies to regional and global tracer transport and energy flux remain poorly constrained. Improvements in high-resolution models have allowed exploration of SCV propagation and evolution behavior [*e.g.,* McWilliams et al., 1985, McWilliams and Gent, 1986, McWilliams, 1988, Morel and McWilliams, 1997, Molemaker et al., 2015], though further observational counterparts are needed [McWilliams, 2016]. In this article, we describe results from persistent, three dimensional spatial surveys of a submesoscale California Current

eddy using near-continuous autonomous observations over three months.

California Undercurrent (CU) eddies, termed "Cuddies" [Garfield et al., 1999, Collins et al., 2013, Pelland et al., 2013], have characteristics similar to those of SCVs and are frequently found in the California Current System (CCS) in the eastern North Pacific Ocean. Cuddies are long-lived monopole anticyclones, with radii 10-30 km and velocity maxima at the base of the permanent pycnocline. Cuddies originate along the continental slope in the CU, which is a wind-forced subsurface jet driven by local and remote alongshore wind forcing, carrying warm, saline, low oxygen, high nutrient Pacific Equatorial Waters (PEW) to higher latitudes [Hickey, 1979, Huyer et al., 1998, Chereskin et al., 2000, Connolly et al., 2014, Thomson and Krassovski, 2015]. Peak poleward velocities of 0.3-0.5 m s^{-1} are observed in late summer and early autumn offshore of the continental shelf break and at a core depth between 100-300 m; in the northern CCS, the peak PEW signature is found on the potential density surface $\rho_\theta = 1026.55$ kg m^{-3} [Hickey, 1979, Thomson and Krassovski, 2010, Pelland et al., 2013]. Offshore of the core jet, the broader surface-intensified California Current (CC) flows equatorward carrying waters from the North Pacific [Auad et al., 2011]. In winter, north of 43°N and near the shelf break, surface currents become poleward and are denoted the Davidson Current [Hickey, 1979].

Collins et al. [2013] analyzed looping anticyclonic RAFOS float trajectories to track Cuddies originating along the continental slope within the CCS. Floats became trapped in Cuddies as they formed and translated offshore, revealing stable, west-southwestward drift into the more quiescent North Pacific interior. This is consistent with expectations of eddy self-advection due to the β-effect [McWilliams et al., 1985, McWilliams and Gent, 1986, Morel and McWilliams, 1997], observed for surface-intensified mesoscale eddies in a global eddy census using gridded altimetry [Chelton et al., 2011]. A notable Cuddy trajectory ended 1600 km to the southwest of the initiation of looping, providing further evidence of these eddies' potentially long life [Collins et al., 2013]. Lukas and Santiago-Mandujano [2001] corroborate these results with observations of an extreme water mass anomaly near the Hawaiian Islands, which they conclude likely originated in the CU. The properties of mature eddies are consistent with a range of generation scenarios including baroclinic instability, topographic interaction, and bottom friction effects. High resolution models explain Cuddy formation as resulting from a combination of flow separation over complex topography and frictional interactions with the continental slope [Molemaker et al., 2015]. Torres and

Gomez-Valdes [2017] suggest that the meandering of the CU induced by synoptic-scale wind events can also play an important role. Observations capturing the formation of a Peru-Chile Undercurrent eddy, a type similar to Cuddies, corroborate flow separation over rough topography and bottom friction as a formation mechanism [Thomsen et al., 2016]. These observations affirm eddy formation as a complex process and highlight the importance of frictional bottom interactions suggested by D'Asaro [1988b] and Molemaker et al. [2015].

Cuddies contain core water properties similar to those of the CU, which distinguish them from cooler and fresher background waters as they move offshore. Spice, a state variable defined as a measure of thermohaline variability along isopycnals [Flament, 2002] is useful for identifying CU water mass properties within Cuddies as well as interleaving of water masses as they move into cooler fresher offshore waters. This pathway for the offshore advection of PEW water can help explain the observed poleward weakening of the CU water mass signal as it mixes with the surrounding Pacific Subarctic Upper Water [Thomson and Krassovski, 2010]. Observations of twenty individual Cuddies in a sequence of repeat Seaglider sections carried out over the Washington continental slope between 2003 and 2009 are consistent with the hypothesis that these eddies act as a primary agent of lateral stirring between the CU and its surroundings [Pelland et al., 2013]. By estimating eddy bulk properties, frequency of occurrence, and the average decay of heat and salt content in the CU with latitude, Pelland et al. [2013] estimated that 44% of the heat and salt lost from the CU as it flows poleward in this region may move offshore via Cuddies. These observations also revealed instances of enhanced fine-structure at Cuddy edges, suggestive of lateral intrusions, though the role that intrusions play in the decay of typical Cuddies remains unclear [Pelland et al., 2013].

In order to investigate mechanisms moderating eddy evolution, we deployed multiple Seaglider autonomous underwater vehicles (AUVs) to identify and track a single Cuddy in the same region sampled by Pelland et al. [2013], with the intent of continuously observing the structure and decay of an individual Cuddy for as long as vehicle endurance and eddy detectability allowed. These surveys combine analysis methods developed from repeat observations of other types of SCVs [D'Asaro, 1988a, Elliot and Sanford, 1986, Hebert et al., 1990] with AUV technology that has the ability to provide relatively high resolution spatial and temporal observations over weeks or months [Martin et al., 2009, Bosse et al., 2016]. The main goals of this study were to dynamically describe

a Cuddy's structure, observe its evolution, and quantify its decay. The following sections detail the methods of data collection and analysis, along with the eddy's kinematic and dynamic evolution, core property changes, and observations of thermohaline interleaving. A discussion and conclusions follow, including consideration of idealized eddy adjustment to the surrounding environment and partial erosion.

2.2 Data Collection

In October 2013, three Seagliders ("gliders"), designated SG189, SG194, and SG195 [Eriksen, 2017a,b,c], were deployed from a chartered sport fishing vessel from Wesport, WA to find and continuously survey a single Cuddy. An additional glider, SG108, operated by the University of Washington Applied Physics Laboratory as part of the Northwest Association of Networked Ocean Observing Systems (www.nanoos.org), simultaneously carried out repeat transects along a track crossing the Washington continental slope (Fig. 2.1). This glider provided a simultaneous description of the background state.

Seagliders are buoyancy driven, autonomous underwater vehicles that profile the upper 1000 m of the water column measuring temperature, conductivity, and pressure on both ascent and descent [Eriksen et al., 2001]. The result of each ∼8 hr glider dive-climb cycle is pair of vertical profiles along a sawtooth (nominal 1:3 vertical:horizontal glide slope) path roughly 6 km in horizontal length. Gliders in this study sampled temperature and conductivity using a SeaBird Electronics thermistor and conductivity cell similar to those employed on SeaBird's SBE-3 and SBE-4 instruments, which were processed to estimate salinity S using methods consistent with those described in Pelland et al. [2013, 2016]. These measurements allowed for computation of potential temperature θ [°C] referenced to the sea surface, potential density anomaly σ_θ ($= \rho_\theta - 1000$ [kg m^{-3}]), and spice π_θ. Spice is used to highlight different water mass properties and to identify Cuddy and CU waters. For a for a given density, high spice is associated with warm salty Cuddy core water. Seagliders also estimate a surface to 1000 m depth-averaged current (DAC), with 0.01 m s^{-1} accuracy, over each dive-climb cycle from the difference between GPS-tracked over-ground and dead-reckoned displacements. Dissolved oxygen concentration per unit mass O_2 (units of μmol kg^{-1}) was also measured using the Aanderaa 4330 Optode, in addition to optical backscatter on 470 nm and 700 nm wavelengths and chlorophyll fluorescence using the WETLabs ECO Puck.

An individual Cuddy was found on November 20, 2013 and tracked along the continental slope offshore of Washington and Vancouver Island coasts (Fig. 2.1). Tracking commenced at 47.55°N, 125.4°W and ended on approximately February 25, 2014 at 49.8°N, 128.1°W due to the inability to further identify a coherent Cuddy from the data returned by the gliders. This region falls within the northern portion of the CCS where winter flow at the shelf break is on average poleward both at the surface and at depth [Pelland et al., 2013]. In this study, the Cuddy path was largely poleward, suggesting that this eddy was caught in the prevailing background flows before reaching the quiescent interior North Pacific Ocean. Glider tracks completed during the Cuddy tracking period, as well as an estimated eddy translation path, highlight this poleward propagation (Fig. 2.1). Eddy center position estimates are separated into segments contributing to Cuddy evolution analysis described below. Including SG108, a total of 1201 glider dive-climb cycles were carried out between November 20, 2013 and March 21, 2014 of which 972 profiles contributed in constructing Cuddy snapshots.

During tracking, basic eddy properties and background flow were estimated by assimilating glider observations of isopycnal separation and depth-averaged current into a simplified model using the extended Kalman Filter (EKF). The EKF is a useful tool for sequentially estimating the properties of systems such as eddies, in which observations are nonlinear functions of the system state [Ide and Ghil, 1997a,b]. After completion of the surveys, a "smoother" – an algorithm for refining initial EKF estimates based on data collected at later times [Gelb, 1974] – was applied, and estimates of eddy position, background flow, and position uncertainty derived from this smoother are used in the analyses that follow. The simple eddy model and estimation procedure are summarized in Appendix A. Pelland et al. [In Press] describes the EKF and smoother methodology and its application to automated glider navigation in greater detail.

2.3 Methods

2.3.1 Cuddy Tracking

Throughout the tracking period, the survey gliders were oriented and directed to make repeat transects across the Cuddy. A complete transect was composed typically of eight dive-climb cycles taking two to three days to complete. A total of 98 Cuddy transects of lengths between 6 km and 53 km were collected. Of these, 58 transects

of at least 25 km are included in this analysis. Nominally, one glider was oriented north-south while a second was oriented east-west; northwest-southeast or northeast-southwest tracks (Fig. 2.1) are due to the east-west transects taking place relative to a poleward-propagating eddy center. Profile data from a sample transect (eleven dive-climb cycles collected by SG195 in December 2013; Fig. 2.2) illustrate the relatively warm, saline weakly stratified layer at the core of the target Cuddy. Here, stratification refers to the magnitude of the vertical derivative of potential density.

The ability to effectively survey the target Cuddy varied through time due to changes in glider availability and communications, details in piloting strategy, and eddy translation speed. Translation speeds approached 0.1 m s^{-1} at times, with a net speed of 0.084 m s^{-1} poleward along the continental slope during the period 6 January to 10 February 2014, though with considerably lower speeds previous and subsequent to this five-week interval of fast translation. Survey tracks were coarser during the period of rapid poleward translation, but still sufficient to provide bulk estimates of eddy structure at some times.

2.3.2 Processing Framework

Throughout the survey period and for the dedicated survey gliders, instances of elevated spice in the main pycnocline (200 m depth), and greater vertical extent of high spice waters, indicate the center of a cross-eddy transect similar to that in Figure 2.2 (Fig. 2.3). Recall that SG108 (Fig. 2.3a) did not sample the Cuddy repeatedly; the variability in spice over longer periods than the other gliders reflects its sampling of CU waters near the shelf break, then cooler, fresher offshore waters on successive cross-slope transects.

All profiles were referenced to the moving Cuddy center position in space and time, using the EKF smoother eddy center estimates (Appendix A). The position of the center at the time of each glider sample was determined and radial distance was computed assuming linear Cuddy translation between each EKF estimate. Each profile was vertically bin-averaged using overlapping bins to grid each profile in 2 m increments from 0 to 150 m, 5 m increments from 150 to 300 m, and 10 m increments deeper than 300 m; bin increments were chosen to reflect varying glider temporal sampling rates. Profiles without bin-averaging were also considered for analysis of vertical fine-structure as will be discussed below.

A total of 11 non-overlapping time windows, each five days long, were used to create 11 Cuddy "snapshots" that could be compared with one another. Contributions to each snapshot from gliders varied throughout the survey period, with at least two profiling the Cuddy at a given time (Fig. 2.3). The time bounds of each window were chosen to reflect the availability of high-quality transects and to maximize the spatial extent of available Cuddy measurements.

In adopting this procedure, is is assumed that changes in Cuddy vertical-radial structure over the course of each five-day window are small relative to bulk evolution over the course of the surveys. This follows from the expectation that at short time scales diffusivity dominates eddy evolution and estimates of an effective eddy diffusivity time scale fall between 80 - 290 days, varying with the strength of radial temperature and salinity gradients [Joyce, 1977, Hebert et al., 1990, Ruddick and Richards, 2003, Pelland et al., 2013]. The time windows do not include all data collected during the surveys, but reflect all periods for which a reliable estimate of eddy structure and dynamics could be obtained (Fig. 2.3e). Variability in Cuddy translation speed corresponds to the variable length of each five-day segment. Time window five is highlighted and used as an example in the subsequent detailing of Cuddy structure and dynamics (Fig. 2.1 inset).

Since the analyses in this manuscript focus on time windows during which the eddy was sampled particularly densely, the results are not overly sensitive to the method used to determine the eddy position (Appendix A). Use of an alternate method to estimate the eddy center during each window, which minimized the square angular differences between observed currents and those from an idealized azimuthally symmetric vortex, resulted in typical differences from the EKF smoother eddy position of < 1 km. While this alternate method did not assume eddy azimuthal velocity structure, vortex strength, or vortex size, the results were still consistent with EKF estimates, but more sensitive to time window selection.

A cylindrical coordinate system was adopted in radius (r), and height (z) where relevant eddy quantities were assumed to be spatially independent of azimuthal angle [Elliot and Sanford, 1986, D'Asaro, 1988a, Pelland et al., 2013]. Though the survey data in this study are not sufficiently dense to test the validity of this assumption, there was little evidence to contradict it in the individual transects that were examined (*e.g.,* Fig. 2.2). Relevant eddy quantities, including spice, were then referenced to the moving center and associated with a radial distance

(Fig. 2.4a). The 51 total profiles collected during time window five were almost entirely collected with their mid-depth point at $r < 23$ km (Fig. 2.4b); gliders were generally instructed to turn around and begin a new transect beyond this radius.

Referenced to the moving center, DAC vectors minus the EKF smoother estimated background mean flow $\mathbf{u}_{\text{back}}$ during each window (DAC$-\mathbf{u}_{\text{back}}$) and the azimuthal component of each of these vectors DAC$_\phi$ were considered in analyzing eddy azimuthal symmetry and velocity structure (Fig. 2.4c). The differences between DAC$-\mathbf{u}_{\text{back}}$ and DAC$_\phi$ may reflect uncertainty in the Cuddy center estimate, the mean background flow vector, aliased variability due to internal waves and tides, errors in the assumption of axisymmetry and spatially uniform background flow, and/or eddy radial currents. Vertical distance separating two isopycnals was also considered in analyzing Cuddy radial structure (Fig. 2.4c inset). The chosen isopycnals ($\sigma_\theta = 26.45$ kg m^{-3} and $\sigma_\theta = 26.65$ kg m^{-3}) vertically bound the Cuddy core and their separation decreases to background levels with radius from the eddy core. Within each time window, DAC$_\phi$ and a smoothed version, computed using an interpolation technique described below, increase with radius to a maximum speed at radii of 10 - 15 km before decaying back towards zero (Fig. 2.4d).

2.3.3 Interpolation

In each time window, one dimensional Gauss-Markov interpolation [Bretherton et al., 1976, Le Traon, 1990] was used to map observed scalar quantities to a regular radial grid extending from the Cuddy center to 28 km, in 0.5 km intervals, on each vertically bin-averaged depth surface. This procedure was used to create radial-vertical grids of θ, S, σ_θ, π_θ, and O_2, along with a radial grid of DAC_ϕ, for each of the 11 windows. Profiles completed within radii less than 2.5 km were copied, paired with negative radius values, and used to extend the observation domain from 0 km to -2.5 km; this enforces the condition that isopycnal surfaces are horizontal and that eddy azimuthal currents are zero at the origin ($r = 0$).

The interpolation was performed using a horizontal decorrelation length scale of 15 km. The choice of decorrelation length scale is intended to filter noise due to internal waves and high-frequency or wavenumber phenomena [Rudnick and Cole, 2011] while retaining robust aspects of the Cuddy structure. By collapsing all glider profiles completed within a five-day time window at various locations surrounding the Cuddy into one horizontal dimen-

sion, data density was greatly increased; this azimuthal averaging decreases the effect of noise, allowing a shorter smoothing scale than used previously to analyze eddies in this region [Pelland et al., 2013].

Use of this interpolation routine required a background field of all scalar quantities. For each window, profiles collected within 10 days of the midpoint time at a radius greater than 20 km and less than 35 km were averaged along depth surfaces to yield background profiles of θ, S, σ_θ, and O_2. These conditions were chosen in order to yield profiles with no observed increase from background levels, like those observed by SG108, in separation between isopycnals bounding the Cuddy core and spice anomaly at the Cuddy core depth. Differing background profiles were estimated for each window because, as the Cuddy translated, it moved through cross-shore horizontal gradients of temperature and salinity evident in SG108 transects (Fig. 2.3).

The results of the interpolation procedure are gridded, spatially smoothed scalar and velocity fields versus r and z (*e.g.* π_θ in Fig. 2.5a). Within these gridded fields, the core region is defined as extending in radius from 0 km to $r_{v_{max}}$, the radius of maximum velocity, which will be defined in the next section. The far-field is assumed to feel little influence of the Cuddy while a transition region includes the area of interaction between the interior Cuddy core and exterior background waters (Fig. 2.5a).

2.4 Analysis

2.4.1 Estimates from Interpolated Fields

The gradient-wind horizontal momentum balance appropriate for describing intense submesoscale and mesoscale eddies includes a non-negligible centripetal term [Holton, 1972, McWilliams, 1985, D'Asaro, 1988a, Hebert et al., 1990, Tokos and Rossby, 1991, Martin et al., 2009, Pelland et al., 2013, Bosse et al., 2016]. In cylindrical coordinates this is defined as

$$\frac{\partial \Phi}{\partial r} = fv + \frac{v^2}{r}, \tag{1}$$

where Φ is geopotential, v the azimuthal velocity, and f the local Coriolis parameter. For each analysis window, we calculated absolute gradient-wind velocity fields $v(r, z)$ referenced to the estimated azimuthal DAC as follows: using the interpolated density field as described above, geopotential was first calculated relative to a deep level of no motion $p_0 = 980$ dbar, (1) was solved using this relative geopotential, and then, at each radial grid station, the

radial gradient of the geopotential at the deep reference level was iteratively adjusted until the vertical average of v from (1) at each station matched the interpolated DAC_ϕ at that station [Pelland et al., 2013]. The radial geopotential gradient at the reference level was then integrated radially from the origin to $r = 28$ km to produce a profile of absolute geopotential at the reference level, defined to within an arbitrary constant. This radial profile was added to the relative geopotential field at each depth level to give the absolute geopotential Φ. This is similar to the method of Bosse et al. [2016, their Appendix A] for determining the absolute depth-averaged radial pressure gradient by referencing gradient-wind velocities to DAC. Using the absolute gradient-wind velocity field, the vertical component of relative vorticity, ζ, was calculated according to

$$\zeta = \frac{\partial v}{\partial r} + \frac{v}{r}. \tag{2}$$

The geopotential anomaly $\Delta\Phi$, a measure of Cuddy strength, was found by subtracting from the absolute geopotential a far-field profile defined as the average along depth surfaces within the range $22 \leq r \leq 28$ km. This far-field profile was removed from the entire field with the result defined as the geopotential anomaly $\Delta\Phi$ associated with the Cuddy (Fig. 2.5b). In analysis window five, the maximum geopotential anomaly is evident at the Cuddy core depth in the main pycnocline.

The Cuddy had clockwise, anticyclonic circulation; in the example fifth window, the maximum azimuthal currents were 0.21 m s^{-1} at 200 m depth and a radial distance $r_{v_{max}} = 10.5$ km (Fig. 2.5b). Here $r_{v_{max}}$ is defined as the radial distance, in each analysis window, along the depth surface of maximum geopotential anomaly at which the strongest azimuthal currents are found. This radius is used to delineate the Cuddy core from the exterior. A second horizontal length scale, $r_{v=c}$, was also calculated as the outermost radial station at the core depth at which the azimuthal velocity v is equal to or greater than the eddy translation speed c. At radii less than $r_{v=c}$, azimuthal currents exceed the translation speed, which is indicative of water that is trapped and can be transported laterally within the eddy core [Early et al., 2011].

2.4.2 Model Derived Dynamics

Note that the geopotential, velocity, and vorticity estimates derived from the interpolated fields assume no Cuddy structure beyond azimuthal symmetry. For some quantities, it is convenient to further assume a radial-vertical

eddy structure (an eddy "model") and fit this to the data in each analysis window. We assume that Cuddy density and geopotential structure can be compactly described by a separable structure, taken as a product of radial and vertical functional forms. The vertical structure of non-dimensionalized eddy density anomaly profiles (Fig. 5c) do not demonstrate evidence of radial dependence and support the assumption of separability. The model geopotential anomaly $\widehat{\Delta\Phi}$ takes the form:

$$\widehat{\Delta\Phi} = \begin{cases} A(\frac{9}{8} - (\frac{r}{\lambda})^2)e^{-\frac{1}{8}-(\frac{z-z_0}{h})^2} \text{ for } r < \frac{\lambda}{2\sqrt{2}} \\ Ae^{-(\frac{r}{\lambda})^2-(\frac{z-z_0}{h})^2} \text{ for } r \geq \frac{\lambda}{2\sqrt{2}}, \end{cases} \tag{3}$$

where A, λ, and h are the Cuddy strength, radial scale, and vertical scale respectively. For each of the 11 analysis windows the Cuddy core depth z_0 and eddy center are defined as the depth at r=0 where $\Delta\Phi$ is a maximum. The model scale and strength parameters were then estimated by minimizing the squared error between model and observed $\Delta\Phi$. The piecewise model form (3) was chosen to include an inner region $r \leq \lambda/(2\sqrt{2})$ for which azimuthal speed varies nearly linearly with radius to approximate solid body rotation. At greater radii, the Gaussian form was chosen to describe smoothly varying flow that peaks at $r \approx 0.6\lambda$ [McWilliams, 1985, Pelland et al., 2013]. For simplicity, the vertical structure is assumed to be symmetric about the core depth.

In addition to velocity and vertical vorticity fields computed directly from the interpolated grids as described above, these quantities were also computed from (3) for comparison. The resulting model fields, $\widehat{v}$ and $\widehat{\zeta}$, are independent of background flow and describe idealized monopole SCV structure dependent only on the three parameters A, λ, and h. An additional benefit of (3) is that quantities unable to be fully specified from the interpolated fields, such as potential vorticity at the eddy center, can be estimated from the model. Potential vorticity (PV) was computed as [D'Asaro, 1988a, Martin et al., 2009]

$$PV(r,z) = (\widehat{\zeta} + f)\frac{N^2}{g} + \frac{1}{\rho_0}\frac{\partial\widehat{v}}{\partial z}\frac{\partial\sigma_\theta}{\partial r}. \tag{4}$$

The first term in (4), describing the PV vertical component, is the product of the vertical component of absolute vorticity with the buoyancy frequency $N^2 \equiv -(g/\rho_0)\partial\sigma_\theta/\partial z$, divided by the gravitational acceleration g, where $\rho_0 = 1025$ kg m^{-3} is a reference density. The second term describes twisting and tilting. This estimate of PV combines the modeled geopotential anomaly, through velocity and vorticity, with the interpolated density field,

which is used to estimate N^2.

Velocity and vorticity Rossby numbers for the Cuddy were computed as $Ro_v = 2v_{max}/(fr_{v_{max}})$ and $Ro_\zeta = |\zeta_{(0,z_0)}|/f$ respectively [D'Asaro, 1988a]. The velocity Rossby number is the ratio of relative to planetary vorticity and is a measure of the importance of the nonlinear advection term in (1). The factor two arises from writing the momentum balance in terms of the horizontal density gradient and vertical azimuthal velocity shear. The vorticity Rossby number, directly relates the Cuddy core to planetary vorticity. Values greater than one reflect a core susceptible to inertial instability [D'Asaro, 1988a]. The Burger number was additionally computed to explore aspect ratio adjustment. It is defined as the square of the ratio of the baroclinic radius of deformation to the horizontal length scale of the flow ($Bu = (N_0 h/(f\lambda))^2$, where N_0 is the background stratification averaged between 160 m and 240 m. Its value through time describes how an eddy adjusts as it translates into regions of different background stratification and/or planetary vorticity. Initial horizontal and vertical length scales are set by formation processes and the background state, but as an eddy propagates it is expected to adjust to a stable state and shape within a range $0.05 < Bu < 1$ [McWilliams and Gent, 1986].

Total available potential energy (APE) and kinetic energy (KE) in each analysis window were computed as [D'Asaro, 1988a, Hebert et al., 1990]

$$APE = \int_z^0 \int_0^{2\pi} \int_0^{28km} \frac{1}{2}\widehat{\rho} N_b^2 \xi^2 r \; dr \; d\theta \; dz, \tag{5}$$

$$KE = \int_z^0 \int_0^{2\pi} \int_0^{28km} \frac{1}{2}\rho_0 \widehat{v}^2 r \; dr \; d\theta \; dz, \tag{6}$$

where $\widehat{\rho}$ is the observed background density profile plus the model density anomaly found using (3). Here, the background buoyancy frequency profile N_b^2 is calculated using the background density profile, and ξ is the vertical displacement of each isopycnal from its background level. To the extent that any eddy velocity and density anomalies are nonzero deeper than the maximum depth of glider profiling, these expressions will underestimate the true APE and KE. Full-depth sections of Cuddies are rare, but previous observations have shown isopycnal displacements and baroclinic velocities limited to the upper 1200 m [Simpson et al., 1984] or shallower [Huyer et al., 1984]. The near-zero non-dimensionalized density anomalies (Fig. 2.5c) and low azimuthal velocities observed at 1000 m (Fig. 2.5b) in this study are consistent with these observations.

2.4.3 Uncertainty Estimates

Uncertainties in the estimates described above due to errors in the eddy center location were estimated using Monte Carlo sampling. In each analysis window, 100 iterations were performed, in each of which the Cuddy center position was adjusted. For each iteration, randomly drawn, normally-distributed x and y perturbations, with covariance structure specified by the error covariance matrix output by the EKF smoother at the middle time point of each window (Appendix A), were used to shift the position of all center points within that window. The interpolation technique was then reapplied for each iteration and all dynamic quantities were recomputed; 95% confidence intervals were computed as two standard deviations of each quantity across the 100 iterations. This procedure conservatively assumed that center estimate errors between time points were dependent within each time window.

2.4.4 Temporal Change

Temporal changes in Cuddy dynamic fields and bulk tracer properties were analyzed by comparing average properties early during the tracking period and after the Cuddy's rapid translation northward. Quantities were averaged within "early" and "late" analysis windows; late windows were defined as those following the onset of rapid poleward propagation (January 9th). This distinction results in seven early and four late analysis windows (corresponding roughly to the first and second halves of the observation period). The statistical significance of differences in means between these two periods was assessed using a Student's t test [Storch and Zwiers, 2003]; changes between early and late were considered significant if the null hypothesis of no difference in means between the two time periods was rejected at 95% confidence.

2.5 Results

2.5.1 Characteristic Scales

As the Cuddy translated northward, the background stratification at its core depth decreased by 9% and the Cuddy core isopycnal $\sigma_\theta = 26.56$ kg m^{-3} deepened, along with the depth of maximum geopotential anomaly and the depth of maximum azimuthal velocity (Fig. 2.6a). The core isopycnal was selected as the isopycnal that, over

all snapshots, was least vertically deflected from the background at radii less than 10 km. Its depth was estimated for each snapshot using the five glider profiles closest to the Cuddy center. These depths were compared against far-field estimates made using the five profiles completed farthest from the Cuddy center. Throughout the tracking period, the core isopycnal deepened everywhere; core and far-field depth estimates were positively correlated with a square correlation coefficient of over 0.9.

As this deepening occured, the background buoyancy frequency at the Cuddy core depth and the Cuddy core buoyancy frequency converged (Fig. 2.6a). While the horizontal length scale λ and radius of maximum velocity $r_{v_{max}}$ did not significantly change between early and late periods, the radius at which azimuthal currents matched eddy translation speed $r_{v=c}$ decreased by 20% beginning January 6th (Fig. 2.6b). Its decrease in early January is consistent with a concurrent increase in background flow measured by SG108 and estimated by the EKF. The decrease in $r_{v=c}$ during the second half of the survey period is most evident in two estimates where translation speed is strongest (12 and 27 January).

The magnitude of the geopotential anomaly $\widehat{\Delta\Phi}$ decreased by 20% from the first to the last half of the record (Fig. 2.7a), while λ did not significantly change (Fig. 2.7b) and h increased by 38% (Fig. 2.7c). These changes occurred as background stratification weakened by 9% between early and late averages. Coincident with these changes, the eddy core stratification increased from 30% to 55% of local background values (Fig. 2.6a).

2.5.2 Kinematics and Dynamics

Modest temporal changes in eddy rotation and stratification over the observing period are evident from azimuthal velocity, vorticity, and potential vorticity radial profiles along the core depth (Fig. 2.8). Mapped velocity profiles (Fig. 2.8a) reveal a nearly linear gradient, indicative of solid body rotation, only for $r \lesssim r_{v_{max}}/2$ where $r_{v_{max}} = 7 - 10$ km . At larger radii, the profiles follow a roughly Gaussian shape providing the motivation for the model form in (3).

Both model and directly-estimated peak azimuthal velocity decreased modestly over time from a maximum magnitude of 0.23 m s^{-1} in the interpolated field in window two to 0.19 m s^{-1} in window eleven (early average peak speed = 0.21 m s^{-1}, late average peak speed= 0.175 m s^{-1}). The magnitude of the ratio of the core relative

vorticity to f decreased more dramatically from an early average of 0.69 to a late average of 0.46. The radial profile shape of relative vorticity normalized by f reflects the choice of a model permitting an inner core in solid body rotation. Validation of this model choice is further confirmed by the time-averaged vorticity profile from the interpolated fields where at small radii the slope of vorticity flattens (Fig. 2.8b). In time, vorticity weakened particularly within the core, consistent with the weakening of the velocity field. PV at a radius of 0 km and at the core depth increased from 11% of the background value to 20% by the end of the survey. This is seen as an increase (decrease in magnitude) in PV anomaly, a ratio defined as $(PV - PV_{ff})/PV_{ff}$, where PV_{ff} refers to the far-field PV defined as the average PV at radii greater than 20 km (Fig. 2.8c).

Velocity and vorticity Rossby numbers significantly decreased between the early and late period (Fig. 9a and 9b), reflecting an increase in f (by 3%) and a decrease in peak azimuthal velocity. The Burger number did not change significantly between early and late periods (Fig. 2.9c). While the aspect ratio (h/λ) increased by the end of the survey period (Fig. 2.7), this was somewhat compensated by a decrease in the ratio of the background buoyancy frequency to Coriolis frequency. Cuddy total mechanical energy was roughly equally partitioned between APE and KE and while APE significantly decreased by 45% between early and late averages, KE did not significantly decrease (Fig. 2.10).

2.5.3 Bulk Tracer Evolution

Temperature and salinity anomalies along isopycnals within the cuddy core, and their contrast with cool, fresh offshore water in the Washington coastal region, are evident when viewed in θ/S space (Fig. 2.11). Background profiles, averaged between November and January and collected by SG108, indicate spice decreases with distance offshore within the thermocline (profiles collected offshore are cooler and fresher). A pair of profiles collected within the Cuddy when it was located more than 100 km offshore indicate its core is even more spicy, as evidenced by warm and salty waters found between $\sigma_\theta = 26.4$ kg m^{-3} and $\sigma_\theta = 27$ kg m^{-3}. The relatively high values of spice within the Cuddy suggest that it formed at a location equatorward of the SG108 transect and distinguish it from surrounding poleward waters.

Evolution of spice, dissolved oxygen, and potential vorticity within the Cuddy can be seen from a sequence of

r-z sections from representative snapshots (Fig. 2.12). As indicated by the time series of model scale parameters (Fig. 2.7), azimuthal velocity weakens and core depth deepens through the course of observations accompanied by a decrease in spice (Fig. 2.12, left panels). Over the same period, dissolved oxygen change within the core is indiscernible (middle panels), but potential vorticity weakens modestly, as measured by the core volume contained within the PV $= 1 \times 10^{-10}$ m^{-1}s^{-1} contour (right panels), the same volume used to estimate average spice and dissolved oxygen within the core (Fig. 2.12, bottom panels). When early and late averages of quantities in this core region are compared, core spice decreases from -0.13 to -0.15 (a statistically significant change), O_2 by 1% (not significant), and core volume by 6% (not significant).

Despite average O_2 remaining essentially constant, by the survey's end, core oxygen variance had increased by over an order of magnitude (Fig. 2.13a). Vertical profiles within each time window were ordered by radial distance and oxygen variance computed between 26.52 kg m^{-3} $< \sigma_\theta <$ 26.6 kg m^{-3} by averaging over 6 km overlapping radial bins. The use of a strict vertical bound intends to highlight horizontal, not vertical, variations. Initially, core oxygen variance was very low, $< 10(\mu$mol kg$^{-1})^2$ at $r < 10$ km. Outside the core at larger radii, variance was an order of magnitude greater, peaking at $r = 17$ km, and again decreasing to modest exterior values beyond $r > 18$ km (Fig. 2.13a). This initial radial profile is consistent with an inner homogenous core, a transition region of mixing waters, and a more uniform background outside the Cuddy. Over time the radius of maximum variance migrated towards smaller radii and by the end of the tracking period, core oxygen variance had increased tenfold. The radial distribution of spice variance (Fig. 2.13b) displayed a qualitatively similar evolution in time; by the end of the survey period, core spice variance increased by nearly a factor of three.

Vertical profiles of spice at each radial grid station and for each snapshot were interpolated to a density grid to consider changes in core spice. A far-field average profile for each snapshot was removed and resulting spice anomaly profiles at the Cuddy center, $r = 0$ km are considered (Fig. 2.14). From late November through mid-January a relatively compact positive roughly triangular anomaly characterized Cuddy spice. Added for reference is the core isopycnal, as well as shallower $\sigma_\theta = 26.3$ kg m^{-3} and deeper $\sigma_\theta = 27$ kg m^{-3} isopycnals bounding the core (Fig. 2.14). Starting in late January and continuing through the last 3 snapshots, spice anomaly in the core decrease to more uniform values across the range of core densities.

Using salt, a more easily interpretable tracer, we computed the available salt anomaly (ASA) [Pelland et al., 2013]. Instead of using a background profile for each window, one reference profile, collected at the survey midpoint, was used such that anomalies could be compared against each other through time. ASA is defined here as

$$ASA = \int_{z_1}^{z_2} \int_0^{2\pi} \int_0^{\lambda} 0.001\rho_0(S_{\sigma_\theta} - S_{\sigma_\theta}^{ref}) r \; dr \; d\theta \; dz \tag{7}$$

where S_{σ_θ} and $S_{\sigma_\theta}^{ref}$ correspond to salinity and a reference profile all gridded on density surfaces. A volume integral was taken between vertical levels z_1 and z_2, set by the corresponding depths of $\sigma_\theta = 26.3$ kg m^{-3} and $\sigma_\theta = 27$ kg m^{-3}. ASA significantly decreased by 27% between early and late periods (Fig. 2.14, bottom panel).

2.5.4 Vertical Fine-structure

Occurrences of vertical fine-structure, suggestive of lateral exchange among waters of different spice between eddy core and exterior regions, were observed with increasing frequency in time throughout the survey period. Within the Cuddy core, θ/S profiles are self-similar and differ little from one another (Fig. 2.15, left panel). Outside the core, θ/S curves are generally cooler and less salty, but often irregularly vary from these to spicier conditions, indicative of intrusive behavior along selected potential density surfaces (Fig. 2.15, right panel).

Shcherbina et al. [2009] characterized thermohaline lateral intrusions by spice curvature in θ/S space, an approach adopted here to address Cuddy spice variability. Two derivatives of spice with respect to density were calculated after smoothing each glider profile on a density grid using a triangular filter with a half width of 0.03 kg m^{-3}. Local maxima and minima in curvature identify the position, on a density grid, of intrusive features on the order of tens of meters. A threshold of two standard deviations, found using all curvature measurements within each Cuddy snapshot, was then used to identify intrusions relative to the Cuddy core PV boundary and well above levels of background variability (Fig. 2.16).

Interleaving events are most common at the base of the mixed layer ($\sim$ 80 m), somewhat less common at deeper depths, and even rarer near the core depth (Fig. 2.16). As the survey progressed, the occurrence of interleaving events decreased at larger and increased at smaller radii at depths both shallower and deeper than the Cuddy core. Inferred interleaving events ultimately became common at radii less than the eddy radial scale, suggesting that

intrusions reached core waters. The percentage of intrusions found within each time window at radii less than λ increased from 19% in the early period to 72% in the late period (Fig. 2.16, bottom right panel).

2.6 Discussion of Eddy Translation and Erosion

The persistent survey of a Cuddy over the course of three months revealed modest structural changes. Consistency in eddy visual appearance and the core depth estimate, across all analysis windows, suggests the successful tracking of the same feature. The consistent observation of southeastward flow and isopycnal separation consistent with ambient, offshore conditions (Fig. 2.4c) on its inshore edge rule out the interpretation of this feature as a meander of the undercurrent rather than an isolated vortex.

The deepening of the core isopycnal, both within the eddy (Fig. 2.6a) and in the far-field, is indicative of the eddy propagating into waters with a background density structure different from that closer to its formation site. Isolated subsurface eddies like that observed in this study are expected to propagate vertically across potential density and neutral surfaces due to compressibility effects, but these effects are likely very small (movement of $\mathcal{O}(1)$m given conditions in this study; [McDougall, 1987]) relative to the observed vertical displacements.

A unique aspect of this study was the Cuddy's rapid translation to higher latitude, which likely decreased the isolation of core waters in addition to transporting the eddy into different background conditions. Within one week in early January, translation speeds more than doubled to over 0.08 m s^{-1}. Compared to speeds consistently less than 0.04 m s^{-1} over the preceding three weeks, this abrupt alongshore propagation contrasts with the expectation of steady offshore movement as described by Collins et al. [2013], with the exception of a single float tracked off of the Washington coast that similarly exhibited poleward movement. The retention of the eddy within the nearshore region is also similar to the modeled Cuddy trajectory of Torres and Gomez-Valdes [2017] in the southern CCS. In applying an asymptotic theory of SCV motion, Dewar and Meng [1995] state that the beta drift term appears at the next order expansion following terms describing an eddy and a mean flow. This suggests that eddy self-translation due to the beta effect alone can be overwhelmed by a mean flow.

Off of the Washington coast in early winter, as the Cuddy experienced surface and subsurface northward background flows, its trajectory was consistent with the expectation of flow following contours of potential vorticity

($\approx f$/water-depth). Between ∼15 Dec. and ∼30 Dec., a period of southwestward translation, the Cuddy occupied a region of slope with a relatively weak cross-slope topographic gradient, while an increase in slope steepness was coincident with the observed northward acceleration beginning in early January. The degree of connection between this eddy and the seafloor is unknown, since observations did not extend to full depth in this study. The observations do suggest, however, the possibility that eddy azimuthal velocity was non-zero at depths greater than 1000 m. Roughan et al. [2017] discuss the vertical extent of subsurface intensified eddies and relate observations of T/S anomalies many hundreds of meters below an eddy core. The alignment of f/water-depth contours, the magnitude of a presumed barotropic mean flow as compared to an expected eddy westward drift speed, and the possibility of Cuddy interaction with the seafloor are in this case consistent with the hypothesis that steady offshore drift was overwhelmed by advection in topographically constrained background flows.

During the period of southwest translation, spanning a significant portion of the month of December and while the Cuddy occupied a flatter region of the slope, background currents were relatively weak and variable (Fig. 2.6b). It is plausible that at this time translation due to the beta effect may have had a larger influence on the eddy trajectory, in contrast to the stronger northward background flows and translation over steeper sections of the slope observed later in the surveys.

Originally explored through the modeling of eddy formation, adjustment, and evolution [McWilliams and Gent, 1986], Burger number selection was observed as the Cuddy traveled over 400 km in three months. This selection process represents a tendency for a stable equilibrium ratio of vertical to horizontal scales to develop. Values remained in the stable range, increased towards 1, and fell within the range of those observed by Pelland et al. [2013] and cited by D'Asaro [1988a]. Both the aspect ratio and ratio of stratification to f changed in a compensating manner, however, resulting in no statistically signifiant Burger number change. Hebert et al. [1990] similarly studied the evolution of an SCV over the course of two years and observed significant decay along with aspect ratio adjustment. While the ratio of kinetic to available potential energy remained $\mathcal{O}(1)$, total energy decreased fourfold and the Burger number increased in those observations. Here we observed a similar partition of energy as well as decrease in time of potential energy, but a modest and not statistically significant change in Burger number.

Recent repeat observations of the semi-stationary Lofoten Basin eddy made by Seagliders [Yu et al., 2017] reveal

the evolution of an eddy slightly larger and stronger than this Cuddy. Comparisons between radial azimuthal velocity profiles, however, show agreement in profile shape with both eddies in cyclo-geostrophic balance. Yu et al. [2017] report a core in solid body rotation out to $\sim \frac{1}{3} r_{v_{max}}$ and minimum in core vorticity to be $\sim -0.8f$. Along with a vorticity Rossy number of roughly 0.8 and fluctuating Burger number $\mathcal{O}(1)$, these results are comparable to Cuddy observations and help validate the framework used in studying these submesoscale features. Over the course of their multi-year survey, the authors report strong seasonal changes in background waters and an eddy core that remains largely isolated and persistent.

While the individual Cuddy that was tracked in this study was initially quite isolated (evidenced by a core with low spice and O_2 variance), after three months, the eddy geopotential anomaly, Rossby number, potential energy, core spice anomaly, and available salt anomaly all decreased, while core potential vorticity, oxygen variance, instances of fine-structure, and eddy vertical scale increased. After the period of increased translation the Cuddy core was also notably deeper. A possible explanation for the loss of total energy and increase in tracer variance is the effect of thermohaline lateral intrusions, which have been implicated in Meddy decay [Armi et al., 1989, Hebert et al., 1990], and which are suggested here by the presence of vertical fine-structure. These features at first bounded the Cuddy and were found at radii greater than $r = \lambda$, while later in the survey period, most were found closer to the core. Because individual lateral intrusions could not readily be observed or identified in multiple glider profiles, the horizontal heat and salt fluxes cannot be estimated directly. The relatively rapid eddy evolution observed here, and presumably, correspondingly short lifetimes of any horizontal intrusion features, likely invalidates the use of a steady-state parameterization such as that of Joyce [1977], as was done in Pelland et al. [2013], for estimating horizontal fluxes of heat and salt due to intrusions in this eddy [Shcherbina et al., 2010].

The presence of vertical fine-structure, in addition to the rapid poleward propagation and decrease in the radius at which core waters are trapped, suggests mechanisms by which eddy core water may have been eroded during this study. Erosion of eddy waters, along with movement into different background conditions, are both mechanisms that have the potential to drive eddy evolution. We examined the relative influence of eddy erosion and background change on the bulk properties estimated in this study using an idealized model of a symmetric, geostrophic eddy

embedded in uniform stratification. Consider an eddy whose density anomaly takes the form:

$$\rho'(r, z') = \frac{a}{2} sin\left(\frac{\pi z'}{H}\right)\left(cos\left(\frac{\pi r}{L}\right) + 1\right) \tag{8}$$

where a, L, and H are the density anomaly, length scale, and half-height scale respectively and $z' = z - z_0$ is the vertical coordinate relative to the eddy core depth. Half-height refers to the eddy half-thickness and is used recognizing the vertical symmetry of the eddy. This form, although simpler than the density anomaly implied by (3), was chosen as an idealization retaining basic Cuddy characteristics in continuous stratification within a finite domain. The density anomaly and velocity field decay to background levels at the domain limits $r = L$ and $z' = \pm H$. The exercise consists of examining the change of the three eddy parameters that would be necessary to conserve integrated mass, energy, and PV following a geostrophic adjustment to either background changes, or both erosion and background changes. These two cases reflect Cuddy evolution scenarios that could describe the observations. Solutions are sought for which a, L, and H vary to accommodate changes in stratification and latitude while retaining the chosen parametric eddy form specified by (8). The form (8) enables integrals of eddy mass, potential and kinetic energy, and potential vorticity to be expressed analytically as functions of a, L, and H over arbitrary cylindrical domains up to L in radius and $2H$ in height (see Appendix B for details). The constraints of mass, total energy, and potential vorticity conservation uniquely determine a, L, and H for modest changes in Coriolis parameter and stratification. Adjustment to erosion of an outer radial annulus or vertical layer can be simulated by seeking final parameters that describe an eddy with reduced amounts of mass, energy, and PV, where reductions are those given by limiting the range of integration of the quantities in the initial eddy over a radius less than L and for a half height less than H. Observed ratios of the late to early period eddy properties (maximum geopotential anomaly Φ, height scale H, radius scale L, Rossby number, Burger number, kinetic, and potential energy) along with 95% confidence intervals are used in referencing this idealized model to the Cuddy observations (Fig. 2.17, right). The most robust observed changes include an increase in the vertical scale H, a decrease in geopotential amplitude, and a decrease in Rossby number.

Predictions of these ratios in an eddy adjusting to erosion are considered as a function of fractional radial erosion (corresponding to integration over the full original domain). Here, the model results also reflect a 3% increase in Coriolis parameter and 9% decrease in background stratification from early to late period observations.

Idealized eddy parameter changes resulting from movement northward into less stratified waters only partially explain observed Cuddy evolution with a decrease in geopotential amplitude and Rossby number. With the inclusion of modeled erosion however, an increase in Burger number and decrease in potential energy result in better agreement with observed Cuddy changes (Fig. 2.17). In order to estimate the influence of erosion (from both horizontal and vertical limits), a cost function was constructed by comparing observed and modeled changes in geopotential anomaly, height scale, length scale, Rossby number, Burger number, kinetic energy, and available potential energy. The sum of the differences between each observed and modeled ratio divided by the corresponding standard deviation of the ratio of late to early observed t-distributed parameters was used as a cost function to find the combination of radial and vertical erosion that best matched the observations (Appendix B). The results favor a 2.75% radial erosion alone, combined with the effect of weakened background stratification and movement northward yielding a cost function value of 11.4 (Fig. 2.17). The corresponding cost function value associated with background changes and no erosion is equal to 11.9. Any inclusion of modeled vertical erosion further increased the cost function to values greater than 11.9. One notable change that the model does not qualitatively predict is a significant increase in the Cuddy vertical scale. This may be partly explained by remembering that the observed vertical scale change is accompanied by large confidence bounds likely affected by the assumption of vertical symmetry about the Cuddy core used in estimating the Cuddy vertical scale (section 4b).

A combination of horizontal erosion and background changes provides the best fit to the observed Cuddy changes, within the estimated confidence bounds on the observed changes. This supports the hypothesis that the observed changes were due to both poleward translation into different waters and core water loss. Confirming the details of the relative losses of dynamical properties of Cuddies and similar subsurface eddies due to exterior erosion likely requires more direct observation of the erosion processes.

2.7 Summary and Conclusions

Multiple Seaglider autonomous vehicles observed the evolution of a California Undercurrent eddy over the course of three months of intensive surveying. This feature, exhibiting strong radially symmetric anticyclonic rotation and with a core spice greater than inshore undercurrent water levels, had defining characteristics of a submesoscale

coherent vortex. With a radius of maximum velocity smaller than the local first baroclinic deformation radius and a Rossby number of order one, the nonlinearity of the vortex described here makes appropriate the label submesoscale [McWilliams, 1985, Dewar and Meng, 1995, Capet et al., 2008, McWilliams, 2016].

Changes in Cuddy scale and kinematics were detectable as it was swept along in poleward flow. These changes were accompanied by the increased prevalence of thermohaline fine-structure resulting in increased tracer variance within the Cuddy core region. The migration of these interleaving features, identified using spice curvature, toward the Cuddy core is circumstantially consistent with the erosion of core waters.

Use of an augmented 2-D Gaussian model fitted to the Cuddy geopotential anomaly field allowed for the direct computation of velocity, relative vorticity, kinetic energy, and available potential energy. Cuddy evolution was explored by comparing these fields across 11 independent Cuddy snapshots. Between November 2013 and February 2014, Cuddy potential energy decreased while the vertical scale increased. Despite modest decay, the Cuddy retained its bulk shape and structure. Contributing factors to eddy decay were explored using a highly idealized model of a geostrophic eddy and results are consistent, except for changes in the eddy vertical scale, with eddy changes as being due to both erosion of exterior waters and changing background conditions as the eddy moved poleward along the continental slope.

The individual Cuddy tracked in this study did not move significantly offshore during the course of the survey, suggesting that strong alongshore currents carried it, overcoming any dynamic tendency for it to move offshore in the manner observed by Collins et al. [2013]. A Cuddy with a larger geopotential anomaly and found in offshore waters would likely be easier to track and monitor, though it remains an open question what fraction of Cuddies reach this mature state. Further *in situ* observations are needed to resolve the range of behaviors of mature Cuddies and their fate in the energetic nearshore region and beyond. Results of this study indicate that autonomous vehicle surveys are a viable strategy for addressing this need by observing eddy evolution and resolving submesoscale pathways for heat, salt, and energy transport.

2.8 Acknowledgements

This work was funded by the National Science Foundation (Grant OCE-1153980). We would like to thank Kirk O'Donnell for his dedication and patience in ensuring that the Seagliders used in this experiment were deployed, well used, and safely recovered. Thanks to Bill Fredericks for his resourcefulness in field and recovery operations. Thanks to Jim Bennett for managing the data stream and organizing/advising on data processing procedures. We are extremely grateful for the crew of the CCGS *John P. Tully* for assistance in recovering gliders and the USCG Station Grays Harbor for aid in small vessel operations. And many thanks to Tom Young and the crew of the F/V *Tommycod* for their professionalism and capability. We would additionally like to thank the reviewers of this manuscript for their detailed feedback, suggestions on improving clarity, and help expanding the scope of our interpretation of results.

Appendix A Eddy Position Estimates Using the Extended Kalman Smoother

The eddy center position $(\hat{x}(t), \hat{y}(t))$ was estimated using the same framework as in eddy tracking: a simplified model was assumed, and glider observations were assimilated into this model using the extended Kalman filter (EKF; Pelland et al. [In Press]). The simplified model assumed a separable, radially symmetric form of eddy density anomaly

$$\rho'_\theta(r,z) = \Delta\rho_0 F(z) e^{-\frac{r^2}{2R^2}}, \tag{9}$$

where Δ is a dimensionless parameter, ρ_0 is a reference density, R is a horizontal scale, and $F(z)$ is a vertical structure function that was estimated by subtracting an average background profile from Seaglider density data collected 18 December 2013-3 January 2014 . The 0-1000 m average eddy geostrophic azimuthal currents due to (9), $\overline{v}_g(r)$, are

$$\overline{v}_g(r) = \frac{\Delta g r}{fHR^2} e^{-\frac{r^2}{2R^2}} \int_{-H}^{0} \int_{-H}^{z} F(\xi)\, \mathrm{d}\xi\, \mathrm{d}z = A\frac{r}{R^2} e^{-\frac{r^2}{2R^2}}, \tag{10}$$

assuming $v_g(r, -H) = 0$, where $H = 1000$ m. Here $A = \Delta g (fH)^{-1} \int_{-H}^{0} \int_{-H}^{z} F(\xi)\, \mathrm{d}\xi\, \mathrm{d}z$, and g and f are as defined in the main text. Movement of the eddy center was assumed to be due to advection by a uniform background flow $\mathbf{u}_{\mathrm{back}} = (U(t), V(t))$; *i.e.*, $\mathrm{d}(\hat{x}, \hat{y})/\mathrm{d}t = \mathbf{u}_{\mathrm{back}}$. The assumptions of geostrophic flow that vanishes at $z = -H$ simplified the tracking procedure while retaining the basic characteristics of the system.

The six parameters describing this system ($\hat{x}$, $\hat{y}$, U, V, A, R) were sorted into a state vector $\mathbf{s}(t)$ whose values were estimated using the EKF. After the completion of each vehicle cycle, the EKF operated by computing the differences between observations from all gliders within a 56-hour window and those that would have been expected given the previous best estimate of $\mathbf{s}$, known as the forecast. The estimate of $\mathbf{s}$ was then updated based on these differences multiplied by a gain related to the relative uncertainty between the observations and the forecast. The equations and implementation of the EKF in this study followed the descriptions of Gauthier et al. [1993] and Gelb [1974, §6]. Estimates of depth-averaged current over each cycle, and isopycnal vertical separation between $\sigma_\theta = 26.5$ kg m^{-3} and $\sigma_\theta = 26.8$ kg m^{-3} in each profile, were used as observations in the EKF.

The EKF, rather than the linear Kalman filter, was used because it can accommodate systems in which the observations are nonlinear functions of the state vector $\mathbf{s}$, as is the case here [Gelb, 1974]. A forward run of the EKF produces an estimate of $\mathbf{s}(t)$ that reflects observations collected up to t; refining this estimate to take into account measurements made after t is known as "smoothing." The smoother is essentially a Kalman Filter that runs backward using the final estimate of $\mathbf{s}$ from the forward run as its starting guess. As it runs, it updates the smoothed estimate $\mathbf{s}^s$ based on differences between it and the best estimate from the forward run. The smoother was implemented in this study as described in Gelb [1974, their Table 5.2.2]. The smoother algorithm provides an estimate of $\mathbf{s}^s(t)$ and its error covariance matrix, $\mathbf{P}^s = E(\delta\mathbf{s}^s \delta\mathbf{s}^{s\mathrm{T}})$, where $E(\cdot)$ is the expectation of a random variable, $\delta\mathbf{s}^s = \mathbf{s}^s - \mathbf{s}^b$, and $\mathbf{s}^b$ is the true value of the state vector. The ($\hat{x}$,$\hat{y}$) elements of $\mathbf{s}^s$ were used as eddy position estimates to which all observations were referenced, while the elements corresponding to $\mathbf{u}_{\mathrm{back}}$ were used as estimates of the background flow (Section 3b). The elements of the covariance matrix corresponding to eddy position were used in the uncertainty calculation in Section 4c.

Appendix B Idealized Eddy Adjustment and Evolution

Consider an idealized axisymmetric geostrophic eddy of the form (8), with sinusoidal structure limited to radius L, half height H and density anomaly amplitude a. This form, chosen for convenience, is meant to loosely model the Cuddy tracked in this study but with finite radial and vertical extent, in contrast to the form (3). The model eddy is embedded in a background density stratification specified by buoyancy frequency $\overline{N^2}$ so that equivalently, the buoyancy frequency within the eddy can be expressed as

$$N^2(r,z') = \overline{N^2} - \widetilde{N^2} cos\left(\frac{\pi z'}{H}\right) cos\left(\frac{\pi r}{2L}\right) \tag{11}$$

where $z' = z - z_0$ is the vertical coordinate relative to the eddy core depth. Eddy buoyancy frequency deficit $\widetilde{N^2}$ magnitude is given by $\widetilde{N^2} = \frac{ga\pi}{\rho_0 H}$, where g is gravity, ρ_0 is reference density, and total density is given by $\rho = \rho_0 + \rho_1(z') + \rho'(r,z')$. The background density gradient is linear, given by $\rho_1 = -\overline{N^2}\rho_0 z'/g$. With these definition, and the assumption of geostrophic balance throughout, the azimuthal velocity field is given by:

$$v(r,z') = \frac{-\widetilde{N^2}H^2}{fL\pi}\left(cos\left(\frac{\pi z'}{H}\right)+1\right) sin\left(\frac{\pi r}{L}\right) \tag{12}$$

Volume integrated mass (M), kinetic plus potential energy (E), and potential vorticity (PV) are given by:

$$M = 2\int_0^Z \int_0^{2\pi} \int_0^R [\rho_1 + \rho']\, r\ dr\ d\theta\ dz', \tag{13}$$

$$E = 2\int_0^Z \int_0^{2\pi} \int_0^R \left[\left(\frac{1}{2}\rho_0 v^2\right) + (gz'(\rho_1+\rho'))\right] r\ dr\ d\theta\ dz', \tag{14}$$

$$PV = 2\int_0^Z \int_0^{2\pi} \int_0^R \left[(\zeta+f)\frac{N^2}{g} + \frac{1}{\rho_0}\frac{\partial v}{\partial z}\frac{\partial \rho}{\partial r}\right] r\ dr\ d\theta\ dz', \tag{15}$$

where ζ is relative vorticity, the factor two accounts for vertical symmetry, and the integration limits R and Z are limited to L and H, respectively, as specified by the form (8, 11). Expressions for integrated mass, energy, and potential vorticity using (11) and (12) become:

$$M = \frac{-\pi\rho_0\overline{N^2}H^2L^2}{g}\left(\frac{z'^2}{H^2}\right)\Bigg|_0^Z \left(\frac{r^2}{L^2}\right)\Bigg|_0^R + \frac{2\rho_0\widetilde{N^2}H^2L^2}{g\pi}\frac{-1}{2} cos\left(\frac{\pi z'}{H}\right)\Bigg|_0^Z \left(\frac{r^2}{L^2} + \frac{2r}{\pi L} sin\left(\frac{\pi r}{L}\right) + \frac{2}{\pi^2} cos\left(\frac{\pi r}{L}\right)\right)\Bigg|_0^R, \tag{16}$$

$$E^k = \frac{3\rho_0 \widetilde{N^4} H^5}{16\pi f^2}\left(\frac{z'}{H} + \frac{2}{3\pi} sin\left(\frac{\pi z'}{H}\right) + \frac{1}{6\pi} sin\left(\frac{2\pi z'}{H}\right)\right)\Bigg|_0^Z \left(\frac{r^2}{L^2} + \frac{r}{\pi L} sin\left(\frac{2\pi r}{L}\right) - \frac{1}{2\pi^2} cos\left(\frac{2\pi r}{L}\right)\right)\Bigg|_0^R, \quad (17)$$

$$E^p = \frac{-2\pi\rho_0 \overline{N^2} H^3 L^2}{3}\left(\frac{z'^3}{H^3}\right)\Bigg|_0^Z \left(\frac{r^2}{L^2}\right)\Bigg|_0^R + \frac{\rho_0 \widetilde{N^2} H^3 L^2}{\pi}\left(\frac{1}{\pi} sin\left(\frac{\pi z'}{H}\right) - \frac{z'}{H} cos\left(\frac{\pi z'}{H}\right)\right)\Bigg|_0^Z \left(\frac{r^2}{L^2} + \frac{2r}{\pi L} sin\left(\frac{\pi r}{L}\right) + \frac{2}{\pi^2} cos\left(\frac{\pi r}{L}\right)\right)\Bigg|_0^R, \quad (18)$$

$$PV_1 = \frac{2\pi f \overline{N^2} H L^2}{g}\left(\frac{z'}{H}\right)\Bigg|_0^Z \left(\frac{r^2}{L^2}\right)\Bigg|_0^R, \quad (19)$$

$$PV_2 = \frac{-2\overline{N^2}\widetilde{N^2} H^3}{fg}\left(\frac{z'}{H} + \frac{1}{\pi} sin\left(\frac{\pi z'}{H}\right)\right)\Bigg|_0^Z \left(\frac{r}{\pi L} sin\left(\frac{\pi r}{L}\right)\right)\Bigg|_0^R, \quad (20)$$

$$PV_3 = \frac{-f\widetilde{N^2} H L^2}{g}\left(sin\left(\frac{\pi z'}{H}\right)\right)\Bigg|_0^Z \left(\frac{r^2}{L^2} + \frac{2r}{\pi L} sin\left(\frac{\pi r}{L}\right) + \frac{2}{\pi^2} cos\left(\frac{\pi r}{L}\right)\right)\Bigg|_0^R, \quad (21)$$

$$PV_4 = \frac{\pi^2 \widetilde{N^4} H^3}{4fg}\left(\frac{z'}{H} + \frac{1}{2\pi} sin\left(\frac{2\pi z'}{H}\right) + \frac{2}{\pi} sin\left(\frac{\pi z'}{H}\right)\right)\Bigg|_0^Z \left(\frac{r^2}{L^2} + \frac{r}{\pi L} sin\left(\frac{2\pi r}{L}\right) + \frac{1}{2\pi^2} cos\left(\frac{2\pi r}{L}\right) + \frac{4r}{\pi L} sin\left(\frac{\pi r}{L}\right) + \frac{2}{\pi^2} sin^2\left(\frac{\pi r}{L}\right)\right)\Bigg|_0^R, \quad (22)$$

$$PV_5 = \frac{-\pi^2 \widetilde{N^4} H^3}{8fg}\left(\frac{z'}{H} - \frac{1}{2\pi} sin\left(\frac{2\pi z'}{H}\right)\right)\Bigg|_0^Z \left(\frac{r^2}{L^2} - \frac{r}{\pi L} sin\left(\frac{2\pi r}{L}\right) - \frac{1}{2\pi^2} cos\left(\frac{2\pi r}{L}\right)\right)\Bigg|_0^R, \quad (23)$$

where $E = E^k + E^p$ and $PV = \sum_i PV_i$. The 5 PV equations correspond to each term in the substitution and expansion of 15. Given prescribed initial ($_i$) values H_i, L_i, $\widetilde{N_i^2}$, and upper integration limits $Z \leq H$ and $R \leq L$, the equations (B6), (B7+B8), and (B9+B10+B11+B12+B13) describe integrated mass, energy, and PV for the initial eddy, which comprise three constraints on the final ($_f$) state unknowns H_f, L_f, and $\widetilde{N_f^2}$. For modeling eddy adjustment to background stratification and Coriolis parameter variations alone, the integrals and carried out for $Z = H$ and $R = L$. To model eddy adjustment following erosion, the integrals in the above constraints are evaluated over less than the full extent: $Z \leq H_i$ and $R \leq L_i$.

We consider the adjustment of an initial eddy in two different cases. The first represents eddy advection to a location with different background stratification and Coriolis parameter. The second represents eddy decay combined with the effect of the first case.

The first case considers the response of the eddy to a reduction in background stratification by 9% to $\overline{N_f^2}$ and increase in f by 3% to f_f. Final scale and strength parameters are found by integrating equations (B6-B13) over the entire initial eddy extent (i.e. $Z = H = H_i$ and $R = L = L_i$ in these expressions) to find expressions for initial mass M_i, energy E_i, and potential vorticity PV_i. These equal the final values of these quantities expressed in terms of final stratification $\widetilde{N_f^2}$, vertical scale H_f, and horizontal scale L_f by:

$$M_i = \frac{\rho_0}{g}\left(-\pi\overline{N_f^2} + \left(\frac{2}{\pi} - \frac{8}{\pi^3}\right)\widetilde{N_f^2}\right) H_f^2 L_f^2 \tag{24}$$

$$E_i = \frac{\rho_0 3\widetilde{N_f^4} H_f^5}{16\pi f_f^2} + \rho_0\left(\frac{-2\pi}{3}\overline{N_f^2} + \left(\frac{1}{\pi} - \frac{4}{\pi^3}\right)\widetilde{N_f^2}\right) H_f^3 L_f^2 \tag{25}$$

$$PV_i = \frac{2\pi f_f \overline{N_f^2} H_f L_f^2}{g} + \frac{\pi^2 \widetilde{N_f^2} H_f^3}{8 f_f g}. \tag{26}$$

This set of three equations in unknowns is easily reduced to a set of two equations in a pair of unknowns that can be solved numerically to obtain $\widetilde{N_f^2}$, H_f, and L_f. Since the eddy horizontal extent greatly exceeds its vertical extent, an approximate version of the system (B14-B16) neglecting the first (kinetic energy) term in (B15) and last term in (B16) yields a quadratic system that can be solved analytically. The analytic solutions serve as useful initial guesses to the numerical solution of the full equations (B14-B16). The result is that H is independent of background stratification, L varies as its inverse square root, and there exists only a small range in Coriolis parameter, $\sim f_i\ (1 \pm 0.15)$, within which solutions of the specified form exist.

The second adjustment case considers eddy decay along with changes in the background stratification and f. Eddy decay is modeled by evaluating integrals in equations (B6-B13) to Z and R, where $Z/H < 1$ and $R/L < 1$, to form the initial quantities on the left side of (B14-B16). Changes in the ratios of final to initial values of Φ, H, L, Ro, Bu, E^k, and E^{APE} are explored as a function of the radial and vertical erosion of the initial eddy, or alternatively, as the decrease in the extent of radial and vertical integration in the equations (B6-B13) that form constraints on the final parameters. Only the eddy component of potential energy, E^{APE}, is considered and employed below such that comparison can be made to the observed eddy APE.

In order to find the combination of vertical and horizontal erosion that, when combined with the effect of northward translation into less stratified waters, best explains the observations, a cost function was employed to minimize the differences between the seven observed and model predicted ratios (Fig. 2.17). Cost is defined as

the sum of the deviation of each model ratio from its observed value scaled by the standard deviation of assumed t-distributed late to early observed ratios. That is,

$$cost = \frac{\left(\frac{\Phi_f}{\Phi_i}\right)_{model} - \left(\frac{\Phi_{late}}{\Phi_{early}}\right)_{obs.}}{\sigma_\Phi} + \frac{\left(\frac{H_f}{H_i}\right)_{model} - \left(\frac{H_{late}}{H_{early}}\right)_{obs.}}{\sigma_H} + \frac{\left(\frac{L_f}{L_i}\right)_{model} - \left(\frac{L_{late}}{L_{early}}\right)_{obs.}}{\sigma_L} + \frac{\left(\frac{E_f^k}{E_i^k}\right)_{model} - \left(\frac{KE_{late}}{Ke_{early}}\right)_{obs.}}{\sigma_{KE}} + \frac{\left(\frac{E_f^{APE}}{E_i^{APE}}\right)_{model} - \left(\frac{APE_{late}}{APE_{early}}\right)_{obs.}}{\sigma_{APE}} + \frac{\left(\frac{Ro_f}{Ro_i}\right)_{model} - \left(\frac{Ro_{late}}{Ro_{early}}\right)_{obs.}}{\sigma_{Ro}} + \frac{\left(\frac{Bu_f}{Bu_i}\right)_{model} - \left(\frac{Bu_{late}}{Bu_{early}}\right)_{obs.}}{\sigma_{Bu}}. \quad (27)$$

The standard deviation used to scale each cost term is defined assuming that the observed early and late values of each quantity are samples from separate statistical distributions. Using two t-distributions for each quantity, one centered on the early mean and the other on the late mean, the standard deviation is computed of the ratio of late to early distributions. Confidence limits are then computed using this distribution of late to early ratios (Fig. 2.17, right). The total cost was computed for a range of integration limits $Z/H \leq 1$ and $R/L \leq 1$ in equations (B6-B13). This value was then minimized in each case to find the combination of integration limits that best matched the observations. The minimum cost value for case one, reflecting eddy adjustment only to changes in background stratification and Coriolis parameter, is 11.9. In case two, reflecting eddy adjustment in response to changes in background stratification, Coriolis parameter, and erosion, the minimum cost value of 11.4 is associated with no vertical erosion and 2.75% horizontal erosion (Fig. 2.17).

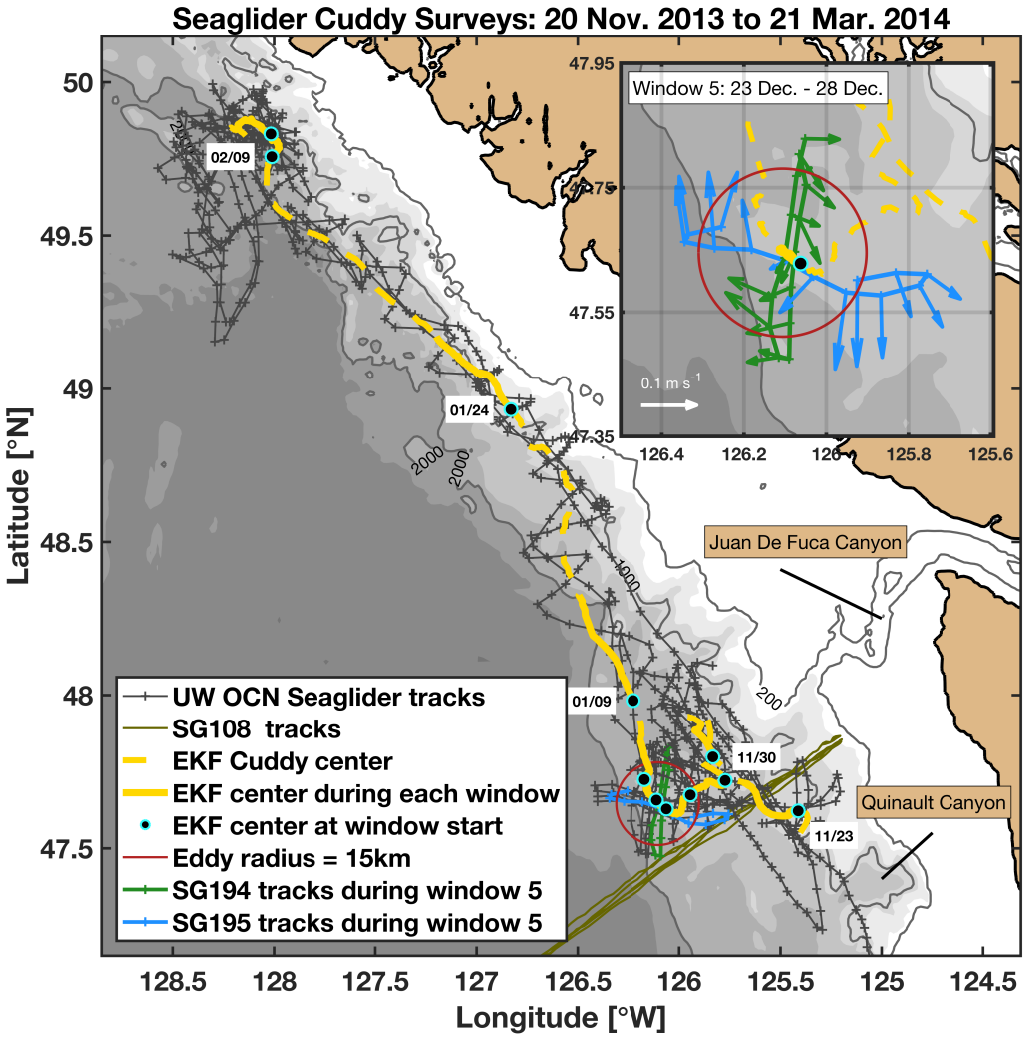

Figure 2.1: SG189, SG194, SG195 tracks from 20 Nov. 2013 to 21 Mar. 2014. Solid and dashed yellow lines are the Cuddy center estimate. Solid portions detail the Cuddy translation path during discrete time windows (Fig. 3e). Scattered in black with blue trim are Cuddy center positions at the start of each time window (select start times labeled). Glider paths and dive-cycle midpoints are in grey with SG108 cross-shore transects completed between 20 Nov. and 20 Jan. in dark green. The red circle is the estimated Cuddy radius at the fifth example time window. Grey shading indicates depth levels with the 200 m, 1000 m, and 2000 m contours added. The insert provides detail of a single time window with the tracks of two gliders (194 in green and 195 in blue) and DAC vectors for each dive-climb cycle.

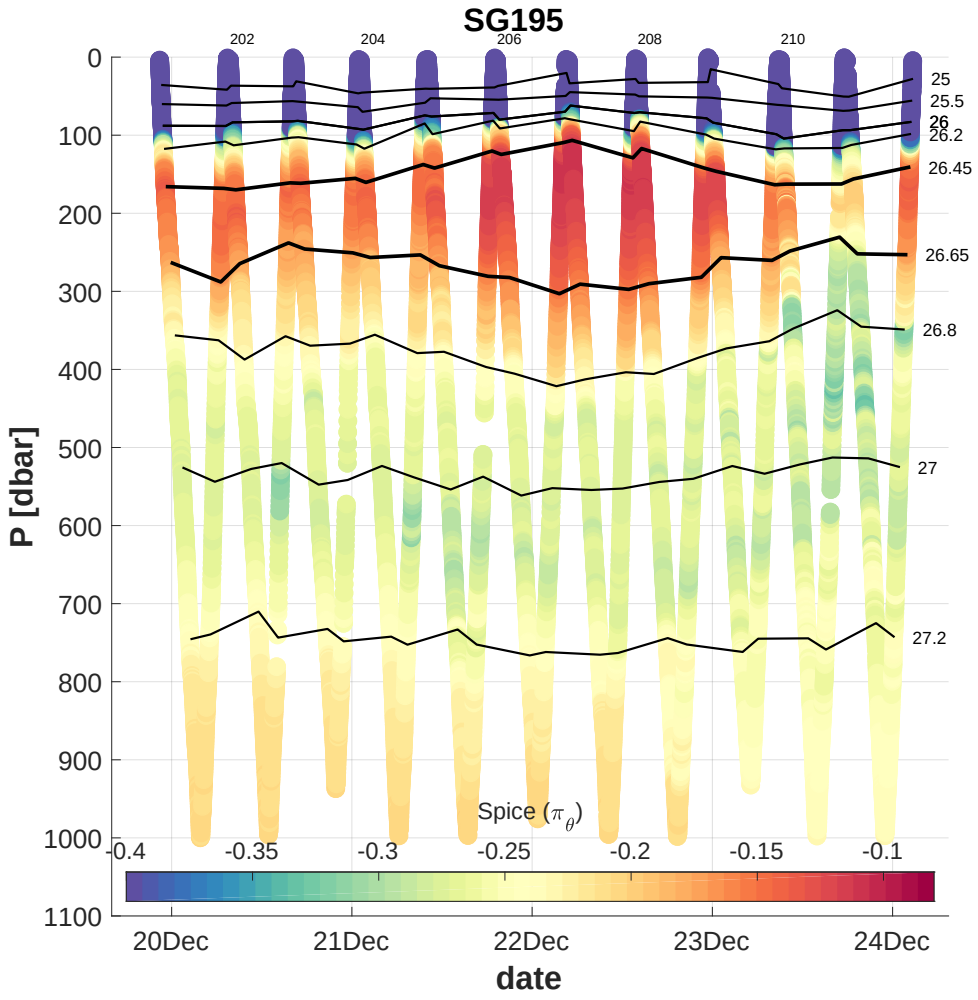

Figure 2.2: A set of eleven dive-climb cycles (in pressure and time) collected by SG195 during an example crossing of the target Cuddy. Even glider dive-climb cycles are numbered. Color indicates spice (Section 2.2); the deep red lens at 200 m depth is the Cuddy core. Isopycnals are contoured in black and deflection bounding the core lens highlights the Cuddy's vertical extent.

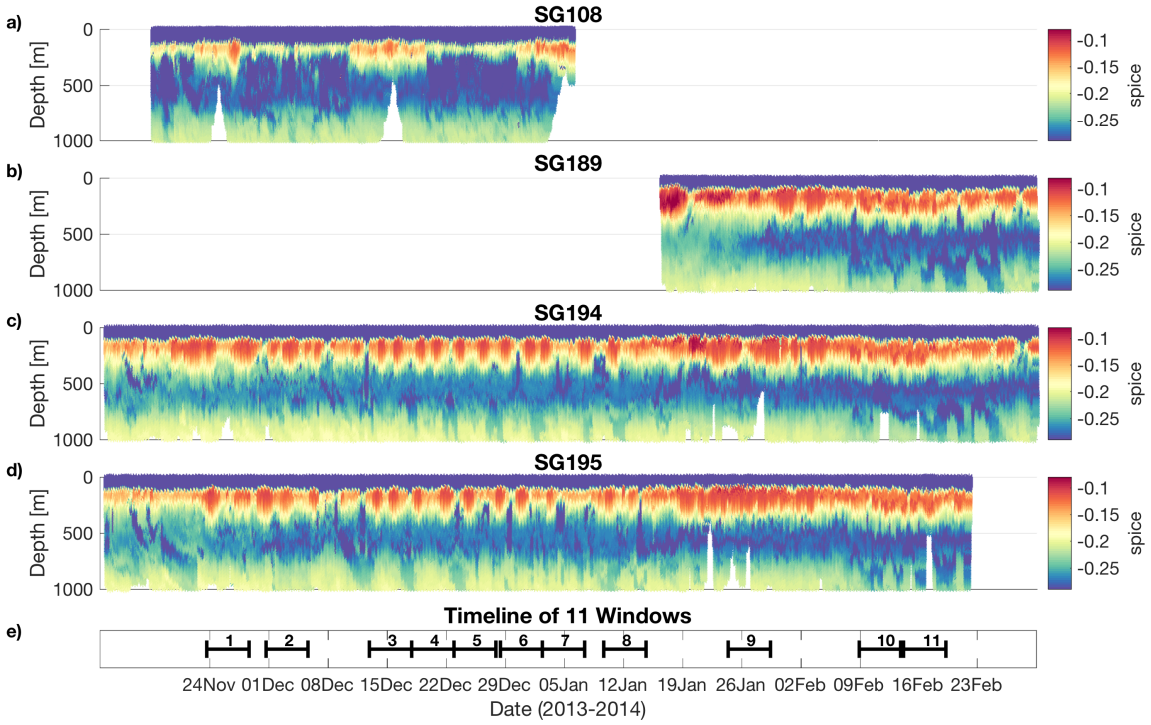

Figure 2.3: a-d) Spice (Section 2.2) collected by all gliders in this study versus time and depth. For dedicated survey gliders (other than SG108), instances of high spice in the main pycnocline indicate the center of a Cuddy transect (*e.g.,* Fig. 2.2). The periodic high spice sections made by SG108 instead reflect its movement on and offshore into and out of CU waters. e) Timeline of the period spanned by each analysis window. Gaps in this timeline in early December and mid January reflect times during which Cuddy translation speeds were increased and tracking became more difficult.

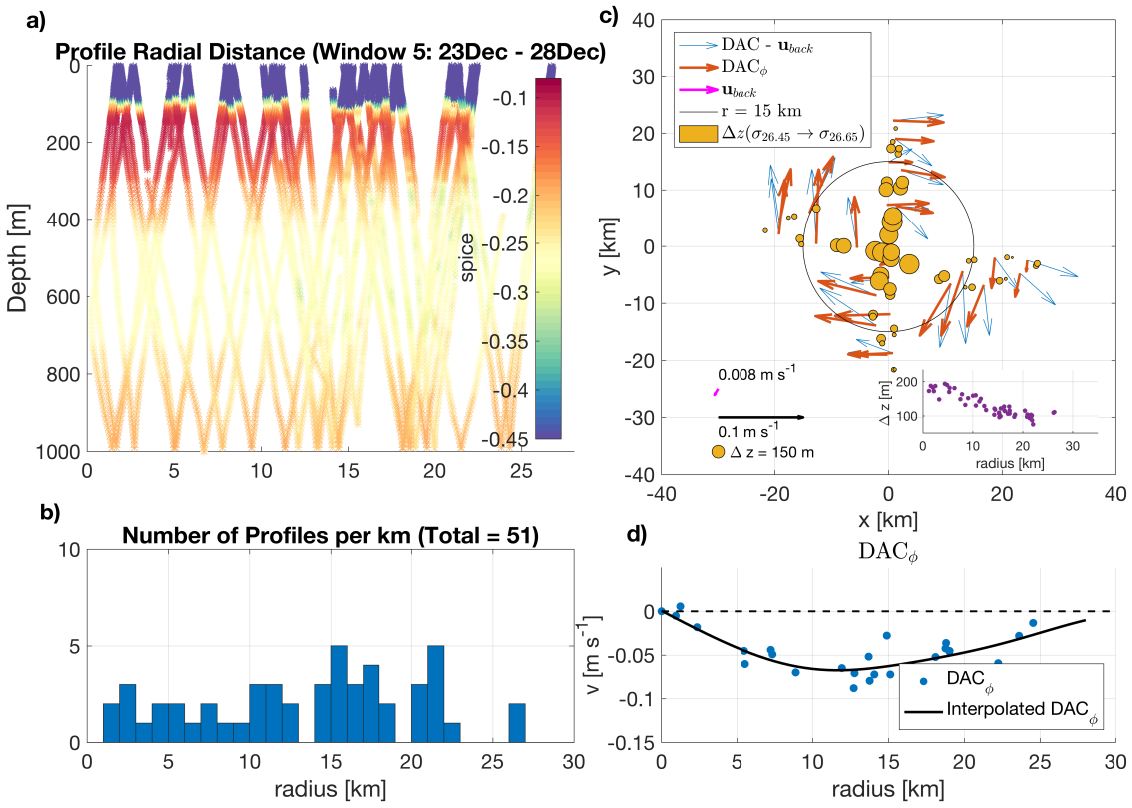

Figure 2.4: Illustration of processing steps in example time window five. a) Individual profiles of spice versus radius and depth made within this window and referenced to the time-varying eddy center. b) Cast frequency versus radius. Gliders were instructed to turn around to begin a new transect near $\sim$ 30 km. c) Dive-climb cycle midpoint location and DACs in plan view, referenced to the Cuddy center. Blue arrows are glider inferred DACs with an average background mean flow $\mathbf{u}_{\text{back}}$, estimated over the time window by the EKF, removed. Red arrows are their azimuthal component, DAC$_\phi$. The pink arrow is the average background flow estimated by the EKF over the time window. Yellow circles represent vertical separation of core-bounding isopycnals (σ_θ = 26.45 kg m^{-3} and σ_θ = 26.65 kg m^{-3}) estimated on each vertical profile. The size of the circle linearly scales with the magnitude of separation. The insert at the bottom right is the true separation as a function of radius. d) DAC$_\phi$ (blue dots: individual cycles, black: interpolated values) vs. radius.

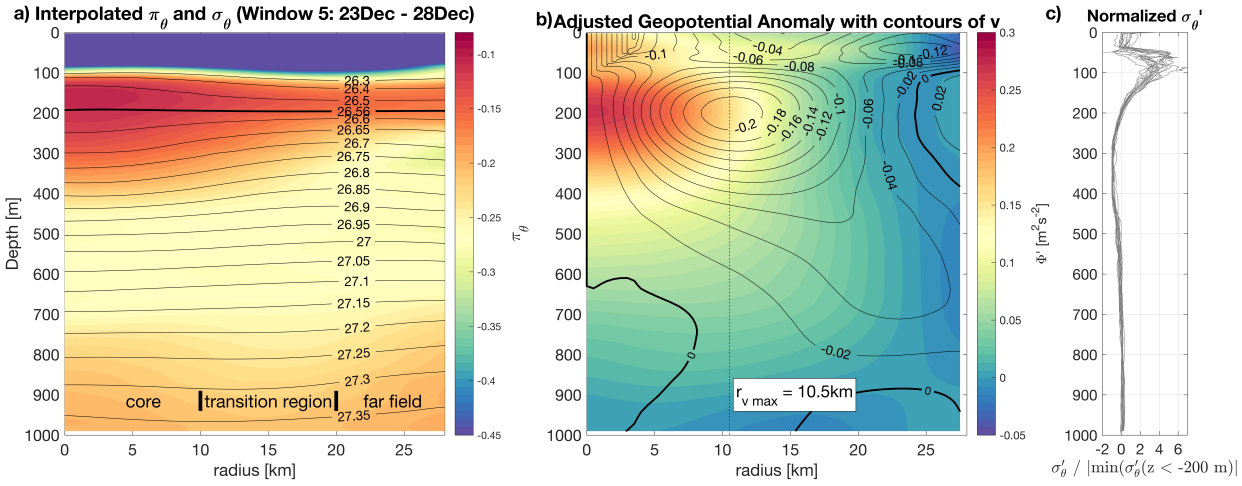

Figure 2.5: a) Interpolated spice (π_θ; colors) and potential density (σ_θ; black contours) for time-window five. b) Geopotential anomaly ($\Delta\Phi$), relative to a far field absolute geopotential background profile, with absolute gradient wind azimuthal velocity (v_ϕ) contoured in black (Section 2.42.4.1). Negative values of velocity reflect anticyclonic, clockwise circulation in cylindrical polar coordinates. c) Sixteen density anomaly profiles from time-window five and at radii $<$ 11 km. Anomalies are computed relative to an average density profile computed using profiles with radii $>$ 15 km. Profiles are normalized by the absolute value of the density anomaly minimum at z $<$ -200 m.

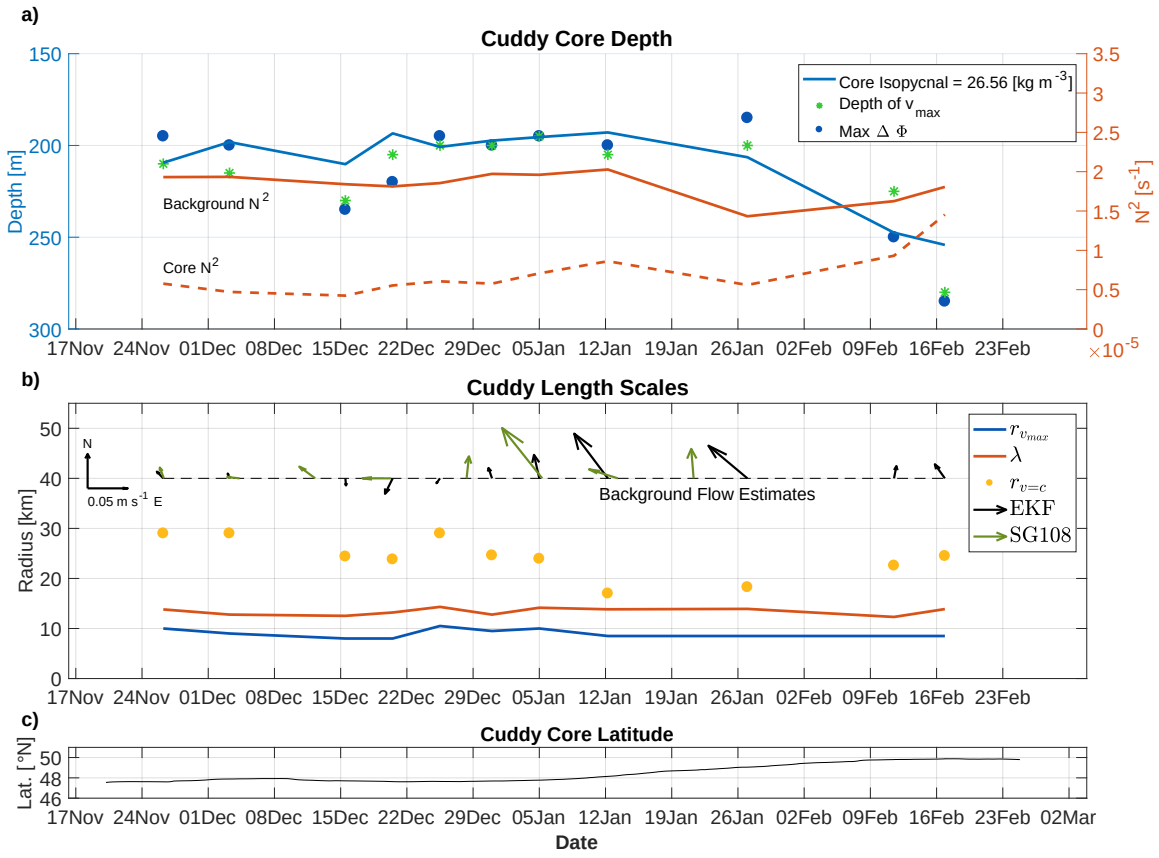

Figure 2.6: a) Depth of the target Cuddy core isopycnal (blue line), estimated maximum geopotential anomaly (blue circles), and maximum azimuthal velocity (green stars) vs. time. Referenced to the second (right) vertical axis are background (solid red) and Cuddy core (dashed red) buoyancy frequency at the core depth vs. time. b) Cuddy horizontal scale indices: radius of maximum azimuthal current $r_{v_{max}}$ (blue curve), model radial scale λ (red curve), and radius at which azimuthal current matches translation speed (yellow circles) vs. time. Average eddy translation vectors estimated from the EKF within each analysis window are in black. Green vectors are independent estimates of the background flow from SG108, averaged over the same time windows and cross-shore domain occupied by the Cuddy. c) Cuddy latitude vs. time.

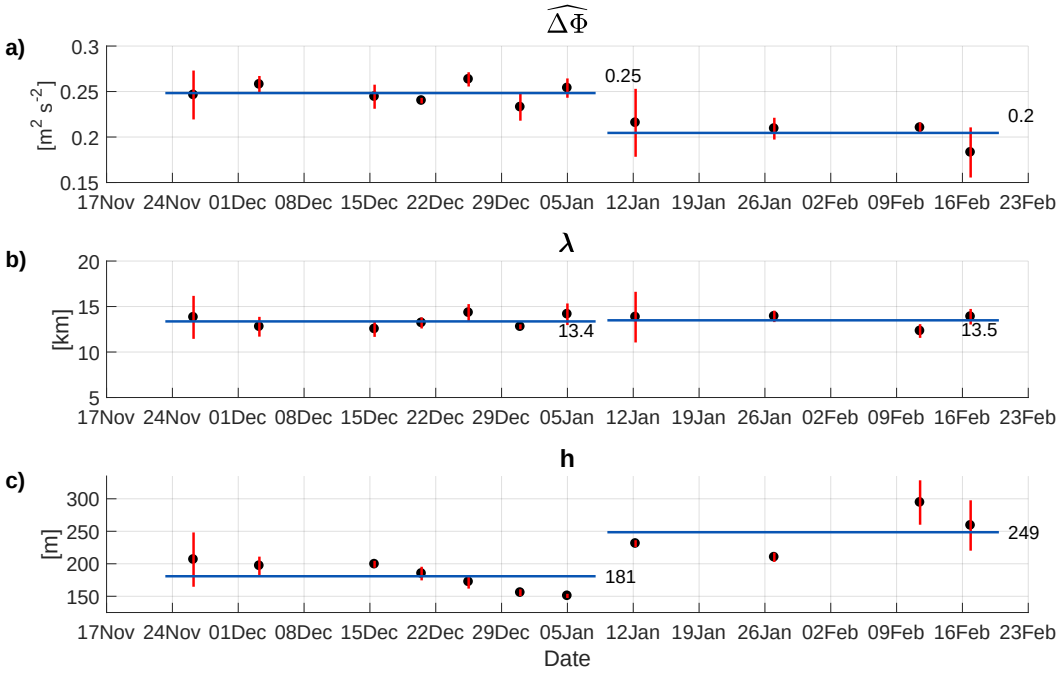

Figure 2.7: Model estimated parameters scattered in black as a function of time. a) $\widehat{\Delta\Phi}$; b) λ; c) h; as defined in Section 2.4.2.17. Vertical red bars are 95% confidence intervals and horizontal blue lines are early- and late-period averages.

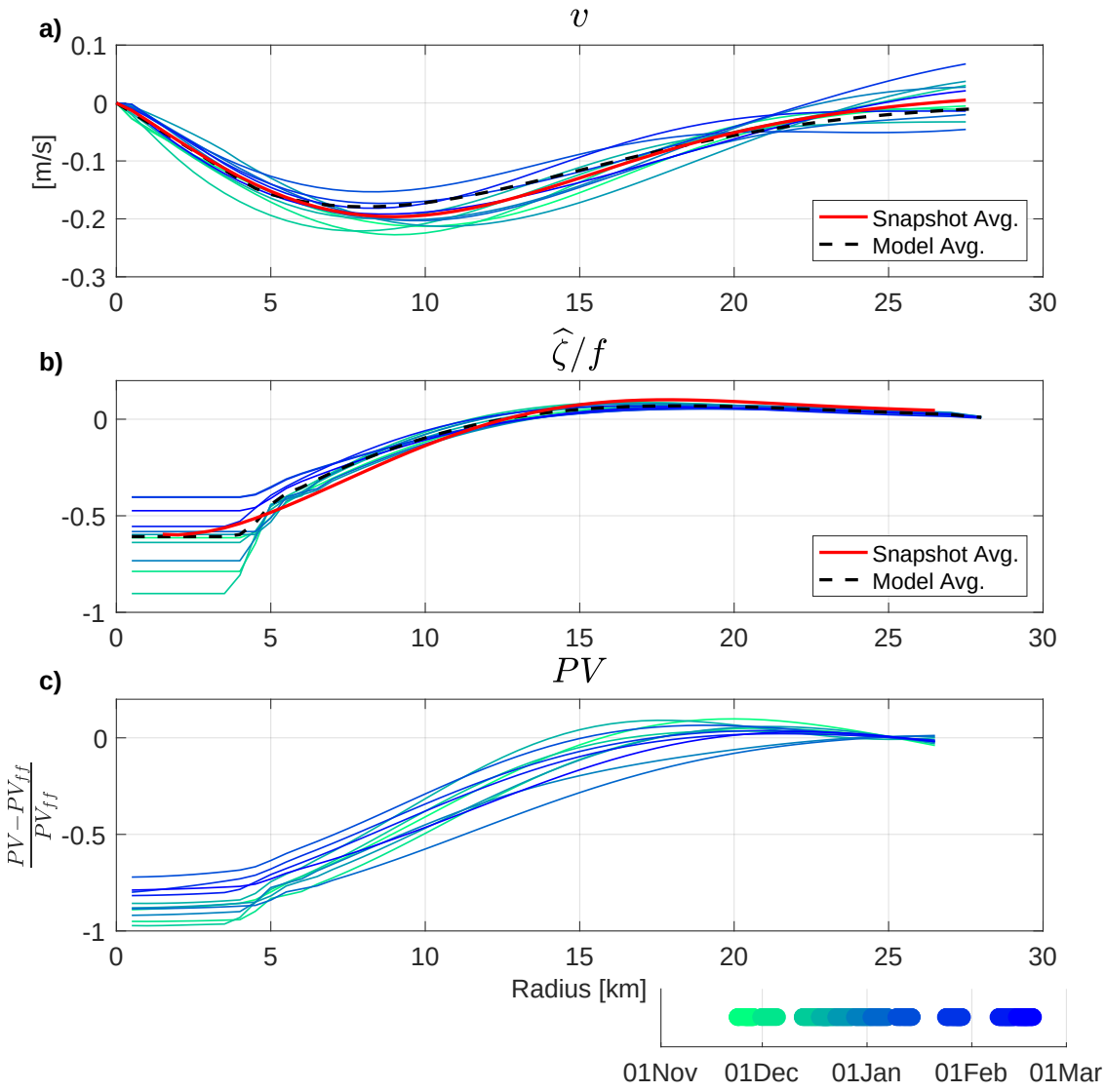

Figure 2.8: a) Radial profiles of azimuthal velocity derived from the interpolated fields (v_ϕ) at the Cuddy core depth ($z = z_0$) in each analysis window. Color corresponds to the window time (advancing green to blue; inset). Solid red profile is an average of these. Dashed black line is an average of model-estimated velocity profiles $\hat{v}$. b) Radial profiles of relative vorticity, in this case estimated from the model $\hat{\zeta}$, divided by the local Coriolis parameter f at the Cuddy core depth; individual and average profiles are colored as in (a). c) Radial profiles of potential vorticity (PV) anomaly at the core depth, subtracted from and normalized by a far-field (ff) average.

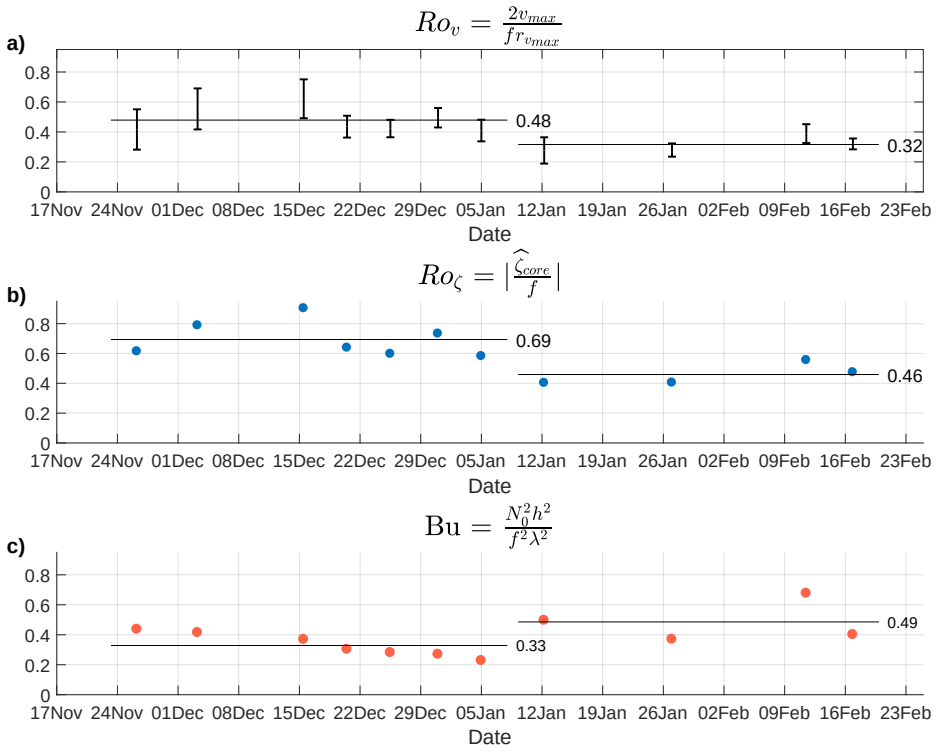

Figure 2.9: a) Rossby number Ro_v, vorticity Rossby number Ro_ζ (b), and Burger number (c) computed using model-derived velocity fields and dimensions versus time. Error bars indicate 95% confidence intervals, while horizontal lines indicate early (first 7 snapshot estimates) and late (last 4) averages.

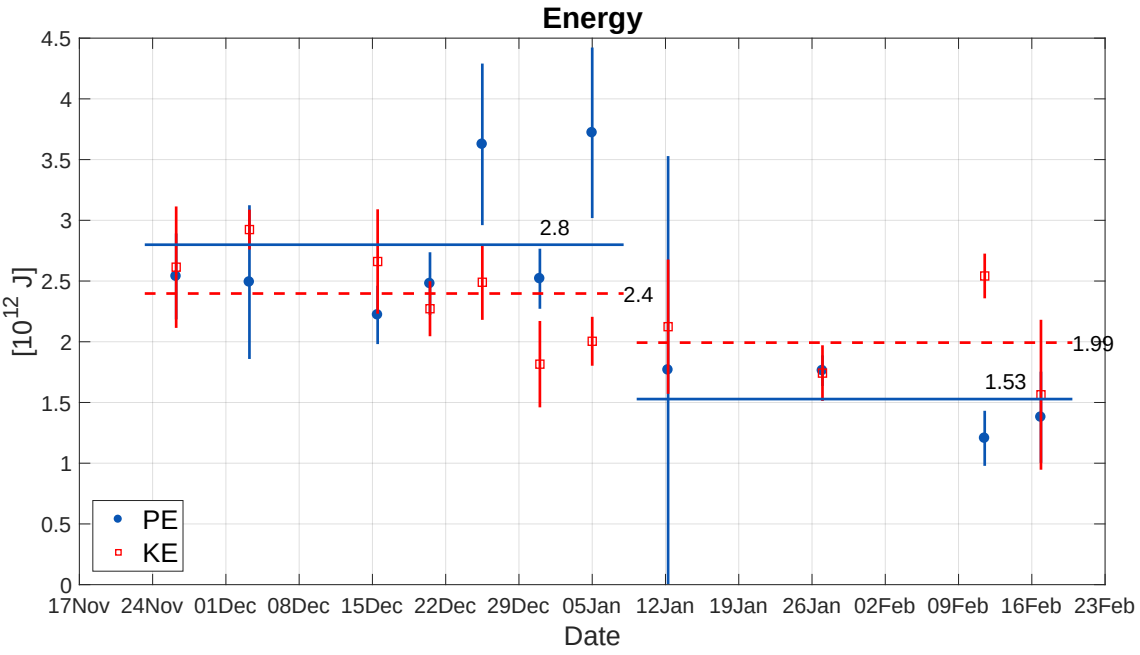

Figure 2.10: Volume integrated available potential (PE; blue) and kinetic (KE; red) energy for each snapshot. Vertical bar are 95% confidence limits accounting for center error estimates. Horizontal lines are early and late time averages with average values labeled.

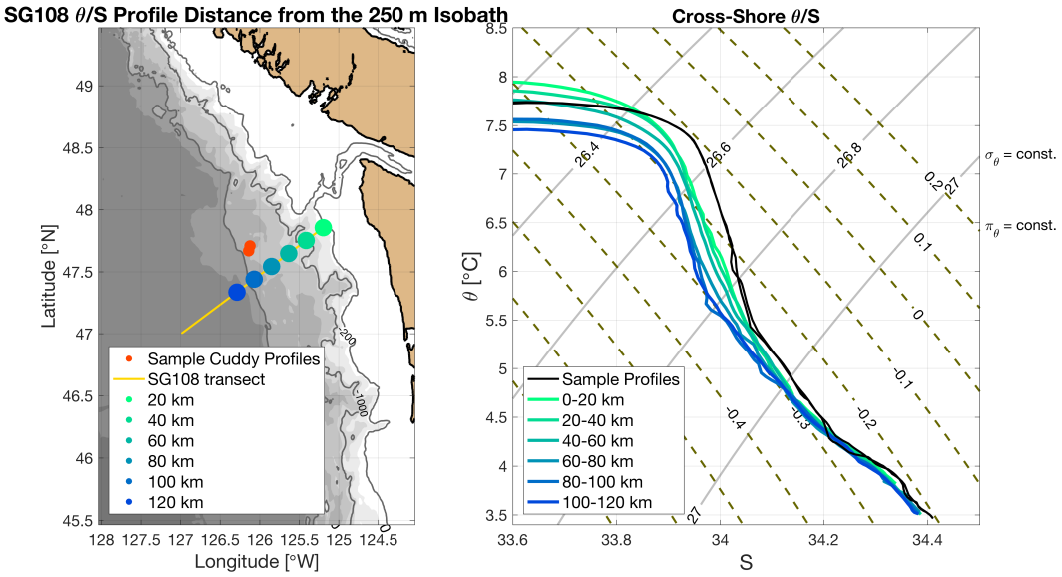

Figure 2.11: Cross-shore average potential temperature salinity (θ/S) profiles collected by SG108 between 20 Nov. 2013 and 20 Jan. 2014. The left insert details the location of the average profiles as well as the position of the Cuddy during mid December. As distance offshore increases color goes from green to blue. T/S curves are colored accordingly (right). Two profiles made through the Cuddy core are in red (left), are in black (right).

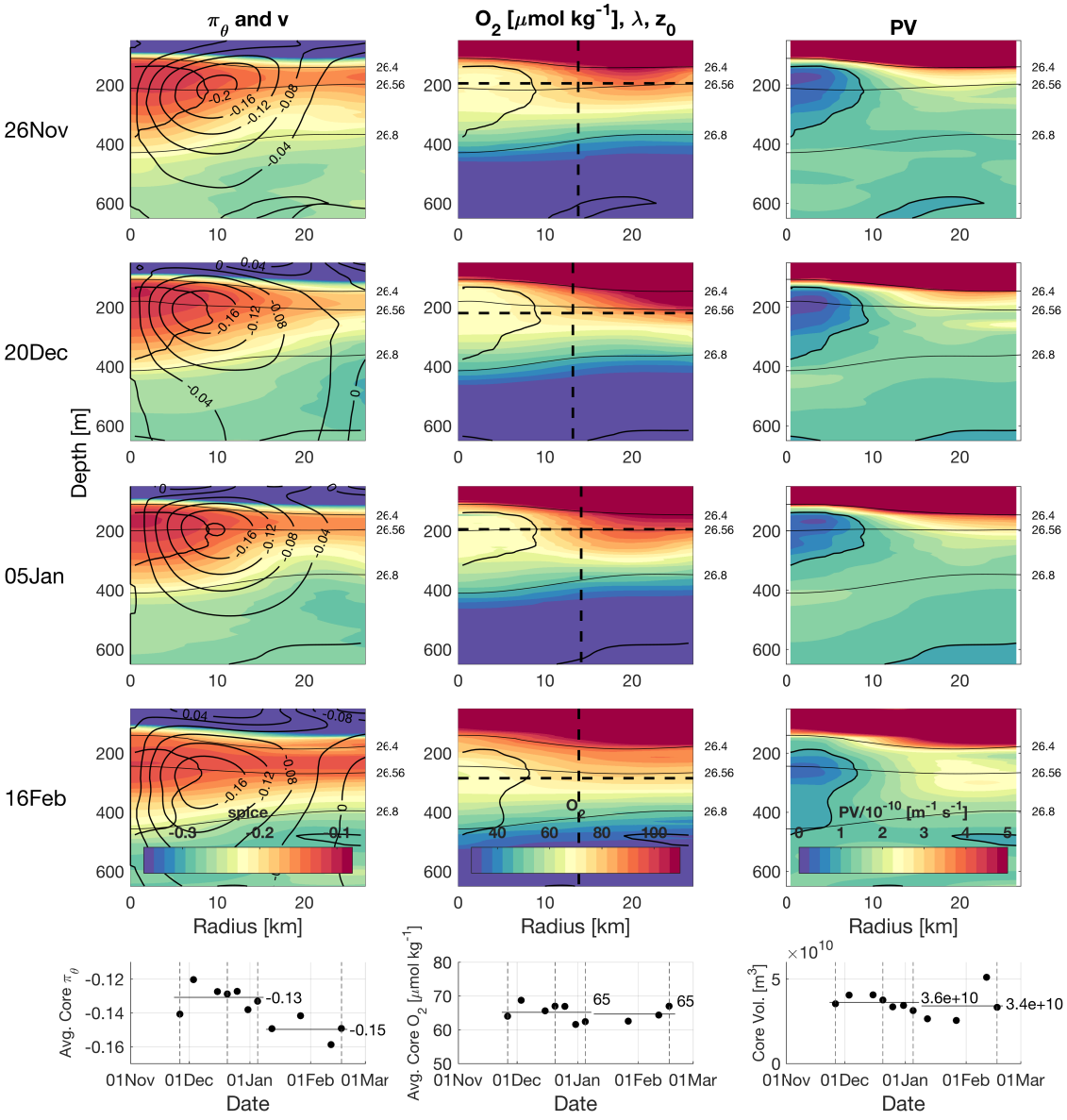

Figure 2.12: Interpolated Cuddy spice π_θ (colored), azimuthal velocity v_ϕ (contours, left column) dissolved oxygen O_2 (center column), and modeled potential vorticity (PV, right column) in four of 11 representative analysis windows (first four rows). In the second column, dashed lines indicate core depth and $r = r_{v_{max}}$. In the second and third column, the solid black contour indicates "core" $PV = 1 \times 10^{-10}[m^{-1}s^{-1}]$. Thin black contours in all columns indicate core and bounding isopycnals. The bottom row depicts respective average core property changes in time within the volume bounded by the contoured PV limit. Vertical dashed lines highlight the four selected time windows.

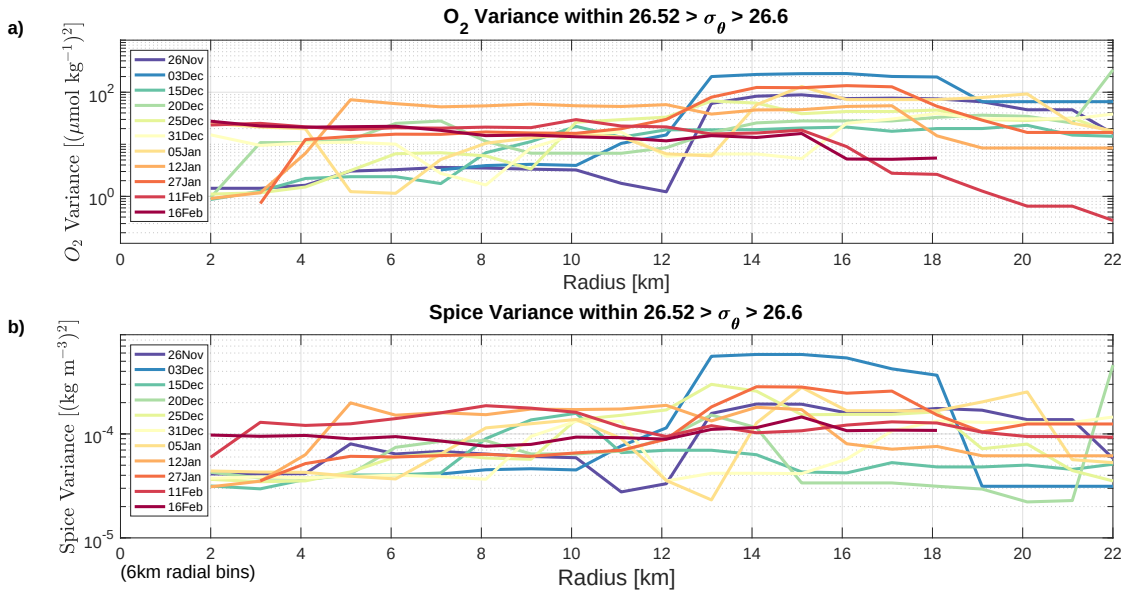

Figure 2.13: Average radial profiles of (a) oxygen and (b) spice variance between $\sigma_\theta = 26.52$ kg m^{-3} and $\sigma_\theta = 26.6$ kg m^{-3} for each analysis window. Note log y-axes with different scales.

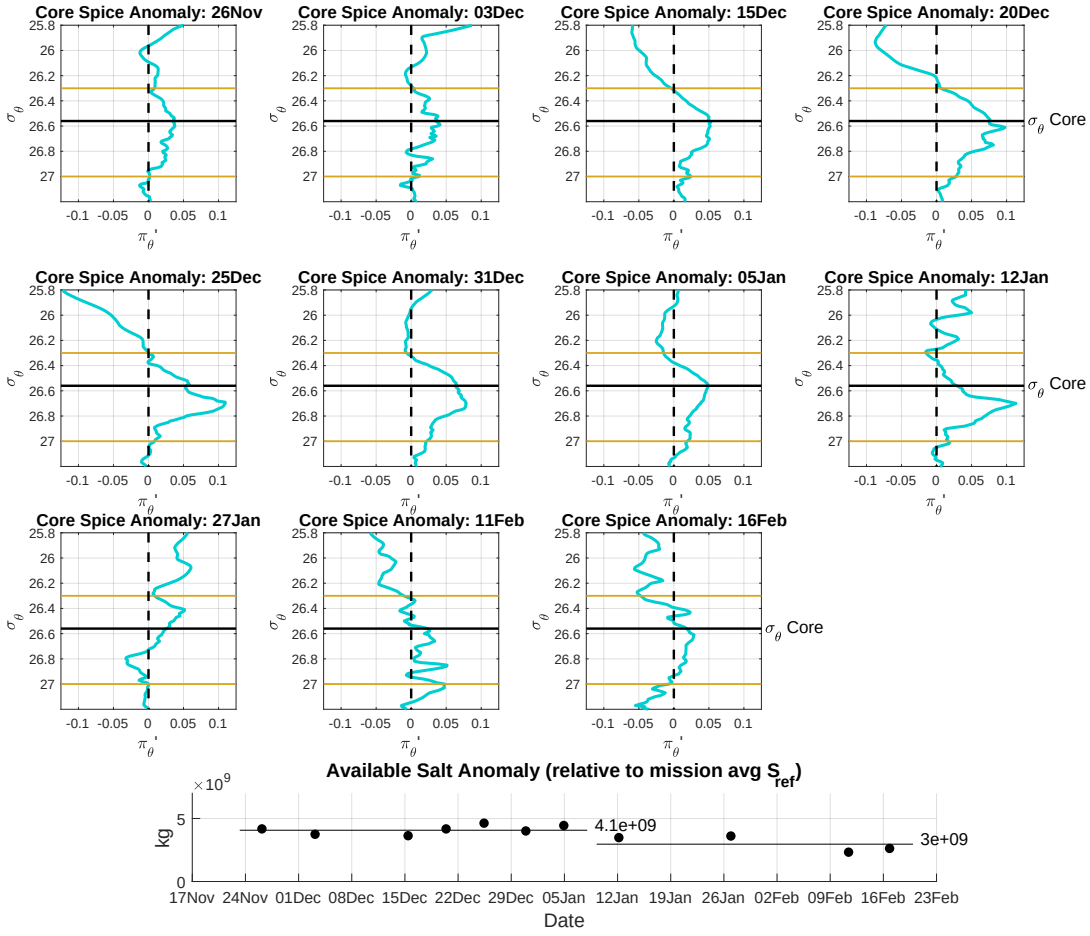

Figure 2.14: Spice anomaly profiles within the eddy center for each analysis window. Horizontal lines are density boundaries of the core region (yellow) and the core isopycnal (thick black). The zero spice anomaly reference is in dashed black. The lower figure is available salt anomaly ASA within each snapshot vs. time, including early and late averages (horizontal lines).

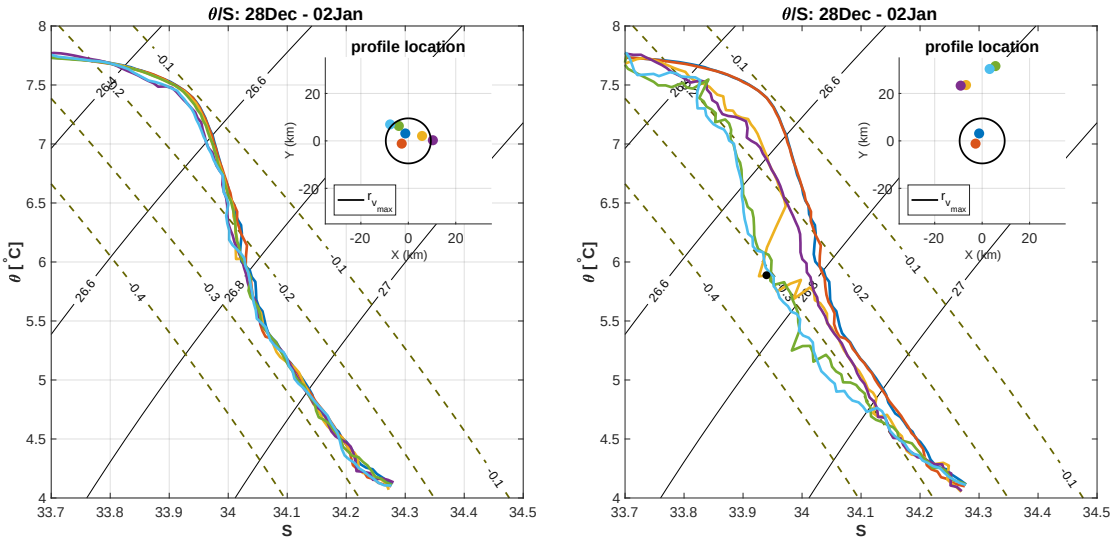

Figure 2.15: Two sets of θ/S profiles, referenced to the Cuddy center position and completed within time window six. Insets detail the midpoint location of each profile relative to the eddy center; black circle indicates the radius of maximum velocity. Profiles are colored according to their location in the inset in each panel with the black dot represents an identified spice curvature extremum.

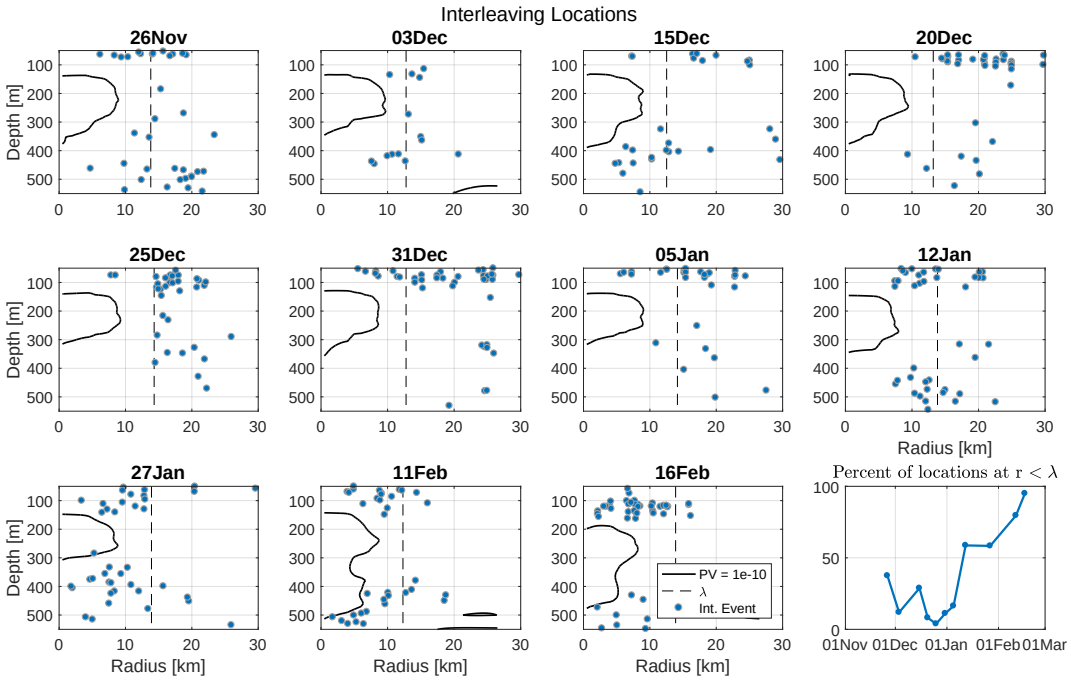

Figure 2.16: Locations of fine-structure events defined by spice curvature extrema identified within each time window, vs. radius and depth. Time advances left to right by row and date labels indicate time window midpoints. Scattered points are instances of curvature larger than two standard deviations above the mean of all curvature values found within each time window. The PV contour defined in Figure 2.12 is added to identify a core boundary. The radial scale index $r_{\zeta=0}$ is in dashed black. The lower right insert is the percentage of of tagged interleaving locations with radii $< r_{\zeta=0}$ vs. time.

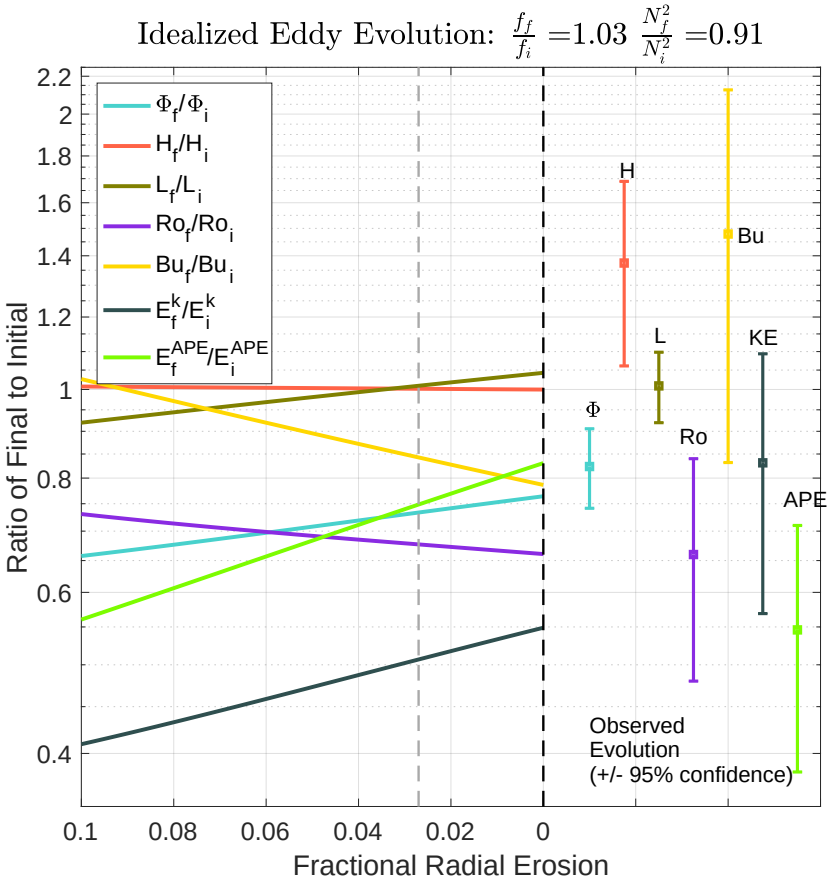

Figure 2.17: Idealized geostrophic eddy adjustment to both changes in background conditions and erosion. Changes in the maximum geopotential anomaly Φ, height scale H, length scale L, Rossby number Ro, Burger number Bu, integrated kinetic energy E^k, and the eddy component of potential energy E^{APE}, are expressed as ratios of final to initial values. The scattered points with 95% confidence intervals at the right correspond to observed Cuddy changes and are arranged in order of variable considered (the horizontal position is arbitrary). The black vertical dashed line identifies idealized model adjustments only in response to the prescribed changes in background stratification (-9%) and Coriolis parameter ($+3\%$). The colored curves to the left of the horizontal axis value of zero are relevant quantity changes in response to modeled erosion as well as the prescribed background changes. Erosion is modeled by integrating conserved quantities horizontally to values less than L. This is expressed as a fractional erosion of the original L (i.e. $0.02 = 2\%$ erosion of L_i). The grey vertical dashed line identifies the fraction of erosion corresponding to the minimum value of the observation-misfit cost function and equals 2.75%.

3 Chapter 3: Glider Sampling Simulations in High Resolution Ocean Models

3.1 Introduction

Since their development nearly twenty years ago, buoyancy driven autonomous underwater vehicles (gliders) have been increasingly used to collect sustained observations of ocean water property and velocity fields. Their successful use in diverse environmental conditions achieving various mission objectives is the result of increased accessibility to the platform, as well as improved endurance and reliability [Rudnick et al., 2016]. While gliders provide the opportunity to persistently observe the evolution of water properties, interpretation of their measurements is dependent upon knowledge of vehicle location in space and time. Without external navigational information (provided by, for example, acoustic ranging) knowledge of vehicle location is based on vehicle hydrodynamics expressed by a flight model together with surface navigation typically provided by Global Positioning System (GPS) fixes. Numerous multi-month deployments of Seaglider, Spray, and Slocum vehicles [Todd et al., 2011, Cole and Rudnick, 2012, Pelland et al., 2013, Timmermans and Winsor, 2013] have helped improve knowledge of flight characteristics, but also highlight glider versatility and implications of piloting choices such as sampling frequency, glider vertical velocity, and glide slope angle. Sampling choices are often made to extend mission duration, but also reflect a trade-off between desired spatial and temporal resolution of ocean phenomena being observed.

Gliders nominally profile with a vertical to horizontal glide slope ratio less than unity at vertical speeds of 0.05 - 0.5 m s^{-1}. The effects of sampling geometry and relatively slow speed on slant profile accuracy, as compared to profiles collected by other platforms, were identified by Rudnick and Cole [2011], specifically the Doppler shifting and aliasing of higher frequency temperature and salinity variability in measurements along depth surfaces onto large scale structure. A shift from depth to isopycnal coordinates removes this effect and permits observations of temperature and salinity variance along isopycnals with horizontal resolution dependent on maximum profile depth and glide slope. Estimates of dynamical fields such as geostrophic velocity and relative vorticity, require consideration of horizontal density gradients along isobars and reference velocity estimates. Two examples highlight relative extremes of glider sampling strategies. Piloting choices made by Pelland et al. [2013] illustrate the approach

of attempting to minimize energy use to collect a near-continuous multi-year record of the mean across-slope density and along-slope velocity structure in the northern California Current System. Seagliders repeatedly profiled to 1000 m every ~ 9 hours along two ~ 200 km transects off of the Washington coast. Interpolation of the cross-slope density field and glider inferred depth average currents resulted in monthly snapshots of geostrophic velocities in the upper 1000 m comprising the California Current System. Aliasing of high frequency vertical isopycnal displacements due to slow sampling speeds was reduced using Gauss-Markov interpolation along depth surfaces. Alternatively, with the approach of attempting to maximize horizontal resolution in the surface ocean, Timmermans and Winsor [2013] piloted Slocum gliders in shallow waters diving to 40 m and back every ~ 15 minutes. This sampling strategy permitted observation of both high wavenumber along-isopycnal temperature and salinity variance, and internal wave displacements with time scales of hours. These examples illustrate different glider sampling strategies to respectively observe large scale density structure and fine scale thermohaline variability.

More recent deployments reveal an increasingly diverse set of glider sampling strategies and objectives. Alvarez and Mourre [2016] consider optimal sampling strategies, not as a function of depth as discussed above, but instead with the aim of best resolving the horizontal structure of an evolving mesoscale field using a stationary mooring as a local reference. Repeat transects, carried out in the Mediterranean Sea, Sea of Japan, and Eastern Pacific likewise demonstrate different settings in which gliders are used to estimate mixing and transport [Cotroneo et al., 2019, Wagawa et al., 2020, Jakoboski et al., 2020]. These observations are all referenced to motivate consideration of the dependence of aliasing and bias on sampling pattern geometry and speed. While aliasing of high frequency motions is unavoidable when considering horizontal gradients, piloting choices based on scientific objectives can be made to reduce it.

Deepglider, a recently developed buoyancy-driven autonomous underwater vehicle operationally similar to Seaglider but with a maximum operating depth of 6000 m, extends glider observational range considerably, prompting further consideration of the effects of sampling slowly along slanted paths in ocean. Because over 98% of the world ocean is shallower than its maximum operating depth, Deepgliders are capable of collecting full-depth temperature and salinity slant profiles daily with vertical resolution of order meters. With the exception of wire-walking instruments deployed on moorings at multiple depths, vertical resolution of temperature and salinity measure-

ments made by gliders is far finer than can affordably be attained by traditional moored instruments [Wunsch, 1997, de La Lama et al., 2016]. Despite limitations of coarse vertical resolution and full-depth deployments at relatively select locations, mooring time series of water properties have provided a description of complete eddy vertical structure limited to the gravest few vertical modes [Wunsch, 1997]. Vertical modes are a dynamical set of orthogonal eigenfunctions, each a time independent solution describing the vertical structures of quasi-geostrophic eddies. These modes are a natural basis set often used in partitioning vertical structure into barotropic and baroclinic components in a dynamically relevant manner. Estimation of the partitioning of energy across modes, akin to a spectral analysis identifying spatial or temporal scales associated with dominant fractions of signal variance, permits consideration of energy containing scales and transfers in the vertical. The ability of Deepgliders to occupy remote regions of the ocean for durations as long as a year permits collection of more highly resolved density structure and motivates renewed consideration of complete eddy vertical structure as well as the accuracy of derived geostrophic velocity profiles based on slow sampling along slanted vertical-horizontal paths in the ocean.

High resolution ocean numerical model simulations provide opportunity to simulate idealized glider flight across a range of speeds and glide slopes. The simulated collection of measurements permits an analysis of glider profiling efficacy analogous to that made by Rudnick and Cole [2011]. We are interested in the accuracy 1) of geostrophic velocity profile estimates referenced to a glider inferred depth average current, and 2) of isopycnal vertical displacement profile estimates, both associated with quasi-geostrophic eddies. Using output from two independent ocean numerical model simulations, one in the eastern North Pacific and the other in the North Atlantic, we simulate glider sampling along zonal and meridional transects and compare glider sampling derived geostrophic velocity fields to instantaneous and multi-day average numerical model velocities.

This paper is organized as follows: Section 2 discusses Deepglider sampling strategies employed during a ten month Deepglider mission in the North Atlantic subtropical gyre to observe evolution of the mesoscale eddy field. Model resolution and output from the HYbrid Coordinate Ocean Model (HYCOM) and LiveOcean, a regional ocean modeling system (ROMS) model, are also detailed. Section 3 describes the simulation of glider sampling through each model, the techniques used in estimating isopycnal vertical displacement and geostrophic shear profiles, and the calculation of vertical modes. Section 4 presents results, discusses glider sampling error of velocity profiles as a

function of glide slope and speed, and quantifies glider geostrophic shear estimate error along with its dependency on a ratio between eddy and high frequency (e.g. tidal) isopycnal variability. Section 5 concludes with some advice on glider piloting strategies.

3.2 Framework

3.2.1 Deepglider Flight and Observations in the North Atlantic

Deepglider is a buoyancy driven autonomous underwater vehicle capable of profiling from the surface to 6000 m and back in approximately 1.5 days. Developed as a Seaglider variant capable of regularly profiling to the seafloor, Deepgliders employ an adapted Seaglider flight model and hydrodynamic framework originally described in Eriksen et al. [2001]. Temperature and conductivity measurements are made by a SeaBird Electronics thermistor and conductivity cell aspirated by vehicle motion, processed to calculate salinity following methods described in Pelland et al. [2013]. Measurements are taken at pilot specified time intervals, typically 10 seconds in the upper ocean increasing to 60 seconds deeper than 1000 m. Vertical bin averaging of measurements to a non-uniform grid, with intervals selected to obtain an approximately equal number of measurements in each depth bin, provides a nominal resolution of 1 m over the upper 150 m, 5 m between 150 m and 300 m, 10 m between 300 m and 1000 m, and 20 m from 1000 m to the seafloor. Using these vertical bin intervals, a typical bin-averaged temperature slant-profile from the surface to 5000 m is comprised of over 400 samples. Gliders also estimate a depth-average current (DAC) as the difference between GPS-tracked overground and dead-reckoned displacement. Temperature, salinity, and depth-average current accuracy are presumed 0.003 °C, 0.01 psu, and 0.01 ms^{-1} [Pelland et al., 2013, Todd et al., 2011], respectively, and subsequently used in scaling simulated random instrument noise.

During descent and ascent, gliders translate horizontally with a vertical to horizontal glide slope dependent on glider pitch, buoyancy, hydrodynamic lift and drag parameters, depth, and horizontal range to a target location. Glide slope s is nominally 1/3, selected to roughly maximize horizontal speed for a given nominal buoyancy and vertical speed. In cross-section, successive dive-climb cycles completed along a track of constant compass heading in still water result in a sawtooth track pattern (Fig. 3.1) with measurements distributed in depth and distance with time along the path. Horizontal temperature and salinity gradients along isobars or isopycnals can then be

estimated from samples along the sawtooth path. The horizontal distances over which these gradients are estimated vary with depth and are a function of maximum sampling depth and glide slope. For a vertical speed of 0.075 m s^{-1} and glide slope s = 1/3, two full-depth slanting tracks to 5000 m, one each in descent and ascent, are completed about every 37 hours and span a horizontal distance of about 30 km through the water.

Deepglider sg035, used for reference in subsequent sampling simulations, was deployed offshore Bermuda and sent to the Bermuda Atlantic Time Series station (BATS) site (31°40'N, 64°10'W) in February 2015 where it collected 350 full-depth slant profiles during a ten month repeat survey mission (Fig. 3.2). Each leg of the bowtie repeat pattern was comprised of two to four pairs of downward and upward slant paths, each pair labeled as a dive-climb cycle. The horizontal track of the dive-climb cycles of Figure 3.1 is shown in Figure 3.2, an example of a relatively straight track along a bowtie leg. The bowtie pattern was selected to permit estimation of gradients and geostrophic velocities in both the directions parallel and normal to Bermuda rise topography. Simulations of glider sampling of ocean numerical model fields follow a similar pattern with uniformly directed transects.

3.2.2 HYbrid Coordinate Ocean Model (HYCOM)

Two weeks of hourly full-depth temperature, salinity, pressure, and horizontal velocity fields were extracted along four transects, each 191 km in horizontal length, from climatologically forced and eddy-resolving HYCOM simulations near the BATS site (Fig. 3.3). The numerical configuration of these simulations is similar to that presented in Xu et al. [2016] and Chassignet and Xu [2017] with domain bounds near 28°S in the South Atlantic and at the Fram Strait (80°N) in the North Atlantic. In the region near BATS, the model is isopycnic with 32 vertical levels and a horizontal resolution of approximately 3.8 km (1/25°). Simulations obtained for this analysis include tides, with 8 tidal constituents, and reflect on-going experiments to incorporate tides into all HYCOM simulations (details will be documented in the future).

Along the extracted slices, vertical levels are spaced at intervals of less than 10 m between the surface and 40 m, $\sim$ 100 m between 50 m and 1200 m, and 250 m increasing to 550 m between 1200 m and the seafloor. Model fields were interpolated to a grid with vertical spacing of 10 m from the surface to 100 m and 20 m from 100 m to the seafloor.

3.2.3 LiveOcean Regional Ocean Modeling System (ROMS)

One month of hourly full-depth temperature, salinity, pressure, and horizontal velocity fields were extracted along a 200 km zonal transect from LiveOcean, a ROMS simulation in the eastern North Pacific (Fig. 3.4). LiveOcean (`https://faculty.washington.edu/pmacc/LO/LiveOcean.html`) is a regional forecast simulation with variable horizontal resolution of 0.5 - 1.5 km and 30 vertical levels. Ocean boundaries are forced by HYCOM ocean fields and the surface is forced by winds, solar heating, and air-sea exchange. This model includes river inflows and tides [Giddings et al., 2014]. A relatively flat region of the model domain was selected with an average depth, offshore of the continental slope, of 2800 m. Along this transect, vertical levels are spaced at a variable interval of 6 m - 175 m and were also interpolated to a grid with vertical spacing of 10 m from the surface to 100 m and 20 m from 100 m to the seafloor.

3.3 Methods

3.3.1 Simulated Glider Tracks

The slanting paths of simulated steady glider flight along model zonal and meridional transects (Figs. 3.3, 3.4) were generated by selecting a starting time and location along a model transect, a fixed vertical speed, maximum dive-cycle depth, and glide slope. Sampling time intervals were set by the specified vertical speed and vertical grid to which fields in both models were interpolated. Beginning at the specified starting surface location, model fields of temperature and salinity were linearly interpolated at each vertical grid point to the time and horizontal location of the simulated glider path at that depth, determined by speed and glide slope specifications. Interpolation continued to the specified maximum depth and likewise to the sea surface during the climb portion of each cycle. The maximum depth attained on each profile is 10 m above the model bottom. For each simulated dive-climb cycle, a depth-average current estimate is calculated as the average of all cross-track model velocities within the spatial and temporal limits of the dive-climb cycle. These depth-average current estimates are subsequently used in referencing glider estimated cross-track relative geostrophic velocity profiles. Sampling error is added to each measurement of temperature, salinity, and the depth-averaged current using random samples from a normal distribution with zero mean and standard deviation equal to half of the instrument accuracy estimates described in section 2a. This

procedure is repeated until the desired number of dive-climb cycles is reached or the glider reaches the end of the model domain.

Along each model transect, sets of four dive-climb cycles were simulated for starting surface positions of 10 km, 40 km, 70 km, and 100 km from the transect's edge, and for starting times at the earliest time of model output and at subsequent 72 hour intervals. Simulated glider profiling beginning at these starting surface positions and start times results in sampling of a variety of dynamic model features including surface intensified eddies with velocities of over 0.5 m s^{-1} and radii of over 40 km as well as the internal wave field in the absence of strong mesoscale features. Simulated glider sampling at these starting locations and start times was repeated for four different realistic glider vertical speeds, 0.06 m s^{-1}, 0.075 m s^{-1}, 0.1 m s^{-1}, and 0.2 m s^{-1} and vertical to horizontal glide slopes of s = 1/2 and s = 1/3.

Simulated glider slant profiles of temperature and salinity along the specified vertical grid are used in the calculation of neutral density γ^n [Jackett and McDougall, 1997]. Slant profiles of neutral density are then used to estimate isopycnal vertical displacement about time mean depths as well as horizontal density gradients along isobars.

3.3.2 'W'/'M' Sampling: Isopycnal Vertical Displacement and Geostrophic Velocity Profile Estimation

Accuracy of the technique employed to estimate isopycnal vertical displacement and cross-track geostrophic velocity profiles at station BATS is explored through simulation of glider sampling along transects of HYCOM and LiveOcean model output. While glider slant profiles completed along each transect leg of the BATS bowtie pattern do not strictly follow a line in plan view (Fig. 3.2, 3.5), the technique used to estimate vertical displacement and a horizontal density gradients as a function of depth and along linear paths is used in practice on sets of dive-climb cycles completed while glider heading does not deviate by more than 40 degrees from an average heading.

In this framework, each displacement and velocity profile estimate is made using samples from two dive-climb cycles that form a pattern similar to the letter 'W' or similarly from a pair of consecutive climb-dive cycles forming a pattern similar to the letter 'M' (Fig. 3.6). Displacement profile estimates are made using four samples at

each depth and geostrophic velocity profile estimates can be derived following the estimation of horizontal density gradients using thermal wind. Each horizontal gradient estimate is calculated from four samples at the same depth along respective slant paths of the pairs of dive-climb ('W') or climb-dive ('M') cycles. The horizontal distance over which gradients are estimated is double at the surface what it is at the bottom for 'W' sampling and conversely for 'M' sampling. The estimated vertical profiles of displacement and along-track horizontal density gradients are located at the center of each pattern, the junctions between the pairs of cycles used.

Because actual glider transects rarely are precisely straight in plan view, horizontal density gradients at each depth are estimated applying a least squares two-dimensional planar fit to four density measurements. The two-dimensional horizontal gradient is then projected onto the mean along-track direction (Fig. 3.5). For simplicity, simulated glider fight paths in LiveOcean and HYCOM are along zonal or meridional transects and errors introduced as a result of deviations in heading are not considered here.

A single simulated glider transect composed of four dive-climb cycles permits estimation of five vertical isopycnal displacement and absolute geostrophic velocity profiles located at the junctions of all dive-climb and climb-dive pairs of slant profiles. Each displacement and velocity profile is computed from two successive dive-climb (climb-dive) simulated tracks to form a vertical profile estimate centered at the midpoint of the sampling 'W' ('M') window. (Fig. 3.6). At grid depths z_i, average vertical displacement ξ in meters, across two consecutive dive-climb or climb-dive cycles, is defined as

$$\xi(z_i) = \frac{\gamma^n(z_i) - \overline{\gamma^n}(z_i)}{\frac{\partial \overline{\gamma^n}(z_i)}{\partial z}} \tag{28}$$

where γ^n(z) is an average density profile of the four contributing slant profiles and $\overline{\gamma^n}(z)$ is a temporal average of all model density profiles at the mid-point location of the 'W' or 'M' pattern along the transect. This temporal average of model density profiles spans the entire record of model output obtained for this analysis, a two-week period in HYCOM and one month in LiveOcean, and is meant to reflect the mean density field atop of which eddy perturbations occur.

Because simulated glider sampling is along a constant heading, one-dimensional along-track horizontal density gradients $\frac{\partial \gamma^n}{\partial x}$ are calculated at each depth, where x is along-transect distance. While these horizontal density

gradients reflect the combined effect of all model dynamics, we seek to capture quasi-geostrophic density gradients, presumed evolving on times scales greater than the approximate time required to complete two dive-climb or climb-dive cycles and unchanging throughout this period over a horizontal distance equal to the greatest distance between contributing measurements. The assumption that these gradients are entirely quasi-geostrophic is incorrect, and aliasing of higher frequency and wavenumber dynamics onto these estimates is subsequently explored, but it permits the estimation of cross-track geostrophic velocity shear as

$$\frac{\partial v}{\partial z} = \frac{-g}{\rho_0 f}\frac{\partial \gamma^n}{\partial x} \tag{29}$$

where $v(z)$ is cross-track geostrophic velocity and is positive to the left of x, g is gravitational acceleration, ρ_0 a reference density, and f the local Coriolis parameter. Following estimation of horizontal density gradients at each depth for each dive-climb (climb-dive) cycle pair, the vertical shear of the geostrophic velocity is calculated, integrated from the seafloor to the surface, and referenced to the glider estimated depth average current to obtain a full-depth profile of absolute geostrophic velocity. The location along the transect of each profile is set at the midpoint location of contributing density profiles.

In what follows, the terms glider velocity profile and glider displacement profile are taken to mean estimates of vertical profiles of these quantities estimated from pairs of consecutive simulated glider cycles (dive-climb for 'W' sampling and climb-dive for 'M' sampling).

3.3.3 Vertical Wavenumber Spectra

Vertical structures of glider and model isopycnal vertical displacement and horizontal velocity profiles are explored through the use of normal vertical modes. Quasi-geostrophic dynamics, descriptive of the mesoscale eddy field, permit a separation of variables solution for horizontal velocities $u, v(x, y, z, t)$ in which eddy vertical structure of slowly evolving geostrophic velocity can be described by a set of m normal modes ϕ_m satisfying

$$\frac{\partial}{\partial z}\left(\frac{1}{N^2(z)}\frac{\partial \phi_m(z)}{\partial z}\right) + \lambda_m^2 \phi_m(z) = 0 \tag{30}$$

where N^2(z) is the Brunt-Vaisala frequency calculated using an average background density profile, λ_m the m^{th} eigenvalue solution with units of s m^{-1}, and ϕ_m the m^{th} eigenfunction describing horizontal velocity structure [Wunsch, 1997]. Numerical solutions to Eq. 30 are obtained for the first thirty modes with flat bottom and free surface boundary conditions (the first three of which are depicted in Fig. 3.7). These functions, the vertical modes, are normalized per unit energy such that

$$\frac{1}{H}\int_{-H}^{0}\phi_m^2(z)dz = 1 \tag{31}$$

where H is the full depth of the water column. This normalization permits water column average kinetic energy to be expressed solely as a function of mode amplitude. Vertical modes are first projected onto i individual cross-track glider and model horizontal velocity profiles generally expressed as

$$v_i(z) = \sum_{m=1}^{30}\alpha_{mi}\phi_m(z) \tag{32}$$

to obtain mode amplitudes α_{mi}. These profiles are squared and vertically averaged:

$$\frac{1}{H}\int_{-H}^{0}v_i^2(z)dz = \frac{1}{H}\int_{-H}^{0}\sum_{m=1}^{30}\alpha_{mi}\phi_m(z)\cdot\sum_{n=1}^{30}\alpha_{ni}\phi_n(z)dz. \tag{33}$$

By the orthogonality of the modes, cross terms in the product of sums drop out giving:

$$\frac{1}{H}\int_{-H}^{0}v_i^2(z)dz = \sum_{m}\alpha_{mi}^2\frac{1}{H}\int_{-H}^{0}\phi_m^2(z)dz. \tag{34}$$

The result is water column average kinetic energy $\langle v^2\rangle$, across the sampling domain, expressed as a function of mode number and amplitude $\langle\alpha_m\rangle$

$$KE_m = \langle v^2\rangle = \sum_{m=0}^{30}\left\langle\alpha_m^2\frac{1}{H}\int_{-H}^{0}\phi_m^2(z)dz\right\rangle = \sum_{m=0}^{30}\langle\alpha_m^2\rangle. \tag{35}$$

Due to the geometry of extracted model transects and the technique used to compute cross-track geostrophic velocity, this kinetic energy estimate includes only a single component of horizontal velocity, its cross-track value. Anisotropy of the velocity field across the model domain and in time is not considered.

Estimates of isopycnal vertical displacement are similarly used to explore the partition of potential energy across vertical modes. Isopycnal vertical displacements, presumed to largely reflect mesoscale eddy isopycnal perturbations about a mean background state, are defined as

$$\xi_i(z) = \sum_{m=1}^{30} \beta_{mi} \frac{1}{N^2(z)} \frac{\partial \phi_m(z)}{\partial z} \tag{36}$$

where β_m mode amplitudes are calculated for i displacement profiles. Actual and simulated glider, as well as model, isopycnal vertical displacement profiles capture vertical motions caused by some combination of internal wave, tide, and eddy displacements. The aliasing of higher frequency and wavenumber internal tide displacements onto eddy structure will be subsequently addressed. The relationship between the vertical structure of geostrophic velocity $\phi_m(z)$ and isopycnal vertical displacement $\frac{1}{N^2(z)} \frac{\partial \phi_m(z)}{\partial z}$ is derived following Wunsch and Stammer [1997a]. Water column average potential energy, as a function of mode number, is then

$$PE_m = \left\langle \frac{1}{H} \int_{-H}^{0} \frac{1}{2} \xi^2(z) N^2(z) dz \right\rangle = \frac{1}{2H} \sum_{m=1}^{30} \left\langle \beta_m^2 \int_{-H}^{0} \frac{\phi_m^2(z)}{\lambda_m^2} dz \right\rangle = \frac{1}{2} \sum_{m=1}^{30} \left\langle \frac{\beta_m^2}{\lambda_m^2} \right\rangle, \tag{37}$$

having substituted into Eq. 30 and normalized per unit energy. Use of basis functions satisfying Eq. 30 to describe vertical structure of velocity and displacement permits an analysis of variability in the partitioning of average water column energy across modes. Profiles and modal projections can be grouped and averaged to compare energy partitioning across modes at different locations, at different times, for different glide slopes, or glider vertical speeds. Individual spectra, grouped by glide slope and/or glider vertical speed, can also be averaged and compared to reveal displacement and velocity mode structure resolution associated with different glider 'W'/'M' sampling patterns.

3.4 Results: Glider-Model Comparison and Discussion

Glider displacement and velocity profile estimates are paired with numerical model displacement and velocity profiles to determine the effect of 'W'/'M' sampling, glide slope, and glider vertical speed on displacement and velocity profile estimate accuracy (Fig. 3.7). Model displacement profiles $\xi_{model}(z)$ are calculated using Eq. 28 with each model density profile $\overline{\gamma^n_{model}(z)_{l_w,t_w}}$ (or $\overline{\gamma^n_{model}(z)_{l_m,t_m}}$) defined as the horizontal and temporal average of

instantaneous model density profiles $\gamma^n_{model}(x,z,t)$ at horizontal grid points and times occurring between the first and last samples of each 'W' (or 'M') pattern (Fig. 3.8). A typical along-transect distance l_w (or l_m) is O[50 km] and duration t_w (or t_m) is O[5 days]. To obtain a model density anomaly, the numerator in Eq. 28, this profile is differenced from an overall background model density profile $\overline{\gamma^n_{model}(x,z)_t}$ defined as the temporal average of all instantaneous model density profiles in the time series (approximately one month in ROMS and two weeks in HYCOM) at the horizontal location x of the 'W' or 'M' profile. Model cross-track velocity profiles $\overline{v_{model}(z)}$ are defined as the horizontal and temporal average of all cross-track velocity profiles within each l_w (or l_m) and t_w (or t_m). The horizontal and temporal averaging of these model profiles permits an appropriate comparison of model output to glider derived profiles, each calculated from samples taken across tens of kilometers and over multiple days. This averaging also serves as a low pass filter, reducing high wavenumber and frequency motions, and as does the 'W'/'M' method itself. Glider-model pairs of displacement and velocity profiles are differenced to obtain average and average square error as a function of depth, glider vertical speed, and glide slope.

The average difference between 364 glider sample and LiveOcean average model velocity profile pairs is less than +/- 0.02 m s^{-1} with maximum absolute differences of $\sim$ 0.05 m s^{-1}. These differences are not a strong function of glider vertical speed (Fig. 3.9). The standard deviation of this glider-model error is enhanced in the upper 250 m, with mean square error between glider and model velocities multiple times greater in the upper 250 m than between 250 m and 2500 m (Fig. 3.10). This enhanced upper ocean error can be attributed to the difference between t_w (or t_m) and the advective time scale of near-surface velocities. Model near-surface velocities evolve on time scales much shorter than the 'W'/'M' sampling period. Additionally, glider finite difference estimates of horizontal density gradients in the upper 250 m are calculated from samples either spanning a greater horizontal distance than estimates made at mid-depths or from samples in two sets, spaced closely together in each (for respective 'W'/'M' patterns). A modest increase in the standard deviation of glider-model velocity error in the deepest 500 m of the water column is similarly the result of sampling pattern geometry with samples spaced either at greater horizontal distances apart or in two sets of closely spaced samples. Neither glider vertical speed nor glide slope has a significant effect on glider-model velocity error, but these errors are slightly reduced for slower vertical speeds and smaller horizontal glide slopes (s = 1/3 vs. 1/2). Sampling simulations were re-run for a larger

depth-average current error of 0.02 m s^{-1}, the upper bound of estimated error from Rudnick et al. [2018], with minimal effect on mean velocity profile error.

Similar patterns of average glider-model velocity profile error are observed in HYCOM simulations of glider sampling. While HYCOM average glider-model velocity profile error remains less than 0.05 m s^{-1} throughout the water column, error standard deviation in the upper 1000 m is roughly ten times larger than values deeper than 1000 m (Fig. 3.11). This marked increase in error variability can be attributed to highly variable upper ocean along-transect velocities of order 0.4 m s^{-1}, absent in LiveOcean simulations, and enhanced internal tide isopycnal vertical displacements with time scales shorter than the 'W'/'M' sampling period. Additionally, maximum sampling depths in HYCOM simulations are ~ 60 % greater that those in LiveOcean simulations. This results in an increased 'W'/'M' sampling period, with samples in the upper 1000 m having a greater time interval between initial and final simulated glider samples. These two factors, highly variable and large magnitude along-track velocities, as well as a longer 'W'/'M' sampling period, result in greater glider-model velocity error variability. Both average error and error standard deviation are reduced in the upper 500m by approximately 50 % for glider vertical speeds of 0.2 m s^{-1} (Fig. 3.11) and overall for a glide slope s = 1/3 (Fig. 3.12).

Displacement and velocity modes were projected onto glider and model profile pairs to obtain mode amplitudes and water-column average potential and kinetic energy as a function of mode number. Energy spectra were calculated from profiles associated with each glider vertical speed and glide slope. Agreement between glider and model water-column average potential and kinetic energy spectra, partitioned by vertical mode, is reflective of the vertical spectral resolution permitted by the 'W'/'M' sampling framework for various vertical speed and glide slope combinations. Across both models, all speeds, and two glide slopes, glider potential energy spectra reproduce model spectra from the first through thirtieth baroclinc mode (Fig. 3.13a, c, 3.14a, c). The local horizontal and temporal averaging of model density profiles across l_w (or l_m) and t_w (or t_m), permits a relevant comparison of glider and model displacement profiles, reducing model potential energy across all mode numbers while retaining the same spectral shape as the model average potential energy spectrum calculated from instantaneous density profiles. This is similarly the case for average and instantaneous model velocity profiles used in calculating kinetic energy spectra.

In LiveOcean simulations, glider kinetic energy spectra do not significantly vary with glider vertical speed (Fig. 3.13b, d). For both glide slopes, glider and model spectra are indistinguishable from the bartropic mode through the $\sim 8^{th}$ baroclinic mode. Spectra derived from slant profiles with a glide slope of 1/2 extend this agreement through mode ~ 13. This suggests that the horizontal distance spanning an 'W'/'M' pattern, across which contributing measurements are separated and dependent on glide slope and water depth, limits vertical resolution at modes higher than 8. This occurs despite the fact that horizontal scales (respective Rossby radii of deformation) associated with modes 2 through 8 are shorter than the distance spanned by each 'W'/'M' pattern.

In HYCOM simulations, similar patterns are observed, with the deviation between model and glider kinetic energy spectra occurring at mode 11 for a glide slope s = 1/3 and mode 20 for a glide slope s = 1/2 (Fig. 3.14b, d). Additionally, increased glider vertical speeds result in better agreement between glider and model kinetic energy levels at low modes. Slow glider vertical speeds result in velocity profiles with speeds greater than average model speeds and a more energetic kinetic energy spectrum. With both models limited to a vertical resolution of thirty vertical levels, expectation of the highest resolvable mode structure should be limited to at most mode 30.

While the projection of dynamical vertical modes onto glider derived displacement and velocity profiles reveals the highest mode vertical structure that glider sampling can resolve, glider-model velocity differences can be explicitly quantified considering the aliasing of high frequency isopycnal variability onto glider derived horizontal density gradient estimates. Both model simulations were selected because they contain internal tide dynamics and offer temporal resolution much greater than an inertial period. These selection criteria ensure the aliasing of high frequency motions onto glider slant profiles, each completed over a multi-hour period. Comparison of model energetics reveal LiveOcean to contain significantly greater high-frequency, high-wavenumber energy than HYCOM. Frequency and zonal wavenumber spectra at 1000 m reveal LiveOcean to be more energetic than HYCOM at time scales between ~ 2 and 24 hrs and across all zonal wavenumbers (Fig. 3.15). Despite these differences, we expect simulated glider sampling in both models, especially LiveOcean, to readily alias motions at high frequencies and across small horizontal scales.

Over the course of an approximately 30 hour 'W'/'M' sampling period in LiveOcean, isopycnals are vertically deflected at each horizontal grid point on hourly time scales with frequencies shorter than a 24 hour period,

reflective of the internal tide (Fig. 3.16). These deflections about a multi-day mean isopycnal vertical structure are aliased into glider horizontal density gradient estimates. The severity of this aliasing is a function of both internal tide amplitude and mean horizontal density gradient magnitude. Mean horizontal density gradients at each depth, unchanging over a multi-day period, reflect mesoscale features in which geostrophic balance is dominant. Considering these gradients a signal, and higher frequency isopycnal vertical displacements a noise, a model signal to noise ratio is estimated for each glider-model profile pair at each depth. At the horizontal location of each glider-model velocity profile pair, and at each depth i, the eddy signal g(z_i) is defined as

$$g(z_i) = \frac{1}{L}\sum_{j}^{L}\left(\overline{\gamma^n_{model}(x_j, z_i)_{t_w}} - \overline{\gamma^n_{model}(z_i)_{l_w,t_w}}\right)^2 \tag{38}$$

where $\overline{\gamma^n_{model}(x_j, z_i)_{t_w}}$ (or $\overline{\gamma^n_{model}(x_j, z_i)_{t_m}}$) is the time average of instantaneous model density $\gamma^n_{model}(x, y, t)$ across the interval t_w (or t_m), $\overline{\gamma^n_{model}(z_i)_{l_w,t_w}}$ (or $\overline{\gamma^n_{model}(z_i)_{l_m,t_m}}$) is the mean model density profile across l_w (or l_m) and t_w (or t_m), and L is the number of horizontal grid points with indices j that fall within l_w (or l_m). A larger value corresponds to a greater horizontal density gradient spanning the 'W' (or 'M') pattern. The noise f(z_i) is defined as

$$f(z_i) = \frac{1}{L}\sum_{j}^{L}\left(\frac{1}{T}\sum_{k}^{T}\left(\gamma^n_{model}(x_j, z_i, t_k) - \overline{\gamma^n_{model}(x_j, z_i)_{t_w}}\right)^2\right) \tag{39}$$

where T is the number of time points with indices k that fall within t_w (or t_m). A higher value corresponds to larger amplitude isopycnal vertical displacements with time scales shorter than t_w (or t_m). The ratio $g(z)/f(z)$ then provides an estimate of the relative strength of the mesoscale eddy gradients as compared to higher frequency isopycnal fluctuations. This quantity can then be used, with some predictive power, to test the ability of the 'W' / 'M' glider velocity profile estimation tool to accurately reproduce model multi-day mean velocities.

Signal to noise ratio estimates derived from model density profiles are used to select glider velocity estimates that should more accurately reproduce model mesoscale velocities. This hypothesis is tested on glider and model estimates of vertical shear of geostrophic velocity. For each glider-model profile pair the difference between glider and model vertical shear, estimated using Eq. 29 from linear horizontal density gradients, is calculated as percent glider-model shear error (Fig. 3.17). Despite the high occurrence of individual shear errors greater than 100 %,

vertical integration and reference to a depth-average current limits average glider-model velocity profile error to less than $\sim$ +/- 0.02 m s^{-1} across a majority of the water column.

The mean of glider-model shear error estimates with a signal to noise ratio greater than unity shows a reduced error of $\sim$ 30 % or less at nearly all depths from a total average of over 100 %. Reduction in average glider-model shear error for measurements associated with a signal to noise ratio greater than unity confirms that glider velocity profile accuracy is improved when sampling mesoscale features with strong horizontal density gradients and relatively weak internal tides. A priori knowledge of internal tide amplitudes and the strength of mesoscale gradients can thus aid pilot decision making in seeking to minimize the aliasing of higher frequency isopycnal fluctuations onto mesoscale density structure. While internal tide and other high frequency aliasing cannot be avoided, geographic surveys identifying regions of increased high frequency energy, like Zhao [2016], can inform to some extent on expected errors. Agreement between glider and model vertical energy spectra is thus improved considering the relative dominance of internal tides or mesoscale features. This is apparent considering simulated sampling of an mesoscale eddy in LiveOcean. Glider-model kinetic energy spectra agree through higher mode number when considering velocity profiles sampling only a mesoscale eddy (Fig. 3.18). For a glide slope s = 1/2, LiveOcean and glider kinetic energy spectra agree through mode 30.

3.5 Conclusions

Results of glider sampling simulations across two models, four glider vertical speeds, and two glide slopes suggest that the 'W'/'M' framework can accurately resolve quasi-geostrophic eddy isopycnal vertical displacements, horizontal density gradients, and geostrophic velocities. In LiveOcean, this accuracy is primarily a function of mesoscale eddy strength and glide slope, while in HYCOM, faster glider vertical speeds decrease glider-model velocity error in the upper 500 m and correspond to better agreement between glider and model kinetic energy spectra. These results suggest that as maximum glider sampling depth increases, near-surface velocity error increases, but in proportion to the magnitude of near surface advective velocities. As Deepglider missions increase in number, consideration of these factors can help in achieving mission goals. Glider sampling strategies always reflect a trade-off between energy usage and desired spatio-temporal resolution. These simulations quantify the effect of some piloting choices

and show that increased glider vertical speeds are not always necessary to resolve quasi-geostrophic features that evolve on multi-day or longer time-scales.

Across all simulations, vertical structure of eddy density anomalies and geostrophic velocities, from the barotropic through at minimum the eighth baroclinic mode, is accurautely reproduced by glider slant profiling and 'W'/'M' velocity profile estimation. Furthermore, the partitioning of energy across these vertical modes, containing over 95 % of observed eddy mechanical energy, reveals a common spectral pattern in which energy decreases with increasing mode number m, or scaled vertical wavenumber, following a log-log linear slope proportional to m^{-3}. This slope agrees with geostrophic turbulence predictions on the partition of energy across modes within the enstrophy inertial range and suggests that model fields reflect quasi-geostrophic dynamics.

These simulations of glider-slant profiling and geostrophic velocity profile error analyses lend confidence to the application of this framework to full-depth Deepglider observations, detailing the evolution of quasi-geostrophic motions with greatly increased vertical and temporal resolution. Analyses of these new observations using this framework thus provide new opportunity to test theoretical predictions of vertical energy partitioning and transfer, as well as identify relationships to the distribution of mesoscale eddy kinetic energy across horizontal scales, of which observations are relatively more numerous.

3.6 Acknowledgments

This work was funded by the National Science Foundation (award number: 1736217). We would like to thank Xiaobiao Xu and Eric Chassignet at Florida State University for providing accesses to HYCOM output from ongoing experiments that include tidal forcings as well as for saving four-dimensional output at hourly time steps. Their advice and assistance helped ensure proper use of the relevant model fields. We would also like to thank Parker MacCready at the University of Washington for providing access to LiveOcean ROMS output and assistance in interpretation of coastal and model boundary dynamics.

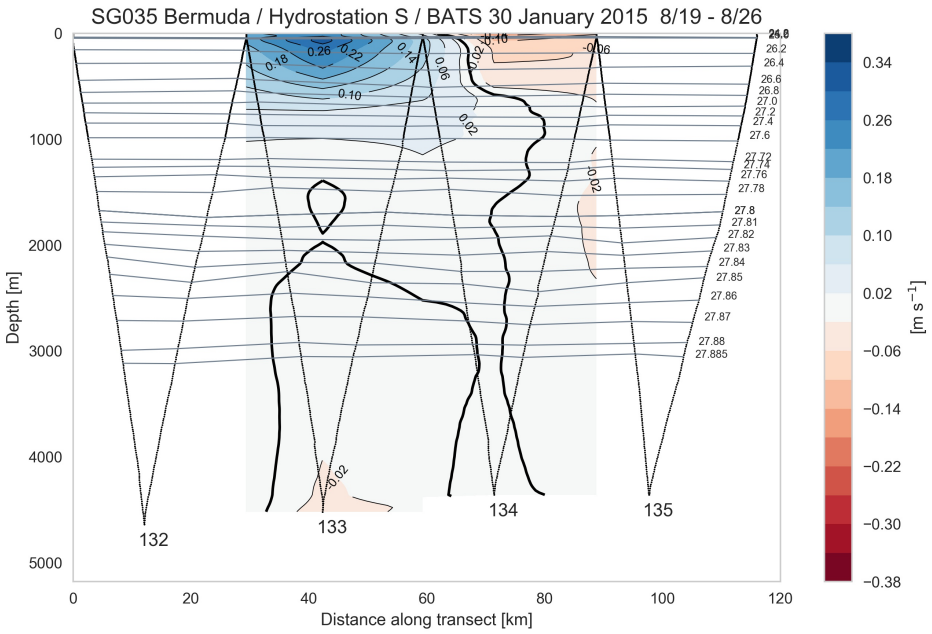

Figure 3.1: Four dive-climb cycles (132-135) in depth vs. distance along transect from Deepglider 35 at station BATS in late August 2015 (initial deployment was on 30 January 2015). Black lines are the glider's path through the water, grey curves are select neutral density surfaces, and colored contours are cross-track geostrophic velocity estimates. The sign convention used is that positive velocities are to port of the glider track.

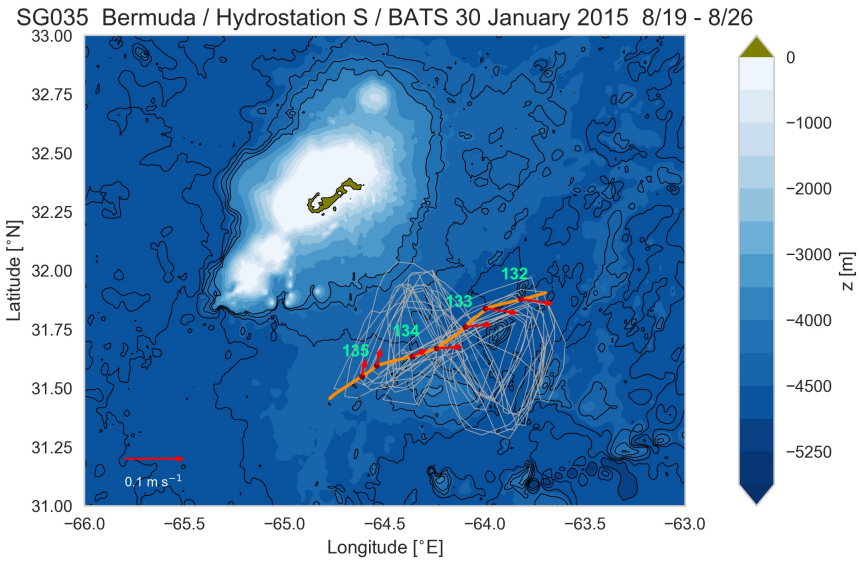

Figure 3.2: Glider path at station BATS between January and November 2015 (grey lines). Bathymetry is contoured in blue. An individual transect (Fig. 3.1) comprised of four glider dive-climb cycles (132-135) is in orange with red points indicating the location along transect at which velocity profiles are calculated. Glider inferred depth-average current vectors, interpolated to velocity profile locations, are in red.

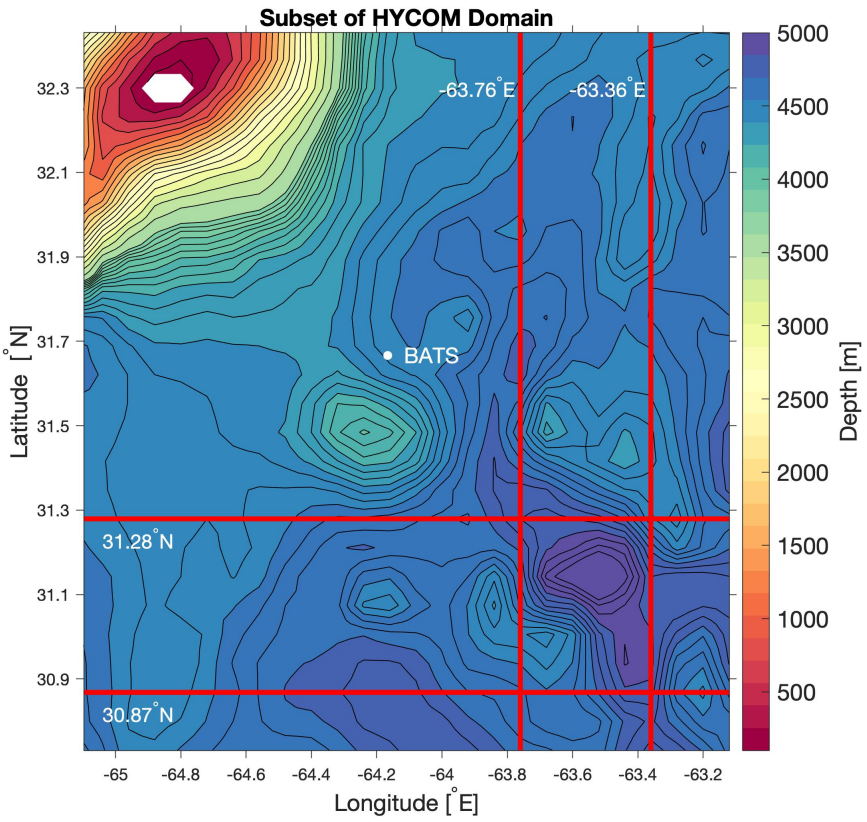

Figure 3.3: Subset HYCOM domain with bathymetry colored and contoured. Red lines identify locations of four extracted transects each 191 km long with horizontal grid spacing of approximately 3.8 km.

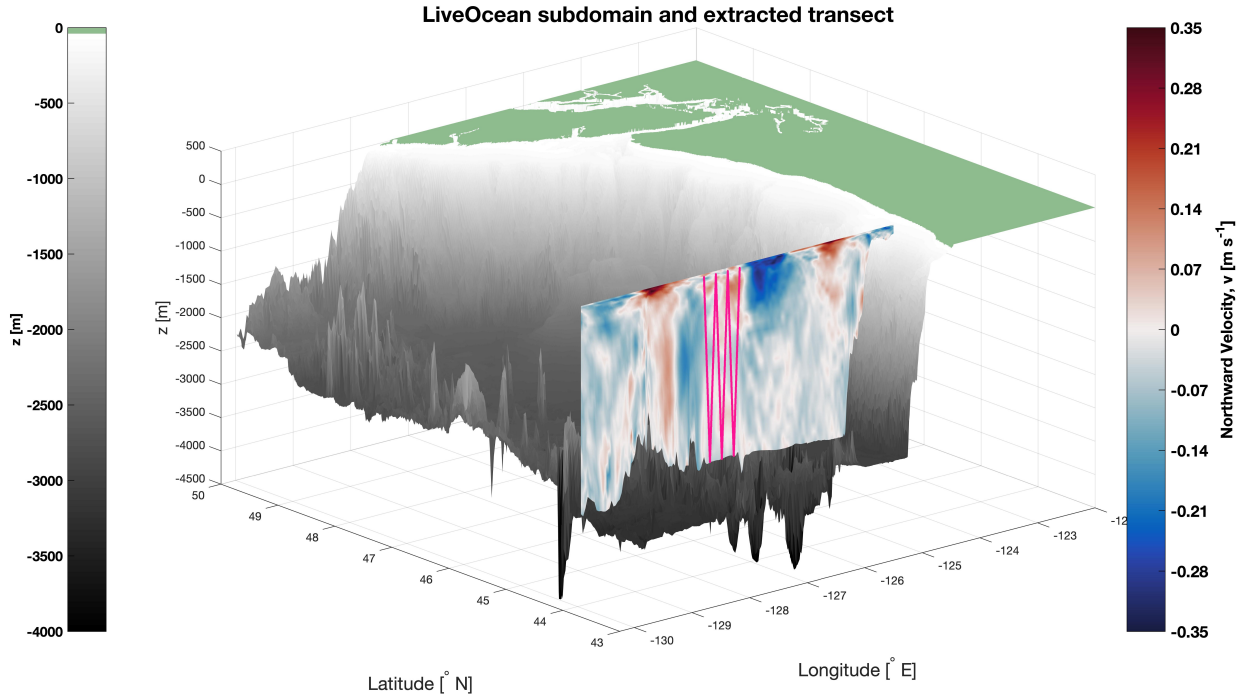

Figure 3.4: Subset of LiveOcean ROMS domain with land in green and bathymetry contoured in grey. The extracted full-depth, 200 km long zonal section is colored and contoured showing a sample meridional velocity field (poleward in red and equatorward in blue). Horizontal resolution decreased from 1 to 1.5 km in the offshore direction. A sample set of three simulated glider dive-climb cycles is in pink.

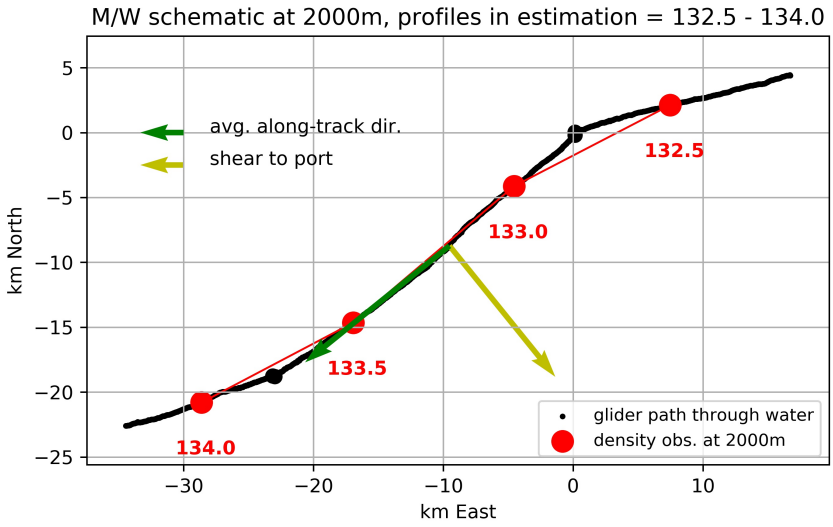

Figure 3.5: Plan-view path through water of four glider slant profiles (132.5-134) from the 2015 station BATS deployment. Distances are locally referenced to the starting location of dive 133. Non-integer labeled slant profiles represent the ascent portion of the integer numbered dive-climb cycle. The locations of density measurements at 2000 m are in red. A planar fit is applied to estimate the density gradient and is then projected onto the average along-track direction (green arrow). The direction of cross-track vertical shear of geostrophic velocity at 2000 m is in yellow. Vector lengths are arbitrary, originate from the midpoint location of the four profiles, and identify the location of the derived geostrophic velocity profile.

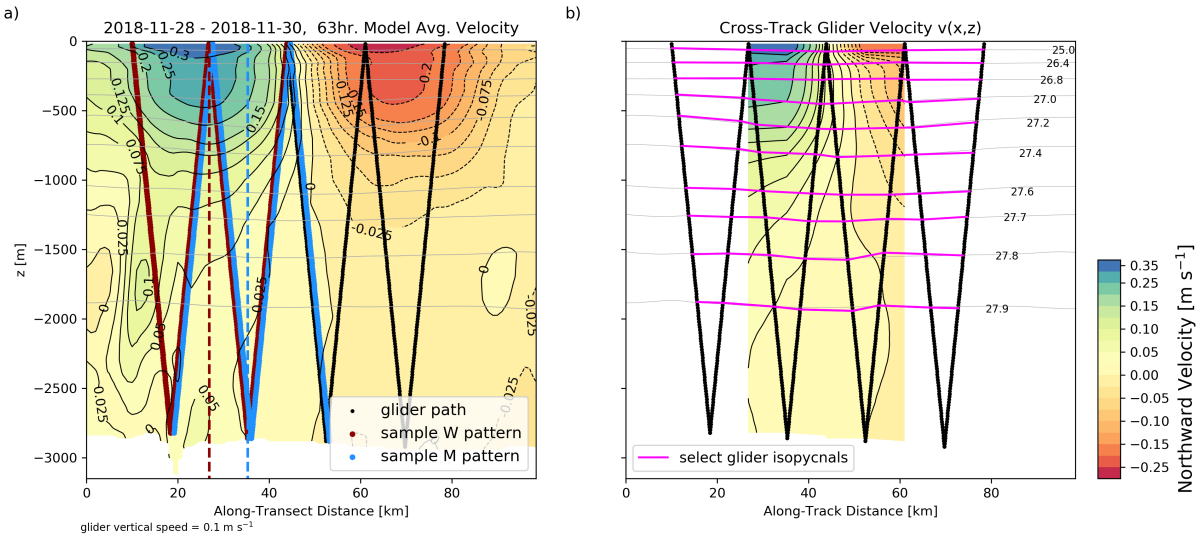

Figure 3.6: a) LiveOcean average northward velocity colored and contoured in black over a 63 hour period between 25 November 2018 and 27 November 2018. This period matches the length of time required to complete four glider dive-climb cycles profiling with a vertical speed of 0.1 m s^{-1}. The simulated glider path through the water is in black with red and blue colored subsections as sample dive-climb ('W') and climb-dive ('M') cycle pairs. Colored vertical dashed lines identify the along-transect locations of respective derived velocity profiles. b) Glider northward geostrophic velocity field estimated from along-track density gradients. Select glider isopycnal depths are in pink with average model isopycnal depths in light grey.

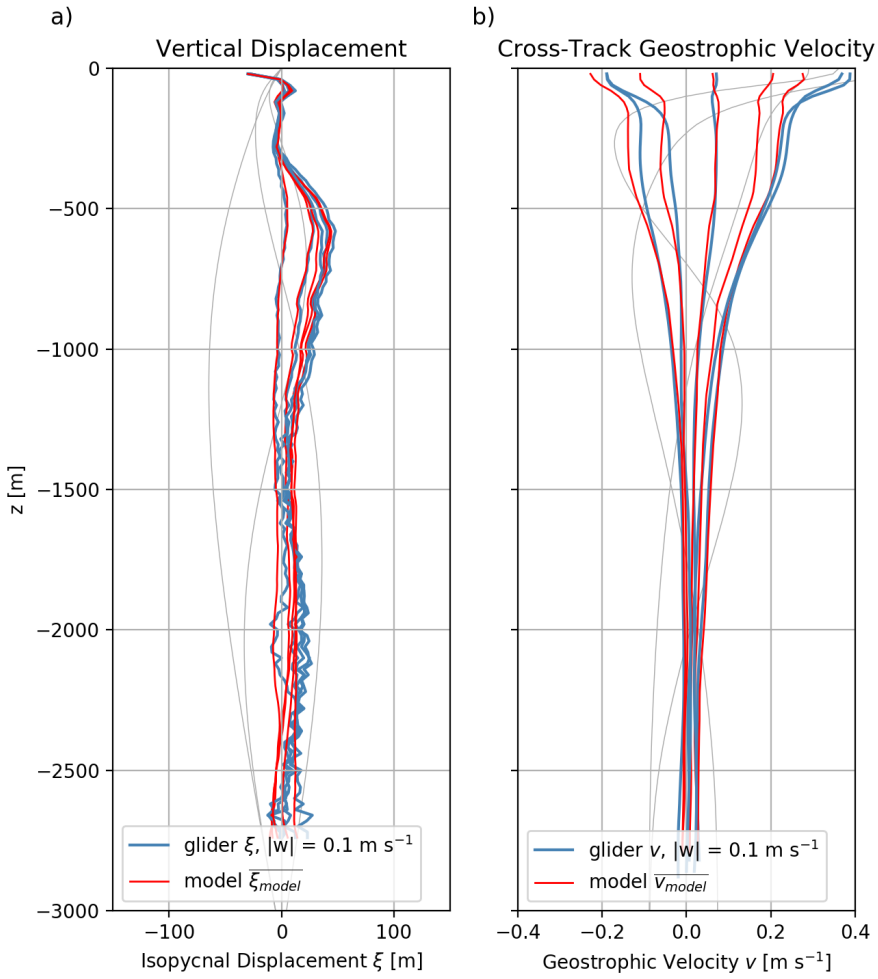

Figure 3.7: Ensemble of five glider-sampled LiveOcean and LiveOcean a) vertical isopycnal displacement and b) cross-track velocity profiles, as function of depth from a sample transect with a glide-slope ratio of 1:3. The first through third displacement $\frac{1}{N^2(z)}\frac{\partial}{\partial z}\phi_{m=1,2,3}(\mathrm{z})$ and velocity $\phi_{m=1,2,3}(\mathrm{z})$ modes are in light grey.

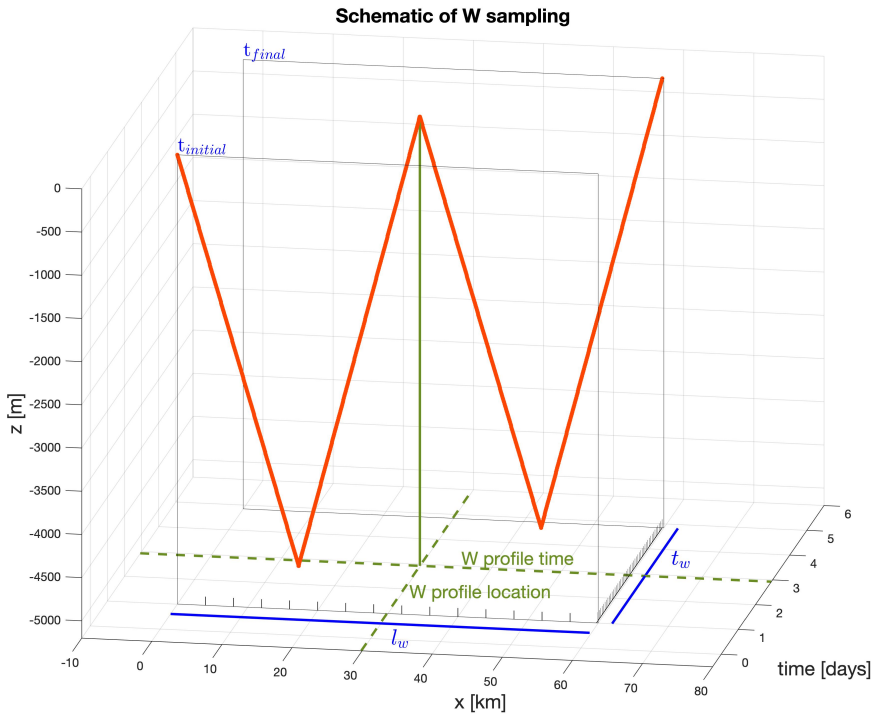

Figure 3.8: Schematic of 'W' sampling pattern used to derive a single cross-track geostrophic velocity profile. Two successive glider dive climb cycles are shown in red as a function of distance along-transect, time, and depth. The along-transect location and time of the resulting velocity profile is in green. The along-transect distance l_w between the first and last glider samples in the 'W' is in blue with model horizontal grid point locations as vertical ticks. The time span t_w between the first and last glider samples in the 'W' is in blue with model time steps as vertical ticks. Each glider velocity profile is paired with a cross-transect model velocity profile computed by taking horizontal and temporal averages of all cross-transect model velocity profiles within l_w and t_w.

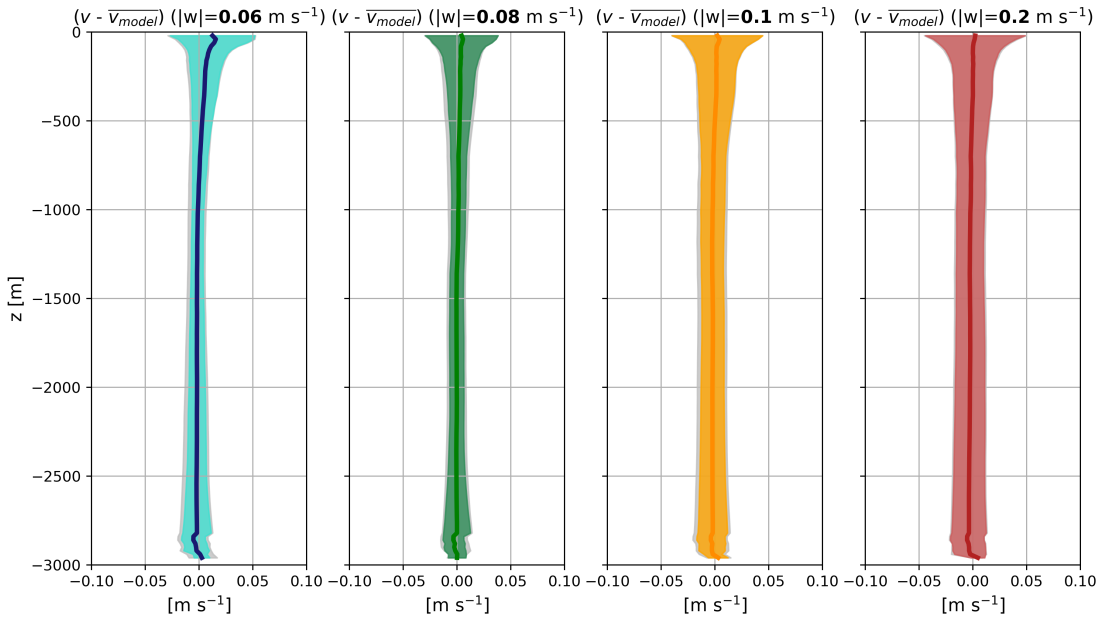

Figure 3.9: LiveOcean mean glider-model velocity error with +/- one standard deviation bands for four simulated glider vertical speeds and a vertical to horizontal glide slope s = 1/3. Each average and standard deviation is computed from 91 glider-model velocity profile error pairs. Mean glider-model velocity error with +/- one standard deviation band for a depth-average current error of 0.02 m s^{-1} is in grey (plotted underneath colored error bands) (note little difference between grey and colored error).

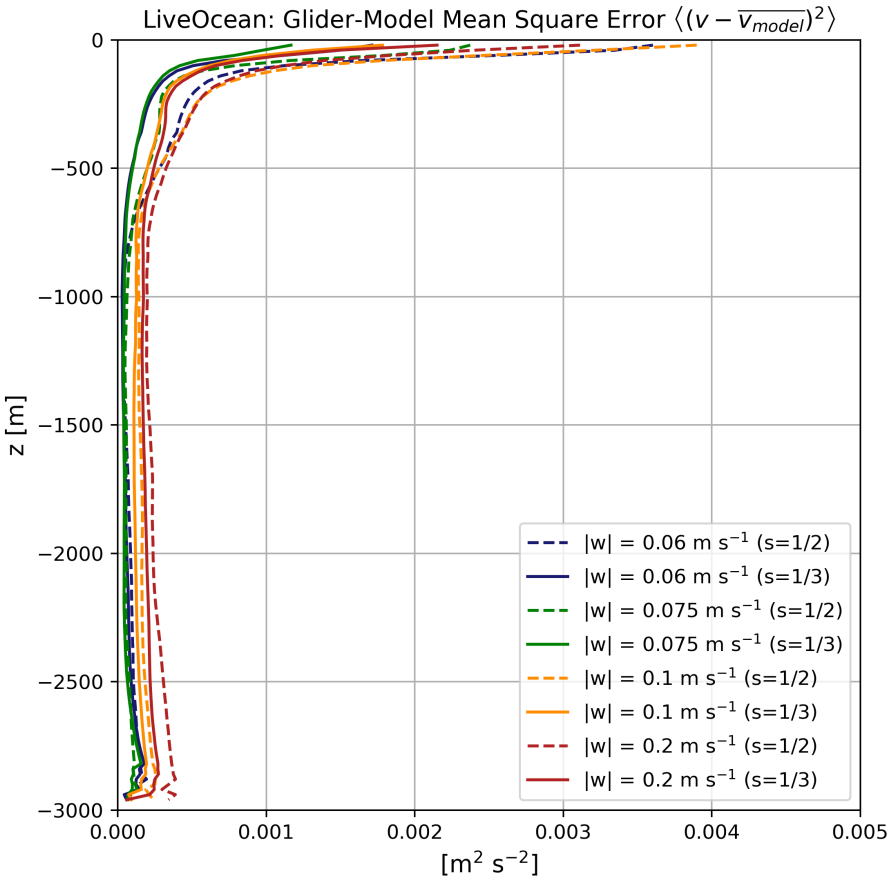

Figure 3.10: Mean square error between simulated glider and LiveOcean model cross-track velocity profiles averaged for each of four simulated glider vertical speeds $|w|$ and two vertical to horizontal glide slopes.

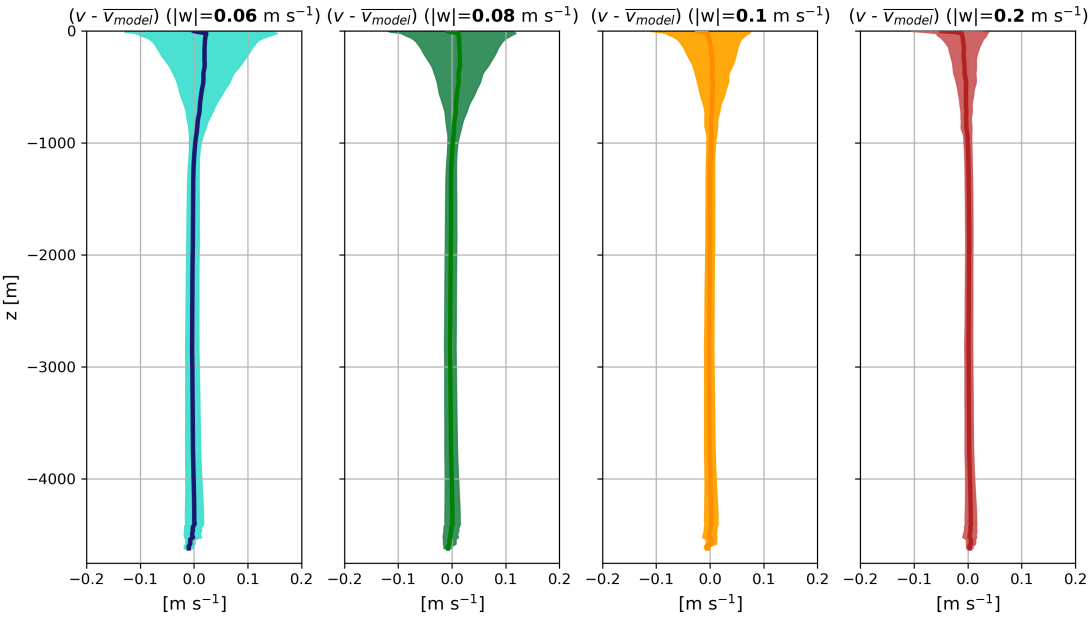

Figure 3.11: HYCOM mean glider-model velocity error with +/- one standard deviation bands for four simulated glider vertical speeds and a vertical to horizontal glide slope s = 1/3. Each average and standard deviation is computed from 81 glider-model velocity profile error pairs. Note different horizontal scale compared to Figure 3.9.

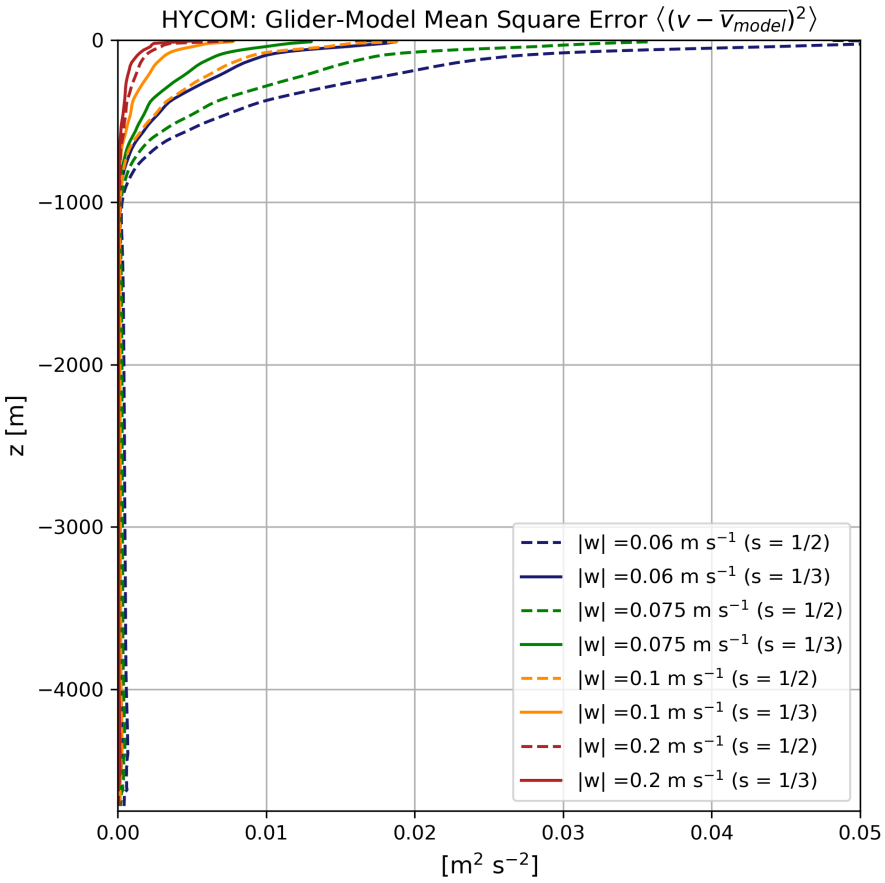

Figure 3.12: Mean square error between simulated glider and HYCOM model cross-track velocity profiles averaged for each of four simulated glider vertical speeds $|w|$ and two vertical to horizontal glide slopes. Note ten times coarser horizontal scale compared to Figure 3.10.

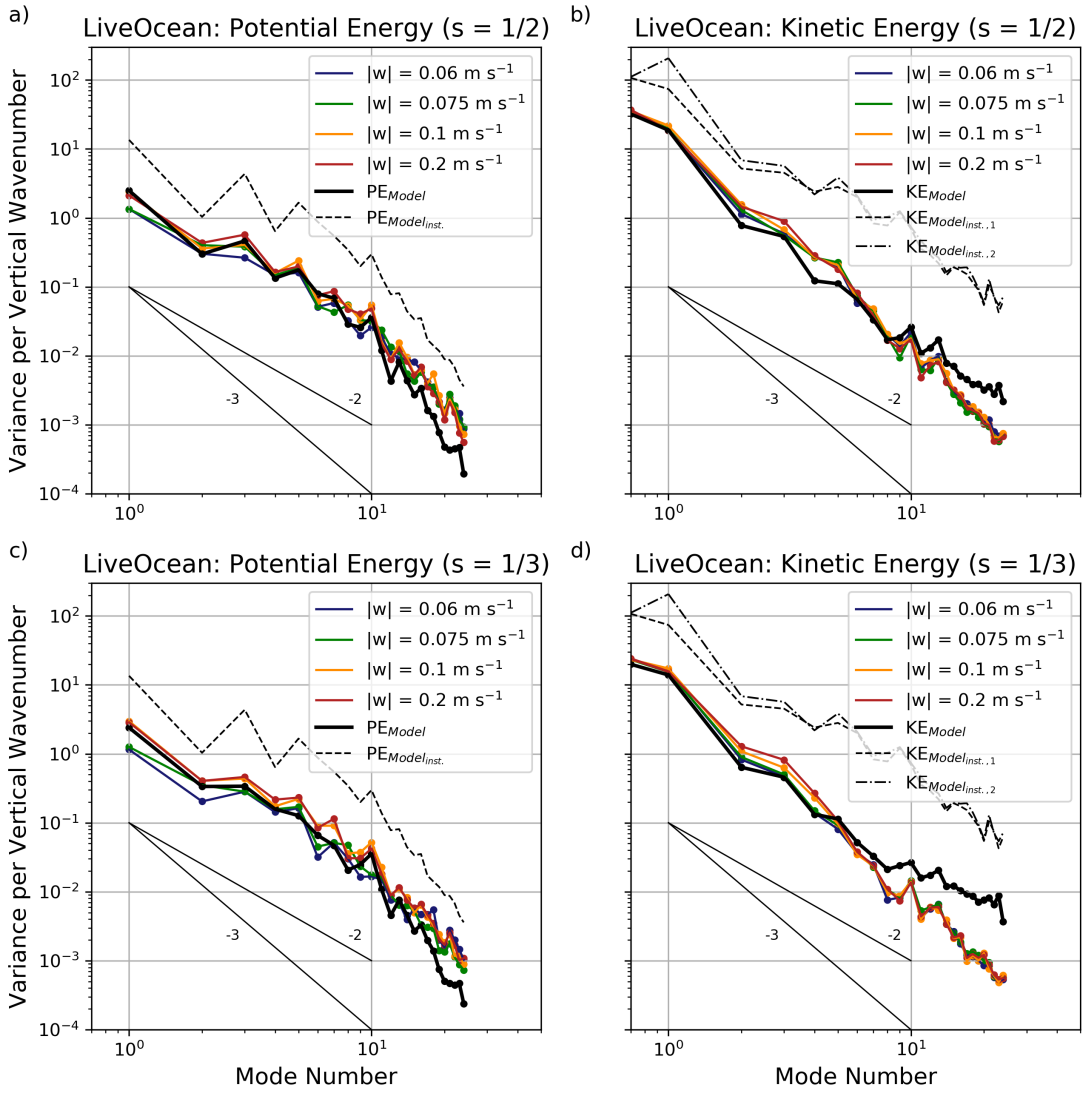

Figure 3.13: LiveOcean potential and kinetic energy as a function of mode number for vertical to horizontal glide slopes s = 1/2 a), b) and s = 1/3 c), d). Colored lines correspond to four glider vertical speeds $|w|$ with average model spectra calculated from $\overline{\xi_{model}}$ and $\overline{v_{model}}$ in thick black. Dashed and dash-dot black lines are the average model spectra computed from instantaneous displacement and meridional ($_1$) and zonal ($_2$) velocity profiles. Thin black lines are reference spectral slopes. For kinetic energies, the value scattered on the vertical axis corresponds to energy in the barotropic mode.

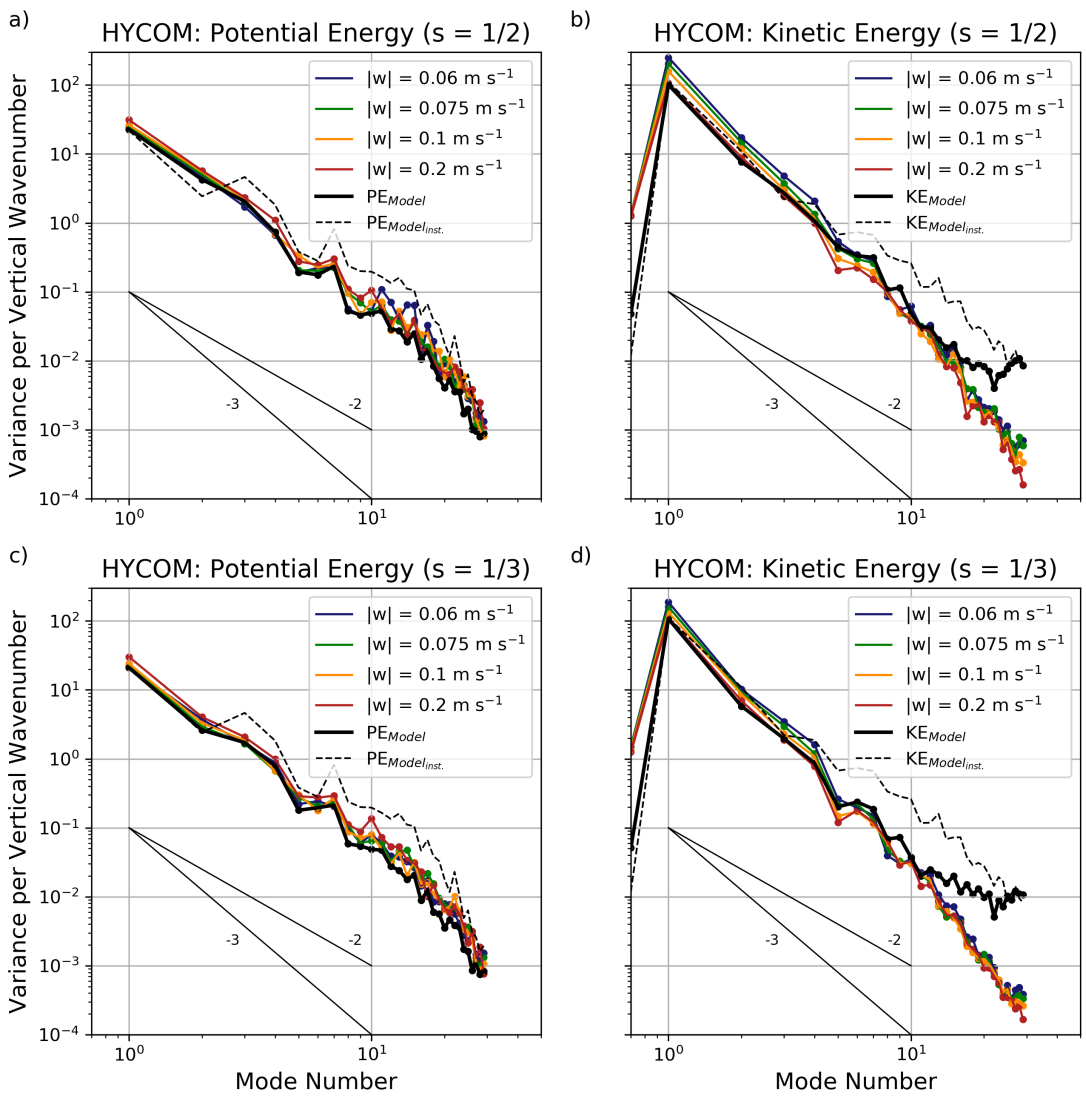

Figure 3.14: HYCOM potential and kinetic energy as a function of mode number for vertical to horizontal glide slopes s = 1/2 a), b) and s = 1/3 c), d). Colored lines correspond to four glider vertical speeds with average model spectra calculated from $\overline{\xi_{model}}$ and $\overline{v_{model}}$ in black. Dashed black lines are the average model spectra from instantaneous displacement and velocity profiles. Thin black lines are reference spectral slopes. For kinetic energies, the value scattered on the vertical corresponds to energy in the barotropic mode.

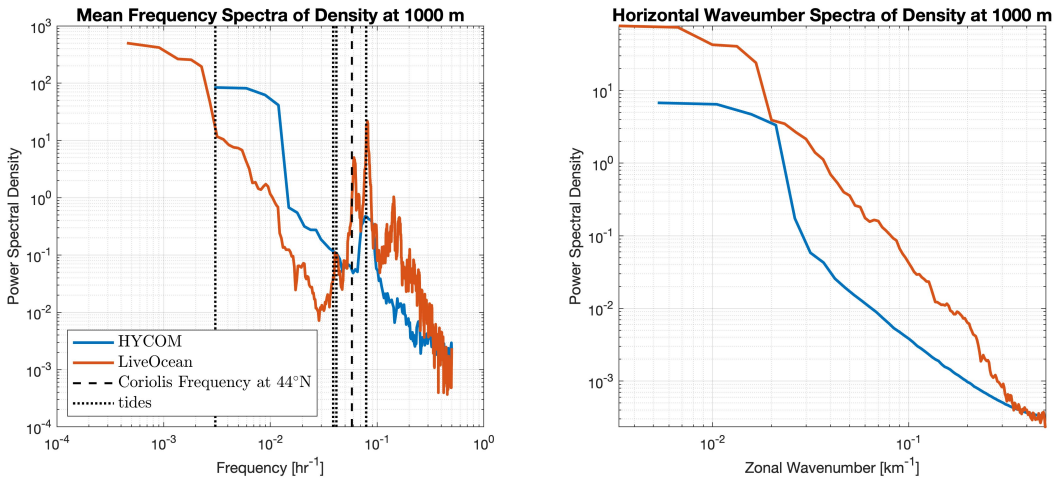

Figure 3.15: Frequency (left) and zonal wavenumber (right) spectra of density fluctuations at 1000 m (HYCOM in blue and and LiveOcean in red). Frequency spectra are estimated sampling each model as if a mooring at the midpoint horizontal location of each transect. Horizontal wavenumber spectra are estimated from density values at 1000 m spanning the horizontal length of each transect ($\sim$ 200 km). Spectra are normalized by the respective signal variance.

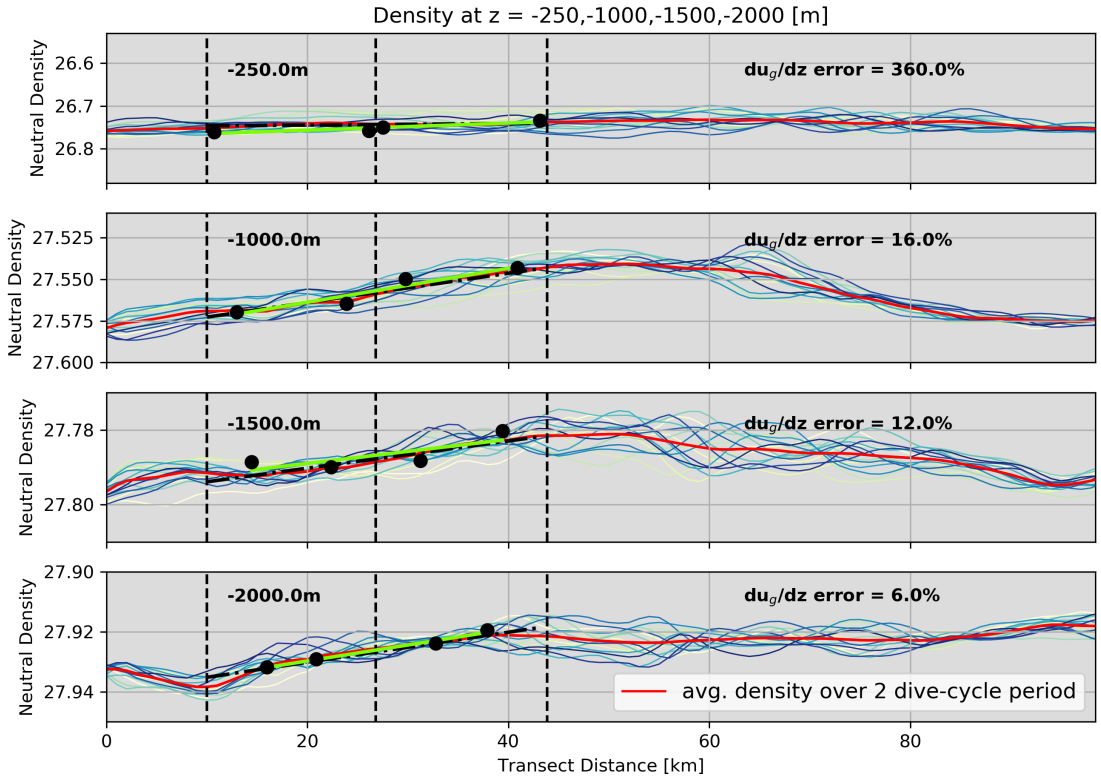

Figure 3.16: Along-transect LiveOcean neutral density at four depths (z=-250m, -1000m, -1500m, -2000m) and 2 hour intervals spanning a $\sim$ 30 hour period. Colored lines are along-transect densities (advancing in time from blue to yellow) at two-hour intervals. The 30 hour average density at each horizontal grid point is in red. Glider density measurements at each of the four depths from four consecutive profiles (one dive-climb 'W' cycle) are in black with vertical dashed black lines identifying the starting and ending locations along-transect of these two dive-climb cycles. Glider estimated linear horizontal density gradients at the four depths, calculated as a linear fit to the four scattered points, are in light green. Model linear horizontal density gradients, fit to the 30 hr. average, are the dash-dot black lines. Glider-model errors of geostrophic velocity shear (Eq. 29) at the four depths are expressed as a percentage.

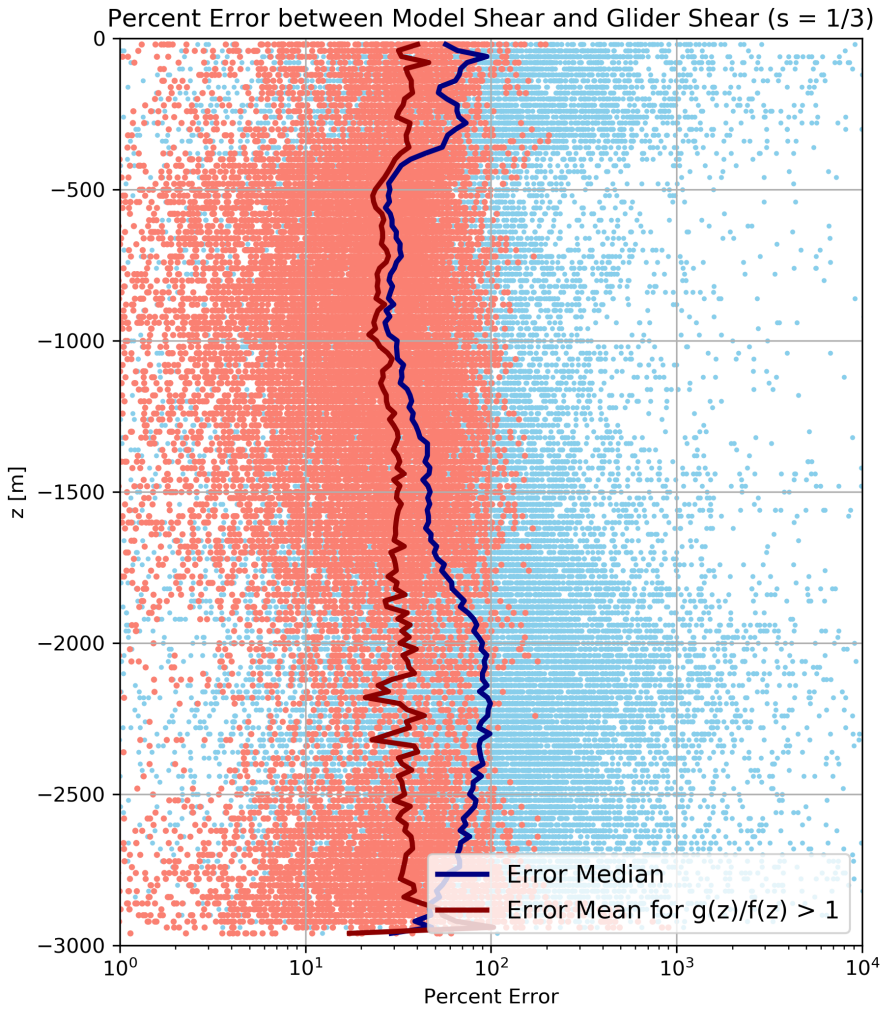

Figure 3.17: LiveOcean error between glider estimated vertical shear of geostrophic velocity and model vertical shear derived from multi-day average density structure. Blue dots are individual estimates while the dark blue curve indicates the median of all points at each depth. Red dots are a subset of all blue dots and are those associated with a signal to noise ratio greater than unity. The dark red line is the mean at each depth of this subset.

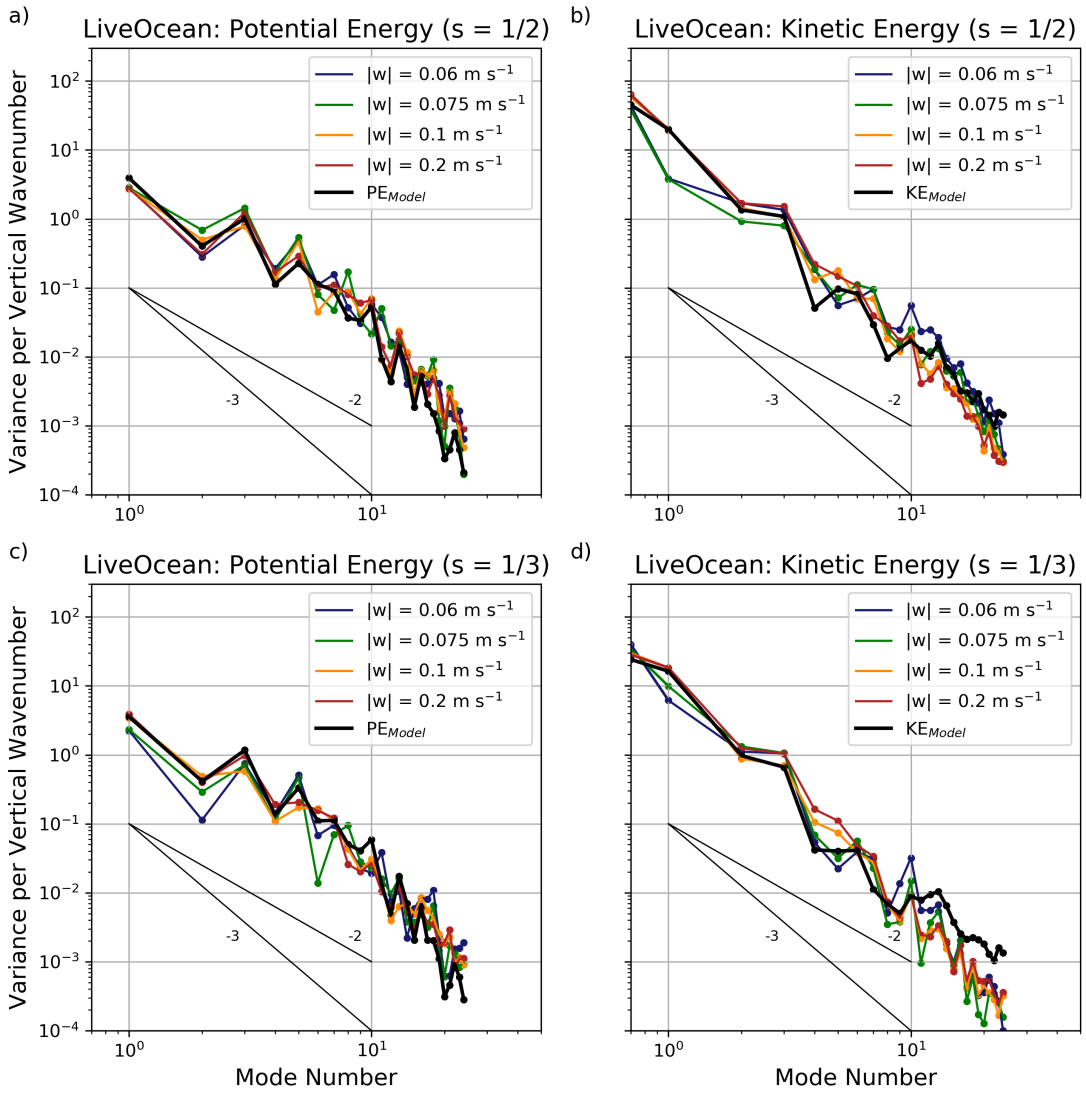

Figure 3.18: Same as Figure 3.13 but for a subset of profiles sampling only the eddy in Figure 3.6.

4 Chapter 4: Eddy Vertical Structure And Variability: Deepglider Observations in the North Atlantic

4.1 Introduction

Energy input into the oceans primarily through surface wind forcing, solar heating, and tides drives a large scale circulation shaping the geographic distribution of oceanic mechanical energy, heat content, and relevant tracers. Of the dynamical processes responsible for such transport and redistribution (i.e. mean circulation, internal waves, tides, etc.), time dependent mesoscale flows contain a dominant fraction of ocean kinetic energy. These motions, manifesting as eddies, meanders, and filaments evolve on time scales greater than a day with spatial scales on the order of 10's to 100's of kilometers. Motions of this class are termed quasi-geostrophic (QG) because their dynamics reflect a dominant balance between pressure gradient and Coriolis forces. The influence of higher order, or unbalanced, dynamics including high Rossby number flows, nonlinear advection, internal gravity waves, and vertical mixing are usually localized, but add complexity at all spatial and temporal scales. This work adopts a QG framework and while we address the influence of unbalanced dynamics on balanced flows in specific cases, our main focus is the mesoscale eddy energy reservoir. Specifically, we explore the partitioning of mechanical energy (kinetic and available potential) across vertical scales, mechanisms of energy transfer across scales, and factors driving observed variability.

The following describes the analysis of hundreds of full ocean depth temperature and salinity measurements collected by Deepglider autonomous underwater vehicles. Motivated by recent deployments of multiple Deepgliders in the North Atlantic each for multi-month missions, glider sampling was concurrently simulated in two high resolution ocean models to explore both spatial and temporal aliasing associated with glider sampling geometries and speeds. The results of these simulations ("Glider Sampling Simulations in High Resolution Ocean Models", Steinberg and Eriksen, J-TECH, *in press*) lend confidence to the use of an analysis framework employed here to explore mesoscale eddy vertical structure using the measurements collected by Deepgliders.

Comparisons between model eddy vertical structures and 'observations' of eddy vertical structures from simulated glider slant profiling show that gliders adequately capture mesoscale eddy vertical structure from the baroptric

through at least the first eight baroclinic modes. These simulations were carried out such that error in geostrophic velocity profile estimation, reconstructed from glider measured horizontal density gradients, could be quantified. Glider derived velocity profile error, enhanced in the upper few hundred meters hundreds for surface flows > 30 cm s^{-1}, remains below ~ 1 cm s^{-1}, the same order of accuracy as the glider inferred depth average current.

Full-depth slant profiles, completed in the western North Atlantic over the past five years, are now analyzed to explore geographic and seasonal variability in eddy vertical structure. Observed structure and variability is predominantly interpreted through the lens of geostrophic turbulence theory [Kraichnan, 1967, Charney, 1971, Fu and Flierl, 1980, Hua and Haidvogel, 1986] seeking an improved understanding of the mechanisms controlling the transfer of energy across spatial scales.

Turbulent eddy interactions at the mesoscale, evolving on time scales of weeks to months are the manifestation of quasi-geostrophic motions that represent the cycling of a dominant fraction of mechanical energy throughout the ocean. Factors controlling energy transfer across scales and pathways to dissipation via viscosity or as bottom drag must be understood. To rephrase Smith and Vallis [2001], our main goal is an improved ability to explain the mechanisms determining the scale, structure, and equilibrium of mesoscale eddies. Hundreds of recently collected full-depth density and geostrophic velocity profiles provide new opportunity to compare measurements with previous observations, theory, and numerical simulation results.

4.1.1 Theoretical and Modeling Background

Quasi-geostrophic dynamics well describe the behavior and evolution of low Rossby number flows with (at mid-latitudes) horizontal scales L greater than ~ 5 km and less than ~ 500 km evolving on multi-day to month time scales. Within these spatio-temporal bounds exists a regime in which the aspect ratio H/L is less than one (where H is the full ocean depth), the local vertical component of relative vorticity ζ is small compared to the Coriolis parameter f, meridional variations in f are small across L, and temporal evolution of flows is advective [Vallis, 2013].

The relatively slow evolution of these flows is governed by a near-balance, in the horizontal momentum equations, between Coriolis and pressure gradient forces, with nonlinear advection and vertical motion smaller in magnitude,

but necessary for energy transfer and mixing. The nature of this framework permits dependent variables in the momentum equations to be expanded in asymptotic series, or considered in terms of background mean and perturbation fields.

Throughout the ocean, the sum of available potential and kinetic energy associated with quasi-geostrophic motions (i.e. eddies, filaments, current meanders) is over an order of magnitude larger than energy contained in mean flows [Smith, 2007]. These motions are excited and energized by surface forcings driving sheared flow instabilities at well determined scales, but theoretical work, observations, and modeling results reveal that the equilibrium distribution of eddy energy across horizontal and vertical scales is determined by and the result of nonlinear energy transfers across scales [Smith and Vallis, 2001]. These interactions among quasi-geostrophic features resulting in energy transfers across wavenumber and frequency space are defined as a new class of turbulence strongly controlled by relative and planetary vorticity. With similarities to theoretical two-dimensional turbulence, geostrophic turbulence is a subject of continued interest as it describes and predicts the distribution and mixing of heat and relevant tracers.

In the limit of unforced turbulence, quasi-geostrophic eddies are expected to interact and equilibrate within an inertial range bounded on the smaller end by the submesoscale (flows with horizontal scales of $\mathcal{O}$[10 km] or less evolving on time scales $\mathcal{O}$[1 day]) and on the larger end by the basin scale (flows with horizontal scales of $\mathcal{O}$[100s km] evolving on time scales $\mathcal{O}$[months/years]) where the gradient of planetary vorticity β becomes relevant [Charney, 1971]. This idealized concept of an inertial range becomes important in characterizing turbulent interactions among flows which result in the transfer of energy across spatial scales. In reality, forcing and dissipation of quasi-gestrophic eddy energy occurs at multiple scales and inertial range theory becomes complicated requiring a revised understanding of energy pathways from forcing to dissipation.

The Rossby radius of deformation is a length scale of fundamental importance in quasi-geostrophy. Defined as the horizontal length scale (or deformation radius) associated with a given isopcynal vertical deflection, it is the scale at which buoyancy and rotational effects become equal. For a continuously stratified ocean, there are an infinite number of baroclinic deformation radii, with the m^{th} deformation radius decreasing in both horizontal and vertical scale with increasing m. At mid-latitudes, the first baroclinic deformation radius L_{d1} is $\mathcal{O}$[40 km], falling

within the above defined inertial range and implying that mean flow instabilities generate eddies with horizontal length scales well described by quasi-geostrophic dynamics and evolving as geostrophic turbulence. Derivation of the deformation radius and its role in controlling eddy scales will be discussed in what follows, but is introduced here because the first baroclinic deformation radius is an important length scale at which energy, extracted from mean flows, is input into the quasi-geostrophic eddy field.

One important characterization explicit in quasi-geostrophy is a small aspect ratio, the vertical scale (full ocean depth) H being smaller than a horizontal length scale L ($H/L < 1$). This makes useful the consideration of the evolution of mesoscale flows as two-dimensional turbulence, first explored by Kraichnan [1967]. Due to twin constraints requiring the conservation of kinetic energy and the square of vorticity (enstrophy), an inverse energy cascade of kinetic energy to larger scales and a forward enstrophy cascade to smaller scales is expected. Away from forcing and dissipative scales, accompanying inertial range theory predicts a relationship between the energy spectrum (partitioning of energy across wavenumber space) and a spectral energy flux through wavenumber space (the flux of energy across scales, or cascade rate). Following a dimensional analysis similar to that originally presented by Kolmogorov [1941], a $k^{-5/3}$ horizontal wavenumber dependence on the energy spectrum is expected in the energy inertial range and a k^{-3} dependence in the enstrophy inertial range.

Charney [1971] adapted this theory, invoking the conservation of quasi-geostrophic potential vorticity, to a more realistic three-dimensional stratified ocean. This work describes geostrophic turbulence as an isomorphism of idealized two dimensional turbulence and similarly predicts an inverse energy cascade and, within an inertial range, a forward enstrophy cascade with k^{-3} horizontal and *vertical* wavenumber dependence on the total energy spectrum under the following constraints: turbulence is homogeneous and isotropic, excitation energies are high such that the advection of relative vorticity ζ dominates the advection of planetary vorticity, nonlinear interactions that result in the transfer of energy across scales are local in wavenumber space (from one wavenumber to an adjacent wavenumber), and the scale of variations in stratification is large compared to the vertical scale of the turbulence. Despite these idealized and restrictive conditions, extensive modelling over the past decades, both idealized and representative of a realistically stratified ocean, has shown that the inverse energy and forward enstrophy cascades do exist [Rhines, 1977, Hua and Haidvogel, 1986, McWilliams, 1989, Vallgren and Lindborg, 2010, Smith and Vallis,

2001, Bachman et al., 2017, Kjellsson and Zanna, 2017]. Additional observational evidence of the inverse cascade centers on the occurrence of peak kinetic energy at scales larger than the scale of baroclinic instability (a dominant source of mesoscale eddy energy) [Scott and Wang, 2005, Smith and Ferarri, 2009].

In a realistic ocean, mesoscale eddy energy is expected to cascade to smaller horizontal wavenumber up to the Rhines' scale ($L_{Rhines} = \sqrt{U_{eddy}/\beta}$, with U_{eddy} a mean eddy velocity scale), the length scale at which the meridional gradient of planetary vorticity β becomes a contributing term in the momentum equations. Tulloch et al. [2009] observe eddy scales to be larger than the associated scale of baroclinic instability, but smaller than the Rhines scale. This suggests presence of an inverse cascade bounded by L_{d1} and L_{Rhines}. Energy cascading upscale to smaller horizontal wavenumber is also expected to barotropize, or become uniform in the vertical. Because energy is input to the ocean primarily at or near the surface, and shear instabilities also occur in the upper ocean, barotropization is a mechanism by which energy can be transferred to greater depths and eventually reach the seafloor, inducing drag and kinetic energy dissipation. Connections between the transfer of energy across horizontal and vertical scales were considered by Rhines [1979] in which he showed, using a two layer idealization, that as the ratio of potential to kinetic energy tends towards unity, barotropization occurs as a consequence of potential vorticity conservation. Enstrophy, on the other hand, is expected to cascade to higher horizontal wavenumbers until turbulence becomes fully three-dimensional and a Kolmogorov-like regime is entered where viscosity acts as a source of dissipation.

Applying this idealization of energy pathways to a realistic ocean is made complicated by vertically varying stratification, irregular bottom topography, sheared mean flows, and the forcing of the mesoscale eddy field across a range of wavenumbers. In a realistic ocean, with vertically varying surface intensified stratification and mean flows, baroclinic instability, identified as a dominant source of mesoscale eddy energy, preferentially occurs in the upper ocean [Smith, 2007]. Understanding of vertical energy transport becomes important considering the inverse cascade of energy to scales at which viscous dissipation is irrelevant. As energy propagates vertically, bottom drag is recognized as a pathway to dissipation. Adaptation of Charney's theory to a realistic ocean helps frame interpretation of observations of full depth density and velocity profiles accounting for the effect of varied stratification and bottom topography on the equilibrium partition of energy across vertical scales.

The effect of vertically varying stratification on energy transfer, originally considered by Rhines [1977] and Fu

and Flierl [1980], is revisited by Smith and Vallis [2001] carrying out numerical simulations of QG turbulence, to include an upper ocean pycnocline. Various simulations were run to test predictions made by Fu and Flierl [1980] regarding the relative enhancement or inhibition of kinetic energy transfer across vertical modes. Vertical modes are an orthogonal basis set of time independent vertical structures, functions of stratification and latitude, that satisfy the quasi-geostrophic momentum equations (derived in section 3). Initializing a simulation with kinetic energy at high vertical and low horizontal wavenumber, generally representative of realistic forcing scales associated with baroclinic instability, the authors show that energy quickly cascades to larger vertical scales, spreads out across a range of horizontal wavenumbers, and then slowly moves to larger horizontal scales. The time scales of these transfers are framed in terms of eddy turnaround time and vary with eddy strength between days and months. These transfers of energy reveal the inverse cascade to occur in both vertical and horizontal wavenumber. With the introduction vertical structure, enhanced upper ocean stratification, the tendency for energy to transfer to the barotropic mode is however relatively inhibited.

Recent modelling work, motivated by observations of seasonality in surface eddy kinetic energy identifies seasonality in mixed layer depth, stratification, and sheared flow as regulating the pool of available potential energy susceptible to baroclinic instability [Qui et al., 2014, Callies et al., 2015, Uchida et al., 2017]. Application of linear instability theory to this variability shows that instability growth rates at scales smaller than the first deformation radius are many times larger in winter than in the summer [Smith, 2007, Uchida et al., 2017]. With a winter-time increased source of eddy kinetic energy and kinetic energy fluxes to larger scales at scales as small as 38 km, simulations show mean mesoscale eddy kinetic energy increase in magnitude to its largest annual value at the end of the winter, lagging the peak in mean submesoscale eddy kinetic energy by roughly one month. These results imply that both geographic and seasonal variability in background density and velocity structure regulate geostrophic turbulence and vertical energy transfer.

The vertical components of quasi-geostrophic motions have traditionally been interpreted through the application and projection normal modes onto observed structures. Use of these modes, similar to a Fourier series decomposition of a signal into a set of sines and cosines, permits consideration of quasi-geostrophic eddy vertical structure as a set of variably expressed physically relevant functions (modes), or scaled vertical wavenumbers. In

a realistically stratified ocean, transfers of energy among higher number baroclinic modes is relatively enhanced compared to transfers among low number modes and the barotropic mode. This relative enhancement results in a 'build-up' of kinetic energy, or peak in wavenumber space in the first baroclinic mode at first deformation radius scales. This interpretation agrees with that of Fu and Flierl [1980] originally employing QG potential vorticity theory to show that nonlinear transfers of energy across vertical modes are a strong function of stratification. Understanding the relative importance of surface intensified stratification on controlling the transfers of energy in the vertical is necessary when employing bottom drag as a sink in a global energy budget. Thus in the ocean, the tendency with which mesoscale flows transfer energy to graver modes should be expected to vary geographically and potentially seasonally.

4.1.2 Observations of Geostrophic Turbulence

Previous observational studies of mesoscale eddy structure and behavior provide an extensive background from which to interpret new observations. With the exception of a few observational datasets, however, because of the relative difficulty in obtaining deep ocean measurements, the majority of previous work has explored QG eddy interactions and turbulence at the surface or in the upper ocean. Where vertical structure has been investigated, observations with high vertical resolution (i.e. shipboard conductivity temperature and depth, CTD, casts) typically have low temporal resolution and those with high temporal resolution (i.e. instrumented moorings), typically have low vertical spatial resolution.

Observationally, QG turbulence has been primarily investigated considering the partitioning of kinetic energy across horizontal wavenumbers [Callies and Ferarri, 2013] and the spectral flux of kinetic energy from satellite observations [Scott and Wang, 2005]. Similar to two-dimensional turbulence theory predictions Kraichnan [1967], geostrophic turbulence theory Charney [1971] predicts a $\mathbf{k}^{-3}$ wavenumber dependence on the energy spectrum $E(\mathbf{k})$ within the enstrophy inertial range ($E(\mathbf{k}) \propto \mathbf{k}^{-3}$). Here $\mathbf{k} = k^2 + l^2 + f^2/c_m^2$ where the last term is a scaled vertical wavenumber that is a function of the local Coriolis parameter f and the mode Kelvin wave speed c_m. While the spectral slope does not inform on the direction of the energy cascade, it is useful in distinguishing QG turbulence from a regime dominated by internal gravity waves where $E(\mathbf{k}) \propto \mathbf{k}^{-2}$ [Garrett and Munk, 1979].

Observations of sea level anomaly from satellite altimetry and of upper ocean horizontal density and velocity structure from underway CTDs and/or acoustic doppler current profilers (ADCPs) permit estimation of horizontal kinetic and potential energy spectra. Scott and Wang [2005] estimate the spectral flux of kinetic as a function of horizontal wavenumber from altimetric observations of sea level anomaly. Authors highlight the presence of an inverse kinetic energy cascade at scales greater than the first baroclinic deformation radius. While this negative spectral flux to larger scales is observed in all ocean basins, variability in dominant dyanmical processes is revealed by Xu and Fu [2010], showing the geographic variability in the slope of horizontal kinetic energy spectra, apparently dependent on mesoscale eddy activity. Disagreement between spectral slope predictions and observations derived from sea level anomalies or upper ocean measurements may be partly explained considering surface quasi-geostrophic theory [Lapeyre and Klein, 2006], permitting the creation and destruction of potential vorticity at the surface. Callies and Ferarri [2013] similarly find geographic variability in horizontal kinetic energy spectra using ADCP measurements near the Gulf Stream and in the Northeast Pacific. Their results show agreement with the predicted spectral slope associated with geostrophic turbulence, but only in the energetic Gulf Stream region. Investigation of disagreement between measurements and quasi-geostrophic turbulence theory has led to use of a technique to decompose along and across track ADCP measurements into balanced and unbalanced contributions [Buhler et al., 2014, Rocha et al., 2016]. Results of this technique, recently employed in the Drake Passage, identify the wavenumber bounds of the quasi-geostrophic turbulence inertial range as 10-200km, but show that unbalanced or ageostrophic motions contribute up to 50% of near surface kinetic energy. At scales greater than 70km additional agreement is shown between ADCP and altimeter data. These results highlight the geographic variability of kinetic energy spectra, but importantly show that in the surface ocean, the creation and destruction of potential vorticity make satisfying Charney's assumptions more difficult.

Klocker et al. [2016] summarize this geographic variability in developing a regime diagram for quasi-geostrophic turbulence dependent on eddy scale and non-linearity (measured as a ratio of eddy rotational speed to translation velocity). Using altimetric observations they show that eddy length scales, normalized by the first baroclinic deformation radius, vary with eddy non-linearity and latitude. This result agrees with analyses of eddy characteristics and scales throughout the world ocean by Chelton et al. [2011]. At low latitudes, eddy scales are larger

and approach the the Rhines' scale while at mid-latitudes eddy scales are at or larger than the first deformation radius. This regime diagram aids in the identification of a dynamical setting, defined in wavenumber space and as a function of eddy strength, in which quasi-geostrophic turbulence described by Charney may be a dominant process setting the spectral distribution of kinetic energy.

In addition to geographic variability, recent observations show seasonality in submesoscale and mesoscale motions at scales up to 200 km [Callies et al., 2015, Uchida et al., 2017]. This seasonal variability is linked to changes in mixed layer depth and subsequently the reservoir of available potential energy. Larger eddies and meanders stir the upper ocean creating lateral buoyancy gradients which eventually become unstable. Baroclinic instability occurring in the winter, when the mixed layer is deeper and the pool of available potential energy is greater, produces a relatively more energetic eddy field. In the summer, increased upper ocean stratification reduces the vertical scale over which baroclinic instability may occur, producing a less energetic spectrum. Changes in the relative partitioning of energy across scales, seen in the steepness of the spectrum, can be partly explained by the dependence of energy transfer across scales on the strength and uniformity of stratification.

Strong geographic and seasonal variability in the scales at which QG turbulence may dominate is presented by Qui and Chen [2018] through interpretation of model and observational data. A crossover scale is identified as a lower limit of the inertial range predicted in idealized two dimensional turbulence vary between 40 km near western boundary currents and 200 km in the tropics. While motions with length scales equal to this value imply that both balanced and unbalanced dynamics are relevant, it is useful in identifying when and where quasi-geostrophic turbulence theory may be relevant.

4.1.3 Observed Vertical Structure of Mesoscale Eddies

In comparison to surface or upper ocean observations of eddy scales and energetics, observations of eddy vertical structure are extremely sparse and generally confined to specific locations. Where eddy vertical structure has been observed, it has been with coarse or incomplete resolution. Despite this relative dearth of measurements, significant insight has been gained through analysis of the vertical partition of mesoscale eddy energy [Wunsch, 1997]. Using the traditional set of flat bottom, rigid lid vertical modes, Wunsch [1997] shows a near equal partition of water

column average kinetic energy in the barotropic and first baroclinic mode. The results of Smith and Vallis [2001] similarly reveal a near equi-partition of kinetic energy between baroclinic and the first barotropic mode for their realistic stratification simulation. At the surface, however, Wunsch [1997] shows the majority of kinetic energy to be contained in the first baroclinic mode. These results show that the projection of interior structures at the surface do not necessarily reflect the relative partition of energy across modes in the interior, but provide evidence to a link between the two.

More recent analyses of the same and now expanded mooring dataset used by Wunsch [1997] identify inherent vertical structures of horizontal velocity and suggest the need to consider the effect of bottom topography on mode shape [de La Lama et al., 2016, LaCasce, 2017]. Employing an alternate bottom boundary condition, now a function of linear topographic slope, in solving for vertical modes the authors seek the smallest set of modes need to capture the largest percentage of variance of observed horizontal velocity vertical structure. Observations from moored velocity measurements with coarse vertical resolution show horizontal velocities decaying to zero at depth and suggest the appropriateness of newly termed sloping bottom modes. The following analyses intend to revisit these conclusions using hundreds of recently collected full depth density profile measurements and velocity profile estimates with vertical resolution of order meters.

While the analysis of Wunsch [1997] considered the partitioning of energy across the barotropic, first baroclinic, and second baroclinic modes, there have been few attempts to explore energy partitioning among higher modes. With the exception of numerical simulations carried out by Smith and Ferarri [2009], seeking to detail the cascade of T/S variance across scales, analysis and interpretation of vertical wavenumber spectra have been lacking.

4.1.4 Motivation

With an improved understanding of geographic and seasonal variability in eddy vertical structure, along with recent observations of upper ocean meso- and submesoscale eddies, we can revisit geostrophic turbulence theory predictions in analyzing new full depth Deepglider observations. Multiple Deepglider autonomous underwater vehicle (AUV) deployments carried out over the last five years, each lasting many months, permit renewed consideration of full depth eddy structure and energy partitioning throughout the water column.

If a dominant source of mesoscale eddy energy is a baroclinically unstable mean flow, the conversion of available potential energy to kinetic energy both energizes mesoscale eddies, serving as an input to a geostrophically turbulent eddy field, and provides a key length scale that can be compared against observed eddy length scales. These eddies have vertical structures linked to the current/feature from which they originate. Once formed, eddies can then propagate away from their formation region, interact with other eddies, and eventually dissipate or be destroyed. This life-cycle represents the conversion of potential energy to kinetic energy, but also the transfer of energy across scales.

Because mean flows are often highly sheared in the upper 1000 m, mesoscale eddy energy is generally surface intensified, but observations of deep velocities and a consistent framework describing vertical energy propagation and barotropization are needed. Geographic and seasonal variability in background density structure plays an important role in regulating this vertical transfer of energy and underlies the key point that geostrophic turbulence and the transfer of energy across scales is driven by different dynamical processes at different locations and at different times. Understanding this geography is important in constructing a global energy budget and tracking energy from input to dissipation scales. Quasi-geostrophic low Rossby number flows are expected to have time independent vertical structures that can be described by a unique orthogonal eigenfunctions subject to relevant boundary conditions. These vertical modes have physical relevance linked to background stratification, bottom topography, and the Coriolis parameter. Various surface and bottom boundary conditions, however, used to solve for their structure, can be employed and require justification for their use. These vertical modes project onto the sea surface with varying amplitudes and an improved understanding of the link between surface projections of interior structure can greatly improve the interpretation of altimetric observations.

Recently collected full-depth measurements of temperature and salinity variability motivate renewed consideration of complete eddy vertical structure, the presence and importance of previously unobserved deep ocean velocities, and potential pathways to dissipation. These observations reveal the evolution and interaction of QG turbulent flows precipitating both inverse and forward cascades of energy and enstrophy.

Over the past five years, observations with spatial resolution $\mathcal{O}$[10 m] and temporal resolution $\mathcal{O}$[1 day] have been made by Deepglider AUVs at multiple sites in the western North Atlantic. These measurements permit the

estimation of eddy isopycnal vertical displacements and geostrophic velocity profiles on a near daily basis. With these observations of eddy vertical structure, we explore the geographic variability of the vertical partitioning of potential and kinetic energy across mission sites.

Section 2 describes Deepglider deployments and data collection between 2014 and 2019. Section 3 derives normal vertical modes and explores the effect of varying bottom boundary conditions on mode structure. QG potential vorticity as a passive tracer is also defined. Section 4 describes data processing, the projection of vertical modes onto density and velocity profiles, and details the framework for interpreting the partition of energy across modes. Section 5 discusses energy transfer across modes, the vertical structure of along isopycnal temperature variance, presents results from multiple Deepglider deployments throughout the North Atlantic, and compares energy partitioning across modes at each site. Section 6 offers a conclusion.

4.2 Data

4.2.1 Deepglider

Deepglider is a buoyancy driven AUV capable of repeatedly profiling from the surface to 6000 m and back in approximately 1.5 days for multiple months at a time. Like Seaglider, measurements of temperature and conductivity are made by a SeaBird Electronics thermistor and conductivity cell aspirated by vehicle motion [Eriksen et al., 2001]. Measurements are processed to calculate salinity following Pelland et al. [2013]. Additional sensors measure pressure, dissolved oxygen, cholorophyll fluorescence, and optical backscatter at pilot specified intervals, typically once every 10 seconds in the upper ocean increasing to 60 seconds below 1000 m. Measurements are vertically bin averaged to a non-uniform grid with intervals selected to obtain an equal number of measurements in each average. Slant profiles have a nominal resolution of 1 m over the upper 150 m, 5 m between 150 m and 300 m, 10 m between 300 m and 1000 m, and 20 m from 1000 m to the seafloor. Gliders also infer a depth-average current (DAC) as the difference between GPS-tracked over ground and dead-reckoned displacement.

For each profile, conservative temperature, absolute salinity, pressure, and location are used to compute neutral density $\gamma^n(\mathrm{z})$. Neutral density is a continuous analog to potential density [Jackett and McDougall, 1997] using

local reference pressures rather than a single reference pressure often taken at the ocean surface. Typical estimation of potential density profiles with a reference pressure at or near the surface underestimates density differences in adjacent samples at depths in the abyssal ocean.

Between 2014 and 2019, ten Deepglider missions were undertaken at various sites in the western North Atlantic (Fig. 4.1). Missions typically lasted between three and ten months, varying in duration as a result of energy constraints and/or hardware failures. Deployment sites were selected as those meeting multiple criteria. Initially, sites repeatedly visited by oceanographic research vessels or those of historical significance were prioritized to both permit comparison of new and old observations, but also to permit the collection of concurrent temperature and salinity profiles by glider and shipboard instruments for calibration purposes. As deployments became more frequent, observations from sites associated with varied levels of mean eddy kinetic were sought to explore geographic variability in eddy vertical structure. A third factor considered in selecting glider mission locations was the steepness and roughness of bottom topography. With the intention of using observations to explore the partitioning of energy across flat bottom modes, sites with minimal topographic slope were sought. While the ocean floor is nowhere flat, sites were selected with vertical to horizontal slopes less than $\sim$ 300 m per 100 km or 0.003.

Initial Deepglider deployment sites include the Bermuda Atlantic Time Series (BATS) station [31°40'N, 64°10'W] and the western section of the RAPID array at 26°N between 77°W and 74°W. Recent deployment sites, selected to observe eddy re-circulation in the North Atlantic subtropical gyre at various locations of varied eddy energy, include the southern flank of the Gulf Stream extension at [36°N, 65°W] and the POLYMODE Local Dynamics Experiment (LDE) site at [31°N, 69°30'W]. With the exception of deployments along the RAPID array line, gliders were instructed to profile following either a repeat a bow-tie or square box pattern, each roughly 100 km across, to sample within a fixed domain and observe the relatively slow passage of quasi-geostrophic features.

4.2.2 Bermuda Atlantic Time Series (BATS) Site [31°40'N, 64°10'W]: sg035 (2014), sg035 (2015)

Deepglider sg035 was deployed from Bermuda in March of 2014, sampling to the southeast of the island for 65 days and again in February 2015 for 276 days. For each mission, gliders collected full-depth slant profiles of temperature and salinity on a near daily basis following a repeat bow-tie pattern centered at station BATS (Fig. 4.2). This

pattern was selected and aligned such that the long transect arms of the bow-tie were oriented in the along-slope and across-slope direction of the Bermuda rise. In 2014, 114 and in 2015, 326 full-depth slant profiles of temperature and salinity were completed.

4.2.3 Abaco [26.5°N, 74-77°W.]: sg037, sg038 (2017); sg037, sg039 (2018)

Deepgliders sg037 and sg038 were deployed in April 2017 from Florida and completed repeat transects along the western end of the RAPID array for approximately a two month period (85 and 61 days respectively collecting 70 and 60 full depth profiles). Repeat zonal glider transects of 125-250 km were completed sampling the North Atlantic's deep western boundary current and meridional flow at the western end of the subtropical gyre (Fig. 4.3). Two gliders were again deployed in 2018 from the Bahamas, for 156 and 112 days respectively, occupying the same 250 km western section of the RAPID array. Gliders experienced meridional velocities exceeding 30 m s^{-1} throughout much of the water column and separately experienced hardware issues preventing the calculation of perturbation isopycnal vertical displacements and geostrophic velocities.

4.2.4 Gulf Stream Extension [36°N, 65°W]: sg041 (2018), sg045 (2019), sg046 (2019)

Deepglider sg041 was deployed from Bermuda in October 2018 and piloted to [36°N, 65°W], occupying a repeat bow-tie pattern for 177 days collecting over 250 full-depth slant profiles of temperature and salinity (Fig. 4.4). This location, due-south of the Gulf Stream extension, was selected to observe a highly energetic eddy field, presumably near the site of eddy formation, while maintaining the ability to pilot gliders effectively while experiencing current speeds in excess of 0.5 m s^{-1}. Deepglider sg045 was deployed from Bermuda in June 2019 and piloted to [36°N, 65°W], where it occupied a box pattern for 56 days completing 2 circuits (36 full depth slant profiles) while continuing to sample the eddy field into the summer. Rather than a bow-tie pattern, the zonally and meridionally aligned box pattern was selected to permit separate estimation of both zonal and meridional cross-track geostrophic velocities (due to the alignment of transects with latitudinal and longitudinal axes). Deepglider sg046, also deployed from Bermuda in June 2019, occupied a box pattern centered at [36°N, 62°W] completing 55 full depth slant profiles, but struggled to complete circuits as it experienced mechanical issues and depth average velocities regularly exceeding 0.2 m s^{-1} associated with a Gulf Stream Ring.

4.2.5 Local Dynamics Experiment (LDE) Site [31°N, 69°30'W]: sg037 (2019)

Deepglider sg037 was deployed from Bermuda in June 2019 and piloted to [31°N, 69°30'W], location of the of Local Dynamics Experiment carried out in 1978 [McWilliams et al., 1983] (Fig. 4.5). This site was selected to permit comparison of observations to those made during the LDE surveys, but also because it is located within the region of eddy re-circulation in the western North Atlantic, but far away from the Gulf Stream. A repeat box pattern was selected with 192 displacement and velocity profiles calculated from 7 circuits completed in 179 days. The orientation of the box sampling pattern permit separate consideration of zonal and meridional geostrophic velocity profiles.

4.2.6 Shipboard Hydrographic Records

Repeat full-depth temperature, salinity, and pressure measurements made by shipboard instruments are employed to complement glider profiles and widen the scope of eddy vertical structure analysis. While glider profiling at the Bermuda Atlantic Time Series (BATS) station was initially timed to match full-depth shipboard sampling by the R/V Atlantic Explorer and provide reference temperature and salinity measurements, a thirty year hydrographic record at BATS (`http://bats.bios.edu/`) is considered in analysis of eddy vertical structure (240 profiles). Monthly density anomaly profiles are computed relative to thirty-year seasonal background density profiles to reveal eddy isopycnal vertical displacements and mean vertical partitioning of potential energy across vertical modes. These data were collected over a time period much greater than our longest glider deployment of 10 months and serve as a robust comparison to glider data.

Similar consideration of full-depth multi-decade long time series at ocean stations PAPA [50°06'N, 144°54'W] (`https://www.pmel.noaa.gov/ocs/Papa`) (50 profiles) and ALOHA [22°45'N, 158°W] (`http://aco-ssds.soest.hawaii.edu/ALOHA/`) (168 profiles) in the North Pacific permits analysis of geographic variability in vertical structure of isopycnal displacements linked to variability in dominant dynamics controlling the mean distribution of kinetic energy across scales. Compared to station BATS and glider deployment sites in the North Atlantic, stations PAPA and ALOHA have characteristically low mesoscale eddy activitity and analyses of eddy vertical in these regions serves as comparison to regions with different dominant dynamics.

4.3 Analysis Framework

This section first presents a derivation of the second order ordinary different equation describing the vertical structure of time dependent quasi-geostrophic motions. The second and third sections consider appropriate boundary conditions, the fourth section describes numerical solution techniques and eigenfunction normalization per unit energy, and the fifth section introduces a more general form of quasi-geostrophic potential vorticity, isomorphic to equations describing the evolution of an ideal tracer.

4.4 Vertical Structure of QG Motions and Basis Functions

Following Wunsch and Stammer [1997b] we employ standard equations of motion for time dependent geostrophic flows and derive the vertical structure equations for perturbations. First we define a free surface pressure perturbation

$$p_a = A_0(k, l, \sigma) e^{ikx+ily-i\sigma t} \tag{40}$$

a function of amplitude A_0, horizontal wavenumber $\sqrt{k^2 + l^2}$, and frequency σ (where $\sigma > 0$ and by construction p_a has a zero mean). We define density as $\rho(x, y, t) = \rho_0 + \overline{\rho}(z) + \rho'(x, y, z, t)$ and as pressure as $p(x, y, z, t) = p_0(z) + p'(x, y, z, t)$. In the rest state the vertical momentum equation satisfies

$$\frac{\partial p_0}{\partial z} = -g\left(\rho_0 + \overline{\rho}(z)\right) \tag{41}$$

where ρ_0 is a constant reference density and $\overline{\rho}(z)$ describes the resting ocean stratification. Making the Boussinesq and hydrostatic approximations, the appropriate scaled equations of motion, mass conservation equation, density equation, and the definition of the buoyancy frequency are then

$$\frac{\partial u}{\partial t} - fv = -\frac{1}{\rho_0}\frac{\partial p'}{\partial x} \tag{42}$$

$$\frac{\partial v}{\partial t} + fu = -\frac{1}{\rho_0}\frac{\partial p'}{\partial y} \tag{43}$$

$$0 = -\frac{1}{\rho_0}\frac{\partial p'}{\partial z} - \frac{g\rho'}{\rho_0} \tag{44}$$

$$\frac{\partial u}{\partial x} + \frac{\partial v}{\partial y} + \frac{\partial w}{\partial z} = 0 \tag{45}$$

$$\frac{\partial \rho'}{\partial t} + w\frac{\partial \overline{\rho}}{\partial z} = 0 \tag{46}$$

$$N^2 \equiv -\frac{-g}{\rho_0}\frac{\partial \overline{\rho}}{\partial z} \tag{47}$$

where f_0 is the local Coriolis frequency, N^2 is the buoyancy frequency, and we consider the nonlinear advective terms contained in the material derivatives of velocities u, v and w (i.e. $u\frac{\partial u}{\partial x}$) as small relative to $\frac{\partial u}{\partial t}$. Following the Boussinesq approximation, the vertically varying background density is approximated as a constant ρ_0 except where a vertical derivative is taken (e.g. Eq. 47). In this application we are interested in the vertical structure of time dependent geostrophic motions. To partition terms into horizontal and vertical components, we assume solutions can be found using a separation of variables technique in which horizontal and vertical structure is assumed separable.

$$u(x,y,z,t), v(x,y,z,t) = A[U(x,y,t), V(x,y,t)]F(z) \tag{48}$$

$$w(x,y,z,t) = AW(x,y,t)G(z) \tag{49}$$

$$p'(x,y,z,t) = A\rho_0 P(x,y,t)F(z) \tag{50}$$

where A is a dimensionless amplitude, and $F(z)$ (dimensionless) and $G(z)$ (dimensions of of length) are unknown functions that vary only vertically. These separated forms are substituted into equations 3-8 to determine $F(z)$ and $G(z)$. We first substitute equation 47 into equation 46

$$\frac{\partial \rho'}{\partial t} = w\frac{\rho_0}{g}N^2 \tag{51}$$

and the result into the time derivative of equation 44

$$\frac{\partial}{\partial t}\left(\frac{1}{\rho_0}\frac{\partial p'}{\partial z}\right) = -\frac{g}{\rho_0}\frac{\partial \rho'}{\partial t} = -\frac{g}{\rho_0}\left(w\frac{\rho_0}{g}N^2\right) \tag{52}$$

$$\frac{\partial}{\partial t}\left(\frac{1}{\rho_0}\frac{\partial p'}{\partial z}\right) = -wN^2 \tag{53}$$

Into equation 53 we substitute the separated forms for the pressure perturbation and the vertical velocity (Eq. 49, 50) and presume the time dependent component of the pressure perturbation $P(x, y, t)$ has the form of Eq. 40,

$$\frac{1}{\rho_0}\frac{\partial}{\partial t}\left(\rho_0 P\frac{\partial F}{\partial z}\right) = -WGN^2 \tag{54}$$

$$\frac{\partial P}{\partial t}\frac{\partial F}{\partial z} = -WGN^2 \tag{55}$$

We next insert the separable form for u, v, w into Eq. 45 to obtain

$$\left(\frac{\partial U}{\partial x} + \frac{\partial V}{\partial y}\right)F + W\frac{\partial G}{\partial z} = 0 \tag{56}$$

Our goal then is to relate horizontal divergence to vertical structure. For simpler notation we introduce reduced pressure $p = p'/\rho_0$. We next take the time derivative of Eq. 42 and substitute in Eq. 43 multiplied by f. We do the same and take the time derivative of Eq. 43 and substitute in the Eq. 42 multiplied by f. The horizontal momentum equations then become

$$\left(\frac{\partial^2}{\partial t^2} + f^2\right)U = -\frac{\partial^2 P}{\partial x \partial t} - f\frac{\partial P}{\partial y} \tag{57}$$

$$\left(\frac{\partial^2}{\partial t^2} + f^2\right)V = -\frac{\partial^2 P}{\partial y \partial t} + f\frac{\partial P}{\partial x} \tag{58}$$

Following Eq. 40, the time derivative becomes $-i\sigma$. We then take the $\frac{\partial}{\partial x}$ of Eq. 57, $\frac{\partial}{\partial y}$ of Eq. 58, and substitute both into Eq. 56 to arrive at

$$\frac{\partial U}{\partial x}+\frac{\partial V}{\partial y}=\frac{\frac{\partial}{\partial x}\left(i\sigma\frac{\partial P}{\partial x}-f\frac{\partial P}{\partial y}\right)}{f^2-\sigma^2}+\frac{\frac{\partial}{\partial y}\left(i\sigma\frac{\partial P}{\partial y}+f\frac{\partial P}{\partial x}\right)}{f^2-\sigma^2}=\frac{i\sigma\left(\frac{\partial^2 P}{\partial x^2}+\frac{\partial^2 P}{\partial y^2}\right)}{f^2-\sigma^2} \tag{59}$$

$$\left(\frac{i\sigma\left(\frac{\partial^2 P}{\partial x^2}+\frac{\partial^2 P}{\partial y^2}\right)}{f^2-\sigma^2}\right)F+W\frac{\partial G}{\partial z}=0 \tag{60}$$

From Eq. 55 we can express W in terms of G, F, and P to write

$$\left(\frac{i\sigma\left(\frac{\partial^2 P}{\partial x^2}+\frac{\partial^2 P}{\partial y^2}\right)}{f^2-\sigma^2}\right)F+\frac{\partial G}{\partial z}\frac{i\sigma P\frac{\partial F}{\partial z}}{N^2G}=0. \tag{61}$$

Cancelling like terms and consolidating horizontally and vertically dependent terms together this becomes,

$$\frac{\left(\frac{\partial^2 P}{\partial x^2}+\frac{\partial^2 P}{\partial y^2}\right)}{\left(f^2-\sigma^2\right)P}+\frac{\frac{\partial G}{\partial z}\frac{\partial F}{\partial z}}{GFN^2}=0 \tag{62}$$

If P has the same form as Eq. 40, this becomes

$$\frac{-\left(k^2+l^2\right)}{\left(f^2-\sigma^2\right)}+\frac{\frac{\partial G}{\partial z}\frac{\partial F}{\partial z}}{GFN^2}=0 \tag{63}$$

Following the separation of variables technique, the two terms must be equal and opposite to a separation constant $\frac{1}{c^2}$, where c is realized as the Kelvin wave speed. While we have ignored meridional changes in f to obtain in Eq. 63, what can be recognized as the dispersion relation for inertia gravity waves ($k^2+l^2=(\sigma^2-f^2)/c^2$). Relaxing this constraint leads equivalently to the dispersion relation for Rossby waves ($k^2+l^2+\sigma k/\beta+f_0^2/c^2$) in the limit of low frequency, where $f=f_0+\beta y$. Vertical structure is governed identically in the two cases. By Eq. 56, F must equal $\frac{\partial G}{\partial z}$, since no other terms have vertical dependence. Making these substitutions, the vertical structure of vertical velocity G then can be determined from

$$\frac{\partial^2 G(z)}{\partial z^2}+\frac{N^2(z)}{c^2}G(z)=0 \tag{64}$$

and recognizing that $\frac{\partial^2 G(z)}{\partial z^2}=\frac{\partial F}{\partial z}$, the vertical structure of horizontal velocity satisfies

$$\frac{\partial}{\partial z}\left(\frac{1}{N^2}\frac{\partial F(z)}{\partial z}\right)+\frac{1}{c^2}F(z)=0. \tag{65}$$

Note that while the first term in Eq. 63 when balanced by c^{-2} gives the dispersion relation for gravity waves, the expression equally describes sub-inertial motions including the QG motions in which we are interested. Either second order ordinary differential equation can be used to solve for vertical modes, with the surface and bottom boundary conditions shaping the structure of the eigenfunctions. Rigid lid and flat bottom boundary conditions are traditionally chosen for their simplicity, but these choices may not always be appropriate. Eigenfunction solutions to Eq. 65 are orthogonal and we freely choose them to be orthonormal as well to satisfy

$$\frac{1}{H}\int_{-H}^{0}F_iF_j dz=\delta_{ij} \tag{66}$$

where H is the full depth of the ocean, subscripts i, j refer to mode numbers m = 0,1,2,3, and $\delta_{ij}=1$ when $i=j$.

4.4.1 Boundary Conditions: Free Surface, Flat Bottom

Traditional boundary conditions assume a flat bottom and rigid lid. We first solve Eq. 64 with more realistic flat bottom and free surface boundary conditions. The bottom boundary condition requires no normal flow at the seafloor and is written as

$$G(z=-H)=\frac{\partial F(z=-H)}{\partial z}=0 \tag{67}$$

The free surface boundary condition is derived by first requiring that pressure at the free surface ($z=\eta(x,y,t)$) be atmospheric. This expression needs to be written in terms of vertical velocity. We first linearize an expression for pressure at the surface

$$p_a=p(\eta)=p(z=0)+\eta\frac{\partial p(z=0)}{\partial z} \tag{68}$$

Remembering that $p=p_0(z)+p'(x,y,z,t)$ and than $p_0 >> p'$ this can be rewritten as

$$\frac{\partial p_a}{\partial t}=\frac{\partial p'}{\partial t}+\frac{\partial \eta}{\partial t}\frac{\partial p_0}{\partial z} \tag{69}$$

$$\frac{\partial p_a}{\partial t} = \frac{\partial p'}{\partial t} + wg\rho_0. \tag{70}$$

If again $\frac{\partial}{\partial t} = -i\sigma$, horizontal derivatives can be taken and p' substituted for w in Eqs. 42 and 43 to obtain

$$-i\sigma u - fv = \frac{g}{i\sigma}\frac{\partial w}{\partial x} \tag{71}$$

$$-i\sigma v + fu = \frac{g}{i\sigma}\frac{\partial w}{\partial y} \tag{72}$$

relating horizontal surface velocities with vertical motion of the free surface. As in Section 3a. we make substitutions such that Eq. 71 is only a function of zonal velocity u and Eq. 72 of meridional velocity v,

$$u(z=0) = \frac{g}{\sigma^2 - f^2}\left(\frac{\partial w}{\partial x} - \frac{f}{i\sigma}\frac{\partial w}{\partial y}\right) \tag{73}$$

$$v(z=0) = \frac{g}{\sigma^2 - f^2}\left(\frac{\partial w}{\partial y} + \frac{f}{i\sigma}\frac{\partial w}{\partial x}\right). \tag{74}$$

Using mass conservation (Eq. 45), we take horizontal derivatives again and arrive at an expression only a function of w. We again substitute the separable form (Eq. 49) and collect horizontal and vertical terms,

$$\frac{g}{\sigma^2 - f^2}\left(\frac{\partial^2 w}{\partial x^2} + \frac{\partial^2 w}{\partial y^2}\right) + \frac{\partial w}{\partial z} = 0. \tag{75}$$

$$\frac{g}{\sigma^2 - f^2}\left(\frac{\partial^2 W}{\partial x^2} + \frac{\partial^2 W}{\partial y^2}\right) G + W\frac{\partial G}{\partial z} = 0. \tag{76}$$

$$\frac{\left(\frac{\partial^2 W}{\partial x^2} + \frac{\partial^2 W}{\partial y^2}\right)}{W\left(\sigma^2 - f^2\right)} + \frac{1}{gG}\frac{\partial G}{\partial z} = 0. \tag{77}$$

With W having the same horizontal structure as p, each term in this equation can be set equal to the separation constant $\frac{1}{c^2}$ to arrive at the free surface boundary condition for w

$$\frac{\partial G(z=0)}{\partial z} - \frac{g}{c^2}G(z=0) = 0 \tag{78}$$

and for u and v as

$$\frac{g}{N^2}\frac{\partial F(z=0)}{\partial z} + F(z=0) = 0. \tag{79}$$

4.4.2 Boundary Conditions: Free Surface, 'Sloping' Bottom

An alternate bottom boundary condition permits vertical velocities at the sea floor and is representative of rough or sloping topography. Rather than require vertical velocity to go to zero at the bottom, the more general requirement of no normal flow is still made. Consider an idealized linear sloping bottom with total depth

$$H = H_0 + h(x, y) \tag{80}$$

where, following the derivation of LaCasce [2017] for a meridional bottom slope, $h(x, y) = \alpha y$. Along the slope, at $z = -H$, no normal flow is required satisfying

$$w = \mathbf{u} \cdot \nabla h = \alpha v. \tag{81}$$

This is incorporated into a bottom boundary condition using equations for $F(z)$, describing the vertical structure of horizontal velocity, the streamfunction, and the quasi-geostrophic density equation (Eq. 46)

$$\frac{\partial}{\partial t}\frac{dF}{dz} + \frac{N^2}{f_0}w = 0. \tag{82}$$

This equation derives from a combination of the vertical momentum equation (Eq. 44) and an equation describing the evolution of density in time as the vertical advection of the background density field (Eq. 46). Substituting into this equation the expression for w at the bottom, and assuming the streamfunction is proportional to $\psi \propto F(z)exp(ikx + ily - i\sigma t)$, the bottom boundary condition becomes

$$\frac{dF}{dz} = \frac{\alpha k N^2}{\sigma f_0} = -\frac{\alpha N^2}{\beta f_0}\left(k^2 + l^2 + \frac{f_0^2}{c^2}\right)F. \tag{83}$$

Note, this bottom boundary condition uses the dispersion relation for planetary waves, $f_0^2/c^2 = -\left(k^2 + l^2 + \beta k/\omega\right)$. LaCasce [2017] solves for vertical modes using an analytic exponentially decaying stratification profile and for a

wave with horizontal wavenumber 1/100 km. We solve for these modes with observed background stratification profiles and for a range of horizontal wavenumbers to compare observed vertical structures with both flat and sloping bottom modal shapes.

4.4.3 Solutions for Vertical Modes

Solutions to Eq. 64 and Eq. 65, describing the vertical structures of vertical and horizontal velocities, are found numerically for the first 40 ($m = 0 - 40$) eigenvalues c_m and eigenfunctions $G_m(z)$ and $F_m(z)$ for free surface, flat bottom, and sloping bottom boundary conditions. For initial comparison, an average wintertime background density profile at station BATS is used as well as a linear slope estimated using bathymetry at the BATS survey site (Fig. 4.6). Each eigenfunction is then normalized for unit energy such that

$$\frac{1}{H}\int_{-H}^{0} F_m^2 dz = 1 \tag{84}$$

$$\frac{1}{H}\frac{gG_m(0)^2}{c_m 2} + \frac{1}{H}\int_{-H}^{0}\frac{N^2(z)G_m(z)}{c_m^2}dz = 1. \tag{85}$$

These basis functions describe one set of vertical structures used to describe quasi-geostrophic motions, but have physical meaning linked to the quasi-geostrophic momentum equations. Each eigenvalue relates to the m^{th} baroclinic Rossby radius of deformation as

$$L_{d_m} = \frac{c_m}{f_0} \tag{86}$$

The inverse $L_{d_m}^{-1}$ is a scaled vertical wavenumber that can be written as $L_{d_m}^{-1} = \frac{f_0 m}{N}$ where in this case only m is a non-scaled vertical wavenumber. All subsequent use of subscript m is in reference to mode number m.

These mode structures vary in shape with background stratification. At locations where the buoyancy frequency profile varies seasonally, higher number mode maxima and minima shoal or deepen in the presence or absence of a strong pycnocline at the base of the mixed layer. The effect of this stretching and squashing increases with increasing mode number. It should be noted that these basis functions, or vertical modes, describe structures that are not unique to quasi-geostrophic motions, but also are useful in describing the vertical structure of internal

tides and gravity waves. These waves, however, have frequencies higher than the Coriolis frequency and generally smaller amplitudes than quasi-geostrophic motions.

4.4.4 Quasi-Geostrophic Potential Vorticity

Section 34.4 derives vertical modes following an initial approximation of low Rossby number flow. The momentum, mass conservation, and thermodynamic equations can be written more completely to derive expressions for the zeroth and first order evolution of quasi-geostrophic potential vorticity q. The nonlinear terms absent in section 34.4 are retained such that their magnitudes can be considered, but also because nonlinear interactions are responsible for the transfer of energy across modes. The momentum, mass, and thermodynamic equations are first rewritten in vector form as

$$\frac{D\boldsymbol{u}}{Dt} + f \times \boldsymbol{u} = -\frac{1}{\rho_0}\nabla_h p' \tag{87}$$

$$\frac{1}{\rho_0}\frac{\partial p'}{\partial z} = \frac{g\rho'}{\rho_0} \tag{88}$$

$$\nabla \cdot \rho_0 \boldsymbol{v} = 0 \tag{89}$$

$$\frac{D}{Dt}\frac{g\rho'}{\rho_0} + N^2 w = 0 \tag{90}$$

where here ρ_0 is again a reference density, ∇_h denotes horizontal derivatives, $f = f_0 + \beta y$, the material derivative $\frac{D}{Dt} = \frac{\partial}{\partial t} + \boldsymbol{u} \cdot \nabla$, $\boldsymbol{u}$ is the two dimensional horizontal velocity $\boldsymbol{u}(u, v)$, $\boldsymbol{v}$ is the three dimensional velocity $\boldsymbol{v}(u, v, w)$, and $N^2 = N^2(z)$. Following §5.4 Vallis [2013], these equations are non-dimensionalized by the horizontal length scale L, vertical scale H, horizontal velocity scale U, advective time scale L/U, vertical velocity scale UH/L, Coriolis parameter scale f_0, pressure scale f_0UL, and density anomaly scale f_0UL/H such that,

$$Ro\left(\frac{D\widehat{\boldsymbol{u}}}{D\widehat{t}}\right) + \widehat{f} \times \widehat{\boldsymbol{u}} = -\frac{1}{\rho_0}\nabla_h \widehat{p'} \tag{91}$$

$$\frac{1}{\rho_0}\frac{\partial \widehat{p'}}{\partial \widehat{z}} = \frac{g}{\rho_0}\widehat{\rho'} \tag{92}$$

$$\nabla \cdot \widehat{\boldsymbol{v}} = 0 \tag{93}$$

$$Ro\left(\frac{D}{D\widehat{t}}\frac{g\widehat{\rho'}}{\rho_0}\right) + \left(\frac{L_d}{L}\right)^2 \widehat{w} = 0 \tag{94}$$

where the hat denotes the non-dimensionalized variable, Ro $= U/f_0 L$, and $\widehat{f} = \widehat{f_0} + Ro\widehat{\beta}\widehat{y}$. For low Rossby number flows, this normalization reveals geostrophic balance as the dominant term in the momentum balance. Reintroduction of the deformation radius $L_d = NH/f_0$ is useful in showing the validity of the system for flows with length scales not significantly larger than L.

An asymptotic expansion (i.e. $\widehat{u} = \widehat{u_0} + Ro\widehat{u_1}$) of each variable $(\widehat{u}, \widehat{p'}, \widehat{\rho'})$ is then substituted into the set of equations to derive zeroth and first order balances. As expected, this reveals the lowest order momentum balance to be geostrophic with horiozntal divergence equal to zero. One implication of this balance is that to lowest order vertical velocity is time independent (the Taylor Proudman effect). Dynamics describing the evolution of the flow are evident in the first order, or perturbation, equations;

$$\frac{D\widehat{\boldsymbol{u_0}}}{D\widehat{t}} + \widehat{\beta}\widehat{y}\boldsymbol{k} \times \boldsymbol{u_0} + \widehat{f} \times \widehat{\boldsymbol{u_1}} = -\frac{1}{\rho_b}\nabla_h \widehat{p_1'} \tag{95}$$

$$\nabla_h \widehat{\boldsymbol{u_1}} + \frac{\partial}{\partial \widehat{z}}\widehat{w_1} = 0 \tag{96}$$

$$\frac{D}{D\widehat{t}}\frac{g\widehat{\rho_0'}}{\rho_b} + \left(\frac{L_d}{L}\right)^2 \widehat{w_1} = 0 \tag{97}$$

Potential vorticity is derived by cross-differentiating the momentum equation followed by substitution of mass conservation and thermodynamic equations such that,

$$\frac{\partial \widehat{\zeta_0}}{\partial \widehat{t}} + (\widehat{\boldsymbol{u_0}} \cdot \nabla)\widehat{\zeta_0} + \widehat{v_0}\widehat{\beta} = -\widehat{f_0}\nabla_h \cdot \widehat{\boldsymbol{u_1}} = -\widehat{f_0}\frac{\partial}{\partial \widehat{z}}\widehat{w_1} = -\widehat{f_0}\frac{\partial}{\partial \widehat{z}}\left(\frac{D}{D\widehat{t}}\frac{g}{\rho_b}\left(\frac{L}{L_d}\right)^2 \widehat{\rho_0'}\right). \tag{98}$$

Collecting terms and expressing all as a function of a single material derivative, this simplifies to

$$\frac{D}{D\widehat{t}}\left(\widehat{\zeta_0}^2 + \widehat{f} + \frac{\widehat{f}_0 g}{\rho_b}\frac{\partial}{\partial\widehat{z}}\left(\left(\frac{L}{L_d}\right)^2\widehat{\rho_0'}\right)\right) = 0. \tag{99}$$

Additional substitution of the following relationships: hydrostatic balance ($g\widehat{\rho_0'} = \frac{\partial\widehat{p_0'}}{\partial\widehat{z}}$), definition of the stream function ($\widehat{u_0} = \frac{\partial\widehat{\psi}}{\partial\widehat{y}}$, $\widehat{v_0} = \frac{\partial\widehat{\psi}}{\partial\widehat{x}}$), and the expression for geostrophic balance in terms of the stream function $\widehat{p_0'}/\rho_b = \widehat{f_0}\widehat{\boldsymbol{\psi}}$ permits the evolution of potential vorticity q (terms inside the parentheses) to be expressed a function of one variable, the geostrophic (lowest order) streamfunction. Dimensionalizing this expresion yields,

$$\frac{Dq}{Dt} = 0 \tag{100}$$

where

$$q(x,y,z,t) = \nabla_h^2\psi + f + \frac{\partial}{\partial z}\left(\frac{f_0^2}{N^2}\frac{\partial\psi}{\partial z}\right). \tag{101}$$

Derivation of the quasi-geostrophic potential vorticity in this manner first reveals the lowest order balance to be geostrophic, but shows both time dependence and non-linear advection terms to be important regarding eddy-eddy interactions. Normal vertical modes, derived in section 3a (equations 64, 65), can be obtained by linearizing Eq. 101 about a state of rest, and introducing a wave solution with separable horizontal and vertical strucure (just as in Eq. 40).

Expansion of the material derivative (Eq. 100) [Hua and Haidvogel, 1986] permits consideration of the contribution of the planetary vorticity gradient and two types of nonlinear interactions,

$$\frac{\partial}{\partial t}\left(\nabla_h^2\psi + \frac{\partial}{\partial z}\left(\frac{f_0^2}{N^2}\frac{\partial\psi}{\partial z}\right)\right) + \beta\frac{\partial\psi}{\partial x} + J\left(\psi, \left[\nabla_h^2\psi + \frac{\partial}{\partial z}\left(\frac{f_0^2}{N^2}\frac{\partial\psi}{\partial z}\right)\right]\right) = 0 \tag{102}$$

where $J(a,b) = a_x b_y - a_y b_x$. These nonlinear interactions represent the horizontal advection of relative vorticity and advection of buoyancy associated with vertical structure. While derivation of normal modes ignores these nonlinear contributions to potential vorticity evolution, they are necessary for energy transfer across both horizontal and vertical (modal) scales.

The evolution equation for eddy potential vorticity, q, is isomorphic to one describing the evolution of an ideal tracer C', where both quantities are Lagrangian tags advected by the flow [Smith and Ferarri, 2009]. The advection of an ideal tracer, including an dissipation operator D_C, satisfies

$$\frac{\partial C'}{\partial t} + \boldsymbol{u} \cdot \nabla C' = D_C. \tag{103}$$

where both the background and eddy velocity field stir and advect tracer anomalies away from their sites of injection. The wavenumber spectra of both eddy potential vorticity variance, potential enstrophy, and ideal tracer variance are predicted to be, in each dimension, proportional to the respective wavenumber raised to the negative one power [Kraichnan, 1967, Smith and Ferarri, 2009]. This follows predictions of the spectral flux of potential enstrophy from larger to smaller scales.

4.5 Glider Isopycnal Vertical Displacement and Geostrophic Velocity Profiles

For each mission, glider profiling patterns were selected to repeatedly sample the same region while permitting the estimation of cross-track geostrophic velocity profiles. Each segment of a bowtie or box pattern comprises two to four dive-climb cycles completed while the glider roughly maintained a course of constant heading. Consideration of successive profiles along each bowtie or box segment then permits estimation of an along-track density gradient. For example, at station BATS the bowtie pattern was aligned such that cross-track velocity estimates could be made in the direction of and perpendicular to a southwestward mean flow aligning with topographic contours of the Bermuda rise (Fig. 4.2). We first summarize methods for estimating eddy vertical isopycnal displacement and cross-track geostrophic velocity, both of which are described in more detail in Steinberg and Eriksen, *in press*. Methods for projecting modes derived in the previous section are then presented along with the estimation of the partitioning of total mechanical energy by mode number.

4.5.1 Isopycnal Vertical Displacement

Displacement profiles $\xi(z)$ are initially computed using four different methods to explore the effect of method choice on displacement structure and magnitude. Each method requires a local and temporal mean background

density profile defined as the average of multiple profiles completed within a certain radius over a specified time interval. Isopycnal vertical displacements about this time mean profile are interpreted as the combined influence of internal gravity waves, tides, and quasi-geostrophic eddies. While these processes can be easily distinguished by their characteristic frequencies, with internal waves and tides having time scales shorter than the inverse Coriolis frequency, displacement estimates calculated from individual glider slant-profiles made over a multi-hour period alias these higher frequency signals.

To address this issue, we take advantage of glider slow profiling speeds and estimate isopycnal vertical displacements and horizontal density gradients using four consecutive slant-profiles collected over a multi-day period (Fig. 4.7). At each depth, four absolute salinity and conservative temperature measurements are averaged to derive a single neutral density profile $\gamma^n(z)$. This average, computed from slant-profiles completed over a time period greater than an entire inertial cycle averages out higher frequency isopycnal displacements while retaining quasi-geostrophic eddy displacements that evolve on time scales greater than the three day period over which the four contributing profiles were collected. Displacements ξ(z) are first estimated at each depth as the vertical distance necessary to traverse to find the equivalent density value at height z_i, $\gamma^n(z_i)$, on a long-term time average profile $\overline{\gamma^n}(z)$. A second estimate $\xi_{dz}(z)$ similarly estimates a density anomaly from a four-profile average and γ_b^n(z), but instead of a direct search to compute vertical displacement, divides by a vertical density gradient profile $\frac{\partial\overline{\gamma^n}(z)}{\partial z}$ such that

$$\xi_{dz}(z) = \frac{\gamma^n(z) - \overline{\gamma^n}(z)}{\frac{\partial\overline{\gamma^n}(z)}{\partial z}}. \tag{104}$$

A third displacement estimate $\xi_{\sigma_\theta,dz}(z)$, computes at each height z_i the average potential density from four consecutive profiles $\sigma_\theta(z_i)$ referenced to local the pressure at z_i and computes the density anomaly from a long-term time average potential density value at the same height referenced to the same local pressure $\overline{\sigma_\theta}(z_i)$. The vertical gradient of the background potential density field is derived from local potential density estimates at heights z_i +/- 2δz referenced to pressure at z_i, where δz is the vertical bin thickness.

$$\xi_{\sigma_\theta,dz}(z) = \frac{\sigma_\theta(z) - \overline{\sigma_\theta}(z)}{\frac{\partial\overline{\sigma_\theta}(z)}{\partial z}} \tag{105}$$

A fourth estimate $\xi_{ind}(z)$ considers individual glider temperature and salinity profiles, calculates neutral density, and estimates displacement following the first displacement estimate. Five sample displacement profiles from the BATS 2015 deployment highlight displacement structure variability during the passage of a subsurface intensified eddy as well as differences among displacement profile estimates (Fig. 4.8).

Comparison among these estimates reveals general agreement, with differences greatest in the deepest 1000 m, where the vertical gradient of the background density is weakest. We subsequently use the first method, a direct calculation of vertical distance between the height of $\gamma^n(z_i)$ and the height at which $\overline{\gamma^n}(z) = \gamma^n(z_i)$, to calculate displacement.

4.5.2 Geostrophic Velocity

Geostrophic velocity profiles are similarly estimated from sets of four consecutive temperature and salinity profiles completed while a glider maintained a course of roughly constant compass heading. These four profiles comprise either two dive-climb or climb-dive cycles each completed over an approximate four-day period spanning a horizontal distance of approximately 50 km. As gliders complete dive-climb cycles, small deviations in compass heading, presumed the result of variable depth dependent currents, are ignored.

The method employed to estimate cross-track geostrophic velocity is termed the 'W'/'M' method because consecutive sets of dive-climb (for 'W') or climb-dive (for 'M') cycles, used in estimating along track density gradients, appear as 'W' or 'M' patterns in cross-section (Fig. 4.7). 'W' estimation results in an estimate centered between a pair of dive-climb cycles, whereas 'M' estimates are centered between a pair of climb-dive cycles. For each set of profiles contributing to an 'W'/'M' set, horizontal linear density gradients are estimated at each depth, vertical shear of the cross-track geostrophic velocity computed using thermal wind, vertical shear profiles integrated vertically, and relative velocity profiles referenced to the glider depth average current estimate of contributing dive-cycles. This technique is used to estimate absolute geostrophic velocity profiles for any set of four dive-climb or climb-dive profiles with the requirement that the glider maintains a near-constant heading throughout the profile collection period. Horizontal, along-track, density gradients are related to vertical shear of the cross-track geostrophic velocity $u_g(z)$ as

$$\frac{\partial u_g}{\partial z} = \frac{g}{\rho_0 f_0} \frac{\partial \gamma^n}{\partial x} \tag{106}$$

where x is the along-track horizontal distance. Profiles of vertical shear are integrated and referenced such that their depth average velocity equals the glider inferred mean depth-averaged current experienced during the four-profile collection period. The resulting absolute geostrophic velocity profiles are oriented perpendicular to the direction of glider flight (in the cross-track direction). Depending on piloting choices, the cross-track direction can be aligned zonally or meridionally, or at a heading that is some combination of the two. Each profile is located at the midpoint longitude and latitude of all contributing measurements (Fig. 4.7). More detail describing this framework and velocity profile accuracy can be found in Steinberg and Eriksen, *in press*.

4.5.3 Mode Projections, Empirical Orthogonal Functions, and Energy Spectra

Isopycnal vertical displacement and cross-track geostrophic velocity profiles are projected onto normalized velocity and displacement modes derived in Section 2 (Eqs. 64, 65) to determine mode amplitudes α_m and β_m for each i^{th} profile. This permits eddy vertical structure to be partitioned into contributions from each mode, each scaled by respective spatially and temporally varying amplitudes, as

$$u_i(x,y,z,t), v(x,y,z,t) = \sum_{m=1} \alpha_{mi}(x,y,t) F_m(z). \tag{107}$$

$$\xi_i(x,y,z,t) = \sum_{m=0} \beta_{mi}(x,y,t) G_m(z). \tag{108}$$

Orientation of glider flight patterns and the method of velocity profile estimation geometrically constrain velocity profiles to represent either zonal velocities u, meridional velocities v, or some projection of the two. Glider velocities are subsequently labeled as u for convenience, unless zonal and/or meridional components were directly estimated.

While the normal modes ($F_m(z)$, $G_m(z)$) reflect vertical structures implicit in the linearized quasi-geostrophic potential vorticity equation, eddy vertical structure is likewise considered using empirical orthogonal functions, EOFs [Emery and Thomson, 1998]. These functions do not presume any vertical structure but derive, via diagonalization of covariance matrices, orthogonal functions that reveal dominant vertical patterns of variability and

their temporal evolution. Following a similar procedure as above (Eqs. 107,108), we seek to express displacement and velocity profiles as a summation of orthogonal eigenfunctions ϕ_n, each scaled by a unique amplitude. For a velocity profile time series $U_i(z,t)$, this takes the general form of

$$U_i(z,t) = \sum_{n=0}^{N} a_i(t)\phi_{ni} \tag{109}$$

where eigenfunctions ϕ_n are calculated solving the standard eigenvalue problem

$$A\phi = \lambda\phi. \tag{110}$$

The covariance matrix $A = (U')(U')^T$ is composed of velocity anomalies and λ_n are eigenvalues. EOF amplitudes associated with each velocity profile are then calculated as the vertical integral of each EOF multiplied by the velocity anomaly profile. Comparison between EOF structure and normal mode structure provides opportunity to diagnose the appropriateness of normal modes and their ability to reconstruct observed eddy vertical structure. EOF and mode amplitude comparisons then reveal the temporal evolution of these structures and the temporal changes in mode amplitude contributions to complete eddy vertical structure.

To derive expressions for water column average kinetic energy (KE) and potential energy (PE) only a function of mode amplitudes, displacement and velocity profiles are first projected onto normal modes (Eqs. 108, 107). Presuming little horizontal variability across a glider's sampling pattern, kinetic energy is estimated by vertically integrating the square of each ith geostrophic velocity profile where

$$\frac{1}{H}\int_{-H}^{0} u_i^2(z)dz = \frac{1}{H}\int_{-H}^{0} \sum_{m=1}^{40} \alpha_{mi}F_m(z) \cdot \sum_{n=1}^{40} \alpha_{ni}F_n(z)dz \tag{111}$$

where m, n are again mode number indices and the first 40 modes are considered sufficient to reproduce velocity structure derived from glider measurements. By the orthogonality of the modes, cross terms in the product of sums drop out giving:

$$\frac{1}{H}\int_{-H}^{0} u_i^2(z)dz = \sum_{m=1}^{40} \alpha_{mi}^2 \frac{1}{H}\int_{-H}^{0} F_m^2(z)dz. \tag{112}$$

The result describes the water column average modal partition of kinetic for each profile. Averaging across i profiles, mean kinetic energy as a function of mode number m and mean mode amplitudes $\langle \alpha_m \rangle$ is

$$KE_m = \langle u^2 \rangle = \sum_{m=1}^{40} \left\langle \alpha_m^2 \frac{1}{H} \int_{-H}^{0} F_m^2(z) dz \right\rangle = \sum_{m=1}^{40} \langle \alpha_m^2 \rangle . \tag{113}$$

Because these velocity profiles, describing flow in the direction perpendicular to glider transects, are oriented across a range of compass headings dependent on glider trajectories, the zonal and meridional velocity field is presumed isotropic. Where sampling patterns permit, separate mean zonal and meridional kinetic energy, partitioned into modes, is approximated as

$$KE_m = \frac{1}{2} \langle u^2 + v^2 \rangle = \frac{1}{2} \left(\sum_{m=1}^{40} \left\langle \alpha_{um}^2 \frac{1}{H} \int_{-H}^{0} F_m^2(z) dz \right\rangle + \sum_{m=1}^{40} \left\langle \alpha_{vm}^2 \frac{1}{H} \int_{-H}^{0} F_m^2(z) dz \right\rangle \right) \tag{114}$$

$$KE_m = \frac{1}{2} \left(\sum_{m=1}^{40} \langle \alpha_{um}^2 \rangle + \sum_{m=1}^{40} \langle \alpha_{vm}^2 \rangle \right) . \tag{115}$$

where subscripts $_{um}$ and $_{vm}$ refer to zonal and meridional mode amplitudes. Estimates of isopycnal vertical displacement are used to determine the partition of potential energy across modes. Using the relationship between the vertical structure of horizontal velocity $F(z)$ and isopycnal vertical displacement $G(z)$, water column average potential energy for the first 40 modes can be written as

$$PE_m = \left\langle \frac{1}{2H} \int_{-H}^{0} \xi_i^2(z) N^2(z) dz \right\rangle = \frac{1}{2H} \sum_{m=0}^{40} \left\langle \beta_m^2 \int_{-H}^{0} F_m^2(z) c_m^2 dz \right\rangle = \frac{1}{2} \sum_{m=0}^{40} \langle \beta_m^2 c_m^2 \rangle , \tag{116}$$

where c_m is again the mode Kelvin wave speed. Exploring geographic and seasonal variability of the partitioning of kinetic and potential energy across modes informs on the mechanisms controlling this relative partitioning and energy pathways towards dissipation.

Sea level anomalies and their associated surface velocities reflect a combined, but unequal surface projection of interior motions. A free surface boundary condition permits non-zero surface displacement amplitudes that decrease rapidly in magnitude with increasing mode number. Velocity modes, however, have non-zero surface values which are dependent upon upper ocean density structure. While higher velocity modes themselves can have

large near surface values relative to interior values, the kinetic energy concentrated in these modes is often quite small. Surface kinetic energy is then generally dominated by energy in the barotropic and first baroclinic modes, but the relative modal partition of surface kinetic energy among higher modes reflects the combined effect of large high mode surface values, but relatively low contribution to total surface kinetic energy. Wunsch [1997] shows a time mean modal partition of kinetic energy can be estimated at any depth z_i as

$$\overline{KE}(z_i) = \frac{1}{L}\sum_{t=1}^{L}\left(\frac{1}{2}\left(u^2(z_i,t)+v^2(z_i,t)\right)\right) \tag{117}$$

$$\overline{KE}_m(z_i) = \frac{1}{2L}\sum_{t=1}^{L}\left(\left(\sum_{m=1}^{40}\alpha_{um}(t)F_m(z_i)\right)^2+\left(\sum_{m=1}^{40}\alpha_{vm}(t)F_m(z)\right)^2\right). \tag{118}$$

where t is the index of a time series of length L and mode amplitude subscripts $_{um}$, $_{vm}$ represent time varying zonal and meridional mode amplitudes. If it is assumed that mode amplitude coefficients are not correlated in time (i.e. $\langle\alpha_{un}\alpha'_{un}\rangle = 0$), the square can be distributed as

$$\overline{KE}(z_i) = \frac{1}{2L}\sum_{t=1}^{L}\left(\sum_{m=1}^{40}\alpha_{um}^2(t)F_m^2(z_i)+\sum_{m=1}^{40}\alpha_{vm}^2(t)F_m^2(z)\right). \tag{119}$$

This is an expression for kinetic energy at any depth and while the magnitude of kinetic energy in each mode is arbitrary, the percentage in each mode suggests which modes dominantly project onto the surface. The degree to which equations 118 and 119 are equal reflects the degree to which mode amplitudes are correlated in time. Both estimates are calculated and where within a factor of one or two, validate the estimates of surface kinetic energy from Eq. 119. Where glider sampling patterns permit a single estimate of geostrophic velocity, surface kinetic energy is estimated as

$$\overline{KE}_m(z=0) = \frac{1}{L}\sum_{t=1}^{L}\left(\sum_{m=1}^{40}\alpha_{uv}^2(t)F_m^2(z=0)\right). \tag{120}$$

The resulting estimates of surface kinetic energy modal partition are dependent in magnitude on mode normalization, but the relative fraction of kinetic energy in each mode reveals which modes contribute significantly to the surface projection.

4.5.4 Inferred Eddy Horizontal Length Scales

This 'W'/'M' velocity estimation technique limits horizontal resolution to tens of kilometers. Four consecutive density profiles used in estimation of along-track density gradients span a horizontal distance of 20 - 50 km, depending on the glide slope and maximum sampling depth, and are completed over a two to four day period. Estimating density gradients from measurements made across these spatial and temporal scales serves to average out motions with frequencies greater than one day, but introduces aliasing that is a function of glider speed, glide slope, the magnitude of eddy horizontal density gradients being sampled, and the speed at which the eddy field is advected (Steinberg and Eriksen, *in press*).

These sampling patterns place a limit on the horizontal resolution of horizontal density gradients. While vertical sampling is highly resolved in space, horizontal density gradient resolution is coarse and estimates are intended to capture mesoscale features evolving on time scales of at least multiple days. Each baroclinic mode is associated with a Rossby deformation radius, decreasing with mode number. At mid-latitudes, the first baroclinic deformation radius $L_{d1} = \sim 40$ km with eddy wavelength $\sim 2\pi L_{d1}$. Mode five is associated with a fifth baroclinic deformation radius L_{d5} of ~ 7 km. While glider vertical resolution is high enough to estimate vertical structure well through at least the tenth baroclinic mode, associated horizontal wavelengths associated with these higher mode density perturbations are much smaller that the horizontal distance covered by two successive glider dive-climb cycles. It is not, however, required that the horizontal scales of motions for a given higher mode vertical density perturbation be at associated deformation radius scales. However, results from model simulations of glider sampling (Steinberg and Eriksen, *in press*) suggest that vertical structures up through at least mode 10 are well resolved by the 'W'/'M' displacement and velocity profile estimation technique. These sampling simulations suggest that for modes 10 and higher, glider potential energy spectra are more energetic and kinetic energy spectra less energetic than model equivalents.

While this framework does not attempt to resolve horizontal eddy structure, consideration of the ratio of kinetic (Eq. 113) to potential (Eq. 116) energy permits inference of mean horizontal eddy length scales for each mode [Vallis, 2013]. This can shown via substitution of $p = p'/\rho_0$ into Eqs. 42, 43, 53 after writing kinetic and potential energy as

$$KE = \frac{1}{2}\overline{(\widehat{u}\widehat{u}^* + \widehat{v}\widehat{v}^*)} \tag{121}$$

$$PE = \frac{1}{2}N^2\overline{\widehat{\xi}\widehat{\xi}^*} \tag{122}$$

where the hat denotes a Fourier transform with respect to time and the * the complex conjugate. We can then write the ratio of the spectra Φ of kinetic and potential energy as

$$\frac{KE}{PE} = \frac{\Phi_{uu} + \Phi_{vv}}{N^2\Phi_{\xi\xi}} \tag{123}$$

with subscripts denoting the spectrum type. These can then be rewritten in terms of reduced pressure for quasi-geostrophic motions. The resulting inferred horizontal eddy length scales are accurate to the extent that frequencies are much lower than f (i.e. in the limit of geostrophic balance). For wavelike solutions kinetic and potential energy follow

$$KE = \frac{1}{2}\frac{k^2 + l^2}{f^2}\Phi_{pp} \tag{124}$$

$$PE = \frac{1}{2N^2}\Phi_{p_z p_z}. \tag{125}$$

Taking the ratio of kinetic to potential energy and using Eq. 50,

$$\frac{KE}{PE} = \frac{\left(k^2 + l^2\right)N^2}{f^2}\frac{\Phi_{pp}}{\Phi_{p_z p_z}} = \frac{\left(k^2 + l^2\right)N^2}{f^2}\frac{F^2}{F_z^2}. \tag{126}$$

Relating the vertical structure of velocity F and F_z to the vertical structure of displacement G, where $F = \frac{\partial G}{\partial z}$, using Eq. 64 this becomes

$$\frac{KE}{PE} = \frac{\left(k^2 + l^2\right)N^2}{f^2}\frac{c^2}{N^2} = \left(k^2 + l^2\right)\frac{c_m^2}{f^2} = \frac{L_{dm}^2}{L_m^2} \tag{127}$$

where c_m is the mode wave speed, L_{dm} is the horizontal length scale associated with mode m (i.e. the mth deformation radius), and L_m is the horizontal eddy length scale. This relationship estimates, based on the relative

partition of kinetic and potential energy, the horizontal eddy length scale compared to the relevant deformation radius. With estimates of depth average kinetic and potential energy in each mode, from the previous section, we can then infer horizontal eddy length scales for each mode. The accuracy of this estimate depends both on the width of the confidence bounds within which we estimate kinetic and potential in each mode, but also the extent to which glider displacement and velocity profiles reflect very low frequency geostrophic motions (i.e. are very low Rossby number). Additionally, this relationship can be expected to break down as mode number increases and associated Rossby deformation radii decrease to length scales shorter than $\sim$ 5 km, or the length scale at which assumptions of quasi-geostorphy break down.

4.6 Results and Discussion: The Partition of Energy Across Vertical Modes

4.6.1 Density Profile Variability and Expectations Regarding Mode-Mode Interactions

Initial comparison among glider observations throughout the North Atlantic as well as with full-depth shipboard density profiles in the North Atlantic and North Pacific centers on background density profile structure. Variability in mean background buoyancy frequency at these sites, between 22°N and 50°N, is largely confined to the upper 1000 m, but vertical mode structure, shaped by this background density structure, is influenced at depths much greater (Fig. 4.9). One approach employed to interpret the effect of varied background density structure on geostrophic turbulence and the transfer of energy across scales is to consider the mode triplet interaction coefficient [Fu and Flierl, 1980, Smith and Vallis, 2001, Zhao et al., 2018].

Of the factors influencing the seasonal and geographic variability of energy partitioning across vertical scales, latitude and background stratification play a significant role. These factors set the horizontal and vertical length scales of eddies, but also regulate the transfer of energy across scales. In a turbulent quasi-geostrophic ocean, eddy-eddy interactions (i.e. eddy merger, destruction, stretching, or eddy advection of other eddies) result in the transfer of energy across vertical modes. The rates or relative ease of transfer, moderated by stratification, can be estimated through calculation of a mode triplet interaction coefficient [Flierl, 1978, Fu and Flierl, 1980, Hua and Haidvogel, 1986, Zhao et al., 2018]. Mode triplet interactions are predicted and derive from the quasi-geostrophic potential vorticity q conservation equation (Eq. 100), rewritten as

$$\frac{\partial}{\partial t}q + J(\psi, q) + \beta\frac{\partial \psi}{\partial x} = forcing + dissipation \tag{128}$$

where ψ is again the geostrophic streamfunction, J the Jacobian operator, and β the meridional gradient of the Coriolis parameter. The second term on the left hand side describes eddy-eddy interactions as the nonlinear advection of potential vorticity. Just as for horizontal velocity (Eq. 107), the geostrophic streamfunction can be expressed generally as a series of vertical modes each scaled by a mode amplitude,

$$\psi(x, y, z, t) = \sum_{m=0}^{N} \Psi_m(x, y, t) F_m(z). \tag{129}$$

and modes $F_m(z)$ satisfy Eq. 65. Conservation of potential vorticity for mode m is formulated substituting Eq. 129 into Eq. 101, then Eq. 128, multiplying by $F_m(z)$, and vertically integrating to obtain

$$\frac{\partial}{\partial t}Q_m + \sum_{i,j} \epsilon_{mij} J\left(\psi_j, Q_k\right) + \beta\frac{\partial}{\partial x}\psi_m = Forcing + Dissipation \tag{130}$$

where

$$Q_m = \int_{-H}^{0} q F_m(z) dz = \left(-k^2 - l^2 - \frac{{f_0}^2}{c_m}\right) \Psi_m. \tag{131}$$

The second term on the left hand side of Eq. 130 describes the nonlinear interactions of modes m, j, k resulting in a transfer of energy across modes. This term is scaled by a triple interaction coefficient ϵ where

$$\epsilon_{mij} = \frac{1}{H}\int_{-H}^{0} F_m(z) F_i(z) F_j(z) dz \tag{132}$$

where m, i, j are mode number indices and ϵ_{mij} is only a function of background stratification. Referencing initial consideration of this term by Flierl [1978], Zhao et al. [2018] re-interpret the second term on the left hand side of Eq. 130 as advection from velocity in the i^{th} mode of potential vorticity in the j^{th} mode resulting in a change in potential vorticity in the m^{th} mode. The interaction coefficient ϵ_{mij} scales this term, thus indicating the relative enhancement or inhibition of energy transfer among modes m, i, and j. Smith and Vallis [2001], using an analytic exponentially decaying background density profile, show that this interaction coefficient increases in magnitude for low baroclinic

mode triplets ($i, j, m = 1 - 3$) with increasing strength of an upper ocean pycnocline. For the same background density profile, mode triplet interaction coefficients involving the barotropic mode do not increase in magnitude. This relative increase among baroclinic mode triplet interaction coefficients corresponds to a relative enhancement of energy transfer among contributing modes and a relative inhibition of transfers to the barotropic mode. The case where $m = i = j$ describes the mode self-interaction, or the relative tendency for energy in a specific mode to remain in that mode. The relative partition of energy across modes can then be interpreted alongside matrices of mode triplet interaction coefficients (Fig. 4.10). As compared to an ocean with constant stratification (Fig. 4.10, left column), as was considered by Charney [1971], mode triplet interactions among baroclinic modes are enhanced for realistic stratification profiles in the Atlantic and Pacific. As one might expect, the self interaction coefficients of modes two and three are enhanced in the summertime, suggesting that a greater fraction of energy might remain in these modes under conditions associated with enhanced upper ocean stratification. Additionally, permanent thermocline structure in the North Atlantic with a region of enhanced stratification at $\sim$ 750 m corresponds to increased mode triplet coefficients for modes greater than one. Interactions among modes two and higher in the Atlantic might be expected to be more significant than the same interactions near Hawaii in the Pacific.

Comparisons of triplet interaction coefficients help quantify an expectation of the relative enhancement or inhibition of energy transfer among barotropic and baroclinic modes. Fig. 4.10 considers coefficient magnitudes for interactions among the barotropic and first three baroclinic modes at each site as well as for an ocean with constant stratification. Compared to the constant N^2 case, surface intensified stratification increases mode one self interaction at all sites, the same result as Smith and Vallis [2001]. Of the sites considered, station ALOHA (Fig. 4.10, column 2) has the largest value for $m = i = j = 1$, suggesting it to be a site with a dominant fraction of energy in mode one. Station PAPA (Fig. 4.10, column 3) has the largest value for $m = i = j = 2$, suggesting that the background stratification at this site has greater vertical structure. A significant difference is also apparent between the interactions of mode 3 with modes 1, 2, and 3 in the North Atlantic summer vs. winter. At station BATS, 36°N, and the LDE site, the self interaction coefficient of mode 3, as well as the interaction coefficients between mode 3 and modes 1 and 2 all increase by a factor of two or more in the summer. These seasonal changes are evident in Figure 4.10 comparing winter values (columns 5, 7, row 3) and summer values (columns 6, 8, 9, row

3). Darker shades of red and orange correspond to larger interaction coefficients, or enhanced triplet interactions. This suggests that mode triplet interactions vary seasonally and that in the summertime one might expect a greater fraction of energy to remain in higher modes than in the winter.

The retention of energy and increased interaction among modes one, two, and three in the summertime likewise implies a relatively reduced rate of barotropization, a result discussed by Smith and Vallis [2001] as in support of observations of a peak in mesoscale eddy energy near mode one [Smith and Ferarri, 2009]. Without this relative inhibition of barotropization, one might expect higher mode baroclinic energy input to the eddy field at deformation radius scales to quickly barotropize and a peak in the energy spectrum to be observed at scales much larger than first deformation radii.

4.6.2 Temperature Variance in the western North Atlantic

Because the evolution of both an ideal tracer and quasi-geostrophic potential vorticity are isomorphic (have the same general form), we can explore the vertical structure of along-isopycnal and along-isobar temperature variance to reveal patterns of variability at each Deepglider mission site detailing characteristics of eddy stirring. Consideration of temperature anomaly profiles serves as a good initial analysis of vertical structure because profiles require minimal processing and do not presume the dominance of specific dynamics. Additionally, interior along-isopycnal temperature and salinity anomalies reveal spatial and temporal patterns of buoyancy anomaly injection, presumably at sites far away from glider sampling sites, as well as the vertical structure of along-isopycnal stirring.

Time series of along-isopycnal temperature anomalies at sites LDE, BATS, and 36°N, reveal markedly different vertical structure and variability (Figs. 4.11, 4.12, 4.13). At the LDE site, away from the Gulf Stream and bathymetry associated with the Bermuda Rise, anomalies are largest in magnitude in the upper 150 m. Between 250 m and 2500 m, anomalies are fairly coherent in the vertical and vary on multi-week time scales. Glider following sea level anomalies and densities at 1000 m simultaneously identify the evolution, on monthly time scales of, of QG flows responsbile for the stirring of these along-isopycnal temperature anomalies (Fig. 4.11). These patterns at the LDe site serve as a baseline from which we note differences in anomaly magnitude and structure at sites BATS and 36°N.

Temperature anomalies at station BATS (Fig. 4.12) are relatively larger in magnitude at depth and display more uniform vertical structure extending to the seafloor. The vertical extent of a single subsurface intensified cold, fresh lens, sampled multiple times in late April early May 2015, extends from 1000 m to 2000 m. Anomalies with this depth band identify it is a layer of high variance. While we do not identify the source of this elevated variance, the proximity of the BATS site to steeper and rougher topography, as compared to the LDE and 36°N sites, suggest the Bermuda rise may play a role. At 36°N, comparatively lower frequency variability is observed with anomalies throughout much of the water column switch from positive to negative in late December 2019 (Fig. 4.13). We again observe increased variance between 1000 m and 2000 m.

Comparison of these sites reveals along-isopycnal temperature anomaly variability both geographically (comparisons across sites) and in time (comparison between BATS 2014 and 2015) (Fig. 4.14). Variances are calculated for each density surface using the time series of anomaly measurements spanning the duration of each mission. The vertical structures of these profiles all display a relatively deep, between 1000 m and 2000 m, high variance layer associated with both Mediterranean Outflow Water and Labrador Sea Water [Lozier and Iorga, 1999, Lozier and Stewart, 2008]. A climatological zonal transect in the North Atlantic along 36°N from the World Ocean Circulation Experimement (not shown), reveals the tongue of Mediterranean water at this depth that is stirred into the interior by QG flows resulting in increased temperature variance among these layers. Also within this depth range and density class are cold fresh waters from the Labrador Sea. Pathways taken by Labrador Sea water into the North Atlantic generally align with deep western boundary current pathways, but complex topography channels some component of this flow into the interior [Bower et al., 2013].

At station BATS in both 2014 and 2015, subsurface cold fresh anomalies were observed coincident with elevated geostrophic velocities, suggesting the presence of subsurface intensified coherent vortices from the Labrador Sea (Fig. 4.15). The vertical structure of geostrophic velocity and isopycnal vertical displacement profiles of these eddies identify core depths greater than 1000m and isopycnal vertical displacements extending from the surface to the seafloor. These features are markedly different from characteristic 'meddy' waters and also the features identified by Prater and Rossby [1999] reinterpreting observations of temperature and salinity anomalies in the western North Atlantic as originating near the Labrador Sea. The observed temperature and salinity anomalies

appear most similar to those observed by Bower et al. [2013], who identified and tracked coherent vortices from formation at the edge of southwestern edge of the Labrador Sea into the Subtropical North Atlantic and southwards to a latitude nearly equal to that of station BATS. Observations of these features in both 2014 and 2015 at the same location suggests a high frequency of occurrence and importance with respect to their role in the transport of tracers and energy.

Another notable feature across Deepglider mission sites is the variability in the magnitude of temperature variance throughout the bottom 2000 m. At 36°N, 36.5°N, and BATS in 2015, variance between $\sim$ 2500 m and the seafloor is over an order of magnitude greater than variance at the LDE site and BATS 2014 (Fig. 4.14). These differences suggest the importance of both inter-annual and geographic variability in along-isopycnal temperature variance reflective of variable eddy activity which stirs these gradients, but also variability in the injection of these anomalies.

Predictions for the spectrum of tracer variance follow those for the cascade of potential enstrophy (Section 3e). Temperature anomaly profiles are then projected onto velocity modes to determine mode amplitudes (Eq. 107) following Smith and Ferarri [2009], who recognize the isomorphism between potential enstrophy and tracer variance evolution equations, where potential enstrophy is expressed in terms of the streamfunction and thus velocity. Predictions of a spectral slope with a negative one wavenumber dependence, a relatively shallow slope, suggest a richness in compensating temperature and salinity variance at high wavenumber that is absent in density anomaly variance associated with geostrophic turbulence [Smith and Ferarri, 2009]. Across the three Deepglider sites sampled most intensively (LDE, BATS, and 36°N) temperature variance spectra are relatively flat with a slope not significantly different than negative one (Fig. 4.16). Consistent with elevated temperature variance at both 36°N and BATS in 2015, spectra reveal a larger fraction of variance to be contained in higher modes at these sites during the sampling periods.

4.6.3 Global Comparisons of Potential Energy Spectra

Displacement profiles at each hydrographic station were computed relative to seasonal background density profiles and displacement modes $G_m(z)$ were projected onto each profile to obtain mode amplitudes (Eq. 108). Mean

potential energy as a function of mode number was then estimated (Eq. 116) and power spectra averaged at each station across the time series to obtain a single estimate of the average modal partitioning of potential energy.

Comparisons of the modal partitioning of mean potential energy at stations BATS, PAPA, and ALOHA demonstrate the BATS site as the most energetic at low modes as well as having the steepest spectral slope (Fig. 4.17). The three spectra converge at approximately mode 20, are roughly equally energetic through mode 60, and maintain a spectral slope steeper than k^{-2} between modes 11 and 60. Empirically derived internal wave potential energy spectra of Garrett and Munk [1979] intersect each site's spectrum at approximately mode 30, implying that at lower modes, isopycnal vertical displacements are greater than would be expected by internal gravity waves alone. This displacement variance identifies the passage of quasi-geostrophic eddies. Vertical scales and deformation radii decrease with increasing mode number such that at modes 20 and higher horizontal scales are less than $\sim$ 5 km. Motions at these comparatively small scales may reflect internal waves and nonlinear dynamics such that assumptions of quasi-geostrophy employed to analyze eddy vertical structure become inadequate. Among low modes, however, comparison among stations shows BATS to be the most energetic due to its proximity to the Gulf Stream, followed by stations ALOHA and PAPA. Across all modes, the spectrum at station PAPA, a site in the North Eastern Pacific associated with little quasi-geostrophic eddy energy, is closest to the predicted Garrett and Munk [1979] internal wave spectrum in both magnitude and slope.

4.6.4 BATS Station Deployment 2015

Between February and November of 2015, Deepglider sg035 completed 175 dive-climb cycles along a repeat bow-tie pattern centered at station BATS (Fig 4.2). Completion of each bow-tie pattern took approximately two weeks. The depths of four neutral surfaces (γ^n =26.5, 27.25, 27.75, and 28.05) over a nine month period reveal displacement variability at a range of frequencies and identify the passage of an individual subsurface intensified coherent vortex passing through the sampling domain in April-May 2015 (Fig. 4.18). The depths of these isopycnals in time, determined from individual slant-profiles as well as four consecutive profile averages, reveal that eddy isopycnal displacements at depths greater than 2000 m regularly exceed 100 m.

The first 40 flat-bottom, free surface displacement and velocity modes are projected on glider displacement

and velocity profiles to determine the partitioning of eddy vertical structure across modes. EOFs independently identify dominant patterns in displacement and velocity profile structure. The first three velocity EOFs together explain over 95% of velocity profile variance (Fig. 4.19) and initial visual comparison between these EOFs and the first three flat-bottom, free surface velocity modes (Fig. 4.6a,c) reveals marked similarities. While the first EOF decays with depth, it remains non-zero at $\sim$ 4200 m. Interpretation of this structure, along with the shape and magnitude of the second EOF, lends support to the hypothesis that the principle velocity structure represents some combination of barotropic plus first baroclinic flat-bottom velocity mode structures. The third velocity EOF describes a small fraction of velocity profile variance, but bears resemblance to the second flat-bottom baroclinic mode (with maxima/minima at the surface, $\sim$ 1000 m, and at the seafloor). Furthermore, high temporal correlation between the first *displacement* EOF amplitude and flat-bottom first baroclinic mode amplitude suggests that the free-slip bottom boundary condition for horiozntal velocity is physically relevant (Fig. 4.20). This hypothesis is supported by high temporal correlation between isopycnal vertical displacement at the depth of flat-bottom displacement mode one maximum amplitude and glider-following sea level anomaly.

Consideration of individual velocity profiles reveals a majority to have zero-crossings at depths in the upper 1500 m, within a few hundred meters of the depth of the zero crossing of the first baroclinic flat-bottom velocity mode (Fig. 4.21). The depth of the first zero crossing of the first baroclinic sloping-bottom mode, however, increases in depth with increasing bathymetric slope. At station BATS this depth is much greater than 2000 m. These results, similarities between the first velocity EOF and flat-bottom velocity mode structures as well as the depths of velocity profile zero crossings suggest that flat-bottom modes appropriately describe velocity profile structure. Additionally, velocity profiles with no zero crossing do not decay with with depth, but rather asymptotically to nearly constant non-zero values with mean current speeds at depths greater than 4000 m order 0.05 m s^{-1}. These observed velocity structures can be explained as a barotropic offset to the first baroclinic flat-bottom mode and suggest a phase locking between the modes.

It is important to note the concern of Wunsch [1997] regarding the interpretation of the first velocity EOF as a linear combination of the barotropic and first baroclinic mode, where this combination could then serve as evidence of modal coupling. The author demonstrates that uncorrelated barotropic and baroclinic modes may

appear correlated in EOF structure. Wunsch [1997] additionally notes that modes may not be orthogonal after vertical integration of samples with coarse vertical resolution, whereas EOFs are by design. Our interpretation of EOF structure, with the aid of over an order of magnitude greater vertical resolution, focuses on non-zero near-bottom amplitudes rather than the specifics of dynamical mode coupling. de La Lama et al. [2016] and LaCasce [2017] suggest that deep velocities, like those observed here, can be described by bottom trapped topographic waves that in the limit of a flat bottom become the barotropic mode. The analysis framework employed here does not consider the alignment of topographic features nor attempt to resolve topographic waves, but to the extent that a flat-bottom approximation is satisfactory in these glider sampling regions, flat bottom modes appear appropriate and useful in detailing the vertical structure of geostrophic turbulence.

Displacement and velocity mode amplitudes can be calculated with respect to seasonally varying background density profiles. Two background density profiles, representing winter and summer conditions, can be used to calculate the mean buoyancy frequency and mode structure. While seasonal stratification changes occur mainly in the upper 300m, higher mode ($m >= 3$) structure throughout the entire water column is noticeably altered between winter and late summer (not shown). Changing with seasonality in near-surface stratification, baroclinic mode three and higher maxima and minima are shifted towards the surface in summertime and deeper in the winter (by as much as $\sim$ 400 m). Despite this seasonal vertical shifting of mode maxima and minima towards the surface or seafloor, the fraction of energy contained in these higher modes is less than 10%. Among the barotropic and first three baroclinic modes, the partitioning of potential energy across modes varies between winter and summer both in eddy energy and the relative partition across modes (Table 1, Fig. 4.22). Aside from a decrease in barotropic energy and increase in the fraction of kinetic energy in baroclinic modes one through three in summer, the spectral slope at higher modes does not change significantly. Displacement and velocity profiles contributing to mean winter spectra were completed between February and April, while late-summer spectra were completed between September and November. These time bounds were selected to exclude the passage of the individual eddy, but also to highlight seasonal differences that would be otherwise absent if including profiles from transition periods.

Compared to summertime values, both wintertime mean kinetic and potential energy are elevated in modes one through four with a spectral slope at modes greater than two steeper than k^{-2}. This pattern is consistent with a

late summer decrease in satellite derived surface eddy kinetic energy in 2015 (not shown) and with observations from Callies and Ferarri [2013], showing a wintertime increase in upper ocean available potential and eddy kinetic energy. Mean displacement amplitude for mode one is less energetic in the late summer than in the winter by a factor of two to three (Fig. 4.22). This is coincident with a greater fraction of potential energy in modes two through six. In winter, a greater percentage of kinetic energy is observed in the barotropic mode, while in summmer, energy in the first baroclinic mode exceeds barotropic energy levels. Across higher modes, spectra maintain a seasonally independent slope of $\sim k^{-3}$.

The first eight mean mode displacement amplitudes associated with the individual subsurface intensified coherent vortex are roughly an order of magnitude greater than nominal values while velocity mode amplitudes are also elevated (Fig. 4.22). This identifies the eddy observed in 2015 as containing a significant potential energy anomaly. Displacement and velocity profiles completed within this feature, show eddy structure extends to the seafloor. These observations implicate bottom friction to be a relevant source of kinetic energy dissipation.

4.6.5 BATS Station Deployment 2014

Deployed from Bermuda to occupy station BATS in 2014, sg035 had primary objectives of demonstrating Deep-glider capabilities, reliability, and measurement accuracy completing slant-profiles concurrently with shipboard instruments. This two and a half month deployment resulted in the collection of 42 displacement and geostrophic velocity profiles. As in 2015, a subsurface intensified eddy with a core depth greater than 1000 m was identified, sampled in 9 of the 42 displacement and velocity profiles, revealing full depth eddy displacement and velocity structure extending to the seafloor (Fig. 4.23). The vertical structure of this feature's geostrophic velocity field, with highest speeds at $\sim$ 1300 m, can be explained as a combination of barotropic and second baroclinic mode structure. Peak speeds approach 0.2 m s^{-1} and decay with depth to $\sim$ 0.05 m s^{-1} at the seafloor. Similarly, a dominant fraction of the eddy potential energy is contained in the second baroclinic mode (not shown). One difference observed in this feature, as compared to the 2015 eddy, is the lack of a surface density anomaly or strong surface velocities. Isopycnal vertical displacements (Fig. 4.23) below the core depth approach 200 m in ampltiude and decay with increasing to an average amplitude of $\sim$ 100 m at the seafloor again suggesting a relevant role of

bottom friction in eddy decay. The first three EOFs of non-eddy geostrophic velocity profiles are similar to those from the 2015 deployment. The first EOF, describing over three quarters of the variance, decays with depth, but to a near constant non-zero value. The second EOF has similar structure to the first with an offset while the third again resembles the second flat-bottom baroclinic displacement mode.

4.6.6 ABACO 26.5°N Deployment 2017

Displacement and velocity profiles estimated from measurements along the western end of the RAPID array at 26°N reveal both intensified surface and deep meridional velocities and enhanced isopycnal vertical displacement between 2000 and 4000 m. These varied structures, different from station BATS, reflect sampling in a western boundary current system. Northward surface flows join with waters moving through the Florida Strait to become the Gulf Stream while deep velocities highlight the deep western boundary current southward return flow. Along the repeatedly profiled zonal transect, Deepgliders sampled mean flows at the western end and a turbulent eddy field at the eastern end, like that observed at station BATS and the LDE site. Compared to profiles from station BATS, geostrophic velocities are generally greater in magnitude throughout the water column (Fig. 4.24). Velocities at depths greater than 4000 m regularly exceeded 0.1 m s^{-1} while surface velocities approached 0.5 m s^{-1}. The first and second EOFs of velocity profiles again suggest some combination of barotropic and first baroclinic flat bottom modes. As an independent comparison, full-depth lowered ADCP profiles collected along the western end of the RAPID array during these glider missions were analyzed in the same fashion. Profiles and EOFs from these data compare favorably with those derived from glider observations. The first lowered-ADCP EOF appears more barotropic than the glider equivalent while EOFs two and three are similar to first and second flat-bottom baroclinic velocity modes. While the assumptions employed to derive normal modes (i.e. no mean flow and horizontal isotropy) are more likely violated near the western boundary current, these full depth profiles reveal varied vertical structure and significant kinetic energy throughout the water column.

4.6.7 36°N 2018

Deepglider sg041, deployed from Bermuda to sample along the southern flank of the Gulf Stream Extension amidst eddy activity, collected profiles though the winter of 2018 into 2019. Displacement profiles reveal order 100 m

departures from a mean background density profile throughout the water column. Depth-averaged velocities consistently to the southwest align with AVISO surface velocities of ten of centimeters per second and are suggestive of the return 'eddying' circulation of the North Atlantic subtropical gyre. Compared to station BATS, surface and deep velocities are stronger, regularly exceeding 0.15 m s^{-1} at depths greater than 2000 m (Fig. 4.25). While velocity profile EOFs across all mission sites generally decay with depth, at 36°N first and second EOF amplitudes between 2000 m and seafloor are the largest. This is the result of velocity profiles reporting speeds exceeding 0.10 m s^{-1} between 2000 m and the seafloor. A single displacement profile of a Gulf Stream Ring (Fig. 4.25, purple curve) reveals full depth structure with maximum displacements exceeding 200 m in the upper 1000 m decaying to $\sim$ 100 m near the seafloor.

4.6.8 36°N 2019

Velocity profiles from Deepglider sg045, deployed from Bermuda in early summer 2019 to continue occupation of the same site as sg041 over the previous winter, similarly report speeds of well over 0.1 m s^{-1} at depths greater than 2000 m. Because of the sampling pattern geometry, velocity profiles can be separated in zonal and meridional groups and separate EOFs computed to test the assumption of horizontal isotropy. EOFs of zonal and meridional velocities again reflect a combination of barotropic and first baroclinic modes decaying to non-zero values. One noted difference between zonal and meridional EOF structure is the 96% fraction of variance explained by the first EOF of meridional velocity. This structure again decays with depth to a near constant non-zero value and can be imagined as a barotropic offset to the first flat-bottom baroclinic mode (Fig. 4.26). The first two zonal velocity EOFs appear as the normal first and second baroclinic modes followed by a third EOF, describing almost 20% of velocity profile variance, that appears near barotropic. This set of zonal velocity EOFs is unique compared to the meridional velocity set, but also when compared to other sampling sites, in that the first two EOFs appear as normal baroclinic modes with no barotropic offset and the third EOF, describing a much more significant fraction of the variance, is near barotropic. This suggests a lack of horizontal isotropy of the geostrophic velocity field, but may be expected due to the proximity to the east-bound Gulf Stream and west-bound return circulation.

While these measurements were only collected over only a two-month period, they are more energetic than

those from the winter 2018-2019 sampling by sg041 at the same site. Surface eddy kinetic energy maps at the same site from altimetric observations similarly show a more energetic eddy field at this site in the summer than throughout the previous winter. This result contradicts a general result from Qui et al. [2014] that late winter is more energetic at the mesoscale than in the summer. This may be at least partly explained however, by proximity to the Gulf Stream and the non-seasonal generation of Gulf Stream Rings that were sampled.

4.6.9 LDE Site Deployment 2019

Isopycnal vertical displacement and geostrophic velocity profiles (Fig. 4.27) estimated from measurements at this site reflect low mode, slowly evolving quasi-geostrophic features to a greater extent than the other sampling sites (Fig. 4.28). This site was selected to observe the QG eddy field well within the 'eddy' re-circulation of the North Atlantic, but also to overlap with the region originally sampled multiple decades ago first revealing the richness in mesoscale eddy structure [McWilliams, 1989]. The sampling domain occupies a relatively flat region, with a mean slope of $\sim$ 100 m / 100 km, and is hundreds of kilometers removed from the Gulf Stream and prominent or rough bathymetric features. Away from regions generally associated with various types of instability and away from rough topography, eddy activity at this site may best reflect equilibrium QG dynamics. These factors also arguably make the use of flat-bottom modes most appropriate, as compared to the other sampling sites.

Principle EOFs of zonal and meridional velocity reflect first and second baroclinic mode structures with barotropic offsets. Glider following sea level anomaly, the depth of an neutral surface in the permanent pycnocline, the first displacement EOF amplitude, and the first displacement mode amplitude all correlate at absolute values greater than 0.8. With a decorrelation time scale of approximately one month, this time series reveals the slow evolution of the eddy field in the absence of individual coherent vortices sampled at station BATS at at 36°N.

At the LDE site, the mean horizontal length scale associated with the first baroclinic mode, estimated from the ratio between mean potential and kinetic energies in the first mode (Eq. 127) (Fig. 4.29), is larger than at any other Deepglider mission site, roughly twice as large as the first deformation radius (PE $\sim 4\times$KE for mode 1). In terms of quasi-geostrophic turbulence theory, this can be explained as the result of the inverse cascade of energy presumably released at first deformation radius scales or smaller. This is also the case for all higher modes. Mean

potential energy in each mode exceeds kinetic energy by roughly a factor of four, whereas Charney [1971] predicted an equal partition of energy between potential and each component of kinetic energy.

The first two velocity EOFs, together describing over 90% of both zonal and meridional velocity profile variance, have near identical vertical structure offset by different barotropic amplitudes (Fig. 4.27, panels 3 and 4). First displacement EOF amplitudes, with a decorrelation time scale of approximately one month, reveal the slow evolution of mode one amplitudes (Fig. 4.28).

4.6.10 Energy Spectra Comparison Across Sites in the North Atlantic

Throughout the western North Atlantic, mean potential and kinetic energy spectra generally exhibit more similarities than differences. The wavenumber spectra are quasi-universal. With the exceptions of ABACO and the LDE site, potential and kinetic energy is nearly equi-partitioned in the first and second baroclinic modes. However, among higher modes, potential energy dominates by a factor of two or higher (Fig. 4.30). A mean horizontal eddy length scale associated with each mode deformation radius is then calculated using Eq. 127 [Vallis, 2013] for each site. Potential energy dominates at spatial scales greater than the deformation radius and kinetic energy dominates at scales shorter than the deformation radius. With the exception of ABACO, the inferred horizontal length scale at each site associated with the first baroclinic mode is estimated as no smaller than $\sim 90\%$ of the of the first deformation radius, but up to nearly twice as large (at the LDE site) (Fig 4.30, lower right panel). Excluding the ABACO and LDE sites and within confidence bounds, horizontal length scales associated with the first and second baroclinic modes are approximately equal to first and second deformation radii, since KE $\approx$ PE (Fig. 4.30, left four panels). At the LDE site, however, potential energy dominates kinetic at the first and all higher modes. The approximated horizontal length scale associated with the first mode is then nearly double the first deformation radius. At the ABACO site, mode one kinetic energy exceeds potential energy by nearly a factor of two, implying a horizontal scale smaller than the first deformation radius. This is consistent with the expectation that at sites with increased susceptibility to instability (i.e. in a western boundary current system), eddy length scales should be no larger than the first deformation radius, but also that QG dyanmics assumptions and geostrophic turbulence theory predictions are less likely upheld.

Across all sites and all years, both potential and kinetic energy spectra exhibit a spectral slope steeper than minus two and not significantly different than the predicted slope of minus three associated with the forward enstrophy cascade of geostrophic turbulence [Charney, 1971]. Among the barotropic and roughly first ten baroclinic modes, spectra at each site are more energetic than those expected if internal waves were the dominant dynamics. At most sites, however, potential energy and predicted internal wave spectra converge at high wavenumber ($\sim$ mode 20 or higher) with a slope of minus two. This result suggests internal wave dynamics to dominate at these smaller vertical scales.

Differences across sites may reflect the local or non-local generation of observed eddies and the strength of an inverse cascade. Altimetric observations generally report eddy length scales everywhere larger than first deformation radii with this result at least partly interpreted as evidence of an inverse energy cascade of kinetic energy to horizontal scales larger than that of the first deformation radius [Chelton et al., 2011]. At sites farther from presumed locations of eddy generation (i.e. the Gulf Stream Extension), such as the LDE site, we estimate eddy length scales to be nearly twice the first deformation radius. Among modes three and higher, horizontal eddy length scales associated with each baroclinic mode are estimated to be at least a factor of two larger than the modal deformation radii.

Kinetic energy at each mode across sites varies by roughly an order of magnitude (Fig. 4.31, right panel). At the upper end of this distribution are 36°N and ABACO, as might be expected for their proximity to the Gulf Stream and deep western boundary current respectively. These sites are characteristically more energetic as a result of their proximity to boundary currents. The BATS site in 2014 and the LDE site, on the other hand, are least energetic, as might be expected due to their location away from sites of increased eddy activity. Interestingly, potential energy in mode one at the BATS site in 2015 and the LDE site is nearly equal to that at 36°N in 2019 (Fig. 4.31, left panel). While these sites generally exhibit relatively less eddy activity, increased levels of mode one potential energy may be explained as a result of the inverse cascade in an ocean with surface intensified stratification.

4.6.11 Surface Projection of Interior Motions and the Model Partition of Kinetic Energy

Due to extensive global coverage and near three-decades long observational record, altimetric observations of sea level anomaly have often been analyzed alongside theory predicting the surface projection of interior motions [Wunsch, 1997, Scott and Wang, 2005, LaCasce, 2017]. A relatively naive but informative initial exercise centers on the correlation between glider-following sea level and density anomalies at all depths (Fig. 4.32). Correlation profiles at the LDE, BATS, and 36°N sites are negative with largest absolute values between 250 m and 1500 m. This suggests sea level anomaly to be a good predictor of permanent thermocline depth with a correlation of $\sim$ -0.8. At depths greater than 2000 m, however, correlations are weaker with varied vertical structure. Deep correlations are strongest at station BATS, consistent with the more vertically coherent along-isopycnal temperature anomalies in Figure 4.12 and suggestive of more uniform vertical structure. Estimation of a density anomaly to instrument precision (or signal to noise) ratio reveals $\sim$ 4000 m to be the depth at which the two are equal.

To explore more explicitly the relationship between surface and interior structure, we project velocity and displacement profiles onto free-surface modes, thus to the extent that Eqs. 119 and 118 are equal (i.e. modes are independent of one another), we can compare the modal partition of kinetic energy at the surface with the depth-averaged modal partition (as was done in section, Eq. 113). This follows the analysis of Wunsch [1997], but with increased vertical resolution, and reveals higher number baroclinic modes to contain a greater fraction of kinetic energy at the surface than for the depth-averaged equivalent.

Prior to making the assumption that sea level anomaly principally reflects interior mode one dynamics (a conclusion of Wunsch [1997]), we compute glider-following sea level anomaly and glider observations of isopycnal vertical displacement, or density anomalies along isobars. At each depth, relative to the local time mean density profile, density anomaly time series are correlated with glider-following sea level anomaly (Figs. 4.20, 4.28). At the LDE site, the linear Pearson correlation coefficient decreases with depth to a minimum value of -0.81 at approximately 800 m (Fig. 4.32). This depth coincides with the deep pycnocline, the lower bound of 18°C water [Forget et al., 2011], as well as the depth of maximum amplitude for the first baroclinic displacement mode. A negative correlation implies that for a downward (deeper) isopycnal displacement, sea level anomaly is positive (Figs. 4.20, 4.28). At depths greater than 800 m, the magnitude of the correlation decreases almost monotonically

to zero. This implies that isopycnal vertical displacements at depths greater than 1000 m are associated with higher mode structure with amplitudes smaller than what altimetric measurements and processing can resolve. The profile of correlation with depth at 36°N reveals similar vertical structure to the LDE site, but with weaker correlations. At BATS however, correlation does not decrease in amplitude with depth. This implies that here, sea level anomalies reflect low mode density anomalies with less vertical structure. This can likewise be seen considering the vertical structure of along-isopycnal temperature anomalies in time (Figs. 4.11, 4.12, 4.13).

In agreement with Wunsch [1997], because of the free surface boundary condition (Eq. 79) and relatively large mode one amplitudes, we observe an increase in the fraction of kinetic energy in modes one and higher at the surface compared to the relative fraction of KE in each mode calculated using Eq. 113. At station BATS, 36°N, and the LDE site, the portion of surface kinetic energy in the barotropic mode is 50-75% less than for the water column average (Figs. 4.33). The relative fraction of energy in the first baroclinic mode is enhanced, increasing to nearly 75% at 36°N in the winter of 2018. The fraction of surface kinetic energy in mode three is also enhanced, especially for summertime conditions (36°N 2019, and the LDE site 2019). Surface kinetic energy in the the third baroclinic mode increases from $\sim$ 5% or less up to 15-35%, with a near equal amount of energy found in modes one and three at 36°N 2019. This suggests an increased importance for the third baroclinic mode in considering altimetric sea level anomaly observations, especially at locations with enhanced upper ocean stratification.

4.7 Summary and Conclusions

Deepglider missions in the western North Atlantic carried out over the last five years have resulted in the collection of hundreds of full-depth profiles and motivate this analysis of eddy vertical structure and variability. These full-depth measurements of temperature and salinity permit estimation of vertical wavenumber spectra of potential and kinetic energy from the barotropic through fortieth baroclinic mode. The partitioning of mechanical energy across vertical modes has only previously been considered for the barotropic through second baroclinic modes [Wunsch, 1997] and in numerical simulations [Smith and Ferarri, 2009]. The increase in vertical resolution that these profiles provide permits analysis of spectral slopes of potential and kinetic energy as a function of vertical wavenumber. Across all sampling sites, observations are consistent with an expected forward enstrophy cascade

from larger to smaller vertical scales. Vertical wavenumber spectra of geostrophic motions vary as k^{-3}, consistent with the predictions of geostrophic turbulence [Charney, 1971]).

Isopycnal vertical displacements of order 200 m, at depths greater than 2000 m, reveal mesoscale eddy vertical structure to regularly extend to the seafloor. In both 2014 and 2015, subsurface intensified eddies were observed at station BATS with cold, fresh water mass anomalies suggesting their origin to be the Labrador Sea. The surface expressions of these features were markedly different between the two years, implying the inadequacy of altimetric sea level anomaly observations in their ability to detail subsurface intensified eddy structure. These isolated coherent eddies in the western North Atlantic extend throughout the water column, in particular, reaching the seafloor. The extent to which these eddies are altered by topographic features is poorly understood, yet new observational efforts [Andres et al., 2020], along with these results, reveal their effect on the abyssal flows to be non-negligible.

Mode triplet interactions describe a mechanism by which energy is transferred across vertical scales. These results suggest that such interactions vary seasonally in response to seasonal changes in upper ocean stratification such as to enhance energy in higher baroclinic modes in the summer vs. winter. These interactions are expected to be enhanced among higher modes for mean density profiles with enhanced near-surface stratification. Increases in stratification at the base of the mixed layer, the seasonal pycnocline, increase higher baroclinic mode near-surface and surface amplitudes. The relative structures of the seasonal and permanent thermoclines can increase the relative importance of higher baroclinic mode ($m > 2$) triplet interactions and the retention of higher mode energy in higher modes. Increases in near-surface stratification thus result in an increase in the relative modal partition of energy among higher modes, as was observed at station BATS in 2015 with a summertime shift to a flatter potential energy spectrum across modes one through five.

Flat bottom baroclinic modes better describe empirical orthogonal functions of geostrophic eddy motions than do sloping bottom modes. Across all sites, the first EOF of velocity profiles (describing $\sim$ 50-90% of the variance) is well described by some combination of barotropic and first baroclinic modes. This suggests a coupling between the two modes, each contributing a varied amount across the different glider mission sites and in time. These differences may be attributed to some combination of proximity to sites of baroclinic instability (i.e. nearer to the

Gulf Stream Extension) as well as the relevance of topography (i.e. proximity of BATS to the Bermuda Rise) where sloping bottom modes may become more relevant. While the linear analysis of Smith [2007] shows the ocean to be baroclinically unstable nearly everywhere, mean eddy length scales associated with the first baroclinic mode vary across Deepglider mission sites. These differences are interpreted considering geographic variability of eddy kinetic in the North Atlantic; the LDE site is generally associated with eddy re-circulation while 36°N is closer to sites of eddy formation within the Gulf Stream Extension. Flat bottom velocity modes capture a larger fraction of EOF variance than sloping bottom modes. This is primarily due to non-zero geostrophic velocity estimates prevalent throughout the deep ocean. Geostrophic velocities greater in magnitude than 0.05 m s^{-1} observed throughout the bottom 2000 m suggest the appropriateness of employing barotropic and first barolinic flat bottom modes to describe interior motion and structure.

Potential energy vertical wavenumber spectra derived from long term hydrographic observations at specific sites (stations BATS, ALOHA, and PAPA) also vary as k^{-3} for high modes, but at levels higher than those found from Deepglider surveys and is ascribable to different averaging schemes. Among modes one through ten, station PAPA is the least energetic, followed by ALOHA, and then BATS. This order matches the order of mean eddy kinetic energy associated with each site. Notedly, the PAPA spectrum is little more energetic than the Garrett and Munk internal wave spectrum [Garrett and Munk, 1979].

At station BATS and at sites north of Bermuda on the Gulf Stream flank, potential and kinetic energy are roughly equal in the first and second baroclinic modes. Across all sites, spectra are most energetic at low modes, decreasing with increasing wavenumber following a linear slope proportional to k^{-3} (that predicted by geostrophic turbulence theory). These observations compare favorably with estimates of upper ocean horizontal wavenumber spectra [Callies and Ferarri, 2013] as well as vertical wavenumber spectra from quasi-geostrophic simulations [Smith and Ferarri, 2009].

Vertical wavenumber spectra at low mode far exceed those of internal waves as described by Garrett and Munk [1979]. Because the 'W'/'M' displacement and velocity profile estimation technique serves as a low pass filter smoothing density and velocity perturbations with time scales shorter than $\sim$ two days and spatial scales of less than $\sim$ 20 km, the resulting vertical wavenumber spectra appear better suited to identify the forward enstrophy

cascade.

Horizontal scales of motions in the first and second baroclinic modes are close to the radii of deformation of these modes. At higher modes, horizontal length scales are somewhat longer than the corresponding baroclinic radius of deformation. At locations associated with enhanced near-surface velocities (i.e. ABACO, 36°N 2019) kinetic energy often exceeds potential in mode one. This is consistent with the idea that at sites with strongly vertically sheared mean flows and more susceptible to baroclinic instability, mean eddy length scales associated with mode one are equal to or smaller than mode one deformation radii. At sites with weakly vertically sheared mean flows, closer in characteristic to idealized geostrophic turbulence, eddy horizontal length scales are equal to or larger than mode one deformation radii (LDE, 36°N 2018, BATS 2015).

Correlations between glider-following sea level anomaly and interior density anomalies vary among sites. At the LDE site, sea level anomaly and density anomalies at depths associated with the permanent pycnocline correlate at $\sim$ -0.8. Correlation magnitudes then decrease with increasing depth to near zero values. Vertical profiles of correlation coefficients suggests that the ability to predict bottom velocities varies across sites (Fig. 4.32), with BATS reporting the highest magnitude correlations between density anomalies at depths greater than 3000 m and sea level anomaly. The vertical coherence of these anomalies is likewise observed in along-isopycnal temperature anomaly profiles (Fig. 4.11, 4.12, 4.13) and is evidence for the creation of anomalies of low mode structure. At BATS, anomaly variance at depths greater than 2000 m is greater than at any other sampling site (Fig. 4.14). If along-isopycnal stirring at QG time scales is presumed responsible for the homogenization of along-isopycnal temperature and salinity variability, these results suggest station BATS to be closer to sites of instability or anomaly generation.

These high resolution observations of full-depth geostrophic eddy structure at various sites in the western North Atlantic offer a first look at the geography and temporal variability of the partitioning of eddy energy throughout the water column. Understanding of this partitioning continues to be important considering pathways of eddy energy into and out of the mesoscale. With the mesoscale containing a dominant fraction of ocean kinetic energy, tracing a pathway to dissipation is necessary to improve our ability to predict the fate of oceanic tracers and heat.

Table 1: Percent kinetic energy in the barotropic and first three baroclinic modes at each site. Where data permit, partitioning is separated by season or velocity component.

Location	KE_0	KE_1	KE_2	KE_3	$\sum_{m=0-3}$	ϵ_{111}	ϵ_{222}	ϵ_{333}
$BATS_w$ 2015	53.7%	35.6%	4.6%	3.3%	97.2%	1.55	0.38	0.14
$BATS_s$ 2015	17%	61.9%	9.4%	7.9%	96.1%	1.58	0.29	1.48
ABACO 2017	26.9%	69.9%	2.3%	1.0%	98.7%	1.68	0.08	0.3
$36°N_w$ 2018	52%	38.2%	4.7%	2.3%	97.1%	1.53	0.32	0.2
$36°N_f$ 2018	38.6%	36.9%	9.2%	10%	94.7%	1.57	0.35	0.98
LDE_u 2019	46.3%	48.5%	1.1%	2.3%	98.1%	1.75	0.21	2.63
LDE_v 2019	55.4%	39.3%	3%	0.7%	98.4%	1.75	0.21	2.63

4.8 Acknowledgments

This work was funded by NSF grant 1736217 and would not have been possible without the help of Kirk O'Donnell, James Bennett, Noel Pelland, and those that have preceded me in the Eriksen lab. Additional thanks to the crew of the R/V Atlantic Explorer and Seakeepers organization for their professionalism, capability, and generous assistance in deploying and recovering gliders.

Table 2: Percent potential energy in the barotropic and first three baroclinic modes at each site. Where data permit, partitioning is separated by season or velocity component.

Location	PE_0	PE_1	PE_2	PE_3	$\sum_{m=0-3}$	ϵ_{111}	ϵ_{222}	ϵ_{333}
$BATS_w$ 2015	-	56.6%	14.7%	10.8%	82.1%	1.55	0.38	0.14
$BATS_s$ 2015	-	43.9%	16.4%	10.4%	70.7%	1.58	0.29	1.48
ABACO 2017	-	33.7%	41.3%	10.5%	89.5%	1.68	0.08	0.3
$36°N_w$ 2018	-	49.8%	12.6%	9%	71.5%	1.53	0.32	0.2
$36°N_f$ 2018	-	36.5%	35.1%	10.2%	81.1%	1.57	0.35	0.98
LDE 2019	-	83.4%	6%	4.3%	93.8%	1.75	0.21	2.63

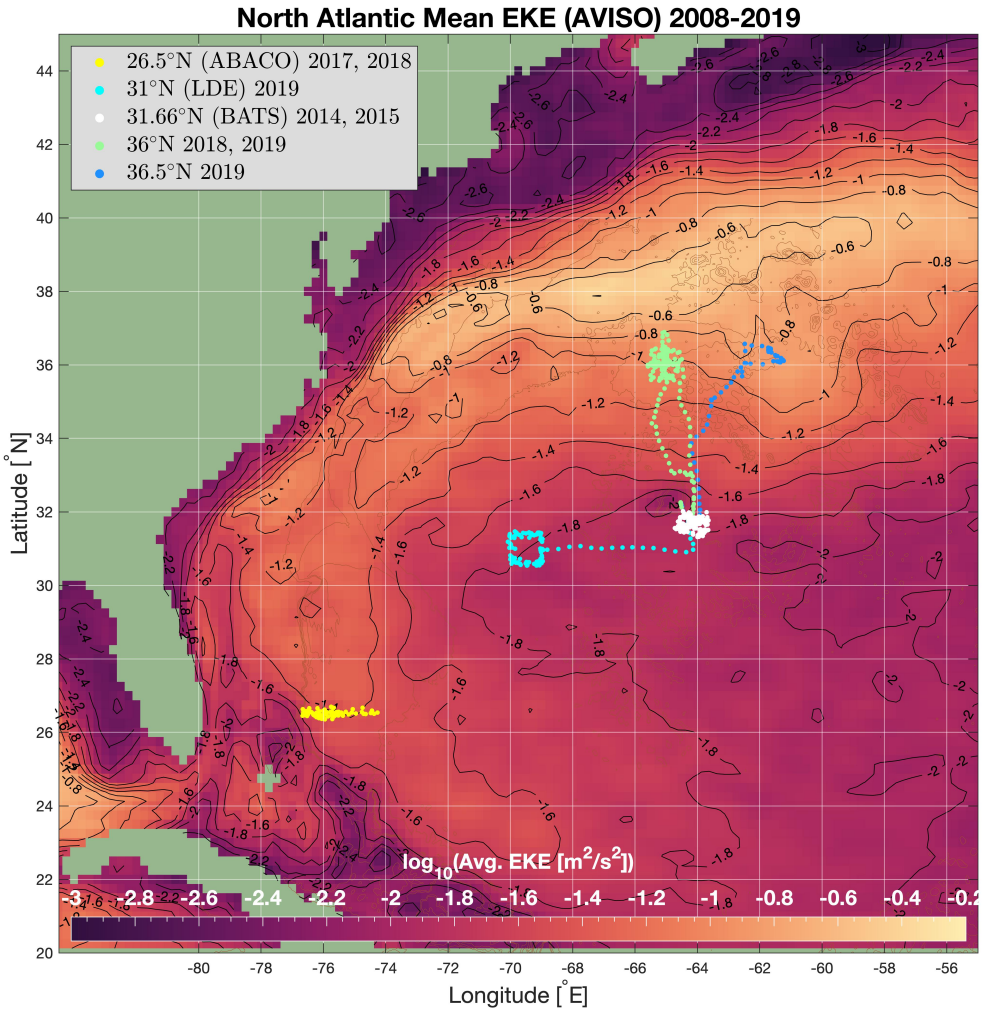

Figure 4.1: Five Deepglider mission sites in the western North Atlantic. Ten year mean eddy kinetic energy derived from AVISO merged and gridded sea level anomaly fields is colored and contoured. Multiple mission sites were revisited between 2014 and 2019 (BATS, ABACO, and 36°N.)

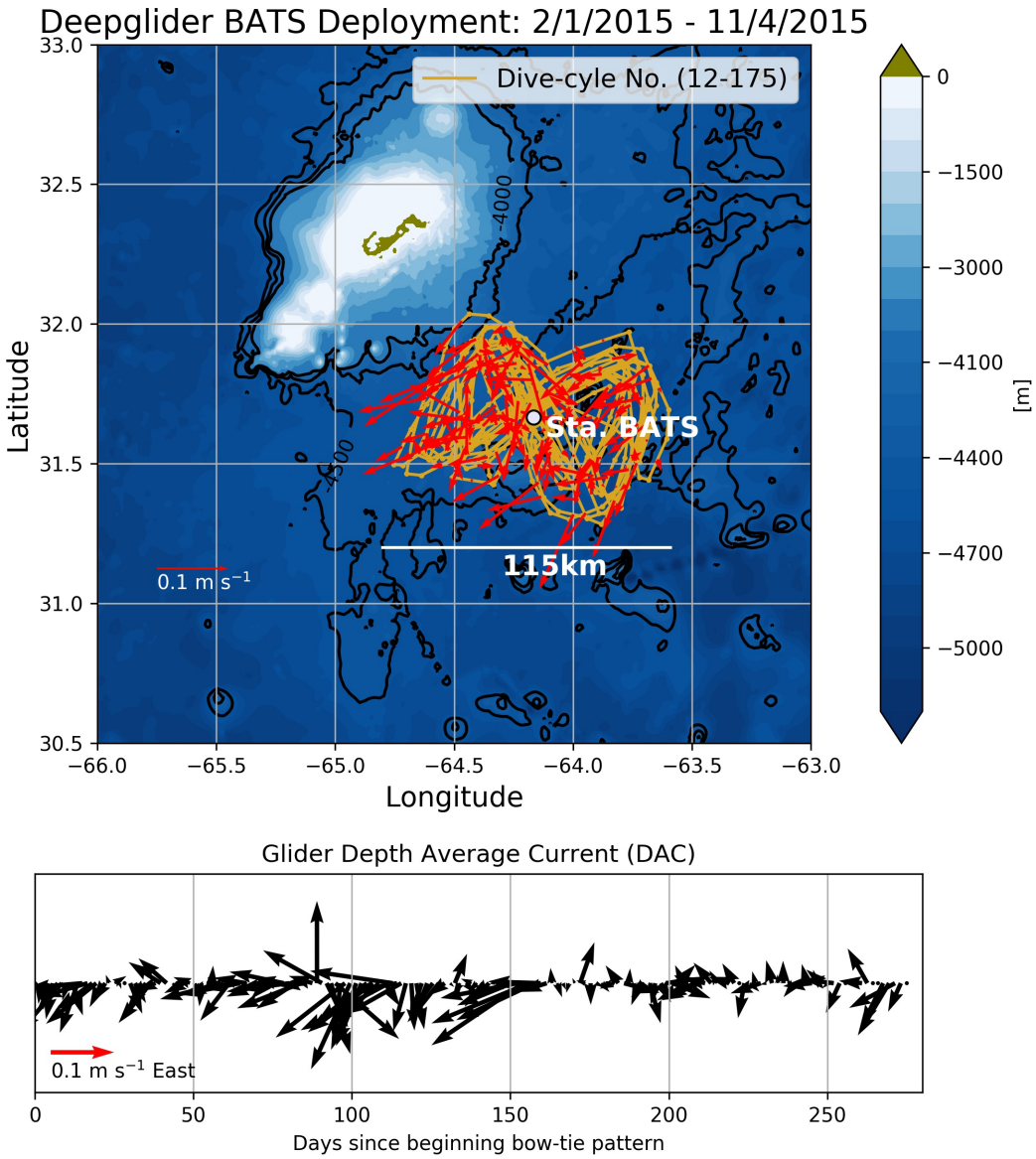

Figure 4.2: Midpoint locations of 163 dive-climb cycles around station BATS completed in 2015 over a 10 month period. The location of station BATS is in white. Depth average current vectors from each dive-climb cycle are in red. Bathymetry contours are in blue. Depth average current vectors are plotted a function of time below.

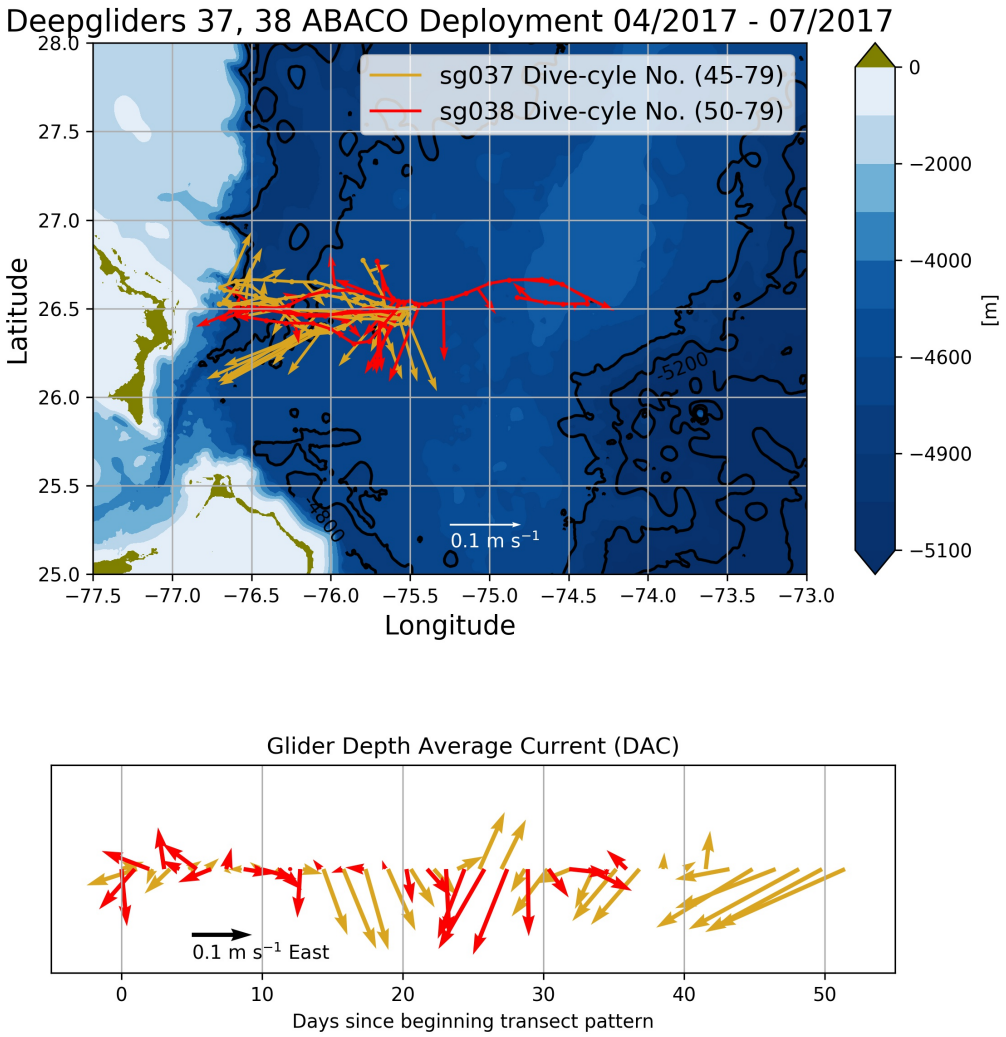

Figure 4.3: Midpoint locations of dive-climb cycles along 26.5°N between 76.75°W and 74.5°W completed in 2017 over a four month period. Depth average current vectors are in white. Bathymetry contours are in blue. Depth average current vectors for each glider are plotted a function of time below.

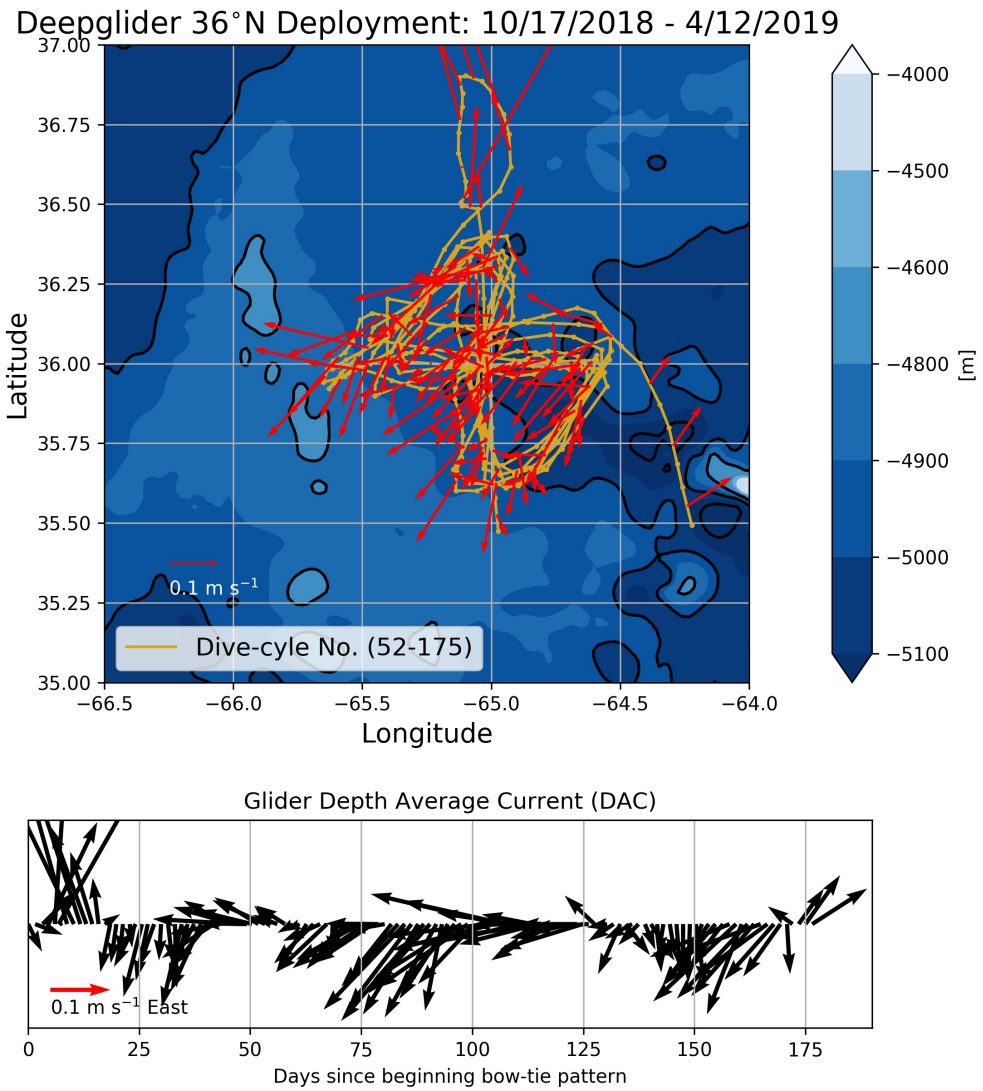

Figure 4.4: Midpoint locations of dive-climb cycles at 36°N, 65°W completed in 2018 over a six month period. Depth average current vectors are in red. Bathymetry contours are in blue. Depth average current vectors are plotted a function of time below.

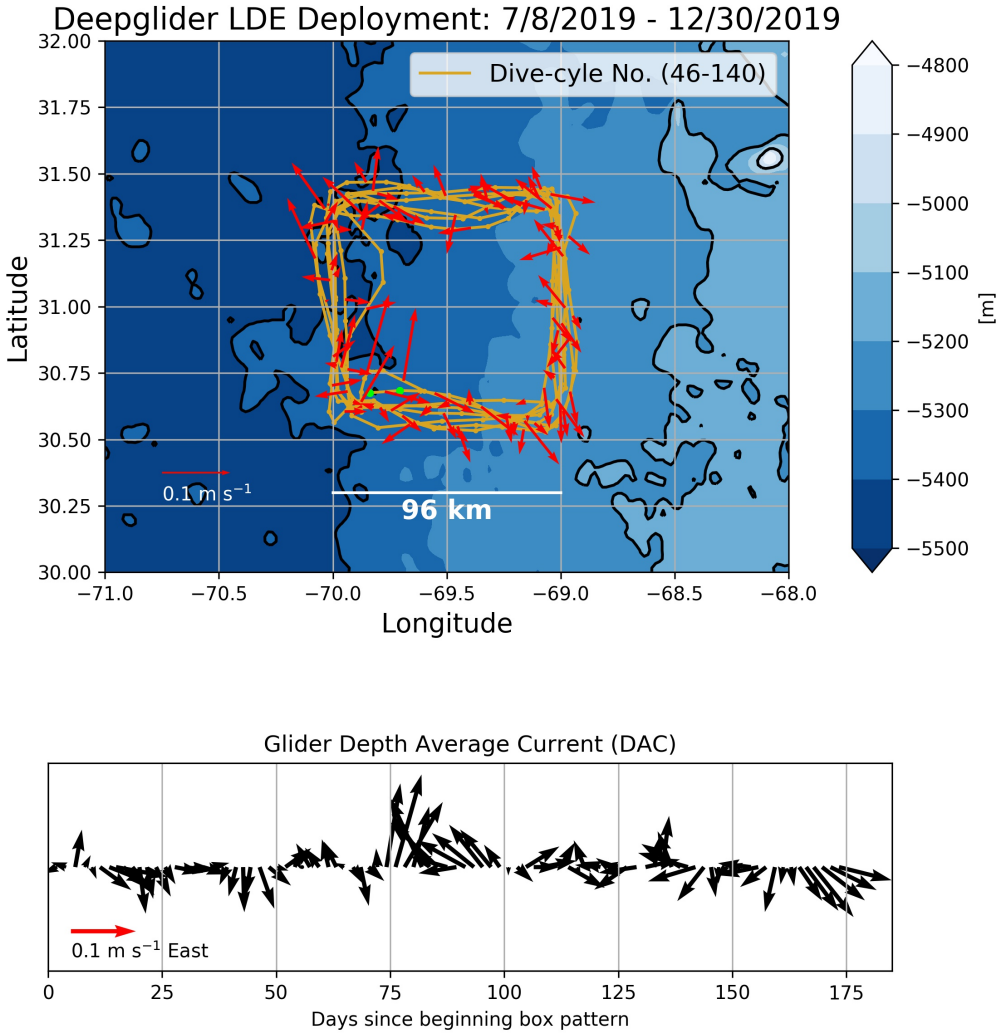

Figure 4.5: Midpoint locations of dive-climb cycles at the Local Dynamics Experiment (LDE) site completed in 2019 over a 4 month period. Depth average current vectors are in red. Bathymetry contours are in blue. Depth average current vectors are plotted a function of time below.

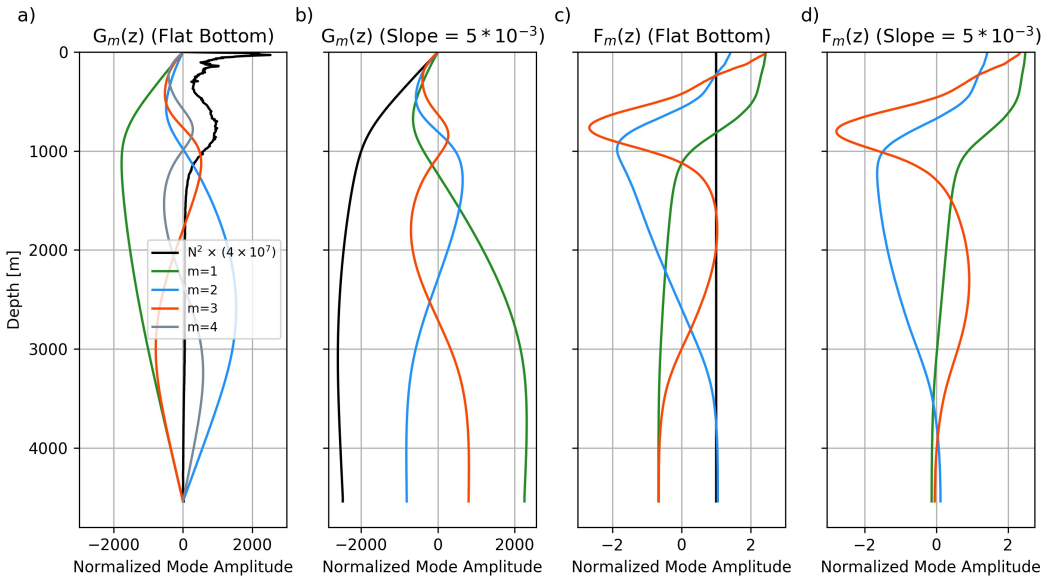

Figure 4.6: a) First four flat bottom displacement modes G_m for a wintertime background buoyancy frequency profile at station BATS, added in black b) sloping bottom displacement modes c) flat bottom velocity modes F_m d) sloping bottom velocity modes.

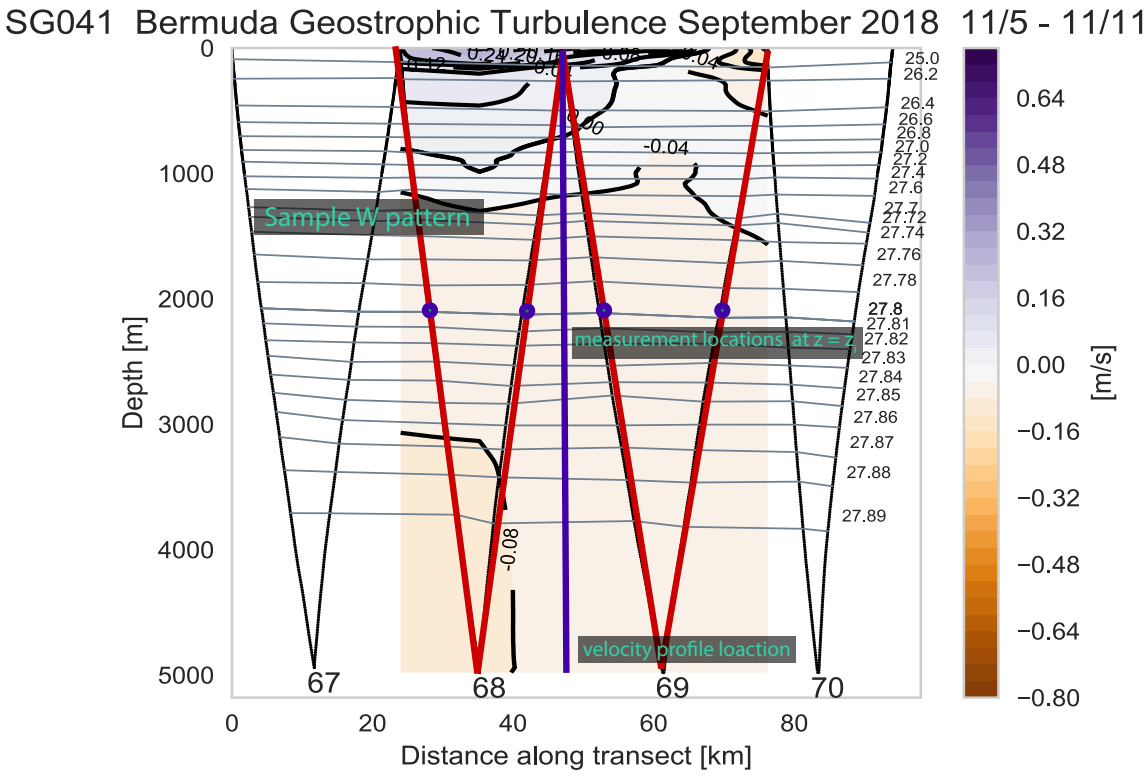

Figure 4.7: Cross-section of four consecutive Deepglider dive-climb cycles at 36°N in 2018. Dive-climb cycles were completed while glider maintained a constant heading. The black sawtooth pattern identifies glider position as a function of depth and distance along transect. Neutral density contours are in grey. Colored contours are the derived cross-track geostrophic velocity field. A sample 'W' pattern comprised of four density profiles is overlain in red and resulting cross-track geostrophic velocity profile location in dark blue.

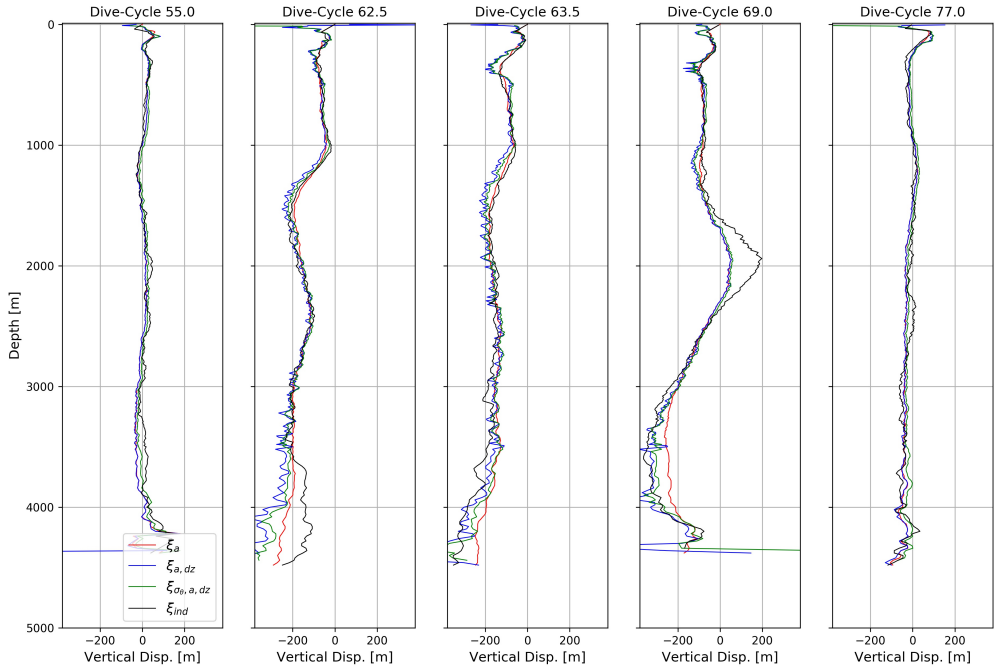

Figure 4.8: Sample of five full-depth vertical isopycnal displacement profiles at station BATS (2015). Glider cycle numbers indicate slant profile as dive (.0) or climb (.5). For each glider dive-climb cycle, displacement profiles are calculated using the four methods described in Section 4a.

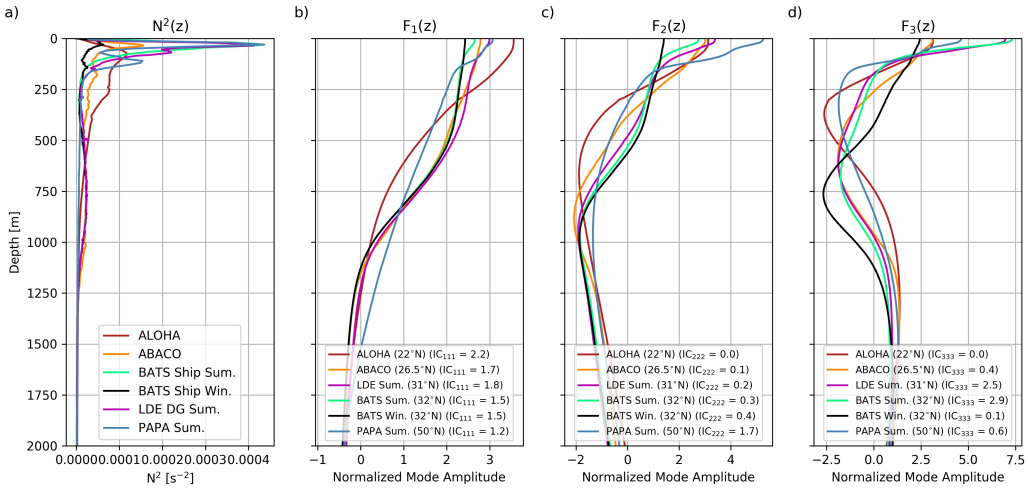

Figure 4.9: a) Mean background buoyancy frequency profiles at station ALOHA, along 26.5°N in the western North Atlantic (ABACO), at station BATS in the summer and winter, and at station PAPA in the Northeast Pacific. This subset of sites was chosen to highlight the greatest variability observed in background buoyancy frequency profiles. b) First baroclinic flat bottom velocity mode at each site. c) Second baroclinic flat bottom velocity mode at each site. d) Third baroclinic flat bottom velocity mode at each site. Modes are calculated from full depth profiles and shown only between 0 and 2000 m to emphasize vertical structure variability in the upper 1000 m.

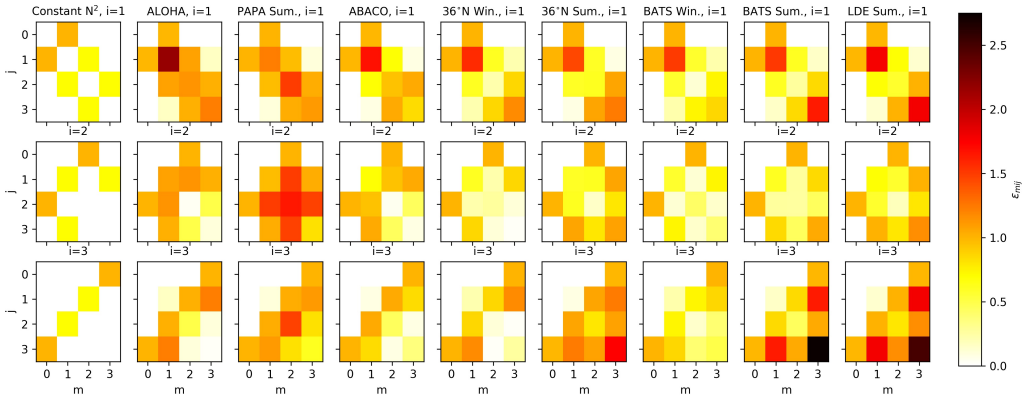

Figure 4.10: Mode triplet interaction coefficients for: an ocean with constant stratification, each glider deployment site, and hydrographic stations BATS, ALOHA, and PAPA. Each column is a different site. Rows identify the first triplet index i, horizontal axes the second index j, and vertical axes the third index m.

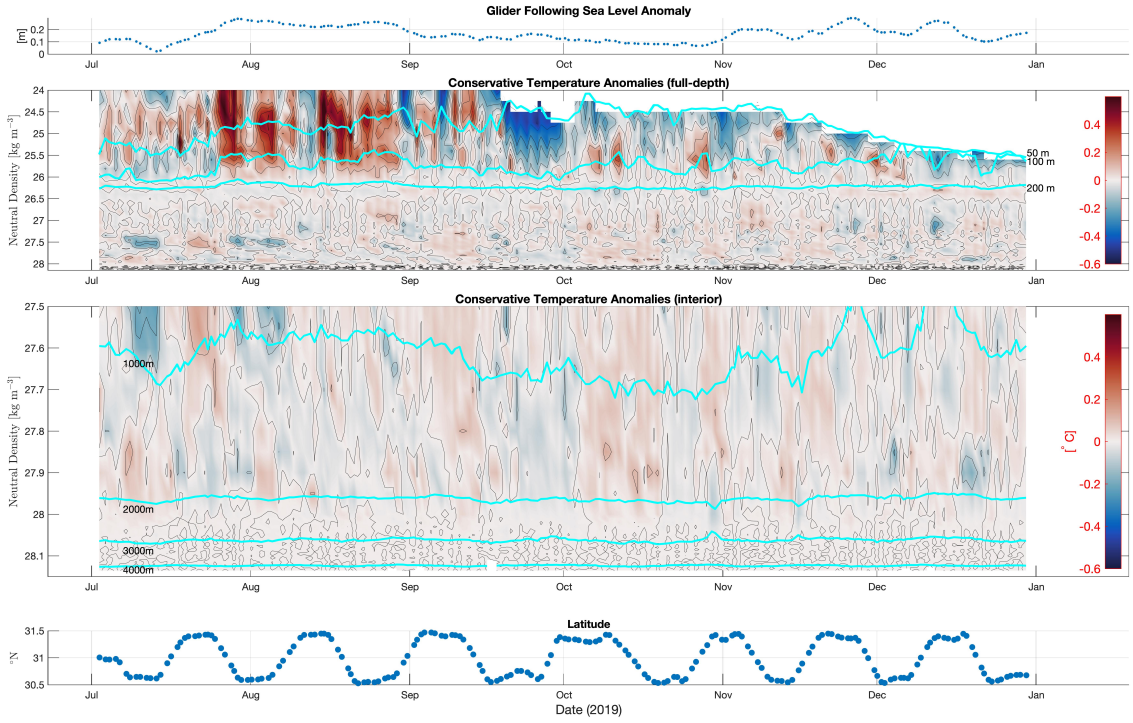

Figure 4.11: Glider following sea level anomaly, along isopycnal temperature anomalies, and latitude at the LDE site. Interior anomalies between $\sim$ 1000 m and the seafloor are replotted with increased density resolution. Cyan contours identify 50, 100, 200, 1000, 2000, 3000, and 4000 m isobars.

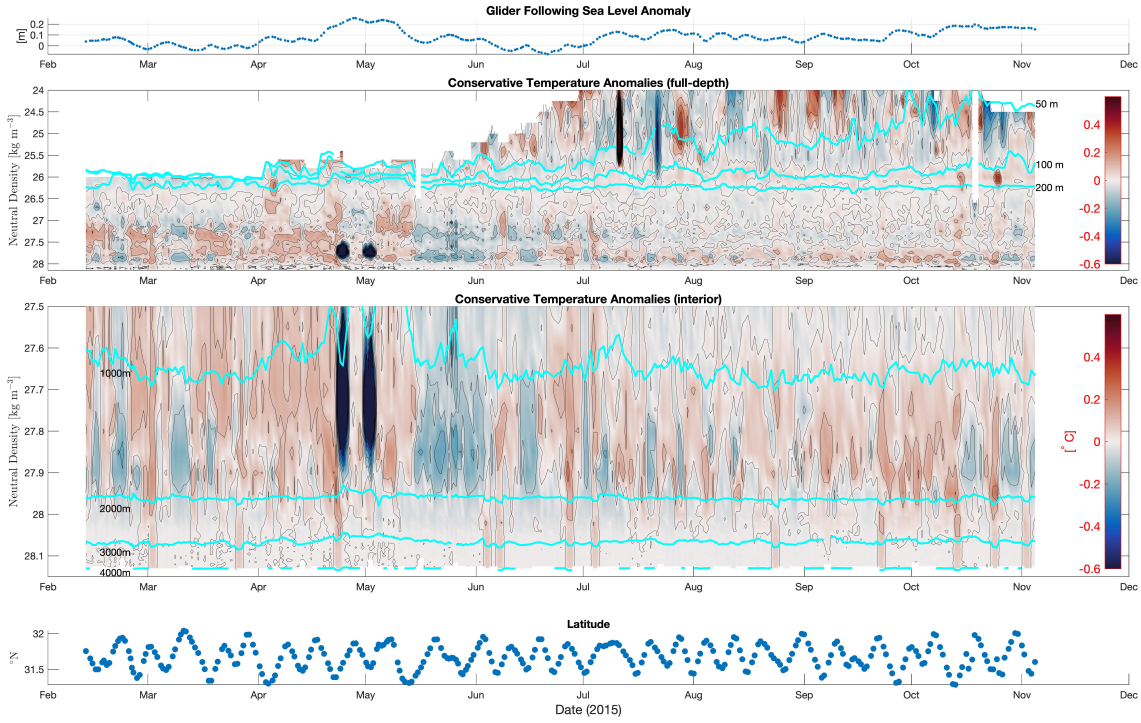

Figure 4.12: Glider following sea level anomaly, along isopycnal temperature anomalies, and latitude at the BATS site (2015). Interior anomalies between $\sim$ 1000 m and the seafloor are replotted with increased density resolution. Cyan contours identify 50, 100, 200, 1000, 2000, 3000, and 4000 m isobars.

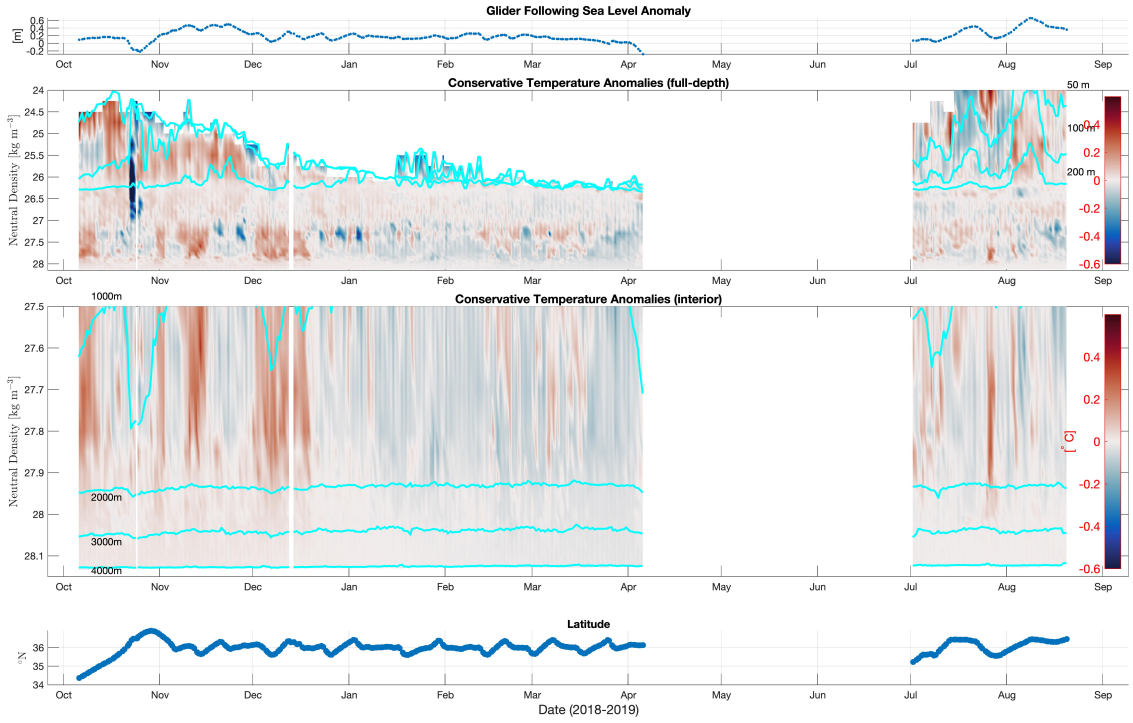

Figure 4.13: Glider following sea level anomaly, along isopycnal temperature anomalies, and latitude at 36°N (2018-2019). Interior anomalies between $\sim$ 1000 m and the seafloor are replotted with increased density resolution. Cyan contours identify 50, 100, 200, 1000, 2000, 3000, and 4000 m isobars.

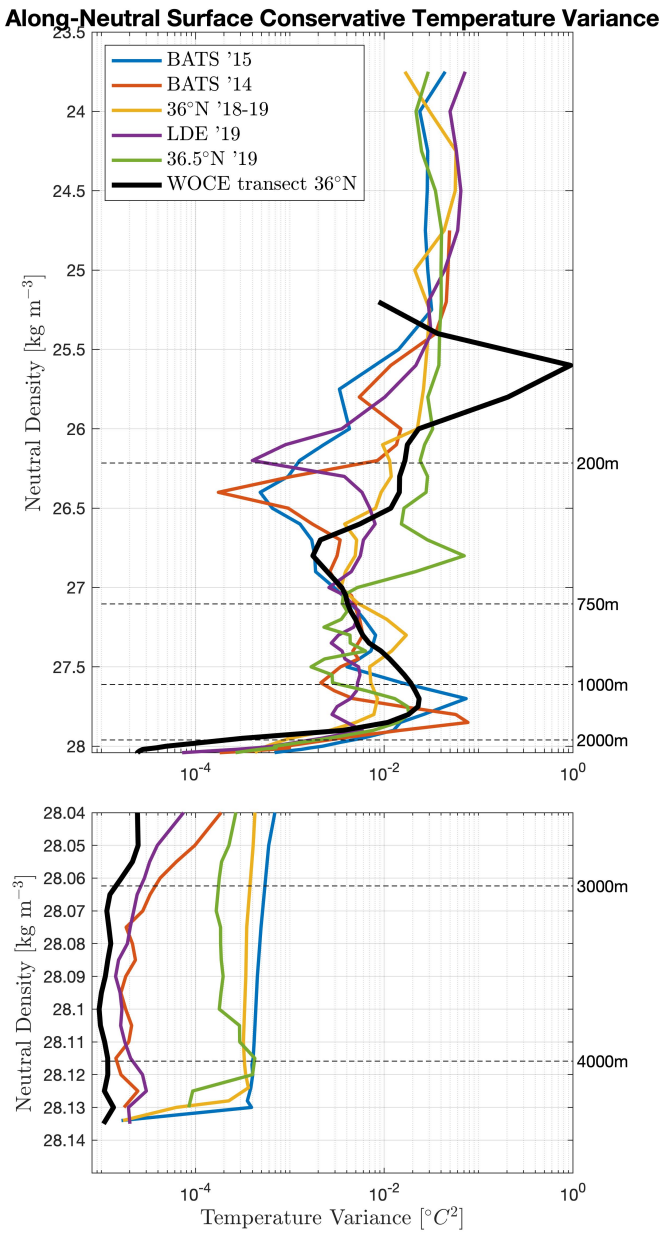

Figure 4.14: Along-isopycnal temperature variance at Deepglider mission sites within the western North Atlantic. The lower sub-figure corresponds to increased vertical resolution over the bottom $\sim$ 2000 m.

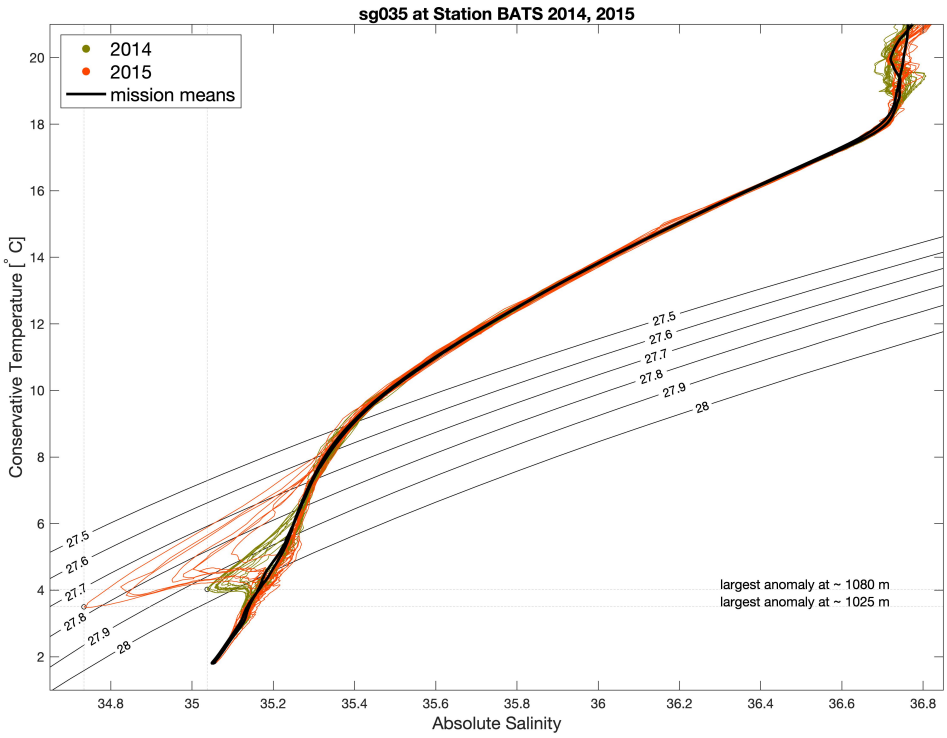

Figure 4.15: Absolute salinity and conservative temperature profiles at station BATS in 2014 and 2015. Neutral surfaces are contoured only in the depth range of increased temperature variance (Fig. 4.14).

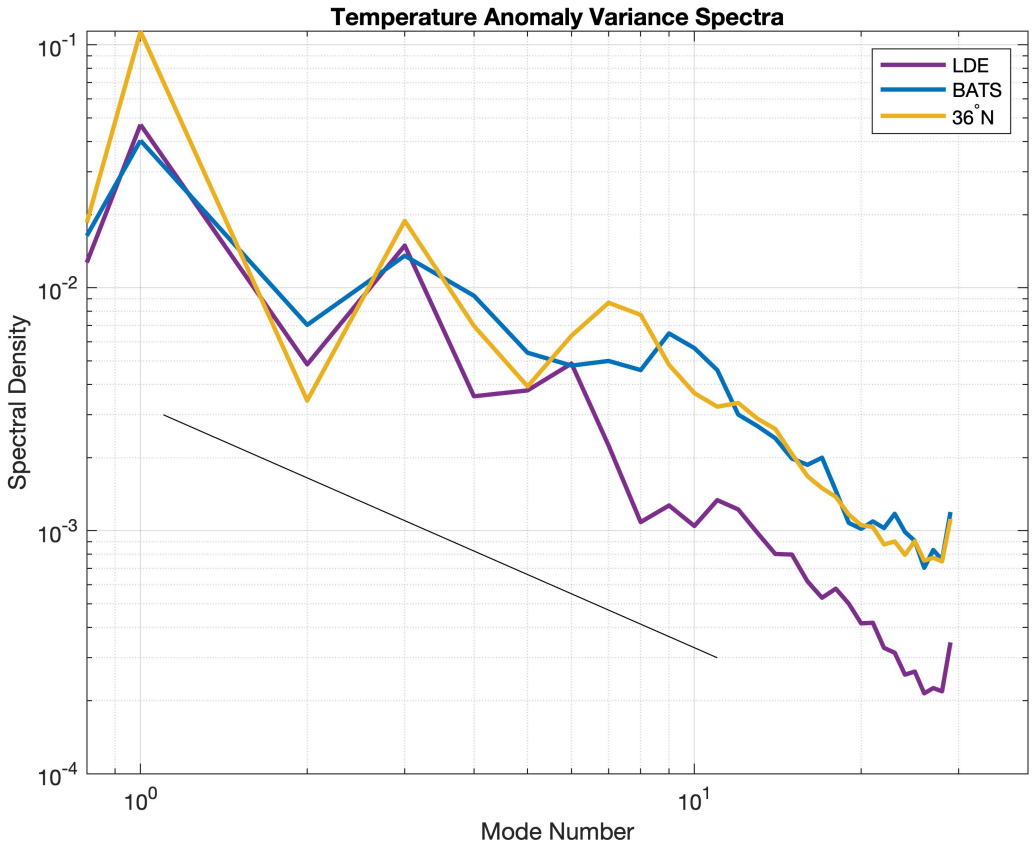

Figure 4.16: Temperature variance spectra as a function of mode number. Variance in the barotroptic mode is plotted along the vertical axis and a reference slope of -1 is in black.

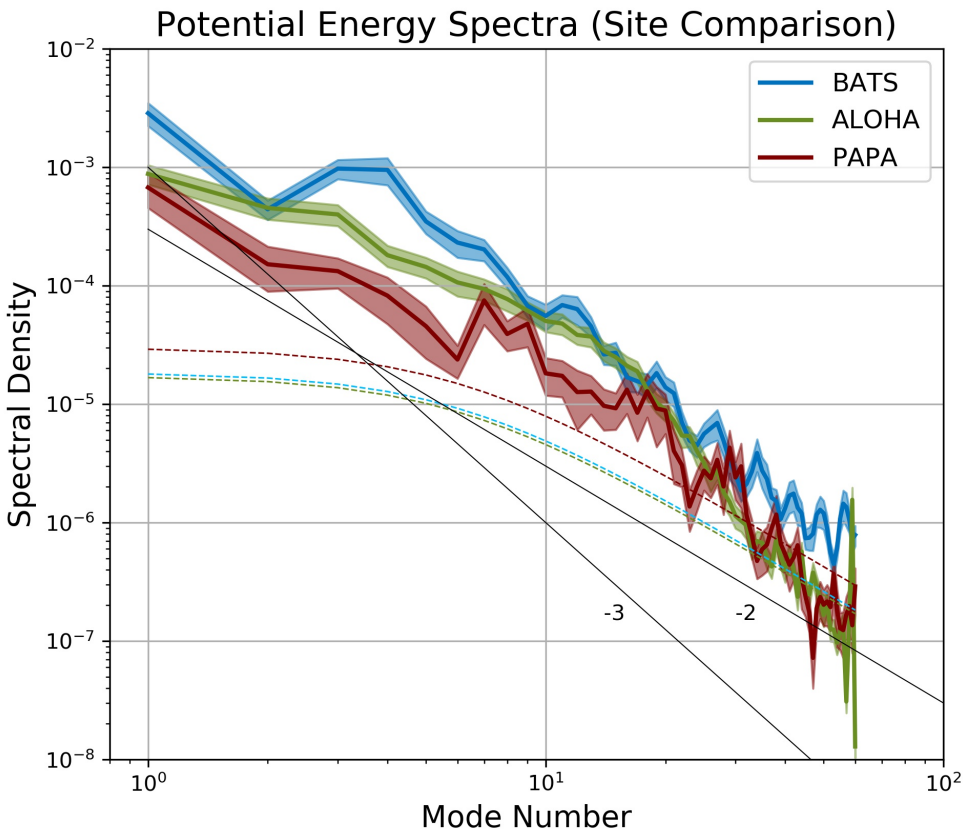

Figure 4.17: Potential energy per mode number at hydrographic stations BATS, ALOHA, and PAPA. Colored dashed lines are the corresponding Garrett and Munk internal wave spectra. Solid black lines are reference linear slopes of k^{-2} and k^{-3}. Shaded bands are 95% confidence intervals calculated using a Student's t-distribution from 240, 168, and 50 profiles at each respective site.

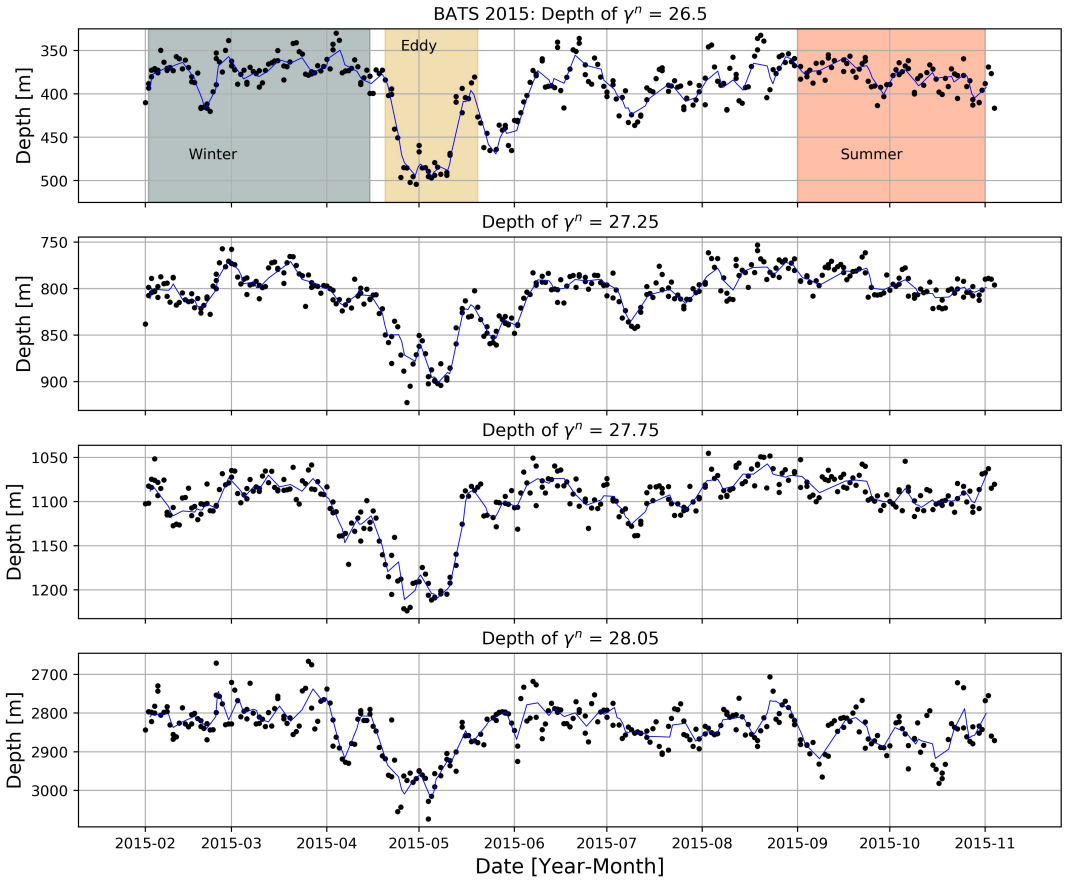

Figure 4.18: Time series of glider observed depths of four neutral density surfaces at station BATS in 2015. Shaded regions identify winter, summer, and eddy periods. Scatter points are depths from individual glider profiles while blue lines are depths from four-profile averages (used to estimate displacement profiles).

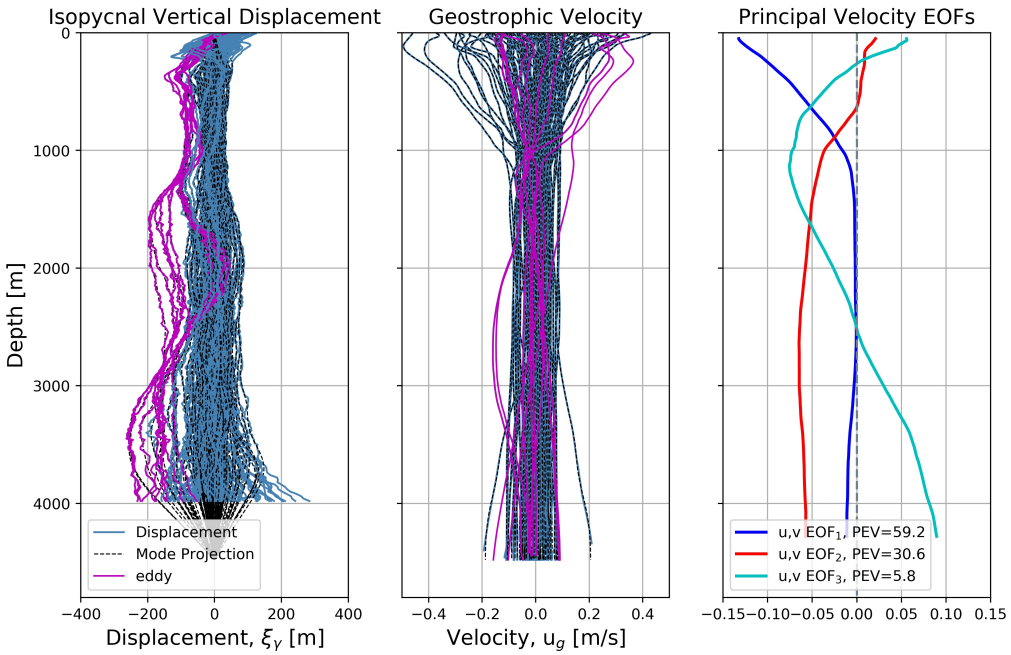

Figure 4.19: Glider derived isopycnal vertical displacement, geostrophic velocity, and first three velocity principle EOFs at station BATS 2015 (Feb.-Oct.). Displacement and velocity profiles of an individual subsurface intensified eddy are in purple. The values labeled PEV in the right panel note the percent explained eddy variance by respective EOFs.

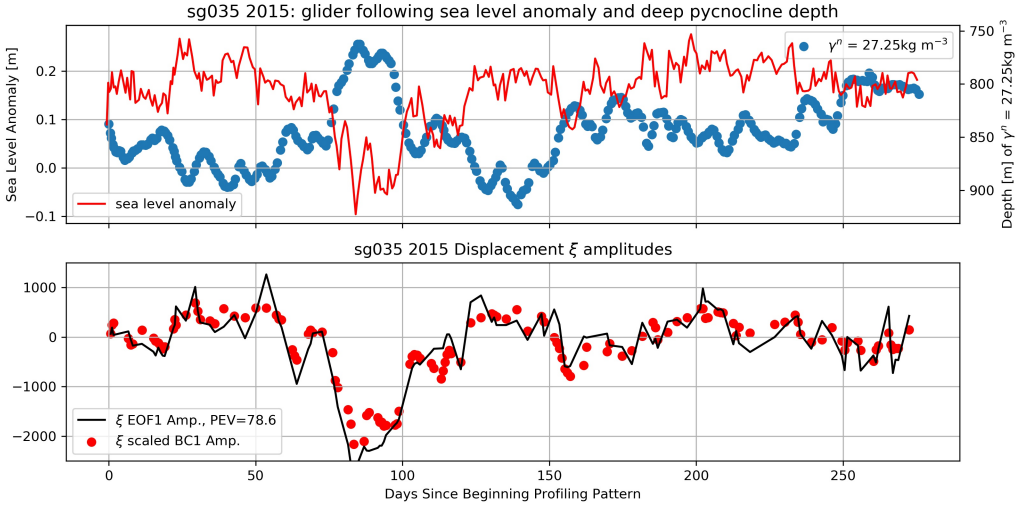

Figure 4.20: Upper) BATS 2015 glider-following sea level anomaly (red) and depth of $\gamma^n = 27.25$ kg m^{-3} (density surface in the deep pycnocline) (blue). Lower) Displacement EOF_1 amplitude as a function of days since mission start. Scaled first baroclinic displacement mode amplitudes are in red.

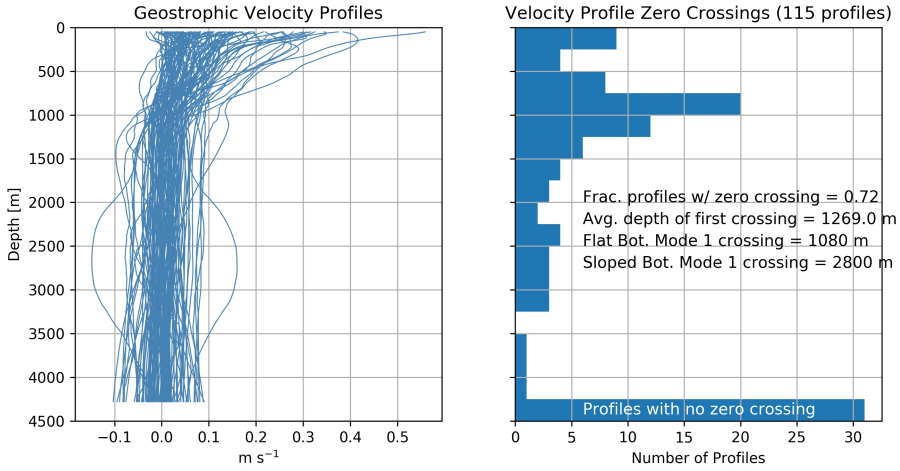

Figure 4.21: Geostrophic velocity profiles at BATS in 2015 with a histogram of the depths of the first zero crossing of each profile.

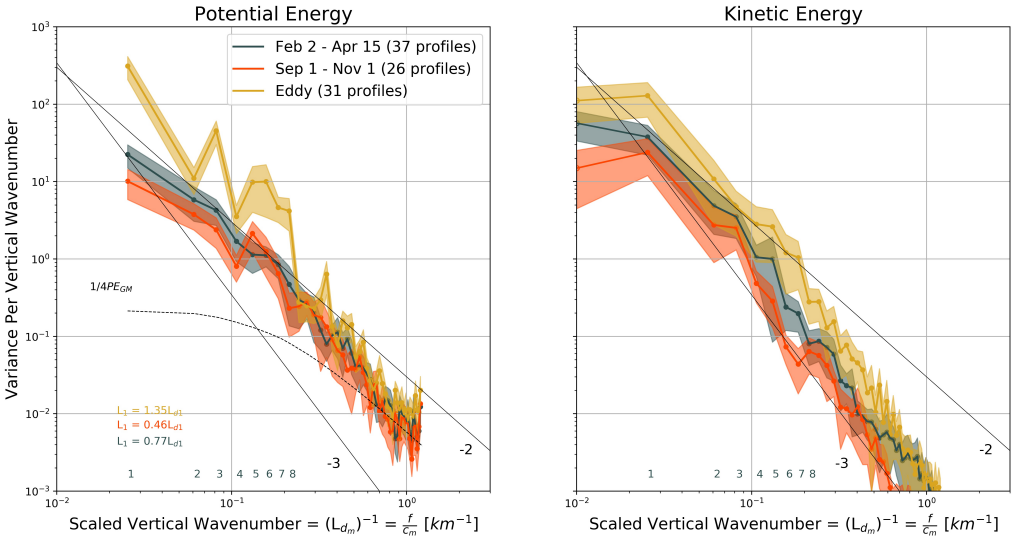

Figure 4.22: Water column average potential and kinetic energy per mode scaled vertical wavenumber at station BATS in 2015. Subsets of velocity and displacement profiles were selected to compare mean winter (grey), late-summer (red), and eddy (yellow) spectra. Profiles in each subset were completed within respective shaded time bounds in Figure 4.18. Scattered points are labeled by corresponding mode number for the first eight baroclinic modes. The shaded regions identify 95% confidence bounds calculated using a Student's t-distribution. Because profiles are not strictly all statistically independent, we estimate approximately four degrees of freedom from a roughly two week decorrelation time scale for displacement mode amplitudes (indirectly seen in Fig. 4.20) and an approximate two month period over which these seasonal spectra are estimated. This implies that over the seasonal periods referred to, we observe approximately four realizations of the eddy field. The black dashed line is the empirical Garrett and Munk internal wave spectra and solid lines are reference slopes k^{-2} and k^{-3}.

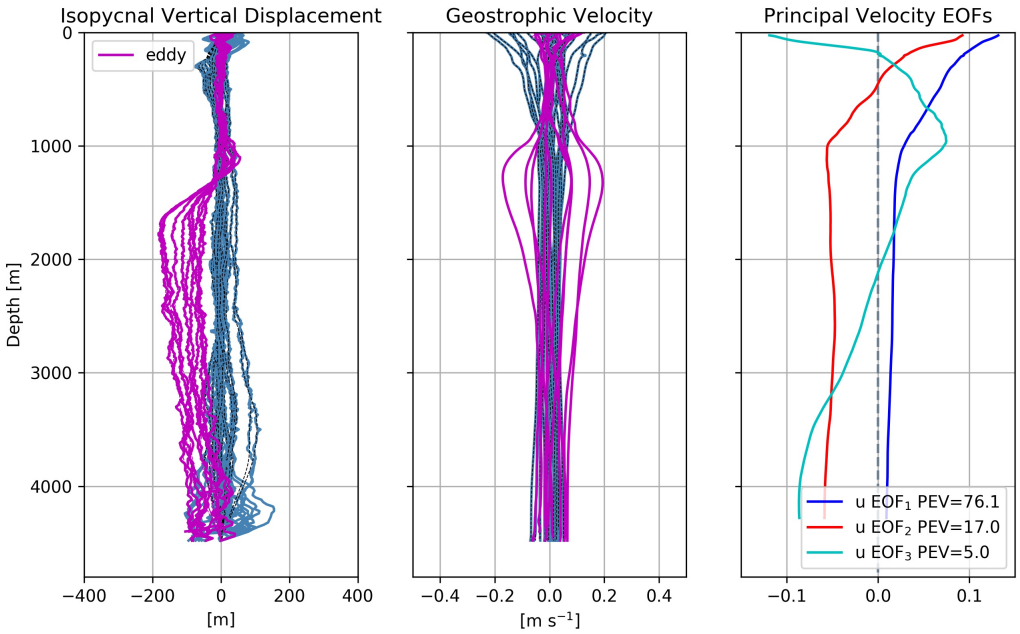

Figure 4.23: Glider derived isopycnal vertical displacement, geostrophic velocity, and first three velocity principle EOFs at BATS 2014 (Mar.-Jun.). Displacement and velocity profiles of an individual subsurface intensified eddy are in purple. EOFs are calculated from all velocity profiles excluding those of the eddy.

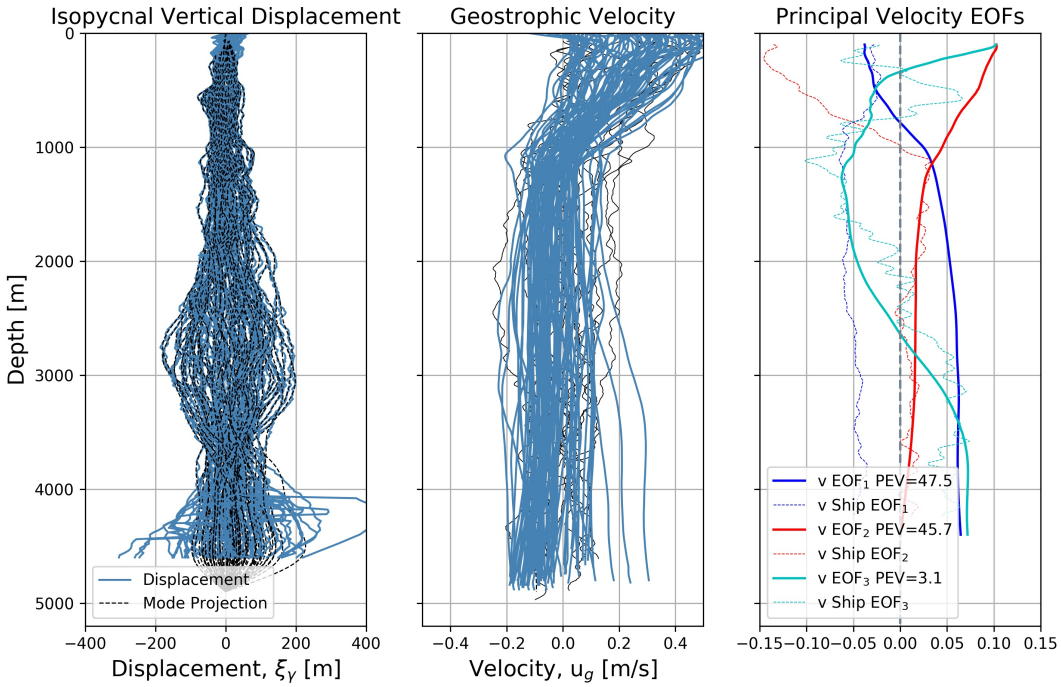

Figure 4.24: Glider derived isopycnal vertical displacement, geostrophic velocity, and first three velocity principle EOFs along 26.5°N in 2017 (Apr.-Jul.). Meridional velocity profiles from a lowered-ADCP concurrently deployed along the transect are in black with lowered-ADCP EOFs in dashed colors.

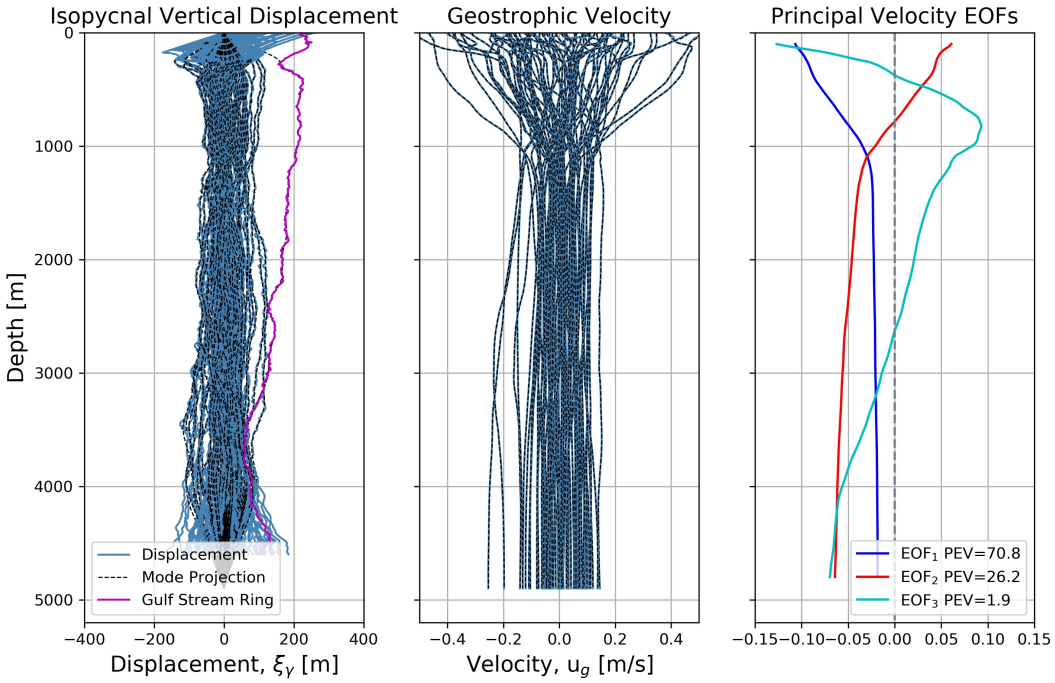

Figure 4.25: Glider derived isopycnal vertical displacement, geostrophic velocity, and first three velocity principle EOFs at 36°N, 65°W in 2018 (Sep.-May.).

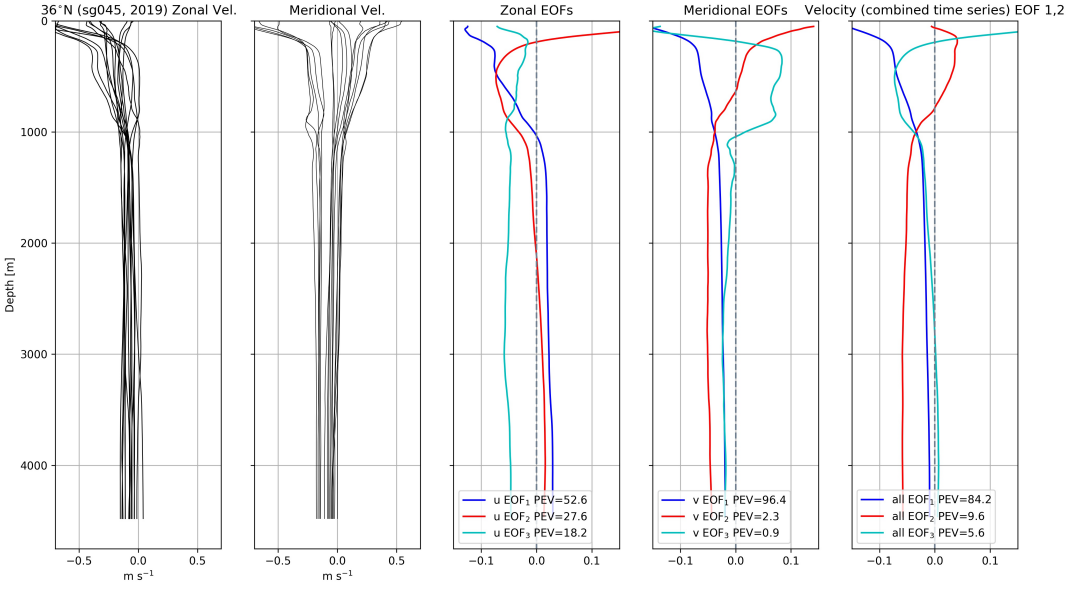

Figure 4.26: Glider derived zonal and meridional geostrophic velocity profiles, and two principle EOFs at 36°N, 65°W in 2019 (Jun.-Aug.). EOFs of all velocity profiles considered as a total time series are in green.

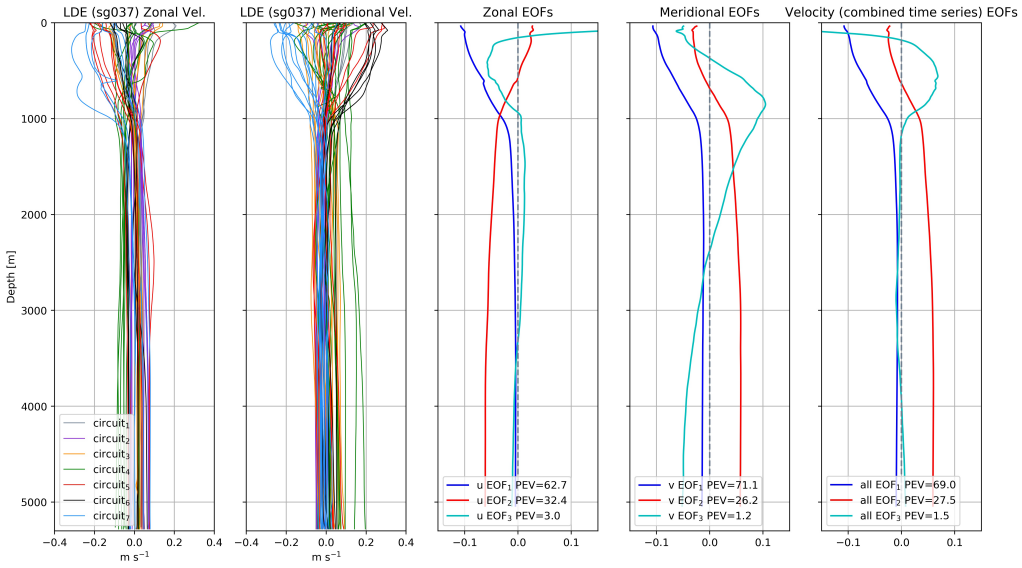

Figure 4.27: Glider derived zonal and meridional geostrophic velocity profiles colored by circuit number (completed number of laps around the box sampling pattern, Fig. 4.5) at the LDE site (31°N) in 2019 (Jun.-Dec.). Respective zonal and meridional principle three EOFs are in blue, red, and cyan. EOFs of combined zonal and meridional velocity profiles (treated as a single time series) are in green.

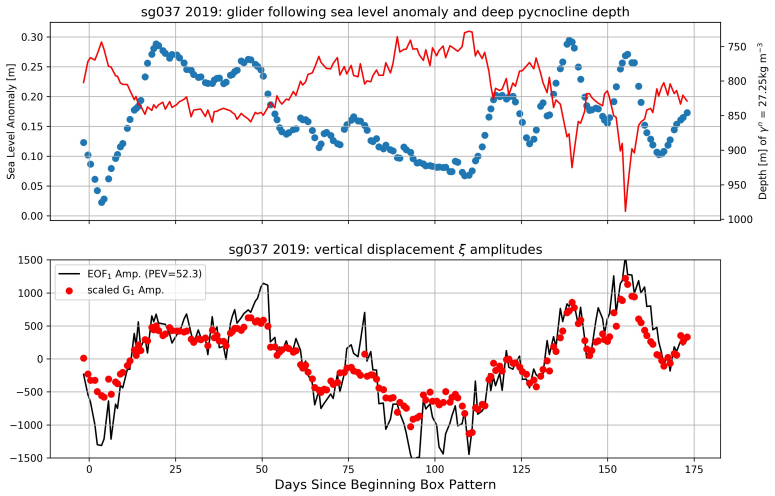

Figure 4.28: Upper) Glider (sg037 2019) following sea level anomaly and depth of $\gamma^n = 27.25$ kg m^{-3} (density surface in the deep pycnocline). Lower) Displacement EOF$_1$ amplitude in time at the LDE site. Scaled first baroclinic displacement mode amplitudes are in red.

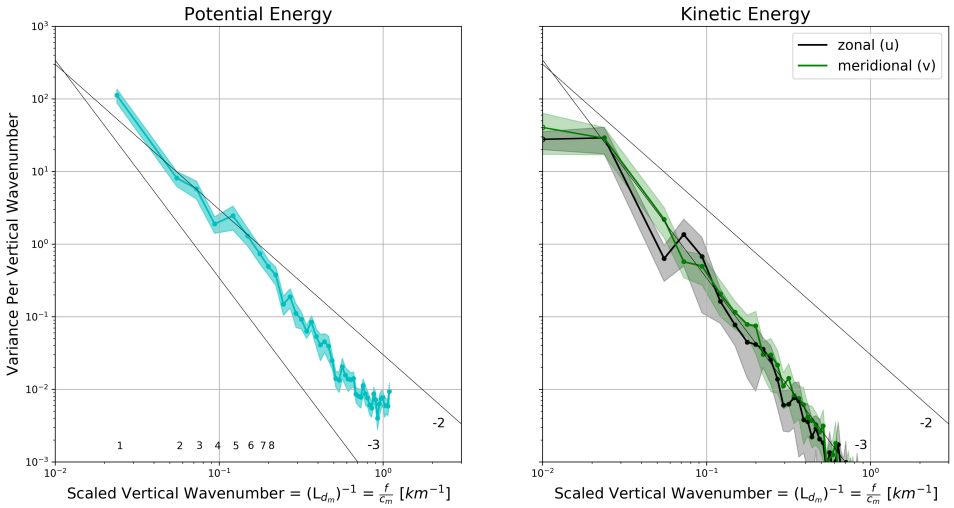

Figure 4.29: Water column average potential (left) and kinetic (right) energy spectra at the LDE site in 2019. Reference slopes are in black.

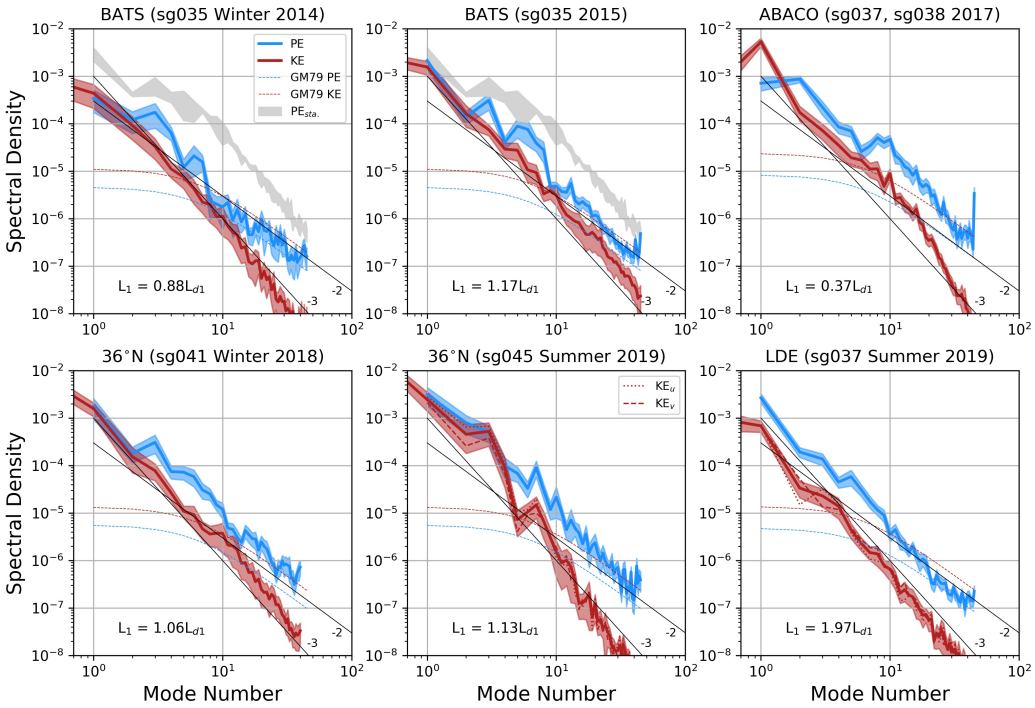

Figure 4.30: Water column average potential (blue) and kinetic (green) energy per mode number at each site in the western North Atlantic. 95% confidence bounds, calculated using a Student's t-distribution [Storch and Zwiers, 2003], are shaded. Kinetic energy in the barotropic mode is plotted along the vertical axis. Garrett and Munk internal wave spectra are dashed [Garrett and Munk, 1979]. Reference slopes of k^{-2} and k^{-3} are in solid black. Where glider sampling geometry permitted (36°N 2019, LDE 2019) dash and dash-dot lines correspond to zonal and meridional velocity components. The square root of the ratio of potential to kinetic energy in mode 1 is labeled L_1 and is the estimated mean horizontal eddy length scale as a fraction of the first baroclinic deformation radius L_{d1}.

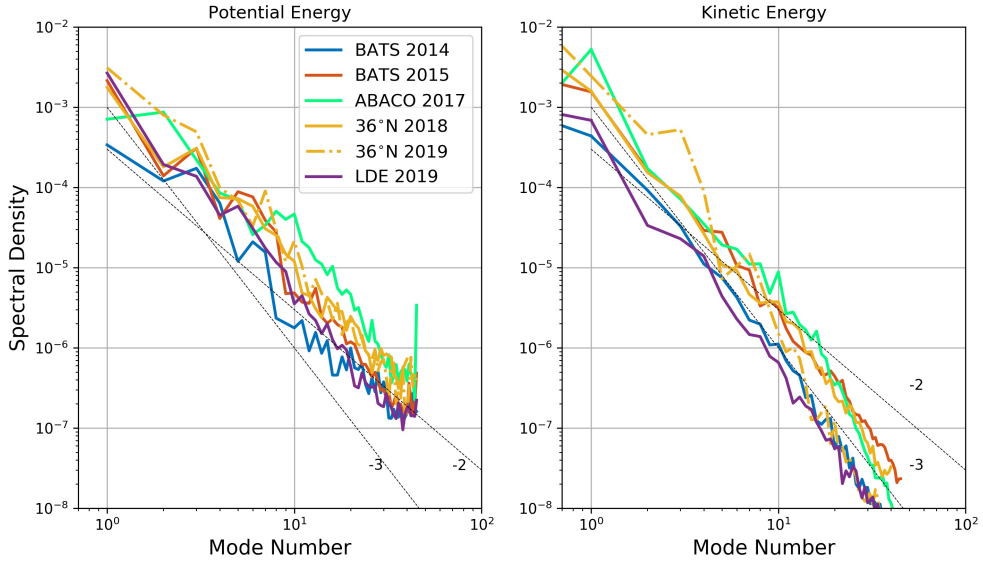

Figure 4.31: Water column average potential and kinetic energy per mode number. Reference slopes of k^{-2} and k^{-3} are in dashed black.

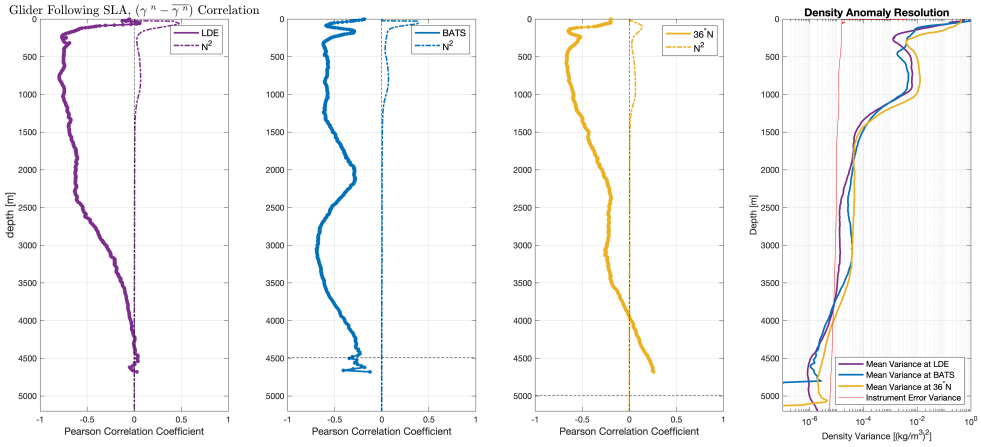

Figure 4.32: Linear correlation coefficients between density anomalies time series at each depth and glider-following sea level anomaly. Thin dash-dot lines are mean profiles at each site of the squared buoyancy frequency. Right Panel) mean density anomaly variance at each site vs. instrument density variance via simulated random instrument noise.

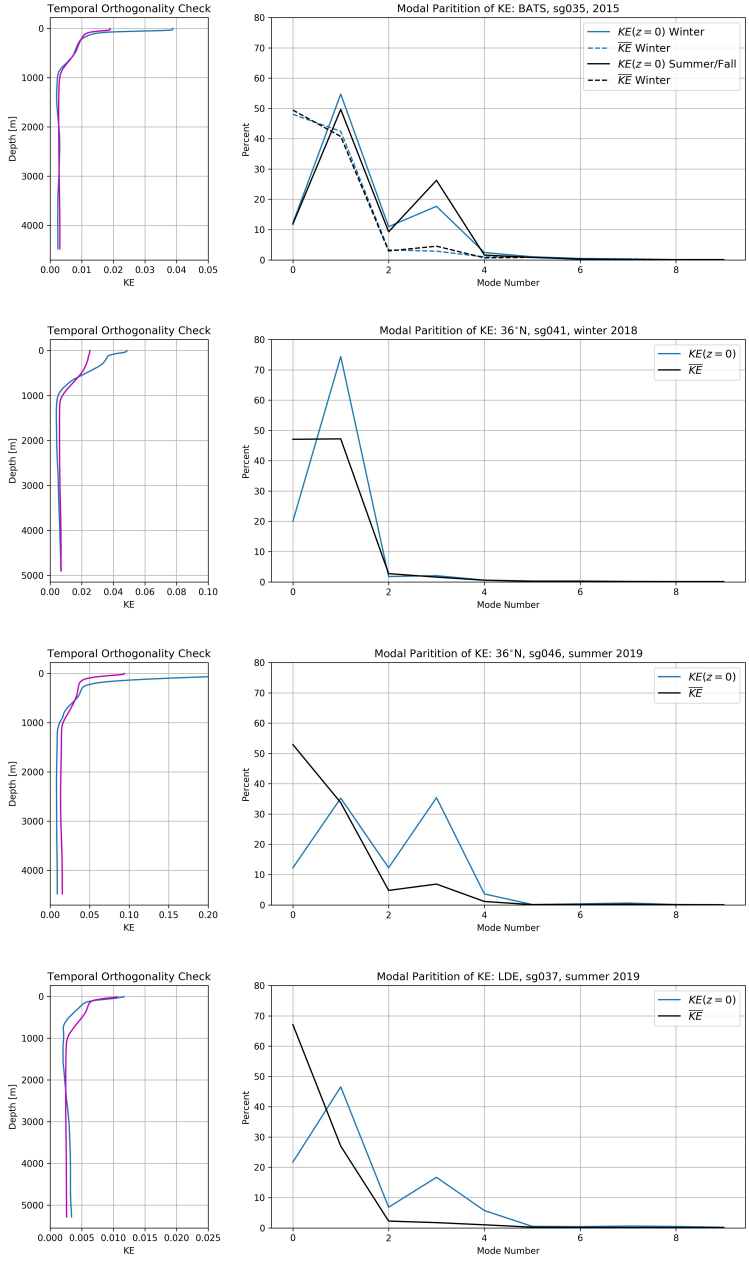

Figure 4.33: BATS 2015, 36°N (Winter) 2018, 36°N (Summer) 2019, LDE (Winter) 2019: Water column average and surface partition of kinetic energy across the first 9 modes. The left column shows as function of depth the difference between Eq. 118 and Eq. 119 and serves as an estimate of the degree of temporal mode amplitude correlation.

References

A. Alvarez and B. Mourre. Optimum sampling designs for a glider-mooring observing network. *Journal of Atmospheric and Oceanic Technology*, 29:601–612, 2016.

M. Andres, M. Siegelman, Hormann V., R.C. Musgrave, S.T. Merrifield, D.L. Rudnick, M.A. Merrifield, M.H. Alford, G. Voet, H.W. Wijesekera, J.A. MacKinnon, L. Centurioni, J.D. Nash, and E.J. Terrill. Eddies, topography, and the abyssal flow by the kyushu-palau ridge near velasco reef. *Oceanography*, 32:46–55, 2020.

L. Armi, D. Hebert, N. Oakey, J. F. Price, P. L. Richardson, T. H. Rossby, and B. Ruddick. Two Years in the Life of a Mediterranean Salt Lens. *Journal of Physical Oceanography*, 19:354–370, 1989.

G. Auad, D. Roemmich, and J. Gilson. The California Current System in relation to the Northeast Pacific Ocean circulation. *Progress in Oceanography*, 91:576–592, 2011.

S.D. Bachman, B. Fox-Kemper, and B. Pearson. A scale-aware subgrid model for quasi-geostrophic turbulence. *Journal of Geophysical Research: Oceans*, pages 1529–1553, 2017.

A. Bosse, P. Testor, L. Houpert, P. Damien, L. Prieur, D. Hayes, V. Taillandier, X. Durrieu de Madron, D. d'Ortenzio, L. Coppola, J. Karstensen, and L. Mortier. Scales and dynamics of Submesoscale Coherent Vortices formed by deep convection in the northwestern Mediterranean Sea. *Journal of Geophysical Research: Oceans*, 2016. doi: 10.1002/2016JC012144.

A.S. Bower, R.M. Hendry, D.E. Amrhein, and J.M. Lilly. Direct observations of formation and propagation of subpolar eddies into the subtropical north atlantic. *Deep-Sea Research II*, 85:15–41, 2013.

F. Bretherton, R. Davis, and Fandry C. A technique for objective analysis and design of oceanographic experiments applied to MODE-73. *Deep Sea Research*, 23:559–582, 1976.

O. Buhler, J. Callies, and R. Ferarri. Wave-vortex decomposition of one-dimensional ship-track data. *Journal of Fluid Mechanics*, 756:1007–1026, 2014.

J. Callies and R. Ferarri. Interpreting energy and tracer spectra of upper-ocean turbulence in the submesoscale range (1-200km). *Journal of Physical Oceanography*, 43:2456–2474, 2013.

J. Callies, Ferarri R., J.M. Klymak, and J. Gula. Seasonality in submesoscale turbulence. *Nature Communications*, 2015. doi: 10.1038/ncomms7862.

X. Capet, J. C. McWilliams, M. J. Molemaker, and A. F. Shchepetkin. Mesoscale to Submesoscale Transition in the California Current System. Part I: Flow Structure, Eddy Flux, and Observational Tests. *Journal of Physical Oceanography*, 38:29–43, 2008.

J. Charney. Geostrophic turbulence. *Journal of the Atmospheric Sciences*, 28:1087–1095, 1971.

E.P. Chassignet and X. Xu. Impact of horizontal resolution (1/12° to 1/50°) on gulf stream separation, penetration, and variability. *Journal of Physical Oceanography*, 47:1999–2021, 2017.

D. B. Chelton, M. G. Schlax, and R. M. Samelson. Global Observations of Nonlinear Mesoscale Eddies. *Progress in Oceanography*, 91:167–216, 2011.

T. K. Chereskin, P. P. Morris, P. M. Niiler, P. M. Kosro, R. L. Smith, S. R. Ramp, C. A. Collins, and D. L. Musgrave. Spatial and temporal characteristics of the mesoscale circulation of the California Current from eddy-resolving moored and shipboard measurements. *Journal of Geophysical Research: Oceans*, 105:1245–1269, 2000.

S.T. Cole and D.L. Rudnick. The spatial distribution and annual cycle of upper ocean thermohaline structure. *Journal of Geophysical Research: Oceans*, 117, 2012. doi: 10.1029/2011JC007033.

Curt A. Collins, Tetyana Margolina, Thomas A. Rago, and Leonid Ivanov. Looping RAFOS floats in the california current system. *Deep Sea Research Part II: Topical Studies in Oceanography*, 85:42–61, 2013.

Thomas P. Connolly, Barbara Hickey, Igor Shulman, and Richard E. Thomson. Coastal Trapped Waves, Alongshore Pressure Gradients, and the California Undercurrent. *Journal of Physical Oceanography*, 44:319–342, 2014.

Y. Cotroneo, G. Aulicino, S. Ruiz, A.S. Roman, M.T. Tomas, Pascual A., G. Fusco, E. Heslop, J. Tintore, and G. Budillon. Glider data collected during the algerian basin circulation unmanned survey. *Earth System Science Data*, 11:147–161, 2019.

E.A. D'Asaro. Observations of Small Eddies in the Beaufort Sea. *Journal of Geophysical Research: Oceans*, 93: 6669–6684, 1988a.

E.A. D'Asaro. Generation of submesoscale vortices: A new mechanism. *Journal of Geophysical Research: Oceans*, 93:6685–6693, 1988b.

M. S. de La Lama, J.H. LaCasce, and H.K. Fuhr. The vertical structure of ocean eddies. *Dynamics and Statistics of the Climate System*, pages 1–16, 2016.

W. K. Dewar and H. Meng. The propagation of submesoscale coherent vortices. *Journal of Physical Oceanography*, 25:1745–1770, 1995.

J. J. Early, R. M. Samelson, and D. B. Chelton. The Evolution and Propagation of Quasigeostrophic Ocean Eddies. *Journal of Physical Oceanography*, 41:1535–1555, 2011.

B.A. Elliot and T.B. Sanford. The Subthermocline Lens D1. Part II: Kinematics and Dynamics. *Journal of Physical Oceanography*, 16:549–561, 1986.

W.J. Emery and R.E. Thomson. *Data Analysis Methods in Physical Oceanography.* Pergamon, 1998.

C. C. Eriksen, T. J. Osse, R. D. Light, T. Wen, T. W. Lehman, P. L. Sabin, J. W. Ballard, and A. M. Chiodi. Seaglider: A long-range autonomous underwater vehicle for oceanographic research. *IEEE Journal of Oceanic Engineering*, 26:424–436, 2001.

C.C. Eriksen. Physical data collected from Seaglider SG189 during Cuddy Survey in the North Pacific Ocean, Coastal Waters of Washington/Oregon deployed from 2014-01-16 to 2014-04-27. NCEI Accession 0162344. Version 1.1. NOAA National Centers for Environmental Information. 2017a. `https://data.nodc.noaa.gov/cgi-bin/iso?id=gov.noaa.nodc:0162344`.

C.C. Eriksen. Physical data collected from Seaglider SG194 during Cuddy Survey in the North Pacific Ocean, Coastal Waters of Washington/Oregon deployed from 2013-10-25 to 2014-05-10. NCEI Accession 0162349. Version 1.1. NOAA National Centers for Environmental Information. 2017b. `https://data.nodc.noaa.gov/cgi-bin/iso?id=gov.noaa.nodc:0162349`.

C.C. Eriksen. Physical data collected from Seaglider SG195 during Cuddy Survey in the North Pacific Ocean, Coastal Waters of Washington/Oregon deployed from 2013-10-25 to 2014-02-22. NCEI Accession 0162357. Version 1.1. NOAA National Centers for Environmental Information. 2017c. https://data.nodc.noaa.gov/cgi-bin/iso?id=gov.noaa.nodc:0162357.

P. Flament. A State Variable for Characterizing Water Masses and their Diffusive Stability: Spiciness. *Progress in Oceanography*, 54:493–501, 2002.

G. R. Flierl. Models of vertical structure and the calibration of two-layer models. *Dynamics of Atmospheres and Oceans*, 2:341–381, 1978.

G. Forget, G. Maze, M. Buckley, and J. Marshall. Estimated seasonal cycle of north atlantic eighteen degree water volume. *Journal of Physical Oceanography*, 41:269–286, 2011.

L.L. Fu and G.R. Flierl. Nonlinear energy and enstrophy transfers in a realistically stratified ocean. *Dynamics of Atmospheres and Oceans*, 4:219–246, 1980.

N. Garfield, C.A. Collins, R.G. Paquette, and E. Carter. Lagrangian Exploration of the California Undercurrent, 1992-1995. *Journal of Physical Oceanography*, 29:560–583, 1999.

C. Garrett and W. Munk. Internal waves in the ocean. *Annual Reviews: Journal of Fluid Mechanics*, pages 339–369, 1979.

P. Gauthier, P. Courtier, and P. Moll. Assimilation of Simulated Wind Lidar Data with a Kalman Filter. *Monthly Weather Review*, 121:1803–1820, 1993.

A. Gelb. Applied Optimal Estimation. *MIT Press*, page 374 pp., 1974.

S.N. Giddings, P. MacCready, B.M. Hickey, N.S. Banas, K.A. Davis, S.A. Siedlecki, V.L. Trainer, R.M. Kudela, N.A. Pelland, and T.P. Connolly. Hindcasts of potential harmful algal bloom transport pathways on the pacific northwest coast. *Journal of Geophysical Research: Oceans*, 119:2439–2461, 2014.

Dave Hebert, Neil Oakey, and Barry Ruddick. Evolution of a Mediterranean Salt Lens: Scalar Properties. *Journal of Physical Oceanography*, 20:1468–1483, 1990.

B.M. Hickey. The California Current System - Hypotheses and Facts. *Progress in Oceanography*, 8:191–279, 1979.

James R. Holton. *An Introduction to Dynamic Meteorology*. Academic Press, 3 edition, 1972. ISBN 9780123543554.

B.L. Hua and D.B. Haidvogel. Numerical simulations of the vertical structure of quasi-geostrophic turbulence. *Journal of the Atmospheric Sciences*, 43:2923–2936, 1986.

A. Huyer, R. L. Smith, and B. M. Hickey. Observations of a warm-core eddy off Oregon, January to March 1978. *Deep-Sea Research*, 31(2):97–117, 1984.

A. Huyer, J.A. Barth, P.M. Korso, R.K. Shearman, and R.L. Smith. Upper-ocean water mass characteristics of the California Current, Summer 1993. *Deep-Sea Research II*, 45:1411–1442, 1998.

K Ide and M. Ghil. Extended Kalman filtering for vortex systems: Part I: Methodology and point vortices. *Dynamics of Atmospheres and Oceans*, 27:301–332, 1997a.

K Ide and M. Ghil. Extended Kalman filtering for vortex systems: Part II: Rankine vortices and observing-system design. *Dynamics of Atmospheres and Oceans*, 27:333–350, 1997b.

D.R. Jackett and T.J. McDougall. A neutral density variable for the world's oceans. *Journal of Physical Oceanography*, 27:237–263, 1997.

J. Jakoboski, R.E. Todd, W. Brechner Owens, K.B. Karnauskas, and D.L. Rudnick. Bifurcation and upwelling of the equatorial undercurrent west of the galapagos archipelago. *Journal of Physical Oceanography*, 2020. doi: 10.1175/JPO-D-19-0110.1.

T.M. Joyce. A note on the lateral mixing of water masses. *Journal of Physical Oceanography*, 7:626–629, 1977.

J. Kjellsson and L. Zanna. The impact of horizontal resolution on energy transfers in global ocean models. *Fluids*, 2017.

A. Klocker, Marshall D.P., S.R. Keating, and P.L. Read. A regime diagram for ocean geostrophic turbulence. *Quarterly Journal of the Royal Meteorological Society*, 142:2411–2417, 2016.

A.N. Kolmogorov. The local structure of turbulence in incompressible viscous fluids for very large reynolds numbers. *Dokl. Akad. Nauk SSSR*, 30:301, 1941.

R.H. Kraichnan. Inertial ranges in two-dimensional turbulence. *The Physics of Fluids*, 10:1417–1423, 1967.

J.H. LaCasce. The prevalence of oceanic surface modes. *Geophysical Research Letters*, pages 11097–11105, 2017.

G. Lapeyre and P. Klein. Dynamics of the upper oceanic layers in terms of surface quasi-geostrophic theory. *Journal of Physical Oceanography*, 36:165–176, 2006.

P. Le Traon. A method for optimal analysis of fields with spatially variable mean. *Journal of Geophysical Research: Oceans*, 95:13543–13547, 1990.

M.S. Lozier and M.C. Iorga. Signatures of the mediterranean outflow from a north atlantic climatology 1. salinity and density fields. *Journal of Geophysical Research*, 104:25985–26009, 1999.

M.S. Lozier and N.M. Stewart. Notes and correspondence: On the temporally varying temporal northward penetration of mediterranean overflow water and eastward penetration of labrador sea water. *Journal of Physical Oceanography*, 38:2097–2103, 2008.

Roger Lukas and Fernando Santiago-Mandujano. Extreme water mass anomaly observed in the Hawaii Ocean Time-series. *Geophysical Research Letters*, 28:2931–2934, 2001.

J.P. Martin, C. M. Lee, C.C. Eriksen, C. Ladd, and N.B. Kachel. Glider observations of kinematics in a Gulf of Alaska eddy. *Journal of Geophysical Research: Oceans*, 114:C021, 2009.

Trevor J. McDougall. The Vertical Motion of Submesoscale Coherent Vortices across Neutral Surfaces. *Journal of Physical Oceanography*, 17:2234–2342, 1987.

James C. McWilliams. Submesoscale, Coherent Vortices in the Ocean. *Reviews of Geophysics*, 23:165–182, 1985.

James C. McWilliams. Vortex Generation Through Balanced Adjustment. *Journal of Physical Oceanography*, 18: 1178–1192, 1988.

James C. McWilliams. Submesoscale Currents in the Ocean. *Proc. R. Soc. A*, 472, 2016.

James C. McWilliams and Peter R. Gent. The Evolution of Sub-Mesoscale Coherent Vortices on the β-plane. *Geophysical Astrophysical Fluid Dynamics*, 35:235–255, 1986.

James C. McWilliams, Peter R. Gent, and Nancy J. Norton. The Evolution of Balanced, Low-Mode Vortices on the β-plane. *Journal of Physical Oceanography*, 16:838–855, 1985.

J.C. McWilliams. Statistical properties of decaying geostrophic turbulence. *Journal of Fluid Mechanics*, 198: 199–230, 1989.

J.C. McWilliams, E.D. Brown, H.L. Bryden, C.C. Ebbesmeyer, B.A. Elliot, R.H. Heinmiller, B. Lien Hua, Leaman K.D., E.J. Lindstrom, J.R. Luyten, S.E. McDowell, W. Breckner Owens, H. Perkins, J.F. Price, L. Regier, H.T. Rossby, T.B. Sanford, C.Y. Shen, B.A. Taft, and J.C. Van Leer. The local dynamics of eddies in the western north atlantic. *Eddies in Marine Science, Springer-Verlag*, pages 92–113, 1983.

M. Jeroen Molemaker, James C. McWilliams, and William K. Dewar. Submesoscale Instability and Generation of Mesoscale Anticyclones near a separation of the California Undercurrent. *Journal of Physical Oceanography*, 45: 613–629, 2015.

Yves Morel and James McWilliams. Evolution of Isolated Interior Vortices in the Ocean. *Journal of Physical Oceanography*, 27:727–748, 1997.

N.A. Pelland, C.C. Eriksen, and C. Lee. Subthermocline eddies over the washington continental slope as observed by seagliders. *Journal of Geophysical Research: Oceans*, 43:2025–2053, 2013. doi: 10.1175/JPO-D-12-086.1.

N.A. Pelland, C.C. Eriksen, and M.F. Cronin. Seaglider Surveys at Ocean Station Papa: Circulation and Water Mass Properties in a Meander of the North Pacific Current. *Journal of Geophysical Research: Oceans*, 121: 6816–6846, 2016.

N.A. Pelland, J.S. Bennett, J.M. Steinberg, and C.C. Eriksen. Automated Glider Tracking of a California Undercurrent Eddy Using the Extended Kalman Filter. *Journal of Atmospheric and Oceanic Technology*, In Press. doi: 10.1175/JTECH-D-18-0126.1.

M.D. Prater and T. Rossby. An alternative hypothesis for the origin of the "mediterranean" salt lens observed off the bahamas in the fall of 1976. *Journal of Physical Oceanography, Notes and Correspondence*, 29:2103–2109, 1999.

B. Qui and S. Chen. Seasonality in transition scale from balanced to unbalanced motions in the world ocean. *Journal of Physical Oceanography*, 48:591–605, 2018.

B. Qui, S. Chen, P. Klein, H. Sasaki, and Y. Sasai. Seasonal mesoscale and submesoscale eddy variability along the north pacific subtropical countercurrent. *Journal of Physical Oceanography*, 44:3079–3098, 2014.

P.B. Rhines. The dynamics of unsteady currents. *The Sea*, pages 189–318, 1977.

P.B. Rhines. Geostrophic turbulence. *Annual Reviews of Fluid Mechanics*, 11:401–441, 1979.

C.B. Rocha, T.K. Chereskin, and S.T. Gille. Mesoscale to submesoscale wavenumber spectra in drake passage. *Journal of Physical Oceanography*, 46:601–620, 2016.

M. Roughan, S.R. Keating, A. Schaeffer, P. Cetina Heredia, C. Rocha, D. Griffin, R. Robertson, and I.M. Suthers. A tale of two eddies: The biophysical characteristics of two contrasting cyclonic eddies in the East Australian Current System. *Journal of Geophysical Research: Oceans*, 122:2492–2518, 2017.

B. Ruddick and K. Richards. Oceanic thermohaline intrusions: observations. *Progress in Oceanography*, 56:499–527, 2003.

D.L. Rudnick and S.T. Cole. On sampling the ocean using underwater gliders. *Journal of Geophysical Research: Oceans*, 116:C08010, 2011. doi: 10.1029/2010JC006849.

D.L. Rudnick, R.E. Davis, and J.T. Sherman. Spray underwater glider operations. *Journal of Atmospheric and Oceanic Technology*, 33:1113–1122, 2016.

D.L. Rudnick, J.T. Sherman, and A.P. Wu. Depth-average velocity from spray underwater gliders. *Journal of Atmospheric and Oceanic Technology*, 35:1665–1673, 2018.

R.B. Scott and F. Wang. Direct evidence of an oceanic inverse energy cascade from satellite altimetry. *Journal of Physical Oceanography*, 35:1650–1666, 2005.

A.Y. Shcherbina, M.C. Gregg, M.H. Alford, and R.R. Harcourt. Characterizing Thermohaline Intrusions in the North Pacific Subtropical Frontal Zone. *Journal of Physical Oceanography*, 39:2735–2756, 2009.

A.Y. Shcherbina, M.C. Gregg, M.H. Alford, and R.R. Harcourt. Three-Dimensional Structure and Temporal Evolution of Submesoscale Thermohaline Intrusions in the North Pacific Subtropical Frontal Zone. *Journal of Physical Oceanography*, 40:1669–1689, 2010.

J. J. Simpson, T. D. Dickey, and C. J. Koblinsky. An Offshore Eddy in the California Current System. Part I: Interior Dynamics. *Progress in Oceanography*, 13:5–49, 1984.

K.S. Smith. The geography of linear baroclinic instability in earth's oceans. *Journal of Marine Research*, 65: 655–683, 2007.

S. Smith and R. Ferarri. The production and dissipation of compensated thermohaline variance by mesoscale stirring. *Journal of Physical Oceanography*, 39:2477–2501, 2009.

S. Smith and G. Vallis. The scales and equilibrium of midocean eddies: Freely evolving flow. *Journal of Physical Oceanography*, 31:554–571, 2001.

H. von Storch and F.W. Zwiers. *Statistical Analysis in Climate Research*. Cambridge University Press, 2 edition, 2003. ISBN 0521012309.

S. Thomsen, T. Kanzow, G. Krahmann, R.J. Greatbatch, M. Dengler, and G. Lavik. The formation of a subsurface anticyclonic eddy in the Peru-Chile Undercurrent and its impact on the near-coastal salinity, oxygen, and nutrient distributions. *Journal of Geophysical Research: Oceans*, 121:476–501, 2016.

R.E. Thomson and M.V. Krassovski. Poleward reach of the California Undercurrent extension. *Journal of Geophysical Research: Oceans*, 115:C09027, 2010.

R.E. Thomson and M.V. Krassovski. Remote alongshore winds drive variability of the California Undercurrent off the British Columbia-Washington coast. *Journal of Geophysical Research: Oceans*, 120:8151–8176, 2015.

M.L. Timmermans and P. Winsor. Scales of horizontal density structure in the chukchi sea surface layer. *Continental Shelf Research*, 52:39–45, 2013.

R.E. Todd, D.L. Rudnick, M.R. Mazloff, R.E. Davis, and B.D. Cornuelle. Poleward flows in the southern california current system: Glider observations and numerical simulation. *Journal of Geophysical Research: Oceans*, 116, 2011. doi: 10.1029/2010JC006536.

K.S. Tokos and T. Rossby. Kinematics and Dynamics of a Mediterranean Salt Lens. *Journal of Physical Oceanography*, 21:879–892, 1991.

H. S. Torres and J. Gomez-Valdes. Erosion of a California Undercurrent eddy by bottom topography. *Journal of Geophysical Research: Oceans*, 122, 2017. doi: 10.1002/2016JC011870.

R. Tulloch, J. Marshall, and K.S. Smith. Interpretation of the propagation of surface altimetric observations in terms of planetary waves and geostrophic turbulence. *Journal of Geophysical Research*, 114, 2009. doi: doi:10.1029/2008JC005055.

T. Uchida, R. Abernathy, and S. Smith. Seasonality of eddy kinetic energy in an eddy permitting global climate model. *Ocean Modelling*, 118:41–58, 2017.

A. Vallgren and E. Lindborg. Charney isotropy and equipartition in quasi-geostrophic turbulence. *Journal of Fluid Mechanics*, 656:448–457, 2010.

G.K. Vallis. *Atmospheric and Oceanic Fluid Dynamics: Fundamentals and Large-Scale Circulation*. Cambridge University Press, 1 edition, 2013. ISBN 9780521849692.

T. Wagawa, Kawaguchi Y., Y. Igeta, Honda N., T. Okunishi, and I. Yabe. Observations of oceanic fronts and water-mass properties in the central japan sea: Repeated surveys from an underwater glider. *Journal of Marine Systems*, 201, 2020.

C. Wunsch. The vertical partition of oceanic horizontal kinetic energy. *Journal of Physical Oceanography*, 27: 1770–1794, 1997.

C. Wunsch and D. Stammer. Atmospheric loading and the oceanic "inverted barometer" effect. *Reviews of Geophysics*, 35:79–107, 1997a.

C. Wunsch and D. Stammer. Atmoshperic loading and the oceanic "inverted barometer" effect. *Reviews of Geophysics*, 35:79–107, 1997b.

X. Xu, P.B. Rhines, and E.P. Chassignet. Temperature-salinity structure of the north atlantic circulation and associated heat and freshwater transports. *Journal of Climate*, 29:7723–7742, 2016.

Y. Xu and L.L. Fu. Global variability of the wavenumber spectrum of oceanic mesoscale turbulence. *Journal of Physical Oceanography*, pages 802–809, 2010.

L. Yu, A. Bosse, I. Fer, K.A. Orvik, E.M. Bruvik, I. Hessevik, and K. Kvalsund. The Lofoten Basin eddy: Three years of evolution as observed by Seagliders. *Journal of Geophysical Research: Oceans*, 122:6814–6834, 2017.

M. Zhao, M.L. Timmermans, R. Krishfield, and G. Manucharyan. Partitioning of kinetic energy in the arctic ocean's beaufort gyre. *Journal of Geophysical Research: Oceans*, pages 4806–4819, 2018.

Z. Zhao. Global observations of open-ocean mode-1 m2 internal tides. *Journal of Physical Oceanography*, 46: 1657–1684, 2016.